DOE/ER-0046/11

Damage Analysis and Fundamental Studies

Quarterly Progress Report
July-September 1982

November 1982

U.S. Department of Energy
Assistant Secretary for Energy Technology
Office of Fusion Energy
Washington, DC 20545

NOTICE

Printed in the United States of America
Available from
National Technical Information Service
U.S. Department of Commerce
5285 Port Royal Road
Springfield, VA 22161

NTIS price codes
Printed copy: A12
Microfiche copy: A01

DOE/ER-0046/11
UC-20,20c

Damage Analysis and Fundamental Studies

Quarterly Progress Report
July-September 1982

November 1982

U.S. Department of Energy
Assistant Secretary for Energy Technology
Office of Fusion Energy
Washington, DC 20545

FOREWORD

This report is the nineteenth in a series of Quarterly Technical Progress Reports on *Damage* Analysis and Fundamental Studies (DAFS), which is one element of the Fusion Reactor Materials Program, conducted in support of the Magnetic Fusion Energy Program of the U.S. Department of Energy (DOE). The first eight reports in this series were numbered DOE/ET-0065/1 through 8. Uther elements of the Fusion Materials Program are:

- Alloy Development far Irradiation Performance (ADIP)
- Plasma-Materials Interaction (PMI)
- Special Purpose Materials (SPM).

The DAFS program element is a national effort composed of contributions from a number of National Laboratories and other government laboratories, universities, and industrial laboratories. It was organized by the Materials and Radiation Effects Branch, DOE/Office of Fusion Energy, and a Task Group on Damage *Analysis* and Fundamental Studies, which operates under the auspices of that branch. The purpose of this series of reports is to provide a working technical record of that effort for the use of the program participants, the fusion energy program in general, and the DOE.

This report is organized along topical lines in parallel to a Program Plan of the same title so that activities and accomplishments may be followed readily, relative to that Program Plan. Thus, the work of a given laboratory may appear throughout the report. The Contents is annotated for the convenience of the reader.

This report has been compiled and edited under the guidance of the Chairman of the Task Group on *Damage* Analysis *and* Fundamental Studies, D. G. Doran, Hanford Engineering Development Laboratory (HEDL). His efforts, those of the supporting staff of HEDL, and the many persons who made technical contributions are gratefully acknowledged. M. M. Cohen, Materials and Raaiation Effects Branch, is the DOE counterpart to the Task Group Chairman and has responsibility for the DAFS program within DOE.

G. M. Haas, Acting Chief
Materials and Radiation Effects Branch
Office of Fusion Energy

CONTENTS

FIGURES

Page

CHAPTER 1

1. RTNS-II Irradiation and Operations (LLNL)

'2. Dual-Temperature Vacuum-Insulated Furnace System (HEDL)

FIGURES (Cont'd)

CHAPTER 3

1. Developments in Small-scale Strength and Impact Testing (UCSB)

FIGURES (Cont'd)

FIGURES (Cont'd)

FIGURES (Cont'd)

FIGURES (Cont'd)

FIGURES (Cont'd)

FIGURES (Cont'd)

FIGURES (Cont'd)

FIGURES (Cont'd)

Page

5. Dependence of Swelling of Fe-Ni-Cr Alloys on Chromium and Nickel Content (HEDL)

TABLES

TABLES (Cont'd)

TABLES (Cont'd)

CHAPTER 1

IRRADIATION TEST FACILITIES

RTNS-II IRRADIATIONS AND OPERATIONS

C. M. Logan and D. W. Heikkinen (Lawrence Livermore National Laboratory)

1.0 Objective

The objectives of this work are operation of RTNS-II (a 14-MeV neutron source facility), machine development, and support of the experimental program that utilizes this facility. Experimenter services include dosimetry handling, scheduling, coordination, and reporting. RTNS-II is dedicated to materials research for the fusion power program. Its primary use is to aid in the development of models of high-energy neutron effects. Such models are needed in interpreting and projecting to the fusion environment engineering data obtained in other neutron spectra.

2.0 Summary

Irradiations were performed for a total of twenty-nine different experimenters during this quarter.

A JEOL 200 CX TEM and other post-irradiation test equipment have been installed.

The last of the present inventory of 50-cm targets was consumed. Performance of these targets was as expected. Conversion to 23-cm targets was accomplished in August.

The second meeting of the U.S./Japan RTNS-II Steering Committee was rescheduled for February 1983.

3.0 Program

Title: RTNS-II Operations (WZJ-16)
Principal Investigator: C. M. Logan
Affiliation: Lawrence Livermore National Laboratory

4.0 Relevant DAFS Program Plan Task/Subtask

TASK II.A.2,3,4.
TASK II.B.3.4
TASK II.C.1,2,6,11,18.

5.0 Irradiation - C. M. Logan, D. W. Heikkinen and M. W. Guinan

The irradiation of Nb, V and Ni for D. Kaletta (Karlsruhe) was completed early in July. The Kaletta capsule was thin (~2 mm) so it was combined with J. Fowler's (LANL) MACOR for effective use of neutrons.

This was followed by a capsule for Kiritani (Hokkaido). This capsule contained a large number of specimens, mostly TEM disks, from many Japanese scientists. Some of these had a beginning microstructure which had been introduced in the HVEM. "Before" photographs had been prepared in Japan before shipment.

In August, we ran for P. Cannon (HEDL). This assembly contained various components and systems which will be utilized in the FMIT Facility.

This was followed by an in-situ measurement of creep in Ni by W. Barmore (LLNL), then resumption of Fowler's (LANL) MACOR.

R. Hopper has conducted an ongoing series of experiments using the "background" thermal neutron flux in the target room. These experiments are investigating a possible method for treatment of optical material to create a broad-band anti-reflective surface "coating". The optical material is placed in contact with a foil of ^{235}U. Fission fragments from the fissioning uranium leave damage tracks in the sample which can be etched. The resulting pitted surface exhibits anti-reflective properties.

Experiments by R. Mallon (LLNL) have continued studying mass transport in a fluidized bed of oil shale. Mallon installed a rabbit system to permit rapid retrieval of an activated oil shale sample from the target room. These samples are positioned ~0.5 m from the neutron source.

Radiation detectors are used to observe movement of the activated material in the fluidized bed. The budget for this work has been sharply reduced in FY 83. Measurements will probably cease soon.

We have begun irradiating more Si for G. Woolhouse (Aracor) to study by TEM. R. Borg's (LLNL) mineral irradiations continue. Fluence is accumulating on K. Kawamura's (TIT) amorphous metal and C. Snead's (BNL) superconductors. These experimenters a17 desire $>10^{17}$ n/cm^2 but *do* not, in general, occupy the highest flux region of the available test volume.

T. Iida (Osaka) has conducted many irradiations, mostly add-on. In this quarter he irradiated: fiber optics, transistors, integrated circuits, synthetic quartz, a photomultiplier tube, diodes, ZnS, LED circuits, a solid state detector, CsI, and plastic scintillators.

5.1 RTNS-II Status - C. M. Logan and D. W. Heikkinen

Target lifetime of the 50-cm diameter targets was considerably better than the 23-cm targets. Neutron production as a function of incident deuterons for these targets is well represented by a function *of* the form:

$$y = A_1(1-e^{-A_2 \cdot X})$$

where

y = total neutron production (units of 10^{18} neutrons)
X = total incident deuterons (units of 10^{23} deuterons)

A_1 and A_2 are constants determined by a non-linear least squares fitting procedure and are given in units of 10^{18} neutrons (10^{18} n) and 10^{-24}/incident deuteron ($10^{-24}/d^+$), respectively. As can be seen from Fig. 1, the fitted points agree very well with the data. The agreement is generally within 2%.

Differences in neutron production rate are perhaps better illustrated by considering that

$$dy/dx = (A_1 \cdot A_2)e^{-A_2 \cdot X}$$

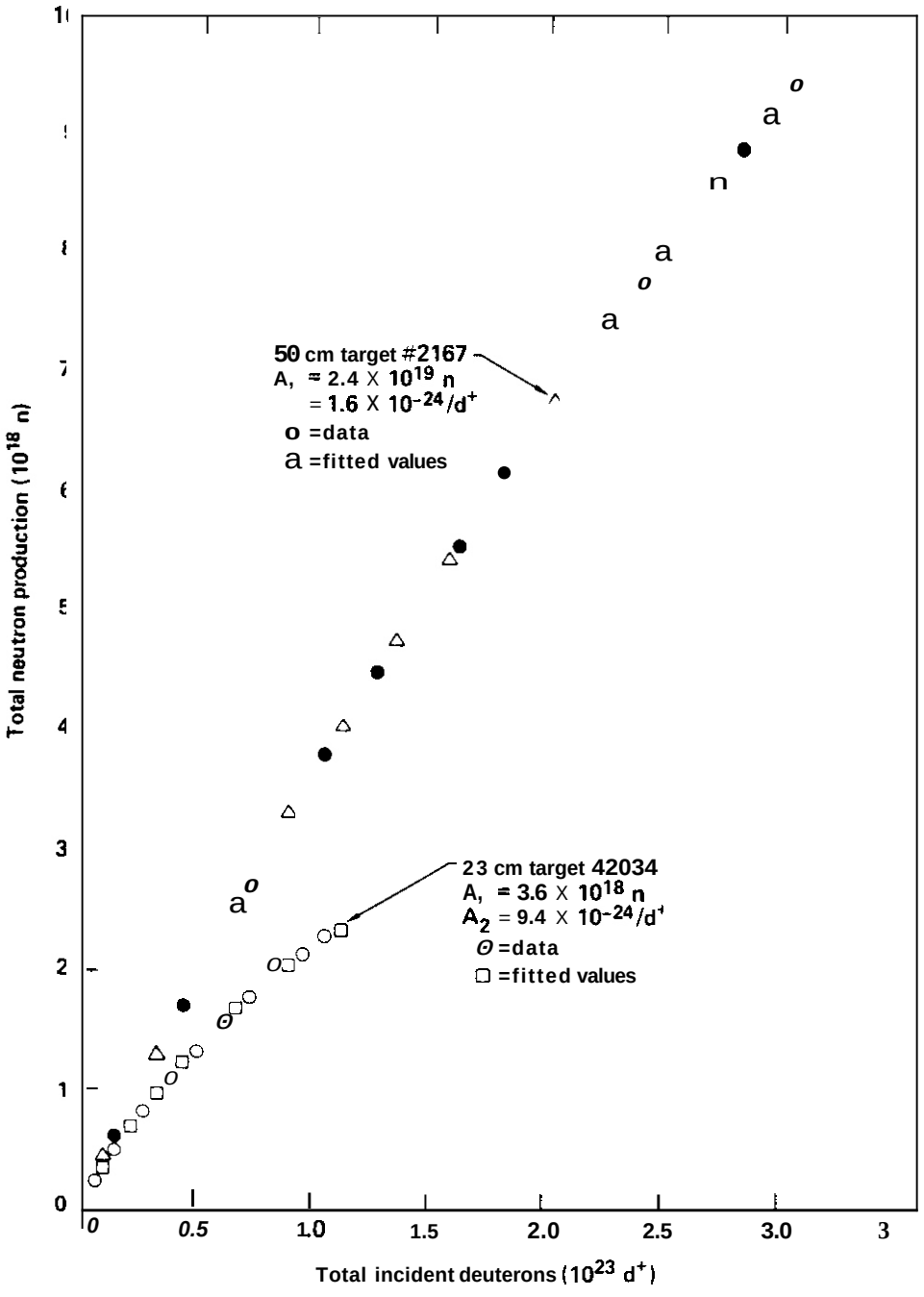

FIGURE 1. Plots of Total Neutron Production vs Total Incident Deuterons for "Average" 23- and 50-cm Targets. Also shown are the fitted values (see text). The data points represent only a subset of the data used in the fitting procedure.

Semi-log plots of this function are shown in Fig. 2 for the same targets as shown in Fig. 1. The y axis intercept gives the initial yield of the target (n/d^+) and the slope an indication of the tritium depletion rate of the target. To illustrate more clearly the difference in depletion rates, Fig. 2 also shows the effect of inadvertent air exposure of a partially used target (#2017). In this case, the target shows a very large depletion rate of tritium.

We have completed this trial run of 50-cm targets. Production of additional substrates was initiated in April 1982. Completed targets are expected early in 1983. In the meantime, operations will be continued with 23-cm targets. The rotating assembly was converted in August.

Soon after changing to 23-cm target operation, we experienced a failure of a commercial brass fitting in an air supply line which provides lift-off air for the target vacuum seal. The ensuing wreck was the major cause of unscheduled outage this quarter. Neutron production also suffered from poor target performance. Twelve 23-cm targets which were stored for about one year as backup for 50-cm operations are no good. Storage conditions are probably the cause. New targets are now on hand.

Sargent Welch turbomolecular vacuum pumps continue to be a major maintenance problem. Three pump failures occurred this period. We are converting to Balzers pumps as rapidly as budget and system redesign permit.

We have received new ion source arc power supplies. Results of right machine testing are encouraging. We will install the supply on the left machine at the first practical opportunity. The order has been placed for higher voltage and current extraction supplies. Delivery is expected in the summer of 1983.

A considerable quantity of post-irradiation test equipment has now been installed at RTNS-II. A room originally destined to house a Van de Graaff accelerator was converted to this use. A new JEOL 200 CX TEM is the principal occupant. We have moved our tritium contaminated SEM to this room. A dark room has also been constructed.

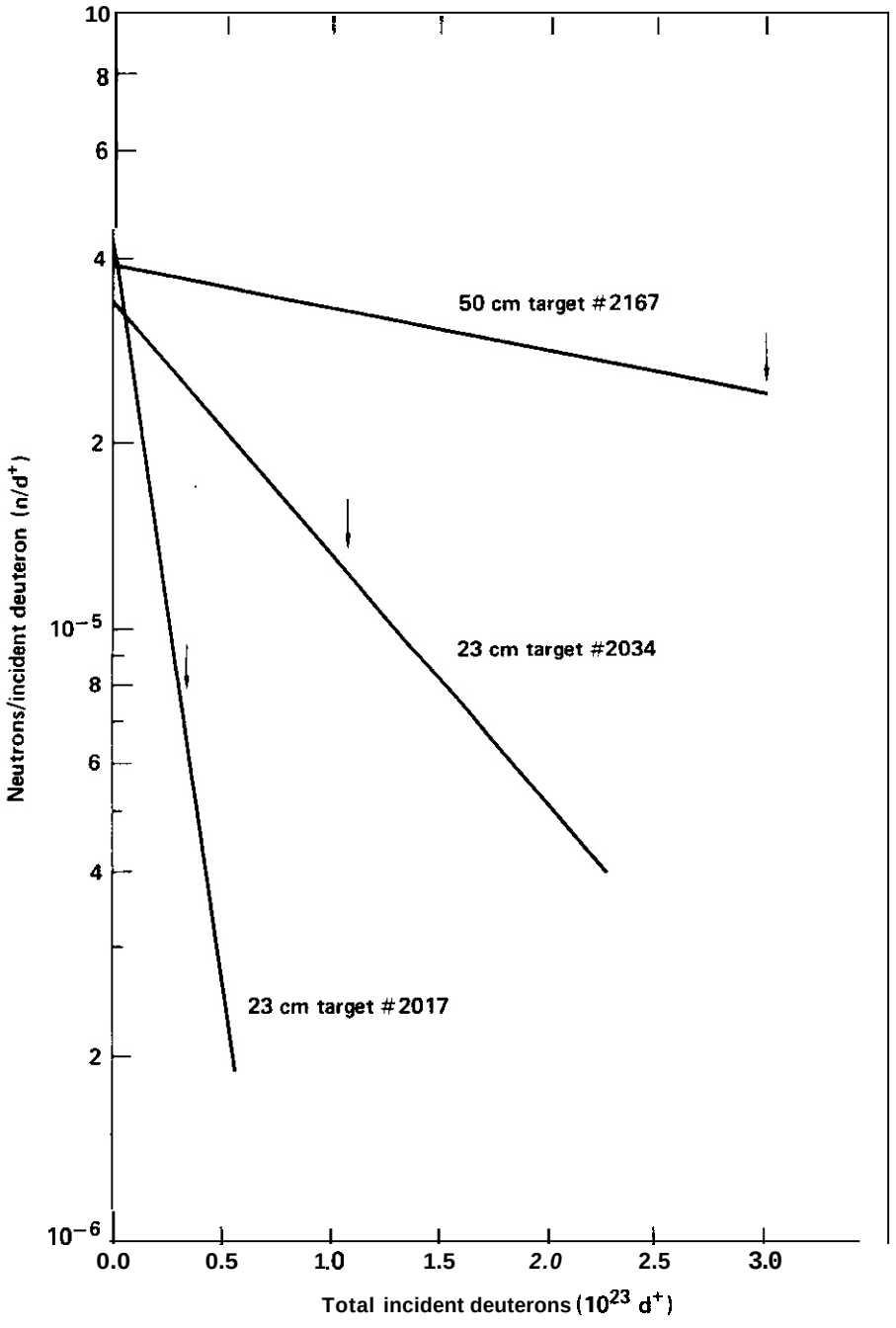

FIGURE 2. Neutron Production Rates vs The Number of Incident Deuterons for the Same Targets as in Figure 1. Also shown in the neutron production rate for a target showing a high depletion rate (see text). These are derived using values of A_1 and A_2 determined in the fitting procedure. The arrows indicate the total number of deuterons incident on each target.

6.0 Future Work

Irradiation of MACOR for J. Fowler (LANL) will continue. Cryogenic irradiation of magnet stabilizer copper for M. Guinan (LLNL) will be performed. Add-ons for T. Iida (Osaka), R. Borg (LLNL) and G. Woolhouse (Aracor) are planned. R. Hartman (Northrop) will resume exposures of LSI circuits. A non-fusion experiment for T. Norris (LANL) is planned.

The second meeting of the U.S./Japan RTNS-II Steering committee will be held February 10-11, 1982.

An upgraded ion source arc power supply will be installed on the left machine. Tests will begin of redesigned ion source electrode apertures. Orders will be placed for prototypes of redesigned accelerator column components.

6.1 Publications

Tritium Targets at RTNS-II, D. W. Heikkinen and C. M. Logan, to be presented at 11th World Conference of the International Nuclear Target Development Society, Seattle, Washington, October 6-8, 1982. UCRL 87806

~~Guide for~~ Experimenters Rotating Target Neutron Source ~~II~~, Manual LLNL M-094 Rev. 1.

High Speed Rotating Vacuum Seal, J. L. Garibaldi and C. M. Logan, submitted to Nuclear Instruments and Methods.

THE DUAL-TEMPERATURE VACUUM-INSULATED FURNACE SYSTEM

N. F. Panayotou (Westinghouse Hanford Company)

1.0 Objective

The objective of this work is to determine the effects of high energy neutrons on damage production and evolution, and the relationship of these effects to effects produced by fission reactor neutrons. The specific objective of the current work is to develop a furnace system which will efficiently utilize the primary irradiation volume of the Rotating Target Neutron Source (RTNS)-II.

2.0 Summary

A new furnace, the Dual-Temperature Vacuum-Insulated (DTVI) furnace system is available for use at the RTNS-II facility. Using this furnace system experimenters can irradiate specimens simultaneously at two closely controlled temperatures, under high vacuum conditions in the primary irradiation volume of RTNS-II. The DTVI furnace system was designed to be reliable and to be easily maintained and operated.

3.0 Program

Title: Irradiation Effects Analysis (AKJ)
Principal Investigator: D. G. Doran
Affiliation: Westinghouse Hanford Company

4.0 Relevant DAFS Program Plan Task/Subtask

Task II.B.3 Experimental Primary Damage State
Task II.C.6 Effect of Rate and Cascades on Microstructure
Task II.C.ll Effect of Cascades and Flux on Flow
Task II.C.14 Models of Flow and Fracture Under Irradiation
Task II.C.17 Microstructural Characterization
Task II.C.18 Relating Low and High-Exposure Microstructures

5.0 Accomplishments and Status

5.1 Introduction

The radiation damage sustained by structural metals is an important consideration in the design of fusion power plants. Next generation fusion devices will subject structural metals to a high energy neutron environment while operating at temperatures in the range 50 to 500°C. The extrapolation of fission reactor data to cover the effects of high-energy neutrons on the mechanical properties of structural metals is not reliable without a better knowledge of the effect of neutron spectrum on neutron induced property changes. Therefore, elevated temperature high energy neutron irradiation experiments must be conducted in support of the fusion materials development program. The Rotating Target Neutron Source (RTNS)-II is a 14-MeV neutron source dedicated *to* fusion materials research.

Current high-energy neutron sources such as the RTNS-II are characterized by a relatively low peak neutron flux and by a rapid decrease in neutron flux with distance from the source. Accordingly, elevated temperature experimental systems designed for use at a facility like RTNS-II must permit the positioning of specimens within the primary irradiation volume while maintaining a controlled environment and minimizing specimen thermal gradients. An innovative system, the Dual-Temperature Vacuum-Insulated furnace system, has been designed and built for this purpose and is currently available at the RTNS-II facility. The purpose of this report is to provide potential users with general information on the design, performance and operation of the DTVI furnace system.

5.2 Furnace System Design

5.2.1 Design Requirements

The furnace system was required to provide two temperature zones, each having equal access to the neutron flux; to minimize temperature gradients in either

zone; to permit a maximum temperature of 400°C and to allow the temperature differential between the zones to be controllable over a wide range; to provide a controlled atmosphere; *to* minimize the added separation between neutron source and specimens due to the furnace; to heat or cool specimens within thirty minutes and to minimize the residual induced radioactivity of the furnace system. Specific requirements were also imposed on this furnace system by the facility. The geometrical configuration had to permit full scanning of the rotating oscillating targets and system reliability had to preclude extended down time due to failures of heaters and vacuum system components.

5.2.2 System Overview

The assembled furnace system is shown in Figures 1 and 2. The two furnace half cores, Figure 2, are mounted on a standard six-inch stainless steel conflat flange. Specimens are contained within the half cores, each of which functions as a separate temperature zone. Each half core is connected to the conflat flange by three large diameter heater or gas cooling wells and one small diameter thermocouple well. Heaters and thermocouples positioned in these wells are in good thermal contact with the half cores and are also accessible since the wells open on the conflat flange. This furnace core assembly is positioned within an ultra high vacuum (UHV) enclosure. Using bakable all metal UHV valves the enclosure can be connected to either a turbomolecular-mechanical vacuum pump combination or to a 20 ℓ/s ion pump. During irradiation only the ion pump, which contains no moving parts, is employed. The other system is valved off and shut down, thus precluding down time due to the failure of mechanical type vacuum components (a problem which plagued previous furnace systems). The vacuum system also includes an up-to-air valve and a thermocouple (TC) type vacuum gage, Figure 1. Pressure readings in the high and ultra high vacuum range are obtained directly from the ion pump control unit. Typical pressures at the ion pump flange are in the range $1 \cdot 10^{-8}$ torr. Pressures at the specimen positions within the furnace core have been estimated to be in the low 10^{-6} torr range.

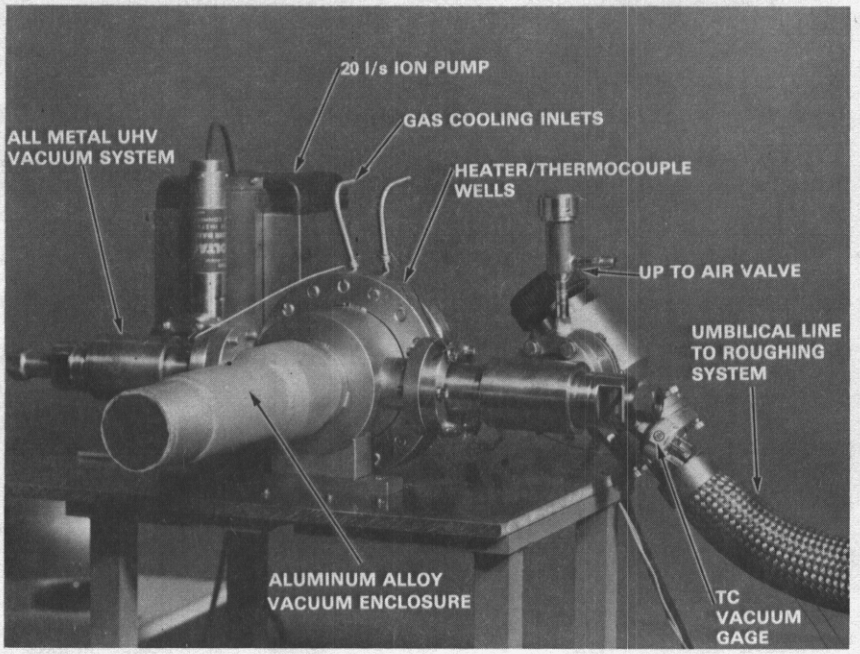

FIGURE 1. View of the Assembled Dual-Temperature Vacuum-Insulated (DTVI) Furnace System.

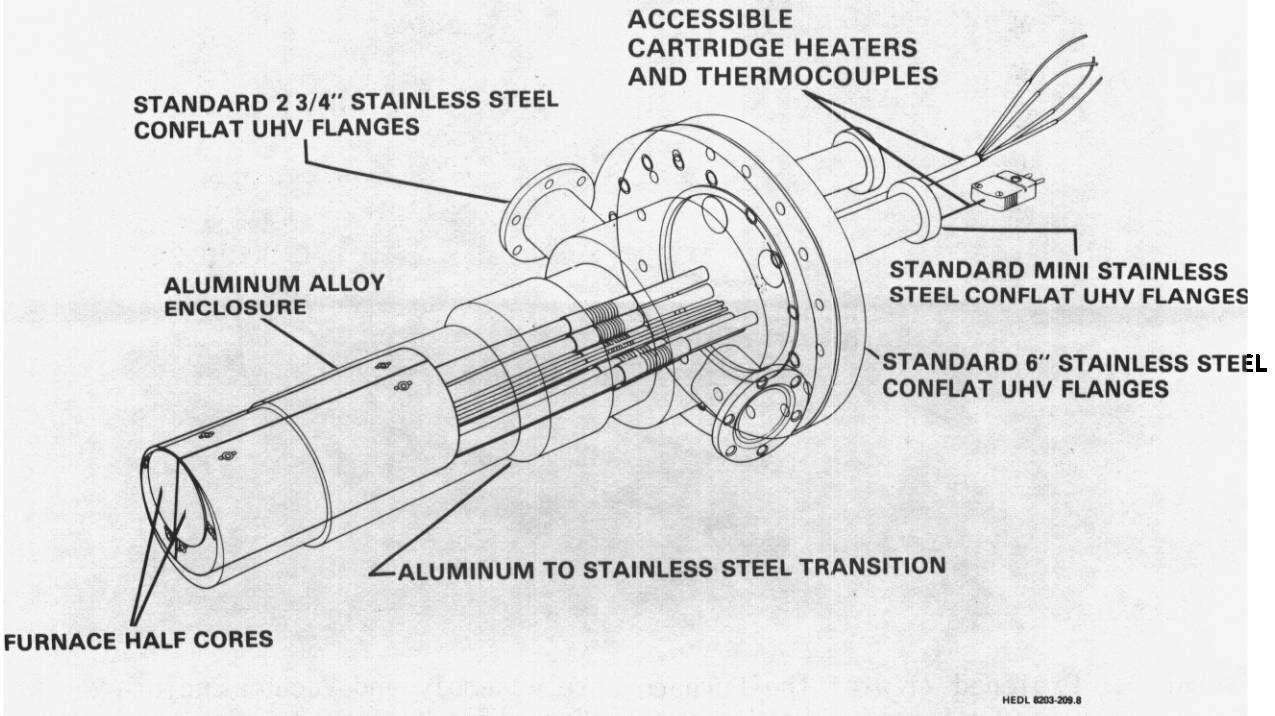

FIGURE 2. Detail of the Furnace Core Assembly and Ultra-High Vacuum (UHV) Enclosure.

5.2.3 System Details

An exploded view of the vacuum enclosure and furnace core assembly is shown in Figure 3. Cartridge type heaters, Figures 2 and 3, are inserted in the large diameter wells which are also used to permit nitrogen gas to be circulated through each furnace half core. The furnace was designed so that up to three cartridge heaters could be positioned within each furnace half core. Furthermore, each heater contains three independent windings arranged in a linear array. However, it was determined that just one heater in each furnace core operating with only its center winding was able to heat each core to the required temperature within one-half hour.

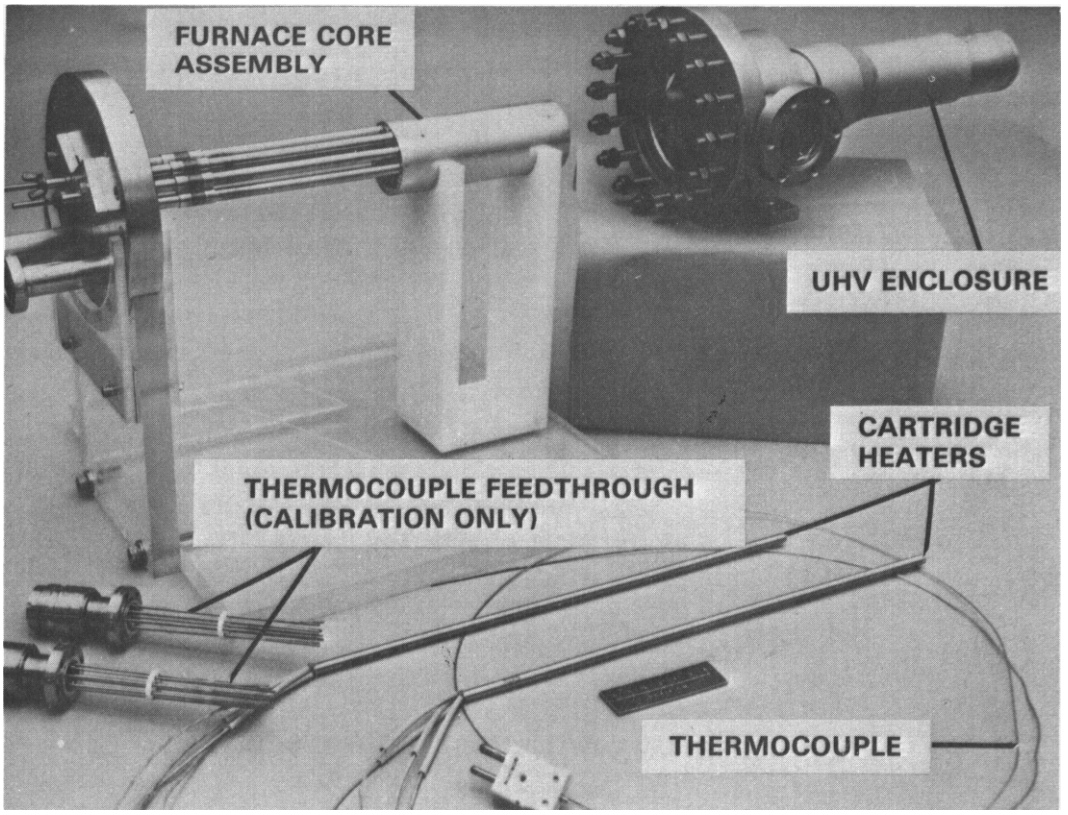

FIGURE 3. Exploded View of the Furnace Core Assembly and Vacuum Enclosure with Calibration Feedthroughs, Cartridge Heaters and Control/ Indicating Thermocouple (One of Two).

Also shown in Figure 3 are two UHV thermocouple feedthroughs. These feedthroughs were used to instrument each temperature zone in the furnace core with up to five thermocouples for calibration. During bench checking the temperature uniformity between specimen positions and between specimen positions and the thermocouple well in either zone was found to be within ±1°C of the nominal temperature. Accordingly, a single thermocouple positioned in the thermocouple well is used to control and measure the temperature in each zone. The layout of these wells and instrument feedthroughs on the conflat flange is shown in Figure 4.

The overall dimensions of the vacuum enclosure are shown in Figure 5. The portion of the enclosure which is positioned closest to the neutron source was fabricated from 6061 aluminum alloy. This section was then joined to a stainless steel weldment. This approach minimized the residual-induced radioactivity of the enclosure while permitting the use of standard vacuum flanges.

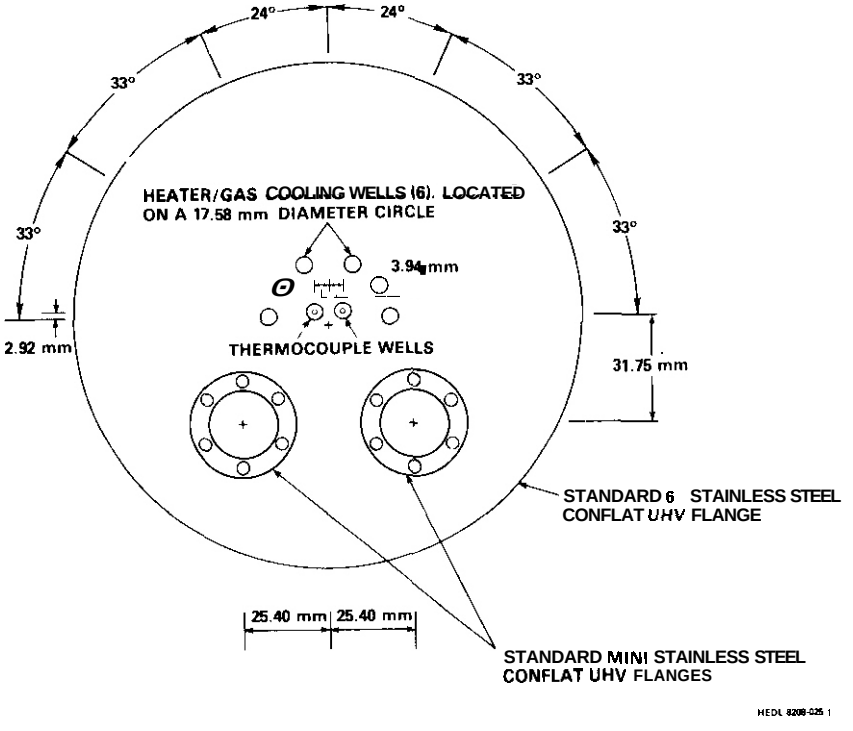

FIGURE 4. Layout of Six Heater/Gas Cooling Wells, the Two Control/Indicating Thermocouple Wells and the Two Mini-Flanges for Calibration Feedthroughs.

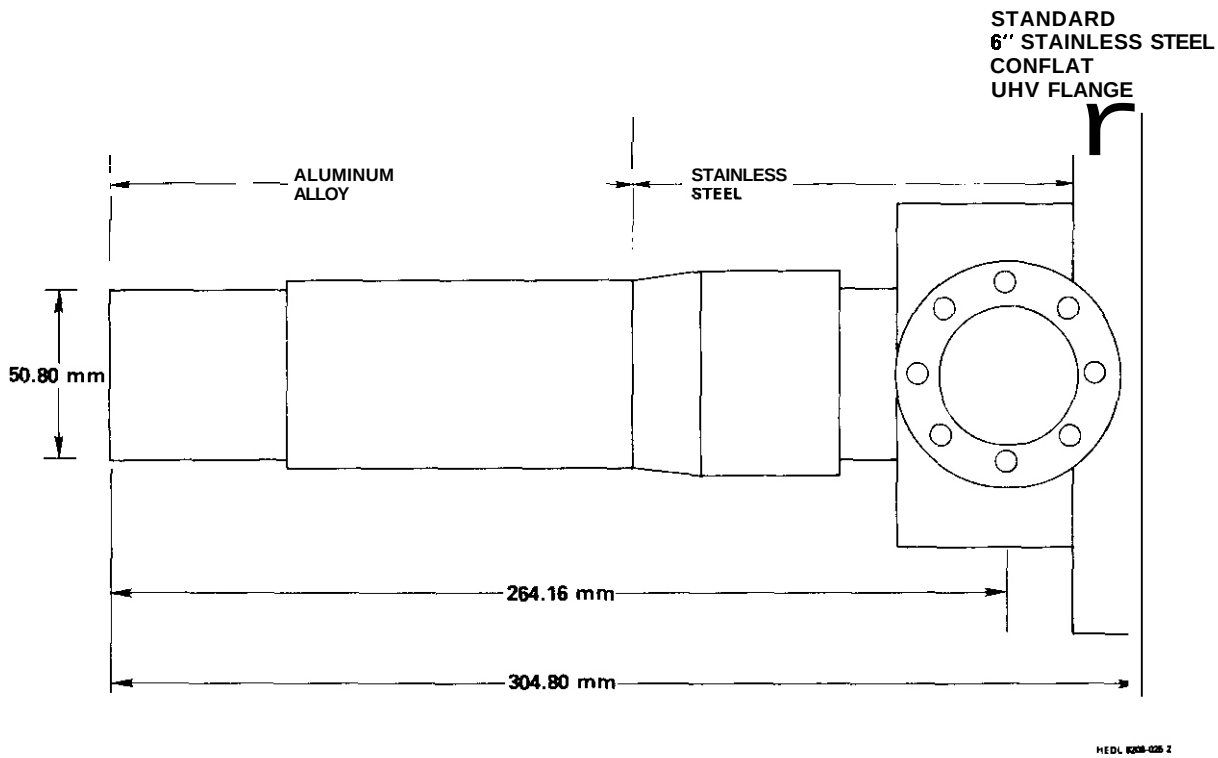

FIGURE 5. Overall Dimensions of the Vacuum Enclosure. Joining an aluminum alloy weldment with a stainless steel weldment reduced handling problems due to residual-induced radioactivity while allowing standard UHV flanges to be used.

As shown in Figure 2 the furnace core consists of two hemi-cylinders which are connected to a conflat flange by wells. These half cores were fabricated from oxygen-free, high-conductivity copper. The external surfaces of each half core were carefully polished to minimize radiative heat transfer. Thin-walled stainless steel tubing, chosen to minimize conductive heat transfer, was brazed to the furnace half cores and welded to the conflat flange to form wells for heaters, cooling gas and thermocouples. The overall dimensions of the furnace core assembly are shown in Figures 6 and 7. Since the furnace was designed to operate at two independent temperatures simultaneously, bellows were installed on each of the six large diameter wells and the two small diameter thermocouple wells to accommodate the resulting differential thermal expansion of the furnace half cores. The two ceramic standoffs on the front of each half core and these bellows allow the position of the furnace half cores, and therefore the specimens, to be referenced to the vacuum enclosure.

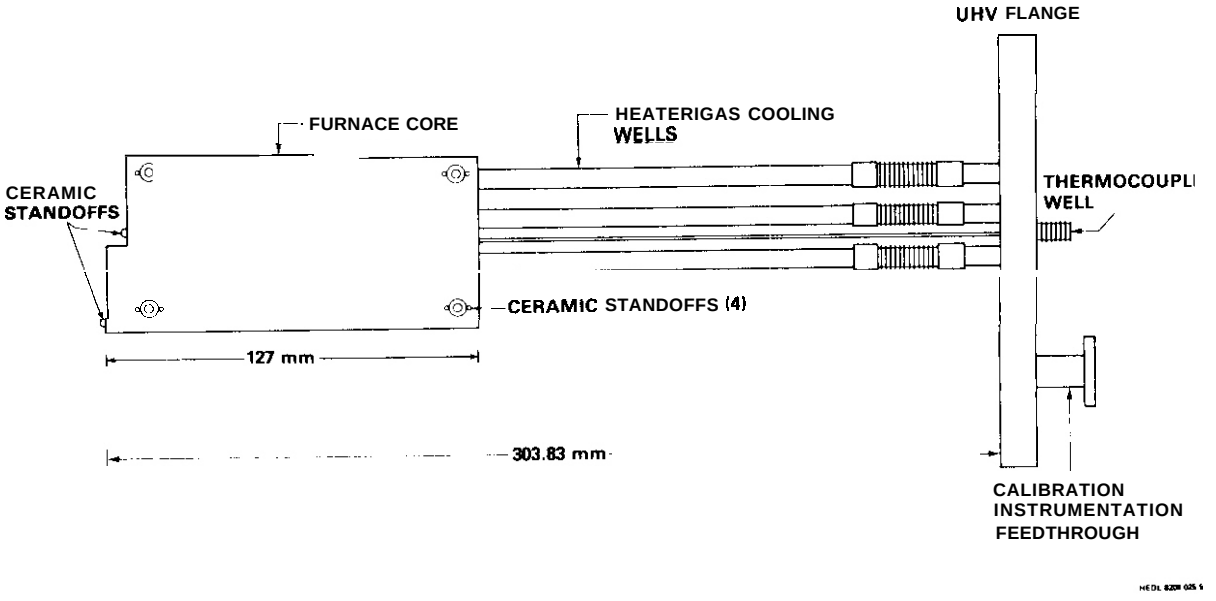

FIGURE 6. Overall Dimensions of the Furnace Core Assembly.

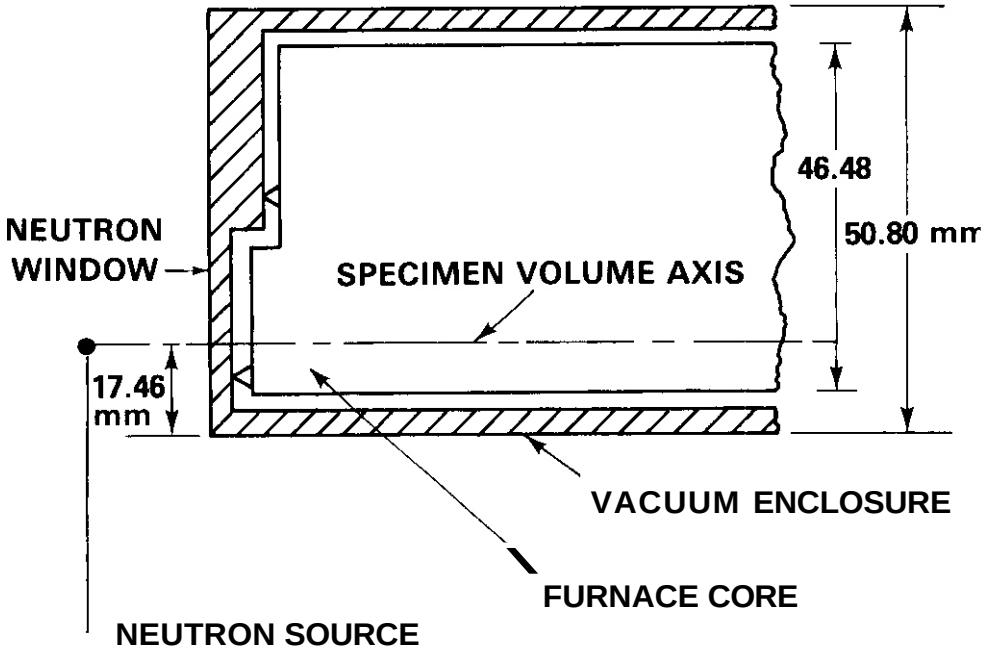

FIGURE 7. Schematic of the Furnace Core Assembly Positioned Within the Vacuum Enclosure. The specimen volume has been displaced from the axis of the furnace core assembly to permit full scanning of the rotating, oscillating, target.

A detail of the alumina ceramic standoffs is shown in Figure 8. Heat losses are reduced by minimizing contact area and by recessing each standoff into the furnace half cores to increase the heat transfer path length. The length of the standoff varies according to the position of the standoff. Four 3.4-mm long standoffs maintain the 0.25-mm separation between the furnace half cores, two 3.54-mm long standoffs are positioned on the front of each half core and four 3.68-mm long standoffs are positioned on the body of each half core. The standoffs are held in position by a retaining ring which is staked in place. This permits easy removal and replacement should a standoff be damaged.

As shown in Figure 7 the axis of the specimen volume of each furnace half core is displaced so that the minimum distance between it and the edge of the vacuum enclosure does not exceed 17.46 mm. This allows the rotating targets to be fully scanned, hence fully utilized, even with the furnace system positioned as closely as possible to the target.

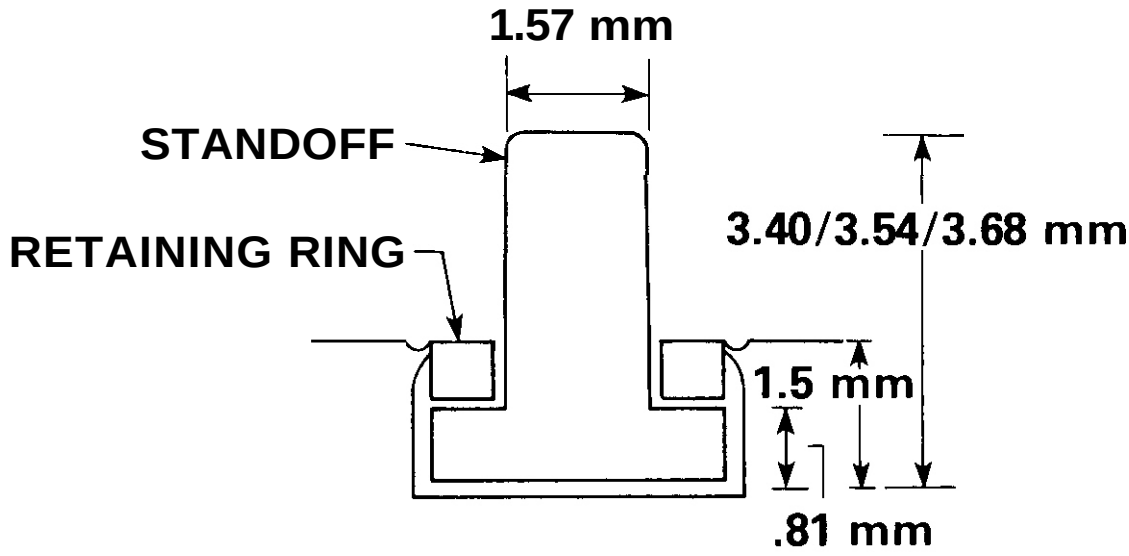

HEDL 8208-025.4b

FIGURE 8. Detail of a Ceramic Standoff Positioned in a 1.5-mm Deep Recess. The standoffs maintain the required clearance between the furnace half cores, between the half cores and the neutron window and between the half cores and the vacuum enclosure. They are designed to minimize conductive heat transfer.

A detail of a furnace half core is shown in Figure 9. This sectional view illustrates the three large diameter penetrations used for heaters and gas cooling and the single small diameter penetration used for the control and indicating thermocouple. The other penetrations shown are used for holding specimens. The positions of the specimen penetrations are shown in Figure 10. A rectangular specimen holder (shown in Figure 9) and three cylindrical specimen holders (not shown) can be inserted into each furnace half core from the rear. Structural components in key locations were designed to be of minimum thicknesses: a 0.02 mm thick cover foil is used on the rectangular specimen holder, and 0.13 and 0.25 mm thick cover foils are used for the furnace half core. Thicker structures are not required and would needlessly reduce the peak flux by increasing the target-specimen separation.

The rectangular specimen holder can accommodate both tensile and transmission electron microscopy (TEM) disk type specimens. Currently the tensile specimens are loaded directly into the specimen holder while the 3-mm diameter TEM disks are first loaded into packets and then the packets are loaded into the specimen holder. The holders for the three cylindrical specimen penetrations accommodate only TEM disk specimens. Given the large gradient in neutron flux and the flat temperature profile of the furnace half cores, specimens positioned at the rear of these holders can be used as thermal control specimens.

A view of the rear of the furnace half cores is shown in Figure 11, illustrating one of two thermal radiation shields. These shields permit access to the specimen penetrations and were designed to complete the high conductivity enclosure around the specimen and to permit efficient vacuum pumping of the specimen penetrations. The shields are indeed effective. Without the shields in place a furnace half core at a nominal temperature of 300°C was found to have a 40°C gradient over the rear half of the furnace half core. This compares with a temperature uniformity of ±1°C over the entire furnace half core when the shield is in place.

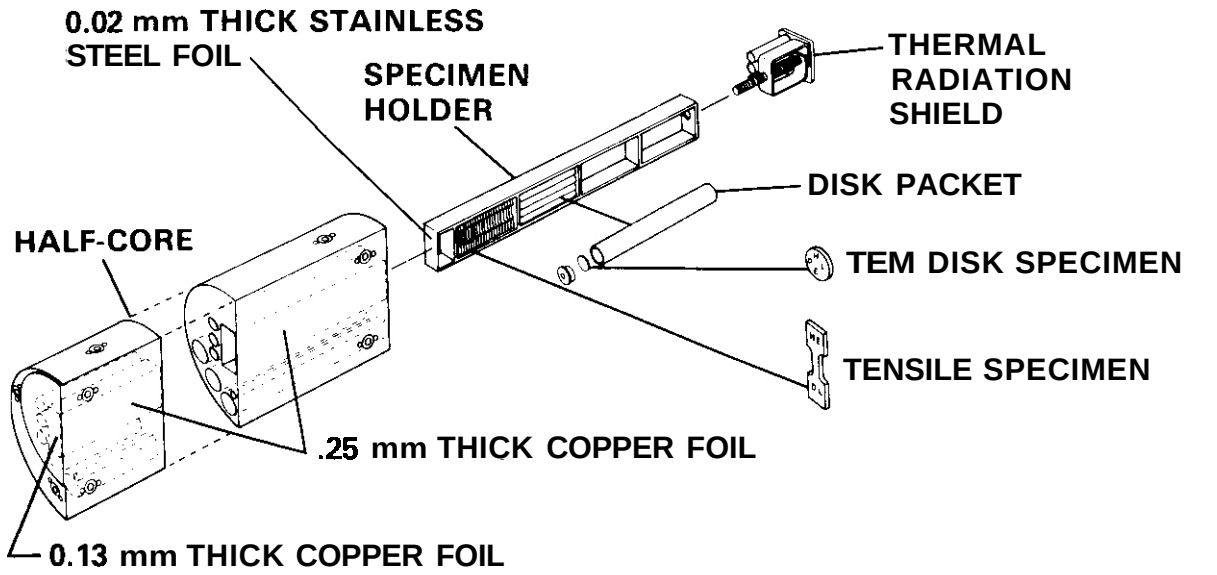

FIGURE 9. Detail of a Furnace Half Core Showing Penetrations for Heaters, Gas Cooling, Thermocouples and Specimens; a Specimen Holder and Miniature Specimens; and a Thermal Radiation Shield.

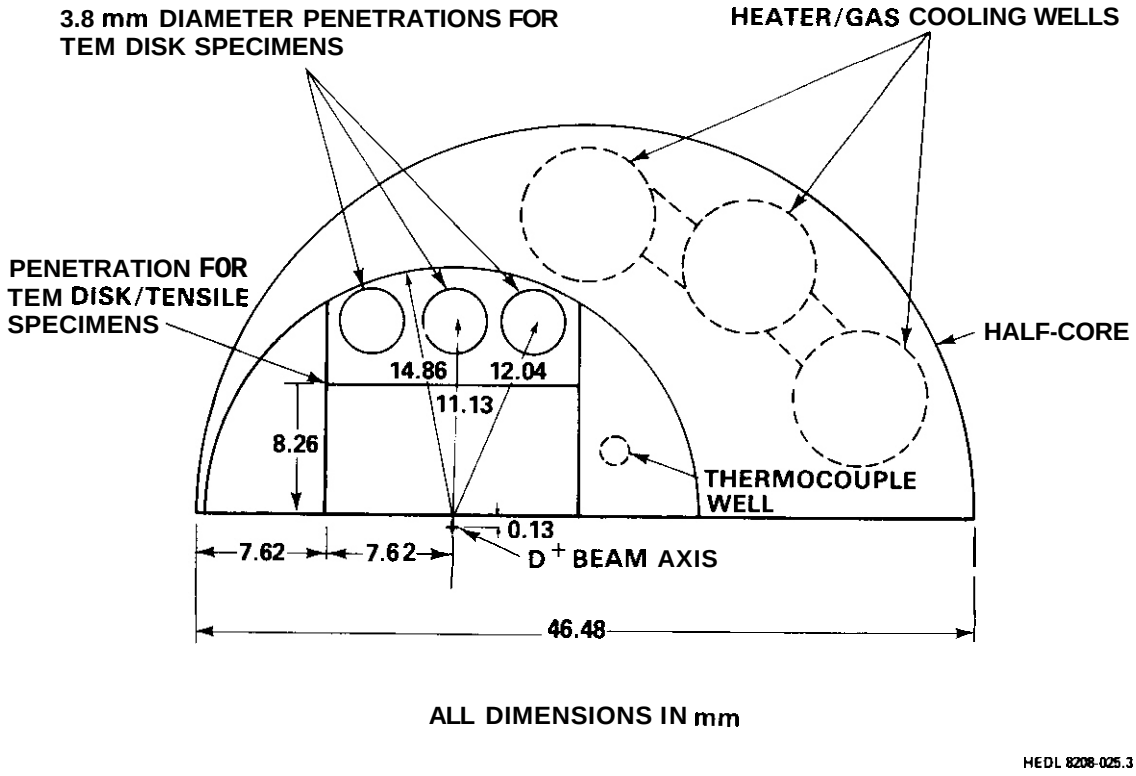

FIGURE 10. Position of the Specimen Penetrations in a Furnace Half Core. This view is a section through the half core at the highest flux specimen position.

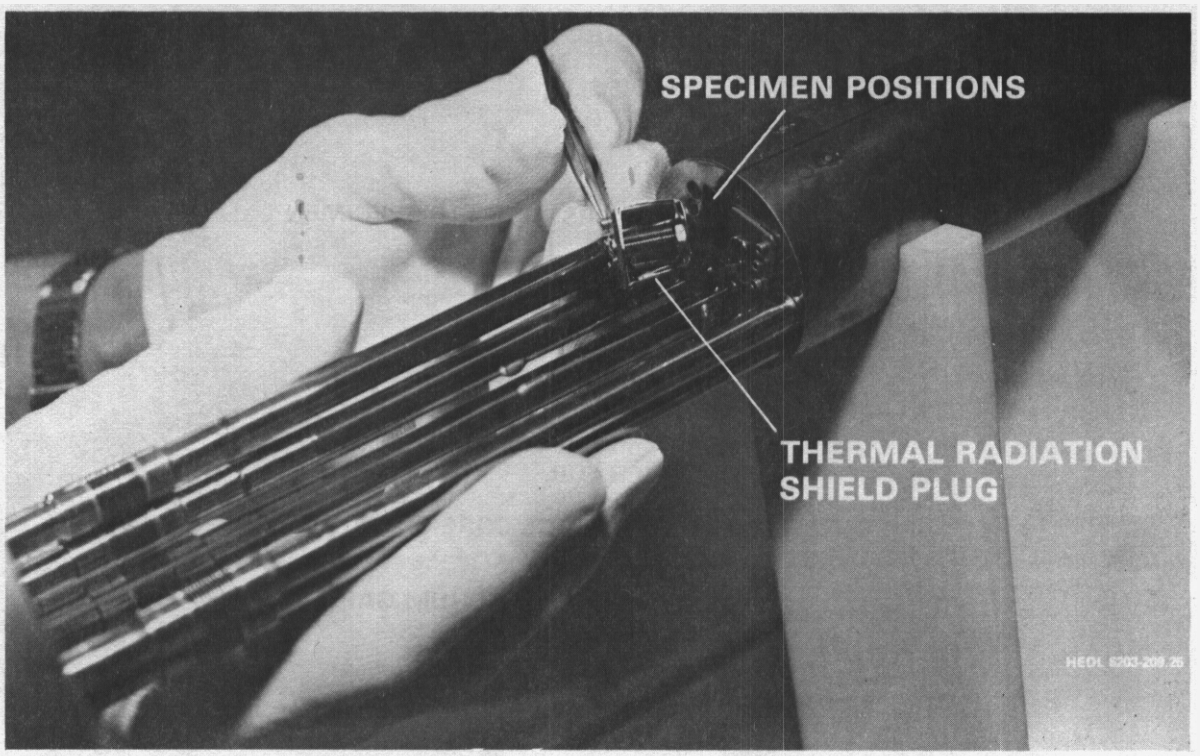

FIGURE 11. View of the Rear of the Furnace Core Illustrating the Access to the the Specimen Penetrations and a Thermal Radiation Shield.

A major goal of the design of the DTVI furnace system was to allow experimenters access to the primary irradiation volume of RTNS-II. The primary irradiation volume of RTNS-II is defined as a cylinder 1 cm in diameter and 2-mm deep centered on the deuteron beam axis. Over this volume the neutron flux drops by a factor of two. If the added separation between neutron source and specimens due to the furnace system is limited to 1 mm, fifty percent of the primary irradiation volume can be accessed. Figure 12 illustrates how this was achieved. In addition to minimizing the thickness of the cover foils used on the furnace half cores and the specimen holders, the thickness of the vacuum enclosure's neutron window, Figure 8, had to be optimized to minimize the total separation. The deflection of the aluminum alloy window was first limited by minimizing the diameter of the window. A 0.50-mm thick neutron window was found to deflect 0.25-mm under vacuum. This deflection could be accommodated in the 0.35-mm of available clearance leaving a 0.10-mm minimum clearance under vacuum and also limiting the total separation to 1 mm.

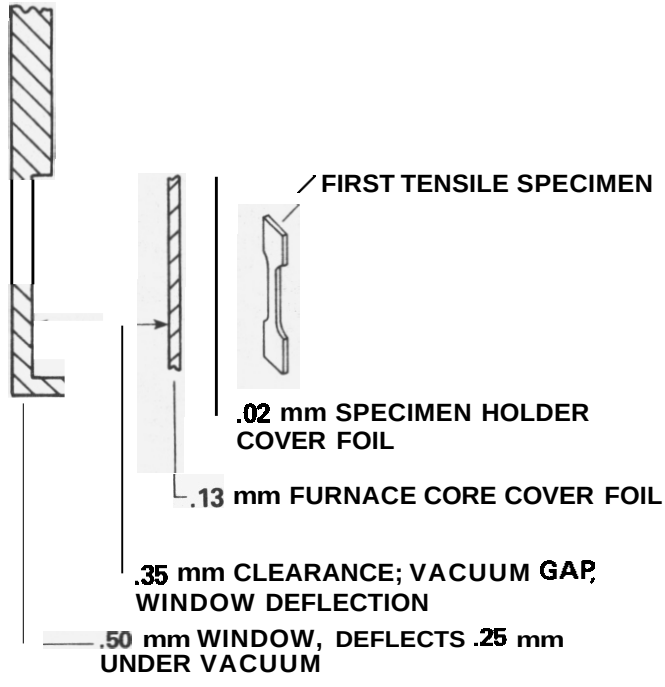

FIGURE 12. Schematic Illustration of the Furnace System Structures, the Neutron Window and the Required Cover Foils and Clearance, Which Together Add Only 1 mm of Separation Between the Neutron Source dnd the Specimens.

5.3 Furnace System Operation

Once the specimen holders have been loaded the large pan head screw on the thermal radiation shield, Figure 11, is tightened which expands the sides of the shield securing it in position. The entire furnace core assembly is then oriented properly and carefully inserted into the vacuum enclosure and secured. Cartridge heaters, thermocouples and gas cooling inlets are inserted into the appropriate wells. A vacuum is obtained and the furnace system is ready for positioning in front of the rotating target. The furnace has been operated at simultaneous temperatures of 288 and 80°C. During actual operation it takes approximately twenty minutes for the temperature of the furnace cores to stablize at these test temperatures. Temperature control is provided by proportional controllers. Nitrogen gas is circulated through the wells on

the cooler half core during normal operation. This is required since, without cooling, the few watts of heat radiated from a 288°C half core would result in a temperature in excess of 80°C in the other half core. Accordingly, the system is operated so that the temperature of the cooler half core is conveniently regulated at 80°C using electrical heating in opposition to a low flow of cooling gas. Overtemperature protection is provided using two additional thermocouples positioned in the spare large diameter wells of each furnace core.

Nitrogen gas is circulated through both half cores and at a higher flow rate when the experimenter decides to quench the experiment. Quenching the specimens to temperatures significantly below the test temperatures is required in order to limit annealing of radiation induced damage. Quenching to 60°C from 288°C and to 40°C from 80°C requires one-half hour. This furnace system can, therefore, be taken from a cold start to the required test temperatures and quenched in fifty minutes. The ability to cycle a furnace system this rapidly is a significant capability at an accelerator-based neutron facility like RTNS-II; the facility does not operate continuously and is also subject to unscheduled interruptions of the neutron flux.

5.4 Conclusions

The Dual-Temperature Vacuum-Insulated furnace system was delivered to the RTNS-II facility on November 2, 1981. Overall the DTVI furnace system has met or exceeded all design requirements. Specifically this system allows an experimenter to efficiently access the primary irradiation volume of RTNS-II for elevated temperature experiments. Specimens are irradiated at exceedingly uniform temperatures and under high vacuum conditions. Irradiations are performed at two independent temperatures which can differ by as much as 320°C with a maximum temperature of 400°C. Specimens can also be heated and cooled rapidly making this furnace system compatible with the operation of an accelerator-based neutron source. This system was designed to be reliable, maintainable and to minimize post-irradiation handling problems associated with residual induced radioactivity. Although long-term reliability has yet

to be tested the system performance has been excellent. A total of 100 hours of actual time at temperature has been logged to date and no problems have been noted.

6.0 References

None

7.0 Future Work

None

8.0 Publications

N. F. Panayotou, D. R. Green and L. S. Price, "A Unique Furnace System for High Energy Neutron Experiments," Proceedings of the Conference on Fast, Thermal and Fusion Reactor Experiments ANS April 12-15, 1982, Volume II, pp. 57-65.

CHAPTER 2

DOSIMETRY AND DAMAGE PARAMETERS

FISSION REACTOR DOSIMETRY

L. R. Greenwood and R. K. Smither (Argonne National Laboratory)

1.0 Objective

To characterize fission reactor irradiation facilities and to provide dosimetry and damage analysis for fusion experiments.

2.0 Sumnary

Samples have been received from the ORR-MFE4A2 and HFIR-CTR 31, 34, and 35 irradiations and analysis is now in progress. Dosimeters have been prepared for several new experiments in HFIR-CTR 39-45. A computerized dosimetry and damage data file has been initiated to permanently record data in a format easily accessible to all fusion experimenters. The status of all dosimetry experiments is summarized in Table 1.

3.0 Program

Title: Dosimetry and Damage Analysis
Principal Investigator: L. R. Greenwood
Affi1iation: Argonne National Laboratory

4.0 Relevant DAFS Program Plan Task/Subtasks

Task II.A.1 Fission Reactor Dosimetry

TABLE 1

STATUS OF DOSIMETRY EXPERIMENTS

	Facility/Experiment	Status/Comments
ORR	- MFE 1	Completed 12/79
	- MFE 2	Completed 06/81
	- MFE 4A1	Completed 12/81
	- MFE 4A2	Samples Received 09/82
	- MFE 4 B,C	Irradiation in Progress
	- TBC 07	Completed 07/80
	- TRIO-Test	Completed 07/82
	- TRIO-1	Samples Sent 07/82
HFIR	- CTR 32	Completed 04/82
	- CTR 31, 34, 35	Samples Received 09/82
	- CTR 30	Irradiation in Progress
	- T1, T2, T3	Irradiations in Progress
	- RB1, RB2, RB3	Irradiations in Progress
	- CTR 39-45	Samples Being Prepared
Omega West	- Spectral Analysis	Completed 10/80
	- HEDL1	Completed 05/81
EBR II	- X287	Completed 09/81
IPNS	- Spectral Analysis	Completed 01/82
	- LANL1 (Hurley)	Completed 06/82
	- Hurley/Coltman	Planned 09/82

5.0 Accomplishments and Status

Samples have been received from the following irradiations: ORR-MFE4A2, HFIR-CTR31, CTR34, and CTR35. The capsules are now being opened in a hot cell at Argonne National Laboratory in preparation for Ge(Li) gamma spectroscopy. Following these analyses, selected samples and helium monitors will be sent to D. Kneff at Rockwell International for helium analysis. A new high-level gamma spectroscopy system is being utilized to handle these samples.

New dosimeters are being prepared for nine planned irradiations in HFIR (CTR 39-45 and RB series). At least fifty new aluminum dosimetry capsules will be required, mostly containing Fe, Co-A1 alloy, Ti, and Mn-Cu alloy, similar to the capsules used in the CTR 34 and 35 irradiations. All results will be referred to our more extensive spectral analyses and fluence and damage parameter maps will be calculated for each irradiation.

A computerized dosimetry and damage data file has been initiated in order to permanently record all dosimetry data in a format that is easily accessible to all fusion experimenters. The data file will be placed on the NMFE computer at Lawrence Livermore Laboratory and a report is now being written concerning access data and formats. The data is written in a simple card-image format similar to the ENDF style. However, alphanumeric titles and headers are included with each file to make the data as readable as possible. Each irradiation file will contain a plain-English description and references to more complete publications, activity data, the input spectrum, output spectrum, a summary of fluences, selected damage parameters, and a complete listing of

input uncertainties and output covariances. Cross sections, self-shielding parameters, half-lives, and branching ratios will be referenced and included in separate files as needed. Retrieval codes are designed so that a user can rapidly retrieve only selected data (e.g., fluence and damage summaries for any or all files). However, it is also intended that all data will be sufficiently-well recorded such that a complete reanalysis could be performed in the future as new data becomes available. Most previous irradiation data are now being placed in the file, starting with the most recent experiments. Older data may need to be reassessed according to changes in cross sections half-lives, and branching ratios. A preliminary version of the file should be available shortly for testing by interested parties.

6.0 References

None.

7.0 Future Work

The ORR-MFE4A2 and HFIR-CTR31, 34, and 35 analyses should be completed in the next quarter. The computerized dosimetry and damage data file will be available shortly; however, we plan to continually update the file as each new irradiation is completed.

8.0 Publications

1. Neutron Source Characterization and Radiation Damage Calculations for Materials Studies, L. R. Greenwood, J. Nucl. Mater. 108, 21 (1982).

EXPERIMENTS AT THE IPNS SPALLATION NEUTRON SOURCE

L. R. Greenwood (Argonne National Laboratory)

1.0 Objective

To characterize the IPNS irradiation facilities and to provide OFE experimenters with dosimetry and damage analysis.

2.0 Summary

Damage calculations have been completed for G. Hurley (LANL) for an IPNS irradiation on February 22-27, 1982. Doses ranged from 1.04 to 2.87 x 10^8 Rads depending on the compositions of the organic insulator materials. Plans are being made for a second irradiation for G. Hurley and R. Coltman (ORNL) during September 1982.

3.0 Program

Title: Dosimetry and Damage Analysis

Principal Investigator: L. R. Greenwood

Affiliation: Argonne National Laboratory

4.0 Relevant DAFS Program Plan Task/Subtasks

Task II.A.2 High-Energy Neutron Dosimetry

5.0 Accomplishments and Status

Dosimetry measurements were reported previously (Damage Analysis and Fundamental Studies, Quarterly Progress Report DOE/ER-0046/10) for the irradiation of organic insulators at 4°K at the IPNS. The average neutron fluence was 1.51 x 10^{17} n/cm^2 (>0.1 MeV) or 2.17 x 10^{17} n/cm^2 (total). Damage calculations have now been completed for this irradiation and the dose values are described below.

In order to routinely calculate doses delivered to insulators, ionization energies must be added to the displacement damage which we usually report for the irradiation of metals. Consequently, we have included the MACKLIB[1] library of Kerma factors in our SPECTER computer code so that dose values are spectral-averaged along with our DPA, PKA, and gas production cross sections. The present version of MACKLIB is based on ENDF/B-IV rather than version V. However, based on the small DPA differences noted between versions IV and V we expect dose rate differences to be less than 10%.

Table 1 lists Kerma and dose values for various elements and organic insulators using the neutron spectrum measured at IPNS.[2] The most striking conclusion evident from the values is the high dose in hydrogen and hence organics compared to inorganics. Polyimides thus suffer less damage than epoxies and glass is less than the organics. Several comments should be made about these values. First of all, characterization of organics is quite important since the exact composition (especially hydrogen) obviously effects the calculated dose.

Secondly, composites such as G10 will have strong, local variations in dose since the glass fibers damage more slowly than the resin. Hence, the average dose delivered to G10 may not be the most representative number to look at. Caution is thus needed to calculate and interpret doses in a standardized manner. To this end the MACKLIB Kerma factors have been included in our latest version of the SPECTER code on the NMFE computer at Lawrence Livermore Laboratory.

TABLE 1

DOSE CALCULATIONS AT IPNS (REF-VT2)
Neutron Fluence = 1.51 x 10^{17} above 0.1 MeV

Material	Kerma (keV-b)	Dose (x 10^{7} Rads)
H	1432.	308.
B	9827.	196.
C	257.	4.60
N	316.	4.86
O	234.	3.14
Si	152.	1.16
SiO_2		2.21
E-Glass (B)		8.01
Polyimide		16.5
Epoxy A (6% H)		22.6
Epoxy B (8% H)		28.7

One uncertainty remaining in our dose calculations at IPNS is that we do not have a reliable estimate of the gamma dose. Several measurements have been made with thermoluminescent dosimeters (TLD-LiF).[3] However, the neutron fraction of the dose so overwhelms the gamma fraction that no reliable value for the gamma dose can be extracted. In fact our best calculations (MACKLIB) of the neutron dose are slightly higher than our measurements (19.1 Rads/μC vs. 18.7 Rads/μC). This may be due in part to the escape of some prays emitted by fluorine. If we place 10% uncertainties on both the calculated and measured doses, then our upper limit on the gamma dose to LiF is about 15%. Other methods have been considered for measuring the IPNS gamma flux, although none appear to be satisfactory. Calorimetry measurements are also dominated by the neutron dose and have accuracies similar to the TLD measurements. Active detectors are difficult to operate due to the pulsed nature of IPNS since the flux is greater than 10^{18} n/cm^2 during a pulse. In any case, the gama dose is a small fraction of the total.

We have also measured the proton flux incident on our samples using the V and Cu (p,n) reactions and a thick (5 cm) lead absorber.[3] Although these data are still being analyzed, initial results show that the secondary proton flux in the irradiation thimble is only about 1/800 of the neutron flux and that the average proton energy is greater than 100 MeV. Hence, we can conclude that the dose delivered by secondary protons is quite negligible for thin samples.

6.0 References

1. Y. Gohar and M. A. Abdou, MACKLIB-IV, A Library of Nuclear Response Functions Generated with the MACK-IV Computer Program from ENDF/B-IV, ANL/FPP/TM-106 (1978).

2. L. R. Greenwood and R. J. Popek, Characterization of Spallation Neutron Sources, DOE/ER-0046/7, p. 17, (1981).

3. L. R. Greenwood and R. J. Popek, Methods of Neutron and Proton Dosimetry at Spaalation Sources, Proceedings of the ICANS-VI International Collaboration on Advanced Neutron Sources, Argonne National Laboratory, June 1982.

7.0 Future Work

A second cryogenic (4°K) irradiation is planned at IPNS in September 1982. Samples will be irradiated for G. HUrley (LANL) and R. Coltman (ORNL). Dosimetry wires will be included to determine the fluence and dose values will be calculated. Experiments are also being proposed to improve our dosimetry techniques, especially at higher neutron energies.

8.0 Publications

1. Neutron Irradiation Facilities at the Intense Pulsed Neutron Source, R. C. Birtcher, T. H. Blewitt, M. A. Kirk, T. L. Scott, B. S. Brown, and L. R. Greenwood, J. Nucl. Mater. 108, 3 (1982).

HELIUM PRODUCTION IN ^{6}Li AND ^{10}B FROM ORR-TRIO

D. W. Kneff, B. M. Oliver, M. M. Nakata, and H. Farrar IV (Rockwell International, Energy Systems Group)

1.0 Objective

The objective of this work is to develop and apply helium accumulation neutron dosimetry to the measurement of neutron fluences and energy spectra in mixed-spectrum fission reactors utilized for fusion materials testing.

2.0 Summary

Helium production measurements have been completed for the ^{6}Li and ^{10}B dosimeters irradiated in the Oak Ridge Research Reactor (ORR) as part of the Argonne National Laboratory (ANL)-Oak Ridge National Laboratory (ORNL) TRIO test irradiation. The ^{6}Li measurements were used to determine the $^{6}Li(n,\alpha)^{3}H$ tritium production rate for this irradiation. The result was found to agree within uncertainties with ORNL's tritium production measurement.

3.0 Program

Title: Helium Generation in Fusion Reactor Materials
Principal Investigators: D. W. Kneff and Harry Farrar IV
Affiliation: Rockwell International, Energy Systems Group

4.0 Relevant DAFS Program Plan Task/Subtask

Subtask II.A.1.1 Flux-Spectral Definition in a Tailored Fission Reactor

5.0 Accomplishments and Status

The ORR-TRIO test irradiation,**) conducted in April 1982 as part of an ANL-ORNL experiment to measure and recover tritium from fusion blanket materials,

incorporated a set of ^{6}Li- and B-doped aluminum alloy dosimetry wires. The purpose of including these wires was to provide helium accumulation neutron dosimetry for the irradiation, utilizing the $^{6}Li(n,\alpha)3H$ and $^{10}B(n,\alpha)^{7}Li$ reactions, and to compare the helium production from ^{6}Li with the ^{6}Li tritium production rates measured by ORNL and calculated by ANL.[1] The alloy wires were selected because their small ^{6}Li and natural boron concentrations (0.705 wt. % and 0.47 wt. %, respectively) introduced minimal self-shielding and flux-perturbation effects. Analysis of these wires is now complete.

A 13-mm length each of the A1-0.7% ^{6}Li and A1-0.5% B wires was irradiated to a total exposure of 253.35 MWH. These wires were then etched, segmented, and analyzed by high-sensitivity gas mass spectrometry for generated helium. The purpose of the sample etching procedure was to remove all possible surface effects of alpha recoil into or out of the materials. The results of the helium analyses are summarized in Table 1, where the helium concentration measurements are given in Column 3, and are converted to atom-fraction burnup of ^{6}Li and ^{10}B, respectively, in Column 4. The Column 4 results have been corrected for self-shielding and flux-depression effects (-1.9% for ^{6}Li and -1.1% for ^{10}B) associated with the sample irradiation geometry. The absolute uncertainties in the helium measurements are about 1%, and gradients of about 2% can be seen along the segmented wires. The quoted uncertainty in the ^{6}Li content of the A1-0.7% ^{6}Li alloy is 3.6%. The average fractional burnups measured for ^{6}Li and ^{10}B are given in Column 5.

The tritium concentrations in the Al-^{6}Li alloy segments were also determined by high-sensitivity gas mass spectrometry. These measurements were performed by analyzing the ^{3}He decay product from the radioactive tritium. The measurement results are given in Table 2, where they are expressed as $^{4}He/^{3}He$ ratios (Column 2). For comparison, the calculated $^{4}He/^{3}He$ ratios for the individual samples, which are based on the equal production of helium and tritium by the $^{6}Li(n,\alpha)^{3}H$ reaction, are given in Column 3. These calculations assume that all of the tritium and helium is retained by the alloy wire and that the tritium half-life is 12.33 years. Since helium and tritium have significantly

TABLE 1

SUMMARY OF HELIUM GENERATION RESULTS FROM THE ORR-TRIO IRRADIATION TEST EXPERIMENT

Material	Sample	Measured ^4He/mg	Atom-Fraction Burnup*	Average Atom-Fraction Burnup
Al-0.7% ^6Li	ORT-ALLI-A	1.672×10^{15}	2.540×10^{-3} ^6Li	2.512×10^{-3} ^6Li
	ORT-ALLI-B	1.664×10^{15}	2.529×10^{-3} ^6Li	
	ORT-ALLI-C	1.654×10^{15}	2.514×10^{-3} ^6Li	
	ORT-ALLI-D	1.643×10^{15}	2.496×10^{-3} ^6Li	
	ORT-ALLI-E	1.633×10^{15}	2.481×10^{-3} ^6Li	
Al-0.5% B	ORT-ALB-A	5.485×10^{14}	1.075 x 10-2 ^{10}B	1.064×10^{-2} ^{10}B
	ORT-ALB-B	5.441×10^{14}	1.067×10^{-2} ^{10}B	
	ORT-ALB-C	5.378×10^{14}	1.054×10^{-2} ^{10}B	
	ORT-ALB-D	5.404×10^{14}	1.059×10^{-2} ^{10}B	

*With respect to ^6Li or ^{10}B; corrected for isotope burnup, self-shielding, and flux-depression effects.

TABLE 2

MEASURED AND CALCULATED $^4He/^3He$ RATIOS FROM $^6Li(n,\alpha)3H$ REACTIONS IN THE Al-0.7% ^6Li ALLOY SAMPLES

	$^4He/^3He$ Ratio		
Sample	Measured	Calculated*	Calculated/Measured
ORT-ALLI-A	75.49	76.05	1.007
ORT-ALLI-B	66.31	66.13	0.997
ORT-ALLI-C	66.31	66.13	0.997
ORT-ALLI-D	65.87	66.13	1.004
ORT-ALLI-E	74.84	76.05	1.016
			Average = 1.004

*Assuming a tritium half-life of 12.33 years

different mobilities in solids, the excellent agreement between the measured and calculated ratios indicates that all of the tritium and helium was retained.

The $^{6}Li(n,\alpha)^{3}H$ tritium production rate determined from the helium measurements is given in Table 3. The ORNL tritium measurement and ANL calculation[1] are also included for comparison. In order to compare the results directly, the helium results were normalized to a 30-MW reactor power level, and increased by 2.3% to correct for the flux gradient between the Rockwell and ORNL irradiation positions. The Rockwell and ORNL results agree to within ~5%, which is within the measurement uncertainties of the two values. The ANL-calculated tritium production rate is about 9% higher than the present results. The small difference that exists between the Rockwell and ORNL measurements is being investigated. The largest uncertainty in the helium measurements is the 3.6% uncertainty in the ^{6}Li concentration in the Al-^{6}Li alloy. The lithium content of this alloy is now being independently measured at ANL.

6.0 References

1. L. R. Greenwood, "Dosimetry Results for the Trio Test in ORR," in Damage Analysis and Fundamental Studies, Quarterly Progress Report April-June 1982, DOE/ER-0046/10, U.S. Department of Energy, 9 (1982).

TABLE 3
SUMMARY OF $^{6}Li(n,\alpha)^{3}H$ TRITIUM PRODUCTION RATE DETERMINATIONS FOR ORR-TRIO AT 30 MW

Source	Tritium Production Rate
Rockwell measurement (helium)	$(8.45 \pm 0.34) \times 10^{-8}$ $^{3}H/^{6}Li$-s
ORNL measurement (tritium)	$(8.91 \pm 0.45) \times 10^{-8}$ $^{3}H/^{6}Li$-s
ANL calculation	9.22×10^{-8} $^{3}H/^{6}Li$-s

7.0 Future Work

Mixed-spectrum reactor dosimetry development and use will continue, with near-term analysis emphasis on current ORR and HFIR experiments.

8.0 Publications

None.

CHAPTER 3

FUNDAMENTAL MECHANICAL BEHAVIOR

DEVELOPMENTS IN SMALL-SCALE STRENGTH AND IMPACT TESTING

G.E. Lucas, J.W. Sheckherd, G.R. Odette, (Department of Chemical and Nuclear Engineering, University of California, Santa Barbara)

1.0 Objective

The purpose of this aspect of the program is to develop test techniques to extract mechanical property information from small volume specimens either being used or planned for use in neutron irradiation experiments for the fusion materials development program.

2.0 Summary

This report updates the developments of two test techniques, namely shear punch testing and miniaturized impact specimen testing. In shear testing, a very strong correlation has been found for a wide range of materials between the uniaxial tensile yield strength of a material and the yield load exhibited during a shear punch test, and between the ulimate tensile strength in tension and the maximum load in shear. In miniaturized impact testing, one-third size Charpy V-notch (CVN) specimens have been tested for a variety of commercial and model pressure vessel steels. Although the curves of normalized impact energy as a function of test temperature do not coincide for the small and standard **CVNs,** the small **CVNs,** do appear useful for tracking transition temperature shift and perhaps upper shelf energy changes.

3.0 Program

Title: Damage Analysis and Fundamental Studies for Fusion Reactor Materials Development.

Principal Investigators: G.R. Odette and G.E. Lucas

Affiliation: University of California, Santa Barbara.

4.0 Relevant DAFS Program Plan Task/Subtask

Subtask B: Fundamental Mechanical Properties
Subtask C: Correlation Methodology

5.0 Accomplishments and Status

Near term devices which are (or will be) available to provide high energy neutron irradiation environments for the fusion materials development program have, by their nature, somewhat limited test volumes. A need therefore exists to develop small volume specimens and the test techniques necessary to extract both microstructural and mechanical property information from them. Two such tests, which have been described previously,[1,2] are the shear punch test and miniaturized Charpy V-notch specimen impact test. Additional data and findings obtained in these tests are reported here.

5.2 Shear Punch Test

As described in Reference 1, the shear punch test is based on a blanking operation common to the sheet metal forming industry. A thin (.5mm) coupon sample is clamped in a die, and a cylindrical punch is driven through it. The load on the punch and the displacement of the punch relative to the sample are both monitored and used to generate a load displacement curve like that shown in Fig. 1. A similar curve is obtained by simply monitoring punch load as a function of time for constant ram displacement rate.

Early tests with the shear punch test were analyzed for ductility information.[1,2] However, it is clear from Fig. 1 that the test results may contain strength information analogous to that obtained from the load-displacement curve of a standard tensile test. In particular, the punch load-displacement curve exhibits a deviation from near-linearity at a load P_Y, which might be related to a tensile yield load and a maximum load P_{max} which might be related to an ultimate tensile load.

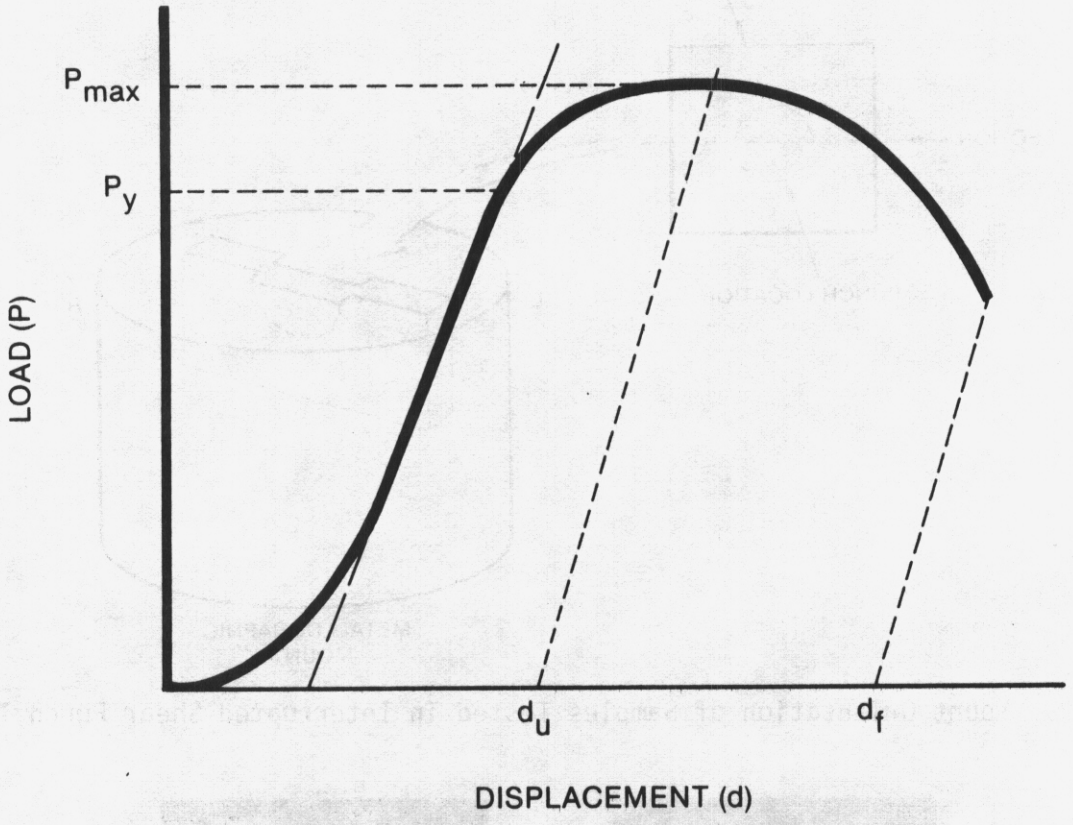

FIGURE 1. Representative Curve Obtained in a Shear Punch Test.

To correlate P_y and P_{max} with tensile strength parameters on a physical basis, a series of interupted tests were performed. Samples were punched to varying fractions of the displacement to failure d_f. Each sample was then sectioned along the diameter of the punch location, mounted in a metallographic mount as shown in Fig. 2, and viewed in a reflecting light microscope.

A series of photographs taken for yellow brass samples which were etched prior to observation to reveal the grain structure is shown in Fig. 3. The following observations were made from the tests:

1. Deviation from linearity in the load-displacement curve appeared to correspond with the onset of permanent punch displacement in the sample. This observation could be made only qualitatively, as there was some nonperpendicularity between the punch and the sample. That

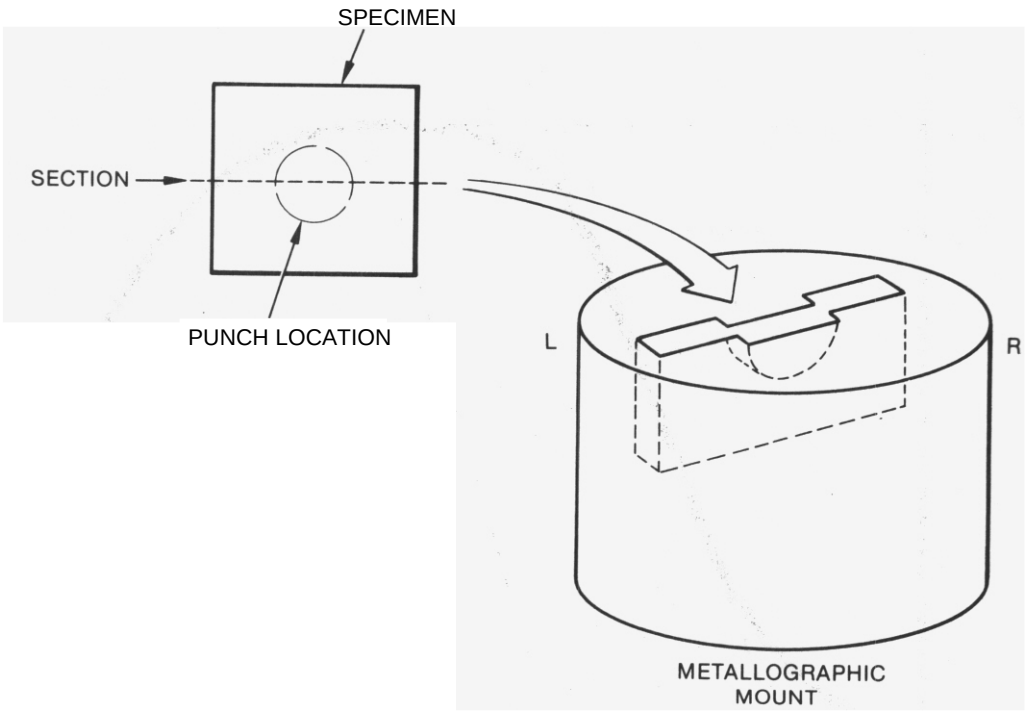

FIGURE 2. Mount Orientation of Samples Tested in Interrupted Shear Punch Tests.

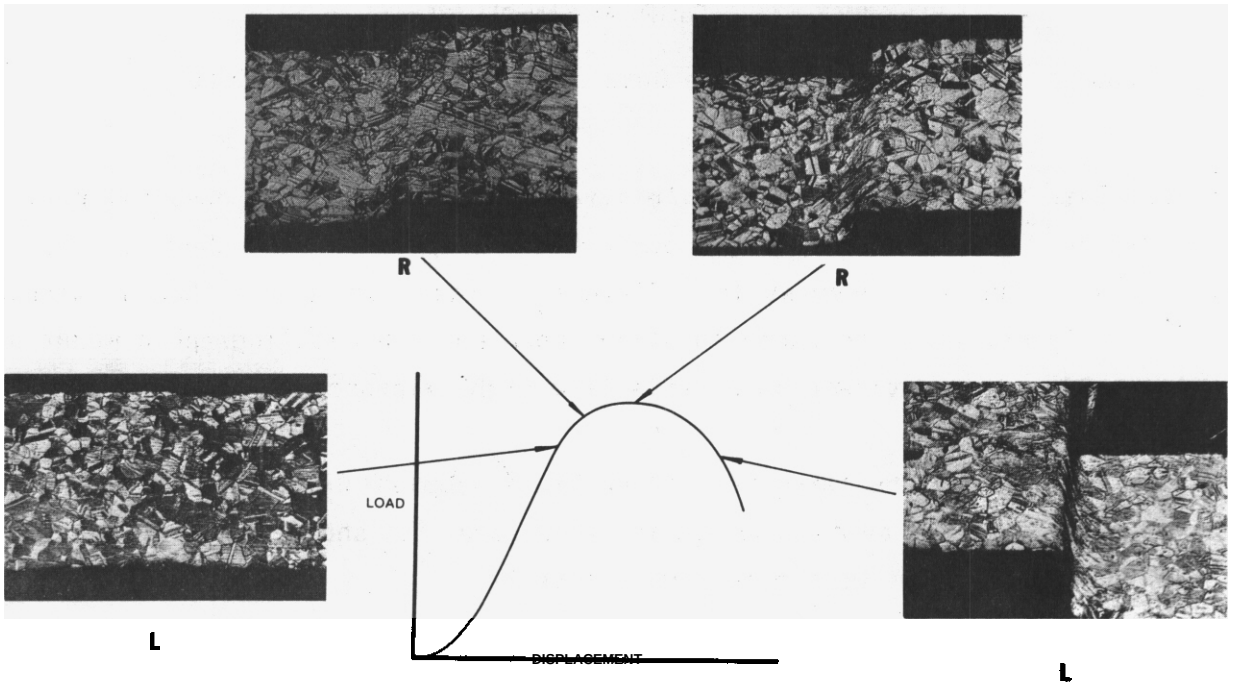

FIGURE 3. Punched Region in Brass Samples Punched to Different Fractions of d_f. The load-displacement curve is used to indicate the corresponding condition of each sample.

is, the punch contacted the sample on one side first, and hence permanent displacement initiated there. Attempts to correct this deficiency in the system are underway as described in Section 7.0.

2. The punching process created a zone of deformation 20-50 μm wide at the location of the punch-die interface. This width was of the order of the gap between the punch and its guide hole in the die. The amount of deformation, as evidenced by grain geometry distortion in the zone, increased in severity with increasing punch displacement; however, the zone width did not appear to increase with punch displacement.
3. The specimen thickness (vertical direction in Fig. 3) within the deformation zone, and hence the load bearing area of the specimen, decreased with increasing punch displacement; however, this was apparently offset by work hardening of the material for loads up to P_{max}.
4. Beyond P_{max}, the specimen "thins", or shears off, rapidly in the deformation zone.

Hence, it appears from such observations that the value of P_Y might correlate with the yield strength of the material, and P_{max} with the ultimate tensile strength. To test this, results from punch tests were compared with uniaxial data for a variety of material ranging from annealed aluminum to highly cold-worked stainless steel. Results are shown in Figs. 4 and 5. These show reasonable correlation between σ_Y and $P_{Y'}$ and σ_u and P_{max} for a wide range of yield strengths and ultimate tensile strengths. Some of the vertical scatter in Fig. 4 is attributable to the difficulty in defining deviation from linearity, and the slope of the linear region itself. The scatter in P_{max}, however, was very small, as the maximum point is well defined. Additional scatter may be introduced by slight misalignments of the punch and die, as well as material variability. It should be noted that the correlations illustrated in Figs. 4 and 5 are sensitive to both sample geometry and punch geometry. Nonetheless, for a given punch geometry and specimen size the technique appears promising for obtaining strength information.

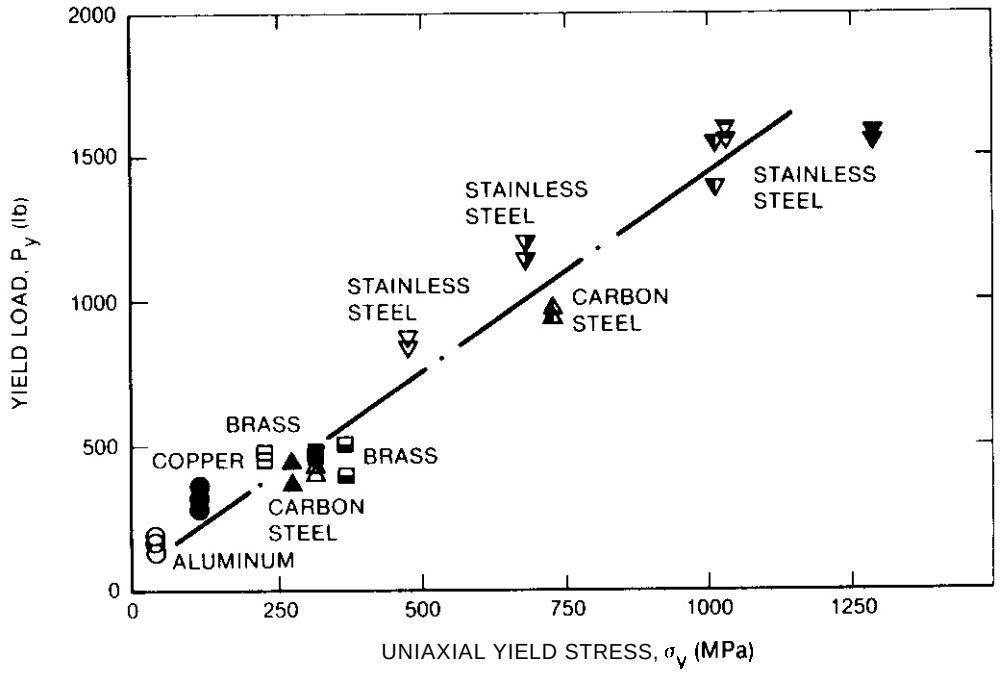

FIGURE 4. Comparison of the Yield Load Obtained in Shear Punch Tests with the Uniaxial Yield Strength of the Material.

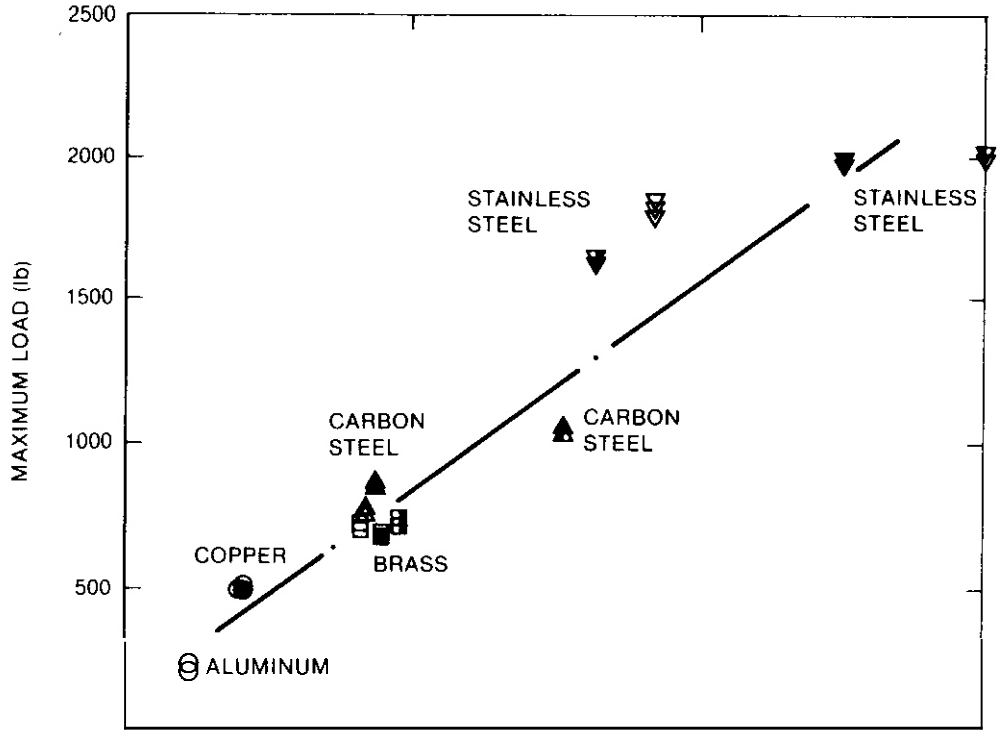

5.3 Miniature CVN Tests

Miniature Charpy V-notch (CVN) specimens are being developed and tested as part of a program on neutron irradiation embrittlement of pressure vessel steels, funded by the Electric Power Research Institute.* However, because the test results may be of some interest to the fusion materials community, they are reported here.

To date, miniature CVNs, 1/3 standard dimensions, have been fabricated and tested for the materials shown in Table 1. Tests are performed on an instrumented drop tower with a mass of 96.7 kg and an impact velocity of .975 m/s. A specially designed, removable anvil was used to improve temperature control. The specimen was mounted on the anvil and heated or cooled to the appropriate test temperature in a temperature bath. Rapid removal of the anvil from the bath and placement in the drop tower permitted testing with little temperature change in the specimen itself.

Table 1

ALLOYS INVESTIGATED BY MINI-CVN TESTING

Designation	Description
A	A 3028 steel
D	EPRI weld, Lin-0080
T	Fe-.1C-.25Cu-.6Ni-1.5Mn-.6Si
A508-2	A508-2 steel; as-received
A508-2 T	A508-2 steel, aged 1 h @ 1900°F

*EPRI Contract RP-1021-7; T. Marston, project manager; Joint program with Fracture Control Corporation, Goleta, CA, J. Perrin, President. The miniature CVN tests were performed at Fracture Control Corporation.

Results for alloys A, D, and T are shown in Figs. 6-8. For alloys A and D the data are compared to standard CVN data. All data are normalized by volume Bb^2, where B is the specimen width (10 mm for CVN and 3.3 mm for mini-CVN) and b is the ligament size (8 mm for CVN and 2.64 mm for mini-CVN). The data are fit by tanh curves which are shown as solid lines for the standard CVN's and dotted lines for the mini-CVNs. While the mini-CVN curves have shapes like the standard CVN curves, there is no clear correlation between the two types of normalized impact energy curves for the materials investigated.

Shown in Fig. 9 are results obtained on an A508-2 steel in the as-received and the temper-embrittled condition (i.e. aged 1 h @ 1900 °F). The standard CVN curves show a drop in upper shelf energy and an increase. in transition temperature upon aging the A508-2 steel. The mini-CVN curves show the same behavior even though the mini-CVN and standard CVN curves do not coincide. For instance, at the normalized energy level of 770 $ft\text{-}lb/in^3$, corresponding to the 30 ft-lb level in a standard CVN test, the shift in NOTT is ~200°F for the standard CVN and ~170°F for the mini-CVN. Hence, there is considerable potential for using these specimens to track changes in the impact energy curves.

6.0 References

1. G.E. Lucas, et al., "Small Specimen Test Development," OAFS Quarterly Progress Report, DOE/ER-0046/4 (1981) 45.

7.0 future Work

The shear punch test is being scaled down. A punch-and-die apparatus has been fabricated to produce 3mm diameter punched discs. Hence, it is envisioned that the shear punch test might be used to extract mechanical properties from sheet material during the blanking operation for TEM discs. Moreover, special precautions have been taken to improve the alignment and perpendicularity of the new punch-and-die based on experience gained with the original apparatus. Punch testing with the new apparatus has been initiated.

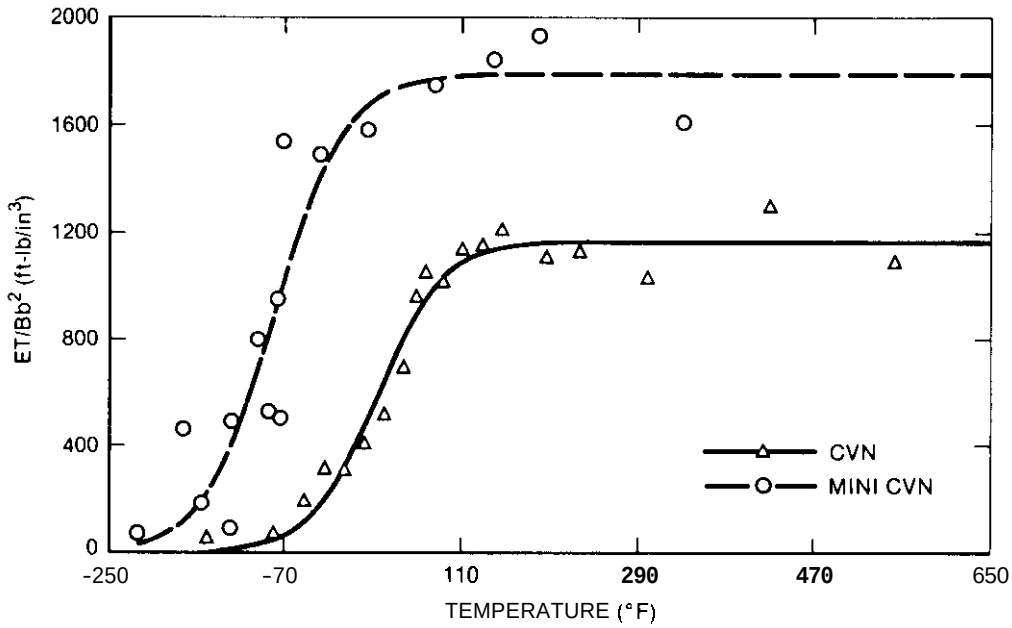

FIGURE 6. Normalized Impact Energy Curves for Alloy A for Both Standard and Mini– CVNs.

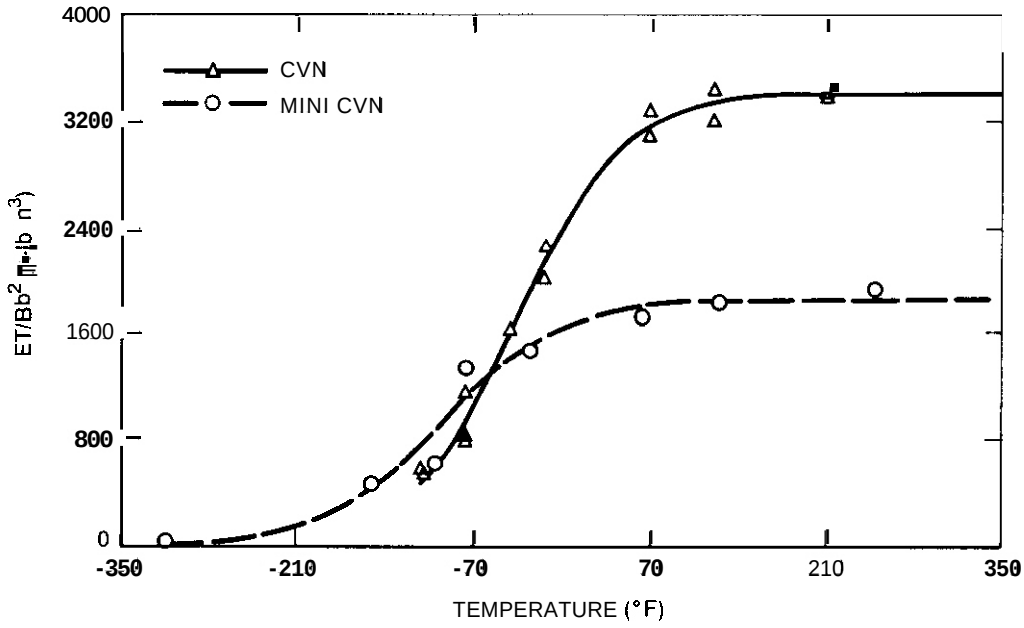

FIGURE 7. Normalized Impact Energy Curves for Alloy D for Both Standard and Mini-CVNs.

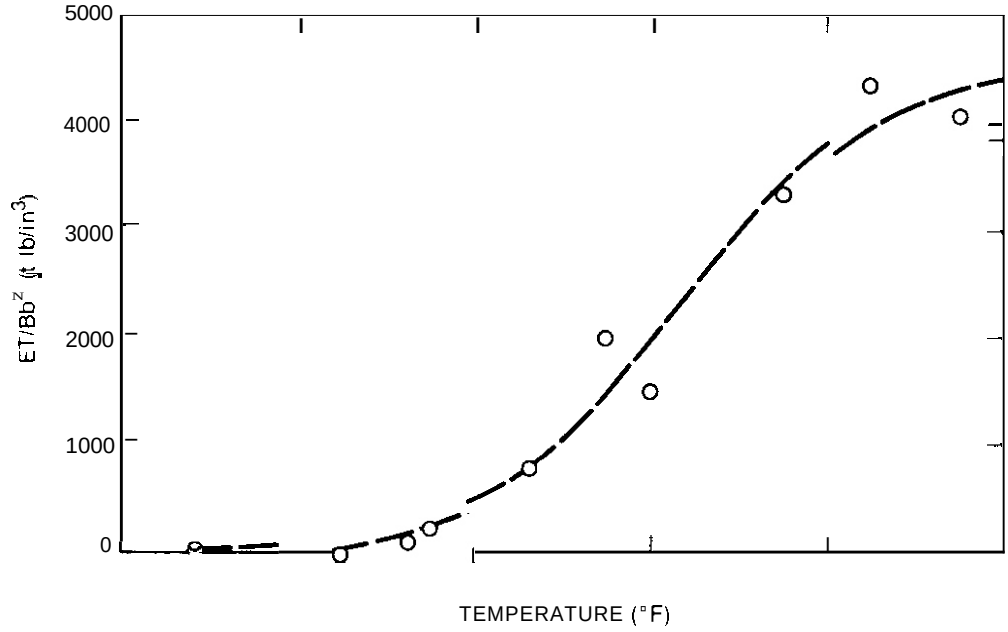

FIGURE 8. Normalized Impact Energy Curve for Alloy T for Mini-CVNs.

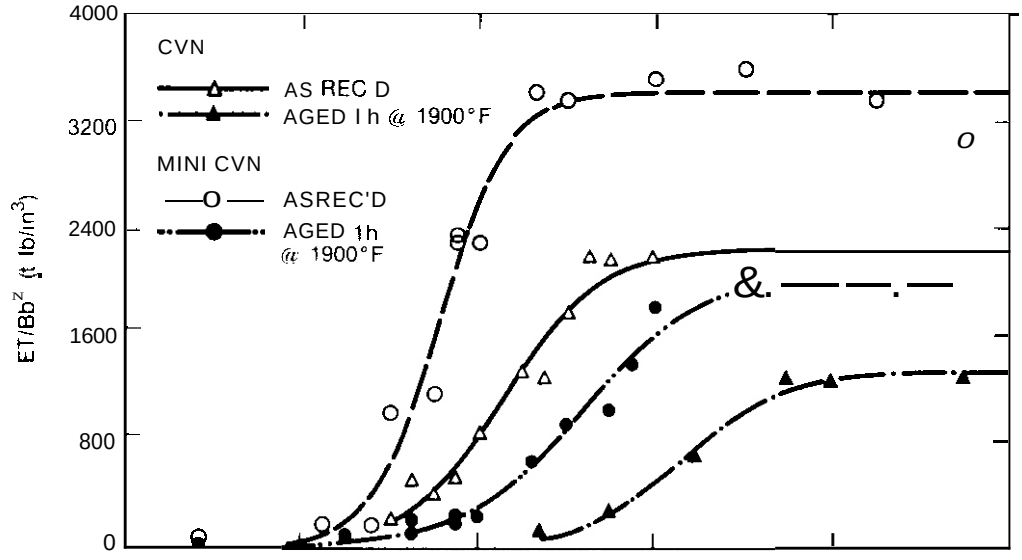

FIGURE 9. Normalized Impact Energy Curves for A508-2 for Standard and Mini-CVNs.

Work will continue on the miniature CVN specimens. In particular testing of mini-CVNs of alloys A, D and T following irradiation at various levels of flux, fluence and temperature are planned. Moreover, testing of alloys A, D, and T as well as a variety of other commercial and model alloys are planned after aging them at various times in the temperature regime 550°F-620°F. Results will be reported in the future.

FUNDAMENTAL FLOW AND FRACTURE ANALYSIS OF PRIME CANDIDATE ALLOY (PCA) FOR PATH A (AUSTENITICS)

G. E. Lucas, M. Jayakumar (Department of Chemical and Nuclear Engineering, University of California, Santa Barbara)
P. J. Maziasz (Metals and Ceramics Division, Oak Ridge National Laboratory)

1.0 Objective

The purpose of this aspect of the program is to use a set of well characterized alloys under investigation in the Alloy Development for Irradiation Performance (ADIP) program to develop an understanding of the relationship between microstructure and fundamental flow and fracture behavior. Such an understanding is vital to the development of correlation methodologies for use in the fusion materials program. Moreover, the mechanical properties data obtained in such an analysis will be of immediate interest to the ADIP program.

2.0 Summary

To date room temperature microhardness tests have been performed on samples of Prime Candidate Alloy (PCA) for the austenitics (Path A) subjected to various thermomechanical treatments (TMT). The TMTs have effected various microstructures, which have been well characterized by optical metallography and TEM. For comparison, microhardness tests have been performed on samples of N-lot, DO heat and MFE 316 stainless steel with similar TMTs. The results indicate that the TMTs investigated can significantly alter the microhardness of the PCA in a manner which is consistent with microstructural changes. Moreover, while PCA had the lowest microhardness of the four alloy types after cold working, its microhardness increased while the others decreased to comparable values after aging for 2 h at 750°C.

3.0 Program

Title: Damage Analysis and Fundamental Studies for Fusion Reactor Materials Development

Principal Investigators: G. R. Odette and G. E. Lucas

Affilation: University of California, Santa Barbara

(This work was performed in collaboration with P. J. Maziasz, Alloy Development for Irradiation Performance (ADIP) Program for Magnetic Fusion Energy, Metals and Ceramic Division, Oak Ridge National Laboratory)

4.0 Relevant DAFS Program Plan Task/Subtask

Subtask B Fundamental Mechanical Properties

Subtask C Correlation Methodology

5.0 Accomplishments and Status

5.1 Introduction

Successful development of structural alloys for fusion reactor systems requires both the experimental investigation of the properties of candidate alloys exposed to various environmental conditions as well as the development of a fundamental understanding of the response of these same materials. The latter can be used to interpret results, to help develop predictive methodologies, and to assist in guiding the alloy development effort. The effectiveness of such a parallel effort in turn requires a close collaboration between researchers in both programs. In keeping with this philosophy, the following collaborative effort was initiated to develop a fundamental understanding of the relationship between the microstructure and the mechanical behavior of Prime Candidate Alloy (PCA). Such an understanding may be used in the design of a superior alloy for structural applications in a fusion environment. PCA is a 14 Cr-16 Ni-0.25 Ti austenite that is otherwise similar to AISI 316 stainless steel. Its exact composition in comparison to several other stainless steels is given in Table 1. PCA is being considered as a candidate

TABLE 1

COMPOSITION OF AUSTENITIC STAINLESS STEELS

Alloy	Content (wt.%)*											
	Cr	Ni	Mo	Mn	C	Ti	Si	Co	Cu	P	S	N
PCA	14.0	16.2	2.3	1.8	.05	.24	.4	-	-	.01	.003	.01
DO heat	18.0	13.0	2.58	1.90	.05	.05	.80	-	-	.01	.003	.01
MFE 316	17.8	12.4	2.1	1.7	.06	<.05	.67	0.3	0.3	.04	.018	-
N-lot	16.5	13.66	2.4	1.64	.056	<.05	.46	.05	.08	.013	.006	<.05

*Balance Fe.

structural material for fusion systems. for a number of reasons, among them the potential for MC carbides which form in the system to control transmutant helium distribution and thus suppress swelling.(1-3) Consequently, considerable effort of the ADIP program has been devoted to engineering microstructures in PCA through thermomechanical treatments (TMT). Tests have also been initiated to evaluate the stability and swelling resistance of these microstructures under neutron irradiation.

However, even if one or more microstructures in the PCA system proves to be swelling resistant, mechanical properties degradation may limit wall lifetime. Therefore, tensile strength, ductility, creep, creep rupture, fracture and fatigue resistance as a function of TMT and irradiation history must all be given consideration in the evaluation of the alloy. This situation -- i.e., the existence of a variety of PCA microstructures which have been well characterized and the need to evaluate the mechanical properties of PCA as a function of these microstructure -- also represents an excellent opportunity, from a fundamental point of view, to investigate the relation between microstructure and flow and fracture behavior in a system of major interest.

To initiate an investigation of mechanical properties of PCA as a function of microstructure, standard room temperature microhardness tests were performed on pre-existing materials having a variety of TMTs. The results were used to screen materials for subsequent testing. Microhardness tests on the N-lot, DO and MFE reference heats of 316 stainless steel were performed for comparison. The results of these screening tests and the consequent planned testing are reported here.

5.2 Materials and Microstructures

The materials tested in this initial screening are listed and briefly described in Table 2. The M series constitutes MFE 316; the O series, DO heat; the N series, N-lot 316; and A, B, C, D series, the PCA microstructures. All materials were fabricated in sheet form .25-.75 mm. in thickness.

TABLE 2

MATERIALS SCREENED IN MICROHARDNESS TESTS

Designation	Description
N1	N-lot 316 -- solution annealed (1 h at 1050°C)
N3	N-lot 316 -- 20% cold worked
N4	N-lot 316 -- 20% cold worked plus 2 h @ 750°C
M1	MFE 316 -- solution annealed (1 h at 1050°C)
M3	MFE 316 -- 20% cold worked
M4	MFE 316 -- 20% cold worked plus 2 h @ 750°C
O1	DO Heat -- solution annealed (1 h at 1050°C)
O3	DO Heat -- 20% cold worked
O4	DO Heat -- 20% cold worked plus 2 h @ 750°C
A1	PCA -- solution annealed (1 h at 1150°C)
A2	PCA -- 10% cold worked
A3	PCA -- 25% cold worked
B2C	PCA -- solution annealed (1 h at 1150°C) plus 8 h @ 800°C, plus 25% cold work plus 2 h @ 750°C
B2F	PCA -- solution annealed (45 min at 1150°C) plus 8 h @ 800°C, plus 25% cold work plus 2 h @ 750°C
CC	PCA -- 25% cold work, plus 2 h @ 750°C
CF	PCA -- 25% cold work, plus 2 h @ 750°C
D	PCA -- 10% cold work, plus 2 h @ 750°C plus 10% cold work

The microstructures of most of these alloys have been described in detail elsewhere,[3-4] but for completeness, and for initiating those unfamiliar with the previous work, the microstructures of all the materials will be summarized

Representative optical micrographs and transmission electron micrographs of the microstructures of the PCA alloys are shown in Figs. 1-5. The microstructures of the A series range from A1, a material almost completely devoid of microstructural features which is characteristic of solution annealed materials (Fig. 1), to A3, a material having a fairly high dislocation density throughout (similar to Fig. 2a). The microstructures of N1, M1 and 01 are similar to A1; and N3, M3 and D3, to A3; and they are thus not shown here. However, the grain sizes are somewhat different. The initial ASTM grain size number is 8 for N-lot, DO heat and MFE 316. It is 5-7 for the fine-grained PCA's (annealed .75 h at 1100°C) and 1-3 for the coarse grained PCA's (annealed 1 h at 1150°C) as described below. For certain microstructures several different grain sizes have been produced. For example, the microstructure B2 has been produced in both the fine-grained (B2F) and coarse-grained (B2C) condition. Some representative micrographs are given in Fig. 3.

The microstructure of B2 was produced by solution annealing plus aging for 8 h at 800°C plus cold working 25% and finally aging 2 h at 750°C (see Table 2). Both B2C and B2F have relatively coarse MC precipitates at the grain boundaries (produced by the first aging) and a fine distribution of MC throughout the matrix (produced by the second aging). The set of transmission electron micrographs in Fig. 4 show the grain boundary carbides in B2. The typical fine matrix MC distribution in B2 is represented in Fig. 2. The ASTM grain size number for B2C is 1-3, while that for B2F is 5-7.

The microstructure of C was produced by aging 25% cold-worked material for 2 h at 750°C. It consists of fine MC carbides both at the grain boundary and throughout the matrix. While the matrix carbide distribution is similar to that of B2 (Fig. 2b), the grain boundary carbides are much finer. An example of this is shown in Fig. 5. Microstructures CC and CF only differ in grain size; CC is coarse grained (ASTM 1-3) and CF is fine grained (ASTM 5-7).

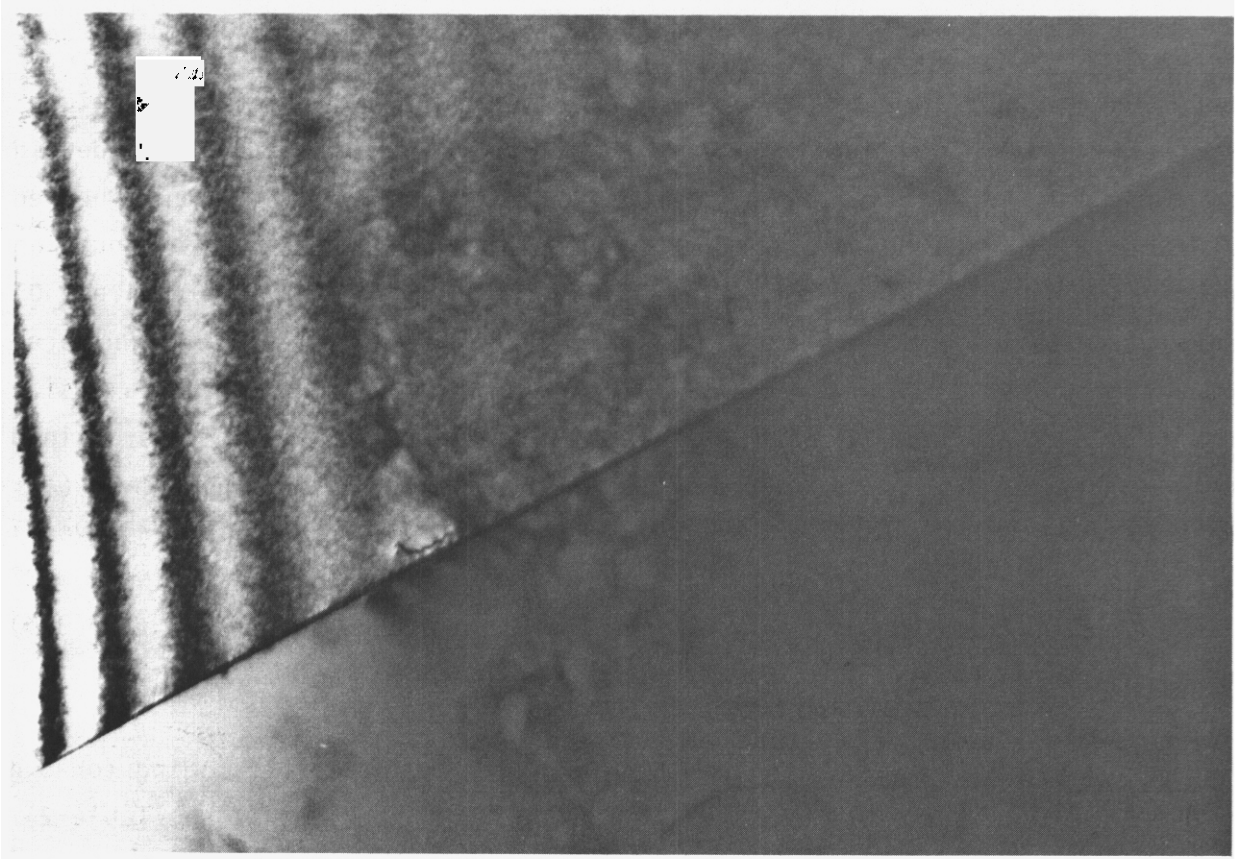

FIGURE 1. Transmission Electron Micrograph of PCA Solution Annealed 1 h at 1150°C (A1). The matrix is relatively free of dislocations, and both the matrix and grain boundaries are quite free of MC. The micrograph is representative of the structures of N1, M1 and 01 as well.

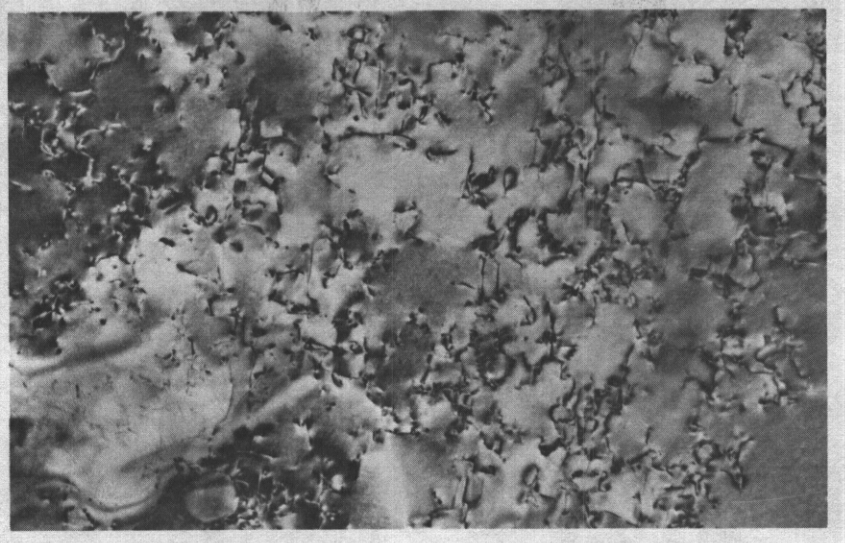

(a)

(b)

0.25μm

FIGURE 2. Transmission Electron Micrographs of PCA, 25% Cold-Worked and Aged 2 h at 750°C (A4) in a) Bright Field and b) Dark Field. The dark field image shows the fine matrix MC which precipitates upon aging PCA; this is characteristic of B2, C, and D. The dislocation structure, however, is retained; therefore, a) is also representative of the cold-worked microstructures of A2, A3, N3, O3 and M3.

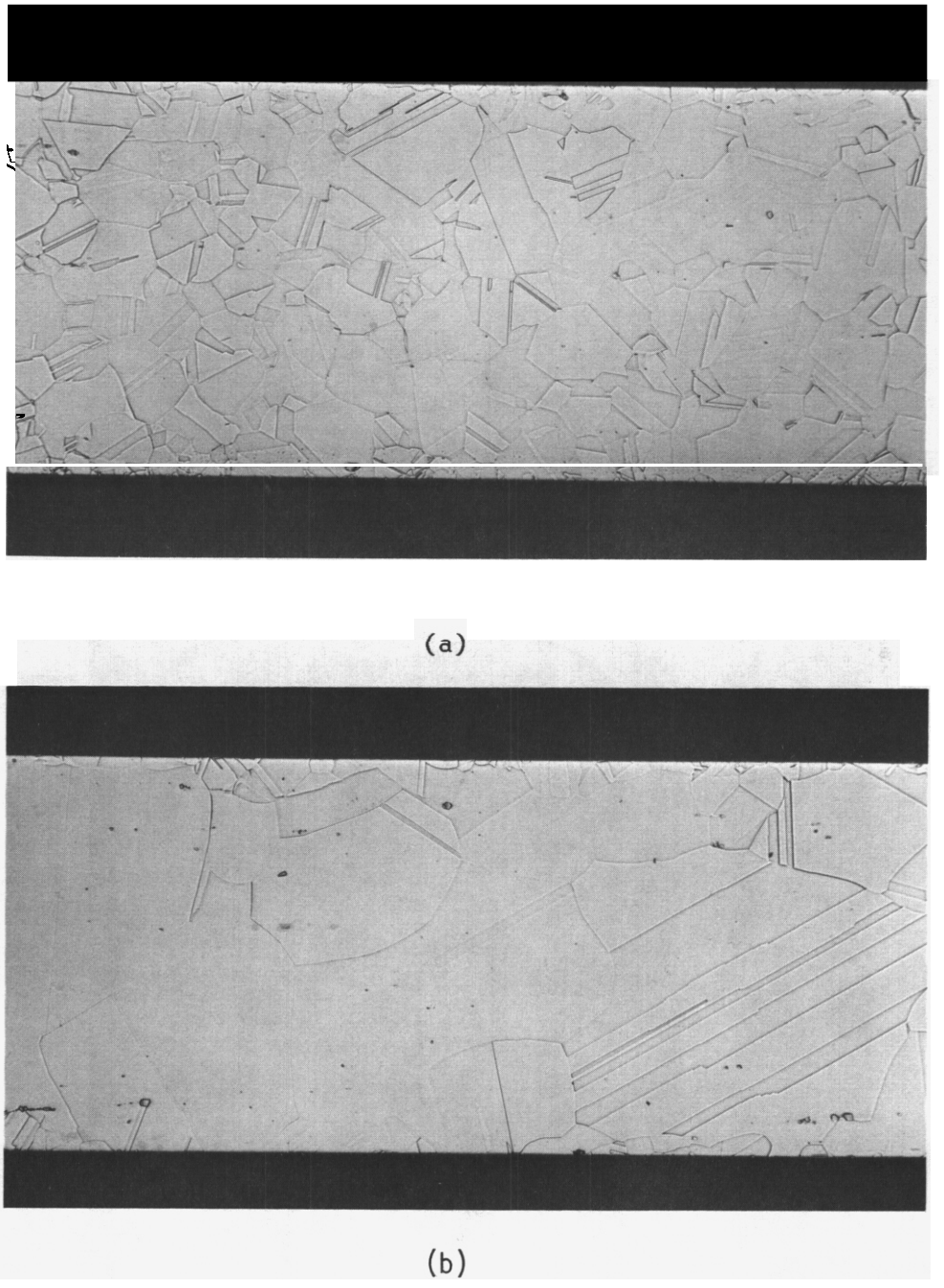

FIGURE 3. Optical Micrographs (100X) of 50% Cold-Worked PCA Annealed for 30 Minutes at a) 1100°C and b) 1150°C. The grain size of a) is characteristic of both CF and BZF. The grain size of b) is characteristic of both CC and BZC.

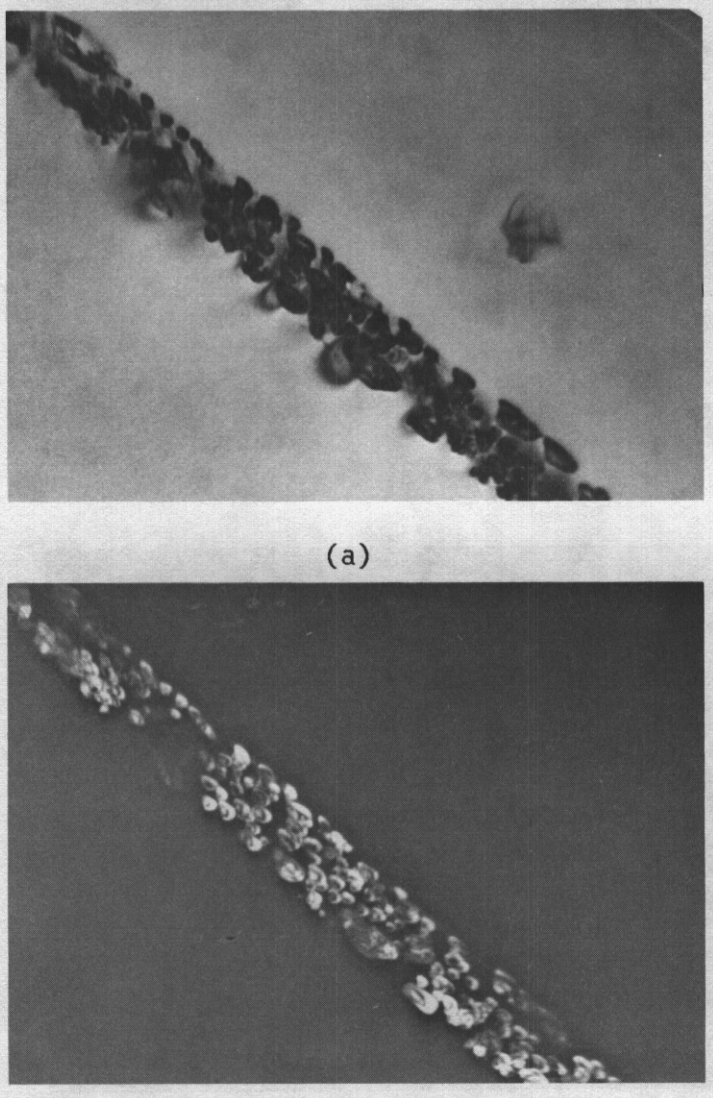

FIGURE 4. Transmission Electron Micrographs of PCA Aged 1 h at 750°C Plus 8 h at 800°C in a) Bright Field and b) Dark Field. The coarse grain boundary carbides which appear are representative of those found in B2C and B2F.

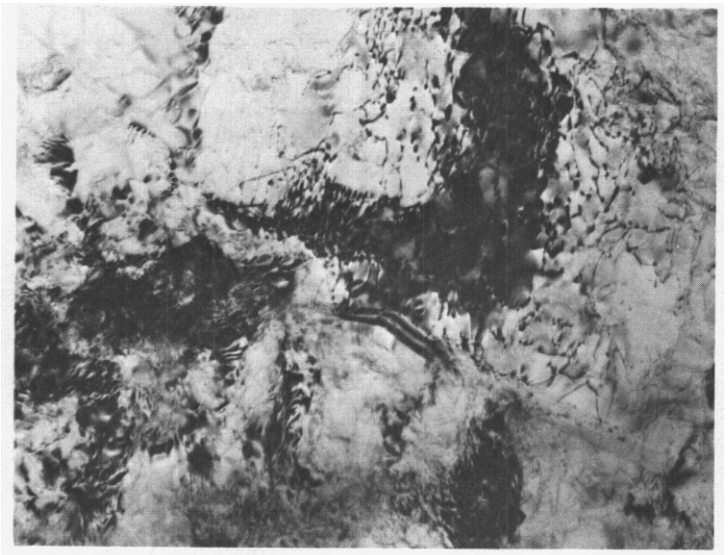

(a)

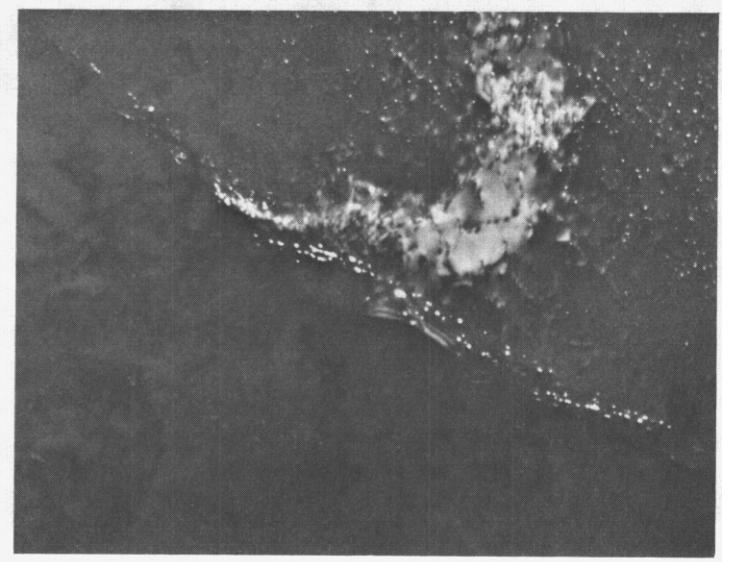

(b)

0.25μm

FIGURE 5. Transmission Electron Micrographs of PCA 25% Cold-Worked Plus Aged 2 h at 750°C in a) Bright Field and b) Dark Field. The fine MC carbide distribution which forms at the grain boundary is characteristic of microstructures CF, CC and D.

Microstructure O was produced by solution annealing plus cold working 10% plus aging at 750°C and finally cold working another 10%. The microstructure is similar to that of C in that it has a fine distribution of MC both at the grain boundaries and in the matrix. However, it appears to have an increased dislocation density in addition.

The microstructures of M4, N4, and 04 are produced by aging M3, N3, and 03, respectively, for 2 h at 750°C to compare the behavior of type 316 to the PCA for this same treatment. M4, N4 and 04 recover relative to M3, N3 and 03 with dislocation density being slightly reduced, and the fractional "dislocation-free" area being larger in the former microstructure. A representative micrograph of the matrix is given in Fig. 6a. The grain boundaries also clearly have precipitation (probably of $M_{23}C_6$ plus M_6C) developing, also shown in Fig. 6b.

The major features of these microstructures are summarized for each of the alloys in Table 3. It should be noted for later reference that microstructures of materials A1, M1, N1 and 01 are similar as are A3, M3, N3 and 03. Moreover, a major difference between the B2 and C microstructures and M4, N4 and 04 is the absence of intragranular MC in the latter microstructures.

5.3 Microhardness Results

Standard diamond pyramid microhardness (DPH) tests were performed at room temperature on each of the materials listed in Table 2. From preliminary tests a load of 100g was selected to provide indentations large enough such that surface effects were negligible, yet small enough that specimen thickness effects were avoided. At least six indentations were performed on each sample. The results are listed in Table 4.

For the various PCA TMTS, the trend was as expected. Microhardness increased with increasing cold work, and was greatest for microstructures in which MC carbides were distributed in the matrix. Beyond this no clear trends were indicated except that the scatter in microhardness data increased with increasing inhomogeneity in the microstructure.

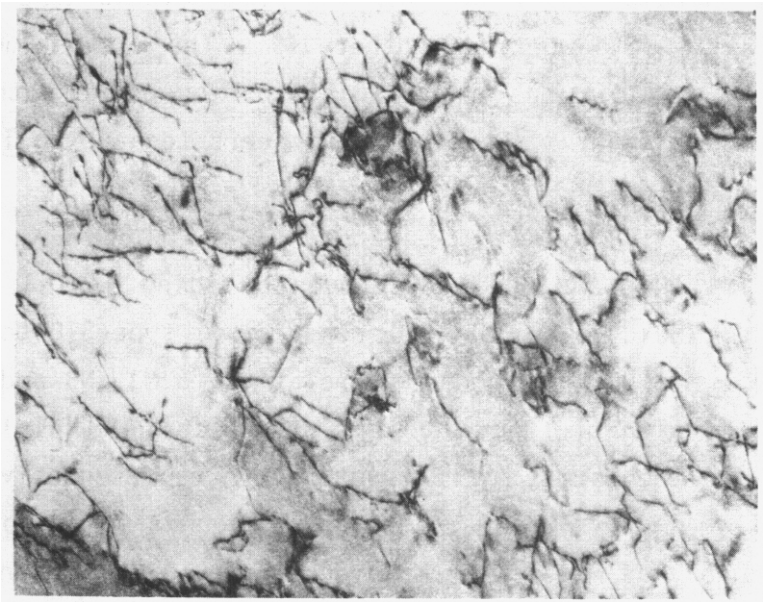

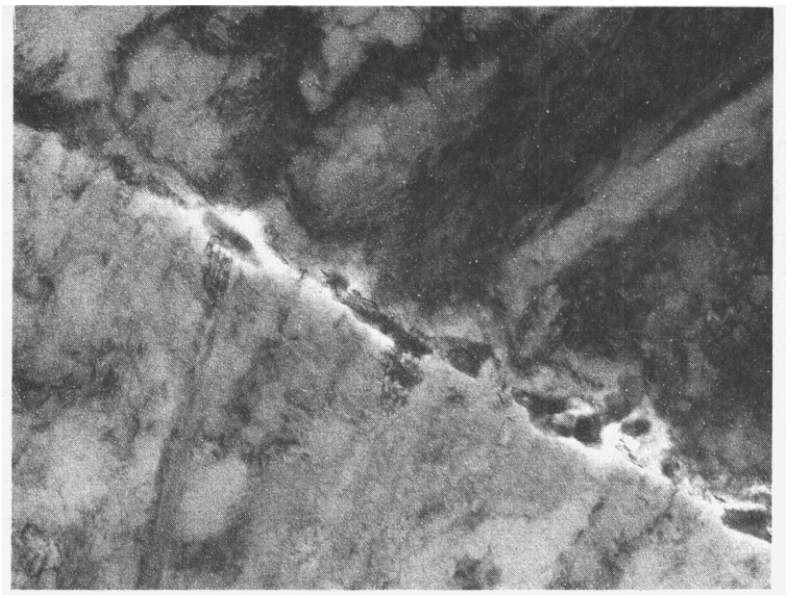

FIGURE 6. Transmission Electron Micrographs of MFE 316 20% Cold-Worked and Aged 2 h at 750°C (M4). As shown in (a) the dislocation network produced upon cold-working is partially recovered. This microstructure is also representative of N4 and 04. As shown in (b) some grain boundary precipitation has already occurred.

TABLE 3

MAJOR FEATURES OF THE MICROSTRUCTURES OF THE TEST MATERIALS

Designation	Microstructure
N1	solution annealed, ASTM grain size number 8
N3	20% c/w dislocation density
N4	partially recovered dislocation density and distribution
M1	solution annealed, ASTM grain size number 8
M3	20% c/w dislocation density
M4	partially recovered dislocation density and distribution
01	solution annealed; ASTM grain size number 8
03	20% c/w dislocation density
04	partially recovered dislocation density and distribution
A1	solution annealed, ASTM grain size number 1-3
A2	10% c/w dislocation density
A3	25% c/w dislocation density
B2C	ASTM grain size number 1-3; coarse MC at grain boundaries; fine MC in matrix
B2F	ASTM grain size number 5-7; coarse MC at grain boundaries; fine MC in matrix
CC	ASTM grain size number 1-3; fine MC at grain boundaries and in matrix
CF	ASTM grain size number 5-7; fine MC at grain boundaries and in matrix
D	ASTM grain size number 5-7; fine MC at grain boundaries and in matrix plus intermediate dislocation population

TABLE 4

RESULTS OF ROOM TEMPERATURE DPH TESTS AT 100g

Material Designation	DPH (kg/mm^2)
N1	130 ± 8
N3	375 ± 10
N4	300 ± 18
M1	158 ± 5
M3	295 ± 22
M4	241 ± 12
01	166 ± 8
03	308 ± 18
04	256 ± 20
A1	143 ± 4
A2	198 ± 4
A3	237 ± 16
B2C	252 ± 14
B2F	242 ± 12
CC	245 ± 14
CF	268 ± 4
D	244 ± 27

In comparing PCA with N-lot, MFE 316 and DO heat the trends illustrated in Fig. 7 and 8 were observed. In the solution annealed condition, both DO heat and MFE 316 were harder than PCA. This was also the case after 20-25% cold work. Moreover, it appears that PCA work hardens to a lesser extent than either DO heat or MFE 316, and that N-lot work hardens to the greatest extent. This will be investigated in subsequent tensile tests. After aging, the cold-worked structures for 2 h at 750°C, however, the N-lot, MFE 316 and OO heat partially recover to produce a softer material, whereas the PCA precipitate hardened to a value equal to or greater than OO heat and MFE 316 in the aged condition. The extent of recovery (slope of the line in Fig. 8) was the same for N-lot, MFE 316 and DO heat, indicating the recovery kinetics are similar, even though the work hardening response is not.

Consequently, it appears the MC precipitation may have some benefits with respect to improved mechanical properties of PCA. The MC formation appears to pin the dislocation structure and inhibit stress-free recovery. It is expected that this will benefit strength at elevated temperatures. Additional tests, particularly elevated temperature strength, ductility and fracture resistance, are warranted.

6.0 References

1. G. R. Odette, P. J. Maziasz, J. A. Spitznagel, J. Nucl. Mater., 103 and 104 (1981) 1289.

2. P. J. Maziasz, F. W. Wiffen, E. E. Bloom, Proc. Intern. Conf. on Radiation Effects and Tritium Technology for Fusion Reactors, CONF-750989, Vol. 1 (March 1976) 259.

3. P. J. Maziasz, T. K. Roche, J. Nucl. Mater., 103 and 104 (1981) 797.

4. T. K. Roche and P. J. Maziasz, ADIP Quart. Prog. Report, DOE/ER-0045/4 (Sept. 30, 1980) 73.

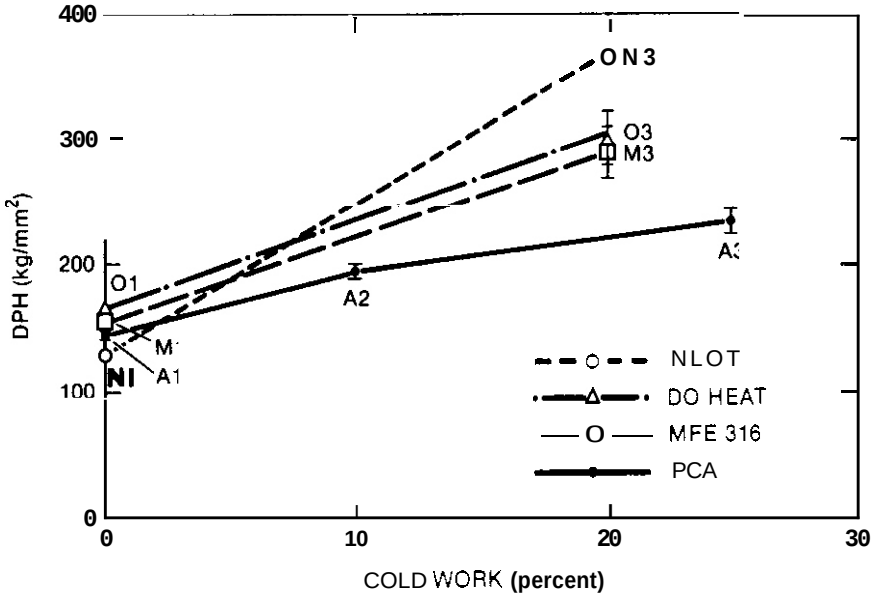

FIGURE 7. **Variation of Diamond Pyramid Hardness (DPH) with Cold-Work for PCA and Three Austenitic Stainless Steels.**

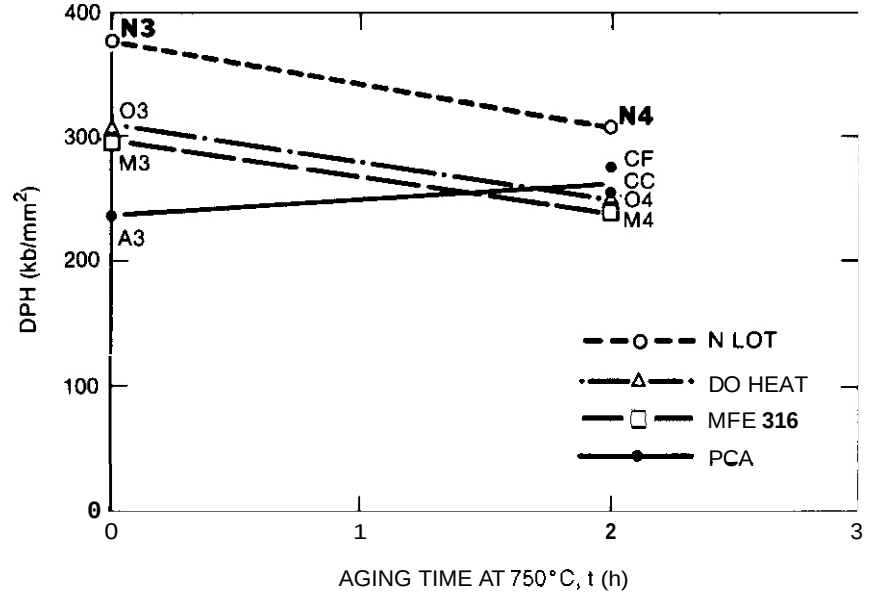

FIGURE 8. **Variation of Diamond Pyramid Hardness (DPH) with Aging Time at 750°C for PCA and Three Austenitic Stainless Steels.**

7.0 Future Work

Room temperature tensile tests are already in progress to increase the nominal flow propery information on PCA. In addition creep and creep rupture tests on selected microstructures of PCA are being planned. In particular, there is interest in evaluating the role of grain boundary carbides on creep and creep rupture life from both a practical and fundamental point of view.

The B, C, and D microstructures should be relatively stable at temperatures less than their corresponding aging temperatures. These aging temperatures in turn are larger than the temperatures at which cold-worked 316 stainless steel begins to lose strength by recovery and recrystallization. Therefore, the B, C, and D microstructures hold some promise of having superior high temperature strength.

EFFECT OF HELIUM IRRADIATION ON FRACTURE MODES

T. Hanamura and W. A. Jesser (University of Virginia)

1.0 Objective

The objective of this work is to determine the crack opening mode during in-situ HVEM tensile testing and how it is influenced by test temperature and helium irradiation.

2.0 Summary

Most cracks were mixed mode I and II. However, between 250°C and room temperature the effect of helium irradiation is to increase the amount of mode I crack propagation. Mode II crack opening was observed as grain boundary sliding initiated by a predominantly mode I crack steeply intersecting the grain boundary. Mode II crack opening was absent in irradiated specimens tested between 250°C and room temperature, but could be restored by a post irradiation anneal.

3.0 Program

Title: Simulating the CTR Environment in the HVEM
Principal Investigators: W. A. Jesser and R. A. Johnson
Affiliation: University of Virginia

4.0 Relevant DAFS Program Plan Task/Subtask

Task II.C.13 Effects of Helium and Displacements on Crack Initiation and Propagation

5.0 Accomplishments and Status

5.1 Introduction

In order to understand the mechanisms of crack initiation and propagation in irradiated materials, in-situ HVEM tensile testing of microspecimens is being conducted under various conditions of irradiation induced microstructure and temperature. Already such crack propagation parameters as crack-tip angles and plastic zone size have been investigated[1-3]. However, more information regarding the characterization of crack propagation is necessary before the mechanisms of intergranular fracture and flow localization can be related to irradiation induced microstructure and tensile test conditions[4]. One such parameter is crack opening mode. Intergranular failure can occur by grain boundary sliding through mode II crack propagation along the boundary or it can occur by other crack opening modes including a mixed mode. Low ductility and radiation hardened material may be expected to fail intergranularly through mode I crack propagation. It is the intent of this report to show the data obtained from conducting in-situ HVEM tensile tests on type 316 stainless steel microspecimens and to determine the effect of irradiation and tensile test temperature on crack opening mode.

5.2 Experimental Details

Foils of commercial type 316 stainless steel, a first wall candidate for the Tokamak, were prepared for tensile testing by annealing at 1000°C for 1 hour in vacuum (pressure < 10^{-4} Pa). Specimens were 12 mm by 3 mm in size punched from the 40-μm thick foil. Next the central portion of the specimen was electropolished to perforation in a 90% acetic acid - 10% perchloric acid solution at 18°C. After thinning, He-ion irradiation induced microstructures were produced in an HVEM-ion accelerator facility[5,6] by bombarding specimens with 80 keV helium ions to fluences up to ~ 3 x 10^{18} ions cm^{-2}. In addition, some samples were given a post-irradiation anneal in vacuum (10^{-4} Pa or better) to coarsen the microstructural features. Tensile testing in the HVEM was carried

out in a hydraulically operated load-elongation tensile stage capable of heating the specimen up to about 600°C[7]. During the crack propagation, data was obtained from still micrographs and video tape. From these sources the mode of crack opening was determined.

5.3 Experimental Results and Discussion

In order to determine the crack opening mode, frames from a video recording of crack propagation were used to measure the crack propagation direction, $\vec{P}$, angle, a, between the tensile axis and $\vec{P}$, and the crack opening displacement vector, $\vec{D}$. The crack geometry is shown in Figure 1 along with the relevant parameters.

Direction of displacement vectors for several directions of crack propagation were measured by using data from video tape. The displacement vectors were determined by measuring the displacements of arbitral points, A and B, near the crack tip. Each displacement vector, $\vec{D}$, may be separated into a segment parallel to the crack propagation vector, $\vec{P}$, denoted by $D_{\parallel}$, and a perpendicular segment, $\vec{D}_{\perp}$. The angle between $\vec{D}$ and $\vec{D}_{\parallel}$ is taken to be e so that $D_{\perp} = D \sin e$ corresponds to mode I crack opening and $D_{\parallel} = D \cos e$ corresponds to mode II cracking. Also, $D_{\perp}^2 + D_{\parallel}^2 = D^2$. Therefore the % mode I is calculated as $100\ D_{\perp}^2/D^2$, which is $100 \sin^2 e$. Similarly the % mode II crack opening displacement becomes $100\ D_{\parallel}^2/D^2$, which is $100 \cos^2 e$. Accordingly % mode I + % mode II = 100%. This last result is a consequence of deleting mode III displacements. From the video recordings, displacements parallel to the electron beam are not measurable and hence any mode III displacements are unnoticed.

The progression of one or more cracks was followed by video recordings through each of four different specimens. As each crack propagated through the specimen, the crack changed directions and propagation characteristics. The % mode I crack opening when the crack was recorded in any of many configurations is plotted against the crack propagation angle α in Figure 2.

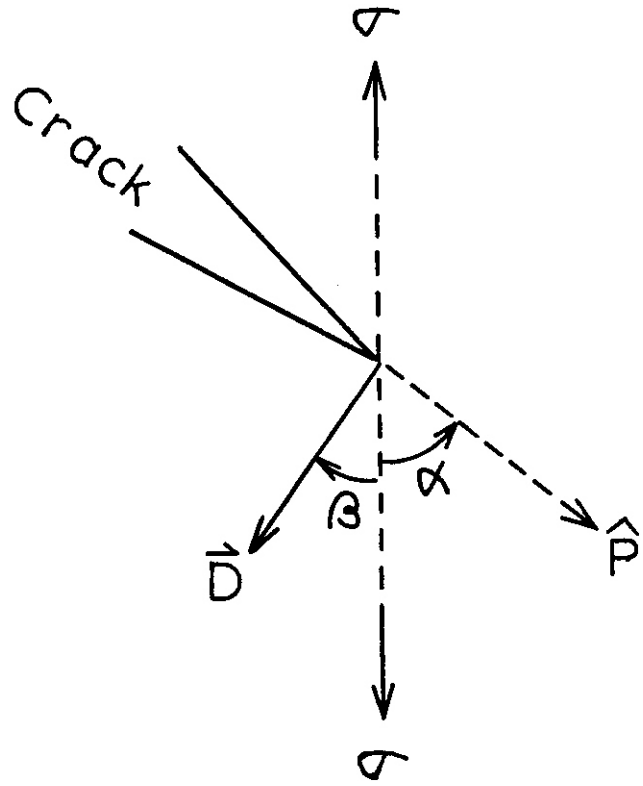

FIGURE 1. Schematic Drawing of a Crack Tip. The crack opening displacement is $\vec{D}$, the crack propagation direction is $\vec{P}$, the angle between the tensile axis and $\vec{P}$ is a, and that between the tensile axis and $\vec{D}$ is β.

* unirradiated, tested at room temperature

+ post irradiation annealed, tested at room temperature
(flux = 1.4 x 10^{15} ions • cm^{-2} sec^{-1}; dose = 4.2 x 10^{17} ions • cm^{-2})
(annealed at 900°C for 10 sec)

⊡ no post irradiation annealing, tested at room temperature
(flux - 3.3 x 10^{14} ions•cm^{-2} sec^{-1}; dose = 6.0 x 10^{17} ions • cm^{-2})
(no annealing)

A post irradiation annealed, tested at 250°C
(flux = 3.0 x 10^{14} ions • cm^{-2} sec^{-1}; dose = 1.0 x 10^{17} ions • cm^{-2})
(annealed at 300°C)
(mixed fracture mode)

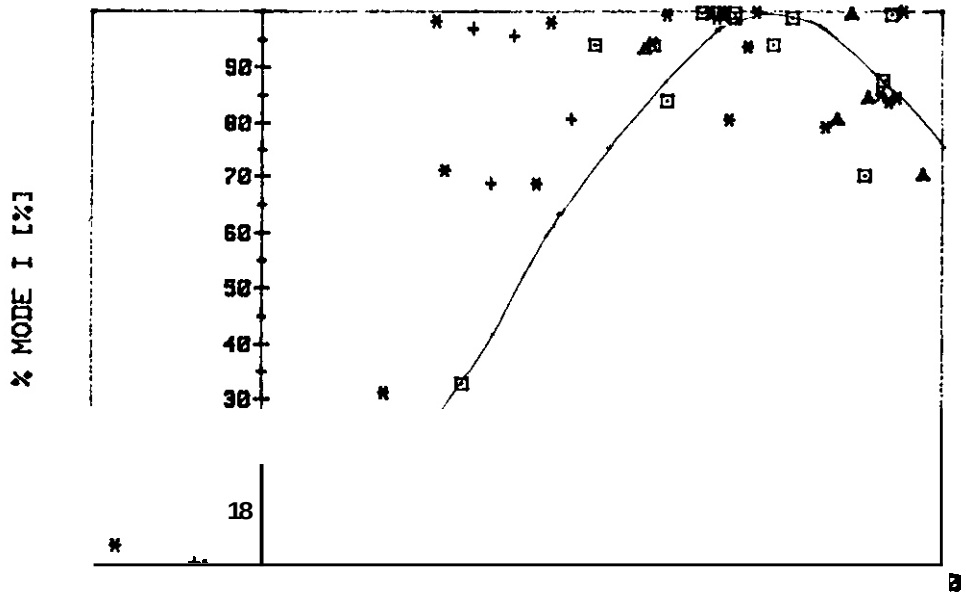

FIGURE 2. Graph of Observed % Mode I Opening of a Given Crack Plotted as a Function of Its Propagation Angle *a*. Specimens were type 316 stainless steel irradiated with 80 keV helium ions. The smooth curve represents a rigid displacement of the crack flanks in a direction parallel to the tensile axis, i.e. $\beta = 0$.

The smooth curve represents the theoretical relationship between % mode I and a when $\beta = 0$. This situation corresponds to a rigid displacement of the crack flanks in a direction parallel to the tensile axis, i.e. $\vec{D}$, parallel to the tensile axis for all values of a. Such a case would approximate a very brittle material.

Grain boundary sliding would be expected to occur when $\vec{G}$ and $\vec{P}$ are parallel. Experimentally grain boundary sliding is observed when a is small or negative, i.e. $\vec{P}$ is approximately parallel to the tensile axis and when essentially 100% mode II crack opening occurs. All of the 100%mode II cracks were along grain boundaries and all were preceded by a crack of strong mode I character intersecting the grain boundary at an angle near 90". The effect of helium irradiation was to inhibit this mode II crack propagation and favor mode I propagation. In the case of the unirradiated specimen tested at room temperature, there is a transition area from mode I cracking to that of mode II at $a \sim 30$". In all cases tested, mode II cracking was only occasionally observed while near mode I crack propagation was common.

Using the unirradiated specimen tested at room temperature as an example of a ductile failure, one can compare the post annealed specimen with the one which was not post annealed and see that according to Figure 2, the effect of post annealing is to increase ductility. The least ductile specimen is taken as the one exhibiting partly intergranular failure and partly transgranular failure. Only one of the four specimens tested showed this mixed mode of failure, which is attributed to the elevated test temperature and to the low temperature of the post irradiation annealing. The absence of 100%mode II failure in this specimen shows that irradiation can promote mode I type intergranular failure.

Another graphical method for revealing brittle-like failure is the angle between $\vec{D}$ and $\$$, $a + \beta$, plotted against crack direction a. The data of Figure 2 are replotted in Figure 3 according to the $\alpha + \beta$ versus a scheme. The rigid displacement case of $\beta = 0$ is represented by the straight line and is found to well represent the set of data obtained at 250" which showed a mixed fracture

⊙ unirradiated SS316 tested at R.T.

• unannealed He-irradiated SS316 tested at R.T.

A annealed He-irradiated SS316 tested at R.T.

⊡ mixed fracture mode He-irradiated SS316 tested at 250°C

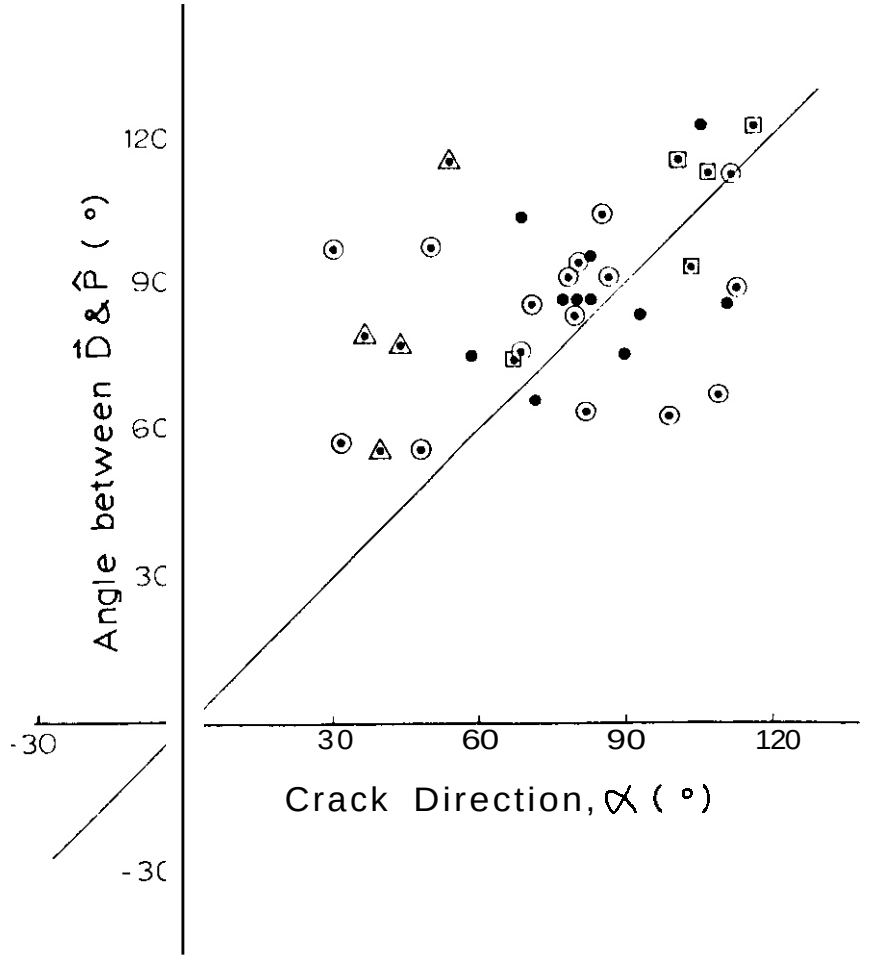

FIGURE 3. Graph of α + β vs α for the Same Four Specimens of Figure 2. The β = 0 line is drawn as a reference line representing brittleness.

mode which was partly intergranular and partly transgranular.

5.4 Conclusions

Grain boundary sliding is initiated by a nearly mode I crack intersecting the boundary at a steep inclination.

Mode II crack propagation was only observed when the displacement vector and tensile axis were parallel to each other and also to a grain boundary.

Mode II failure is hindered and mode I cracking favored by helium ion irradiation when tensile testing at temperatures between 250°C and room temperature.

In irradiated specimens tested between 250°C and room temperature mode I intergranular failure replaces mode II intergranular failure.

6.0 References

1. J. I. Bennetch, R. D. Gerke and W. A. Jesser, "HVEM Observations of Crack Propagation in Helium Irradiated Type 316 Stainless Steel Containing Precipitates", DAFS Quarterly Report DOE/ER-0046/2 (1980) 75.

2. D. S. Gelles, L. E. Thomas and R. W. Powell, "HVEM In-situ Deformation of Neutron Irradiated Fe-0.3 Cu", 109th AIME Meeting, Las Vegas, Nevada (1980).

3. R. D. Gerke, T. Hanamura and W. A. Jesser, "Crack Propagation Characteristics in Helium Irradiated Type 316 Stainless Steel", DAFS Quarterly Report DOE/ER-0046/6 (1981) 97.

4. J. I. Bennetch and W. A. Jesser, "Microstructural Aspects of Helium Embrittlement in Type 316 Stainless Steel", J. Nucl. Mater., 103 and 104 (1981) 809.

5. W. A. Jesser, J. A. Horton, and L. L. Scribner, "Adaptation of an Ion Accelerator to a High Voltage Electron Microscope", Rad. Effects, 29 (1976) 79.

6. W. A. Jesser, "Light Ion Accelerator High Voltage Electron Microscope Facility for CTR Radiation Damage Studies", IEEE Trans. Nuc. Sci. NS-26 (1979) 1252.

7. R. D. Gerke and W. A. Jesser, "Quantitative Load-Elongation Capabilities of an In-situ Hot Tensile Stage for HVEM Use", DAFS Quarterly Report, DOE/ER-0046/8 (1982) 71.

7.0 Future Work

Similar studies are being extended to neutron irradiated specimens and to higher tensile test temperatures.

THE DEVELOPMENT OF ANISOTROPIC DISTRIBUTIONS OF NETWORK DISLOCATION BURGERS VECTORS IN ALLOYS IRRADIATED UNDER STRESS

D. S. Gelles, F. A. Garner (Westinghouse Hanford Company), B. L. Adams (University of Florida)

1.0 Objective

The object of this effort is to provide models for the microstructural development that occurs in irradiated alloys and thereby predict the deformation expected in environments that lie outside the range of available data. The deformation arising from irradiation creep in fusion environments requires knowledge of the evolution of Frank interstitial loops and network dislocations.

2.0 Summary

When stress is applied to a metal during high temperature irradiation, both the Frank loops and the network dislocation products develop an anisotropy in the distribution of Burgers vectors. This anisotropy appears in all three important stages of microstructural development: first in the planar distribution of loops, then in their unfaulting and finally in the post-unfaulting growth of the network components. The first and last of these three stages are dominated by the Stress-Induced Preferential Absorption (SIPA) mechanism of irradiation creep for PE16, the experimental system studied.

One consequence of the anisotropy of network dislocations may be the loss at high fluence of the previously observable microstructural record of the stress state expressed in the distribution of the Frank loops on the various close-packed planes.

3.0 Program

Title: Irradiation Effects Analysis (AKJ)
Principal Investigator: D. G. Doran
Affiliation: Westinghouse Hanford Company

4.0 Relevant Program Plan Task/Subtask

Subtask II.C.14 Models of Flow and Fracture Under Irradiation
Subtask II.C.17 Microstructural Characterization

5.0 Accomplishments and Status

5.1 Introduction

It has been shown in a number of studies that the early evolution of Frank loops in irradiated metals is sensitive to the local stress state.[1-9] This sensitivity is expressed primarily in the unequal partition and growth of Frank loops on the various close-packed atomic planes. The partition is thought to be a consequence of the SIPA* mechanism of irradiation creep responding to the anisotropy of the applied stress field.[3,4,10,11] Prior to this work there has not been demonstrated a corresponding anisotropy in the network dislocations that evolve after unfaulting of the Frank loops.

If both loops and network dislocations evolve in an anisotropic fashion it is expected that there will be significant consequences not only in the microscopic but also the macroscopic behavior of the alloy with further irradiation. In this report the existence of anisotropic evolution of network Burgers vectors is demonstrated, and its origin and some consequences are analyzed.

5.1.1 Dislocation Structure of Nimonic PE16

If the dislocation network analyzed is too far removed in fluence from the loop network from which it originally evolved, a substantial portion of the microstructural record of dislocation evolution may be lost. Therefore it is best to analyze a microstructure which has only recently evolved from one dominated by Frank loops to one dominated by dislocations. Those results can then be compared with other specimens irradiated to higher fluence. Table 1 lists the

*Stress-Induced Preferential Absorption (of interstitials).

TABLE 1

IRRADIATION HISTORIES AND STRAINS FOR NIMONIC PE16 PRESSURIZED TUBES

Specimen Identity	Condition	Irradiation Temperature (°C)	Fluence, $\times 10^{22}$ n/cm^2 (E>0.1 MeV)	Hoop Stress (MPa)	$\frac{\Delta D}{D}$(SD)	$\frac{\Delta \rho}{\rho}$(SD) (6)
AV75	Solution Treated	550	2	155	-0.02	0.12
AV69	Solution Treated	550	2	0	-0.00	-0.60
BT03	Overaged	480	3	331	1.17	1.34
AX41	Solution Treated and Aged	430	3	331	1.26	1.35

$\frac{\Delta D}{D}$ = diameter increase, $\frac{\Delta \rho}{\rho}$ = density change

irradiation conditions of the four Nimonic PE16 specimens studied. All specimens were cut from thin-walled gas-pressurized irradiation creep tubes irradiated in EBR-II. Care was taken to determine the orientation of each microstructural component with respect to the 2:1 biaxial stress state of the tube wall.

Two of the specimens (AV69 and AV75) are at low fluence (~10 dpa) and are exceptionally useful for our purpose because they are identical specimens except that one is stressed and one is not, allowing a determination uniquely of the effect of stress on microstructural evolution. The other two specimens at higher fluence (BT08 and AX41) unfortunately do not have stress-free counterparts. In addition, the loop structure in AV75 is just beginning to break down, which allows comparison in a single grain of the anisotropy of both the unfaulted loops and their products after unfaulting. (Some aspects of the microstructures of AV69 and AV75 have been previously reported in References 4 and 10.)

As shown in Figure 1, the predominant microstructural features of one grain in AV75 are large faulted Frank loops which are just beginning to unfault in some areas. In the faulted regions the planar densities of Frank loops exhibit a strong dependence on the stress component normal to the loop plane, as shown in Figure 2. Note that a similar grain in the unstressed tube AV69 contains planar loop distributions which are much more uniform. In both the stressed and unstressed specimens it was earlier shown that the interstitials that have survived recombination are incorporated into Frank loops and the corresponding vacancies can all be found in voids.[4] No other dislocation microstructure competes with loops prior to the onset of the unfaulting process. The applied stress has increased the number of loops but not their total interstitial content.[4] This causes a small enhancement (~28%) of the loop perimeter in AV75 compared to that of specimen AV69.

When one of the unfaulted areas of AV75 was examined, the resulting perfect dislocation network was found to exhibit a pronounced variation in density for each of the six possible Burgers vectors. Table 2 shows that, in specimen

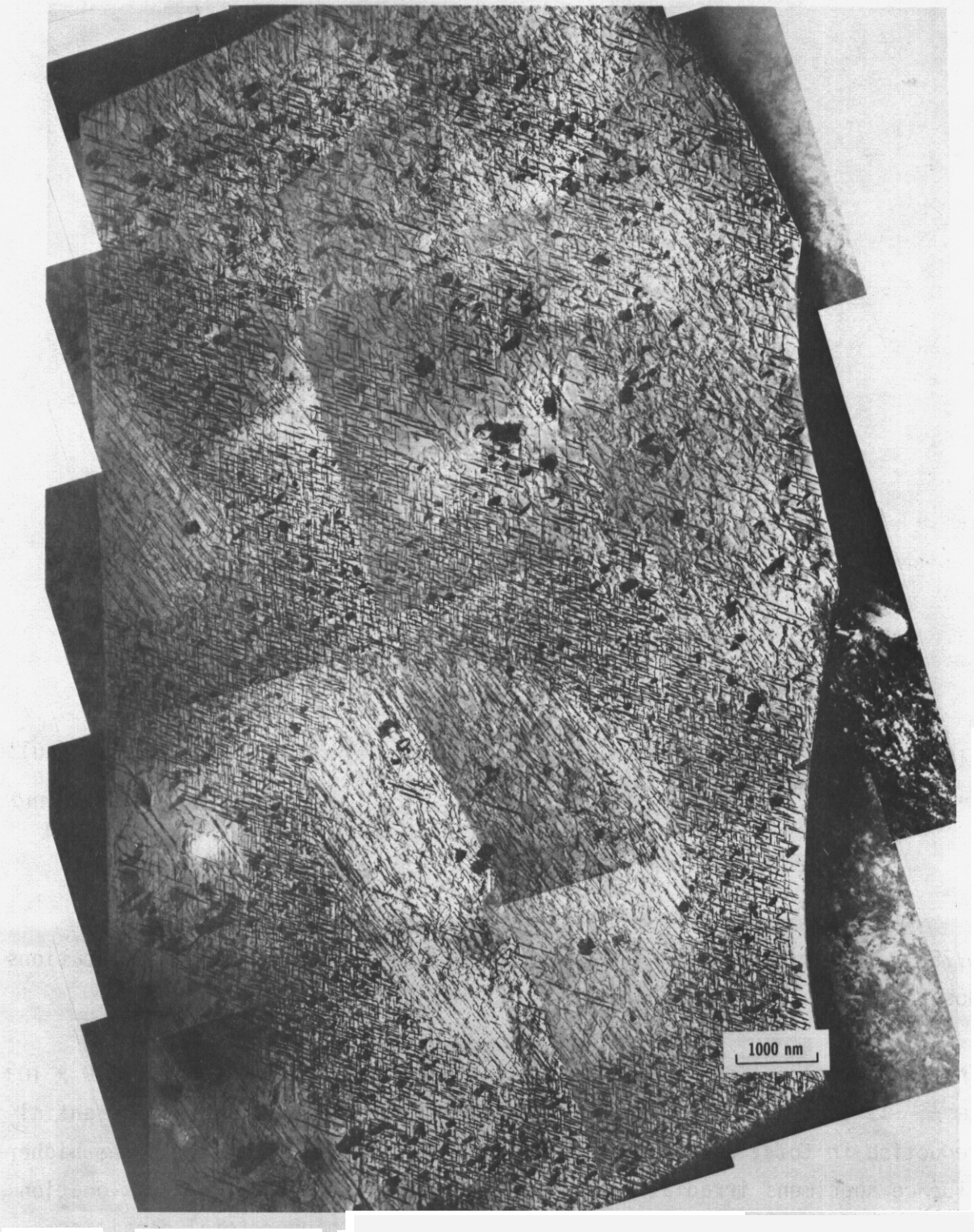

Montage Showing Variations in the Dislocation Microstructure of a Single Grain in a Specimen of Nimonic PE16 After Irradiation to 2.0 x 10^{22} n/cm² (E>0.1 MeV) at 545°C Under a Hoop Stress of 167 MPa. Note that Some Areas are Just Beginning to Unfault.

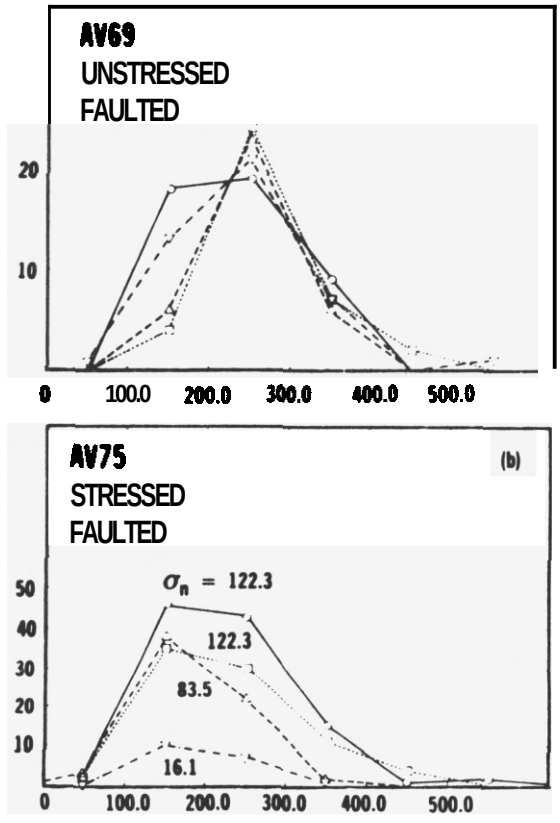

FIGURE 2. Frank Loop Size Distributions (arbitrary units) Observed in Faulted Regions of Solution-Treated Nimonic PE16 Irradiated to a Fluence of 2.0×10^{22} n/cm² (E>0.1 MeV) at 550°C. At Hoop Stresses of 0 and 167 MPa. The Normal Stress Levels for Each Plane are Given in the Figure.

AV75, a factor of twelve difference in density is found between dislocations possessing the most common and least common Burgers vectors.

The total dislocation density in the faulted area of AV75 is only $\sim 2.0 \times 10^{9}$ cm^{-2}. It thus appears that the unfaulting process has led to a substantial reduction in total dislocation density. Note in Table 2 that in the higher fluence specimens irradiated at a lower temperature the network dislocation densities are also quite anisotropic but exist at higher total densities ($\sim 1 \times 10^{10}$ cm^{-2}).

TABLE 2

MEASUREMENTS OF DISLOCATION DENSITY (cm/cm³) FOR THE VARIOUS PERFECT DISLOCATION BURGERS VECTORS IN SELECTED IRRADIATION CREEP SPECIMENS OF NIMONIC PE16

$\bar{b}$	AV75	BT08	AX41
$\frac{a}{2}\langle\bar{1}10\rangle$	6.04 x 107	1.62 x 10'	6.81 x 10^8
$\frac{a}{2}\langle110\rangle$	7.25 x 10^8	3.57 x 109	1.59 x 109
$\frac{a}{2}\langle\bar{1}01\rangle$	6.04 x 107	2.11 x 10^8	2.27 x 10^8
$\frac{a}{2}\langle101\rangle$	5.31 x 10^8	6.05 x 109	2.21 x 109
$\frac{a}{2}\langle0\bar{1}1\rangle$	1.02 x 10^8	2.92 x 10^8	1.36 x 109
$\frac{a}{2}\langle011\rangle$	5.31 x 10'	5.25 x 109	1.60 x 109
Total	20.1 x 10^8	15.5 x 109	7.7 x 109

A further important observation is that the dominant perfect dislocation type in all cases was found to be a/2 <100> (100) edge dislocations. In this configuration glide is thought to be highly restricted and dislocation climb becomes the predominant creep mode. Therefore, a mechanism involving a significant amount of glide cannot be controlling irradiation creep in these specimens.

5.2 Discussion

5.2.1 Low Fluence Specimens

The data of Table 2 clearly show that the network dislocation density that evolves under stress is anisotropic in its distribution of Burgers vectors. If one or more flow processes are operating, the origin of the anisotropy must lie either in the original anisotropy of the Frank loop population, or in the nature of the unfaulting process, or in the post-unfaulting events. As shown below it appears that the anisotropy arises in all three stages of the evolution.

It is easiest to demonstrate the action of some of these stages using the data from specimens AV69 and AV75. No unfaulting has occurred in AV69, and AV75 is obviously just in the process of unfaulting. It can be shown that stress affects the post-unfaulting distribution of line length on the four close-packed planes. If the stress that produced the anisotropy were to be removed and the loops allowed to self-unfault, one would expect to see some relaxation or reduction in the anisotropy of the resulting network. This would occur because each loop Burgers vector can decompose to form any one of three perfect dislocation vectors (as shown in Table 3). Each of these vectors lies on two close-packed planes which are different from the original loop plane.

If one calculates the consequence of an isotropic self-unfaulting process for a stressed specimen based on the detailed unfaulted loop size distribution, the results are seen in Table 4. In this equipartition approach no loss of line length is assumed. Although the equipartition approach would predict densities of the various vectors varying no greater than a factor of 2.8, the actual variation is a factor of twelve. This indicates that the unfaulting process itself is quite anisotropic, since unfaulting is just occurring in specimen AV75 and insufficient time has accumulated for some post-unfaulting mechanism to dominate the evolution.

TABLE 3

POSSIBLE PERFECT DISLOCATIONS FORMED FROM FRANK LOOPS

Loop Plane	Possible Vectors		
(111)	<011>	<101>	<110>
$(1\bar{1}1)$	$<0\bar{1}1>$	<101>	$<\bar{1}10>$
$(11\bar{1})$	$<0\bar{1}1>$	$<\bar{1}01>$	<110>
$(\bar{1}11)$	$<\bar{1}01>$	$<\bar{1}10>$	<011>

TABLE 4

COMPARISON OF MEASURED AND CALCULATED DISLOCATION DENSITY FOR THE VARIOUS POSSIBLE PERFECT DISLOCATION BURGERS VECTORS IN SPECIMEN AV75

$\vec{b}$	Dislocation Density(cm^{-2})	
	Measured	Calculated from Equipartition Model and Loop Data
$\frac{a}{2}<\bar{1}10>$	6.04 X 107	0.88 x 109
$\frac{a}{2}<110>$	7.25 x 10^8	2.43 X 109
$\frac{a}{2}<\bar{1}01>$	6.04 X 107	1.54 x 109
$\frac{a}{2}<101>$	5.31 x 10^8	1.76 x 109
$\frac{a}{2}<011>$	1.02 x 10^8	2.02 x 109
$\frac{a}{2}<0\bar{1}1>$	5.31 x 10^8	1.284 x 10^9

It is generally assumed that even in unstressed specimens the Frank loop unfaulting process can occur in an autocatalytic manner.[12-14] Once a loop grows sufficiently large, it may intersect another microstructural feature that can generate sufficient localized stresses to nucleate an unfaulting partial dislocation of the type $a/6\langle 11\bar{2}\rangle$. This Shockley partial dislocation can then glide in the plane of the Frank loop and react with the Frank partial dislocation according to the relation

$$31121 + \frac{a}{3}[111] = \frac{a}{2}[110] \quad , \qquad (1)$$

thereby transforming the Frank loop into a perfect prismatic loop.

Since a Frank loop can be transformed into any one of three perfect loops with different Burgers vectors, an autocatalytic or equipartition approach would tend to lessen the anisotropy rather than enhance it. Even more important, one would expect to see in a rapidly unfaulting specimen such as AV75 some of the unfaulted perfect loops, but none were found.

An alternative mechanism exists, however, which allows Frank loop unfaulting. It has been demonstrated to operate in the case of Frank loop unfaulting in quenched pure aluminum deformed at room temperature[15,16]. This mechanism differs from the autocatalytic mechanism in that nucleation of an $\frac{a}{6}\langle 11\bar{2}\rangle$ partial dislocation is not required. This unfaulting mechanism *is* initiated by the interaction of a sessile $\frac{a}{3}\langle 111\rangle$ Frank loop with a glissle $\frac{a}{2}\langle \bar{1}\bar{1}0\rangle$ perfect dislocation.

$$\frac{a}{2}[\bar{1}\bar{1}0] + \frac{a}{3}[111] = \frac{a}{6}[\bar{1}\bar{1}2]. \qquad (2)$$

The resulting Shockley partial sweeps across the Frank loop, removes the stacking fault and reacts with the opposite side of the Frank loop according to the relation

$$\frac{a}{6}[\bar{1}\bar{1}2] + \frac{a}{3}[\bar{1}\bar{1}\bar{1}] = \frac{a}{2}[\bar{1}\bar{1}0]. \quad (3)$$

The process diagramed in Figure 3 shows the interaction of a Frank loop in the plane of the figure and a perfect dislocation moving on some other plane and intersecting the loop. Thus, the Frank loop can be annihilated and its only remnant is a coil in the $a/2[\bar{1}\bar{1}0]$ dislocation approximately on the Frank loop {111} plane. Thus, the unfaulting product of a perfect dislocation/Frank loop interaction immediately becomes part of the perfect dislocation network.

Whereas no perfect loops were observed in this alloy to support the assumption of autocatalytic unfaulting, evidence of this second mechanism was easy to find. Figure 4 shows a micrograph of several loops in stage (c) of the unfaulting process.

There are a number of consequences of this mechanism. A given Frank loop can be unfaulted by any one of three of the six perfect dislocation vectors. As the Frank loop contains opposing Burgers vectors on opposite sides of the loop, the sign of the unfaulting perfect dislocation is unimportant. Furthermore, it is possible to unfault all Frank loops in a given area with only two of the six possible Burgers vectors. Therefore the initiation of only one or two dislocations with different Burgers vector can lead to a cascade of unfaulting, with each unfaulting event further multiplying the line length of the impinging perfect dislocation vector. The imposed stress state of course determines the Burgers vectors most likely to be the initiators of the unfaulting cascade.

Another consequence of this anisotropy-producing process can be seen in the details of the Frank loop distribution. Early in the loop evolution process one can capture a record of the stress-state in the anisotropic distribution of loop Burgers vector. At higher fluences, however, the anisotropy of loops cannot be captured in a micrograph.[4] This apparent discrepancy can be rationalized in terms of a fundamental difference in the competitive growth environments in which the loops exist at low and high fluence levels.

Whereas the network dislocation density at low fluence was either nonexistent throughout the majority of the irradiation or consisted of a fairly isotropic distribution, it inevitably becomes quite anisotropic with consequences both on the growth and destruction of Frank loops. As shown by Wolfer[17] the growth of a Frank loop is determined by the difference between the interstitial and vacancy currents. If vacancy emission at the loops is ignored, the radial growth rate of the loop can be shown to be proportional to the bias of the loop being examined minus the average bias of all other microstructure, or $Z_i^{\ell}/\bar{Z}_v^{\ell} - \bar{Z}_i/\bar{Z}_v$. As the network becomes more anisotropic this net bias for favored loop growth will tend to decrease. More importantly the developing anisotropy of the network is expected to change the intersection probability for loops on the various planes. Since loops unfault to form dislocations with Burgers vectors uniquely suited to unfault other loops of the same Burgers vector, the continued anisotropy of Frank loop nucleation would gradually lead to an increased rate of loop unfaulting on those planes favorably oriented to

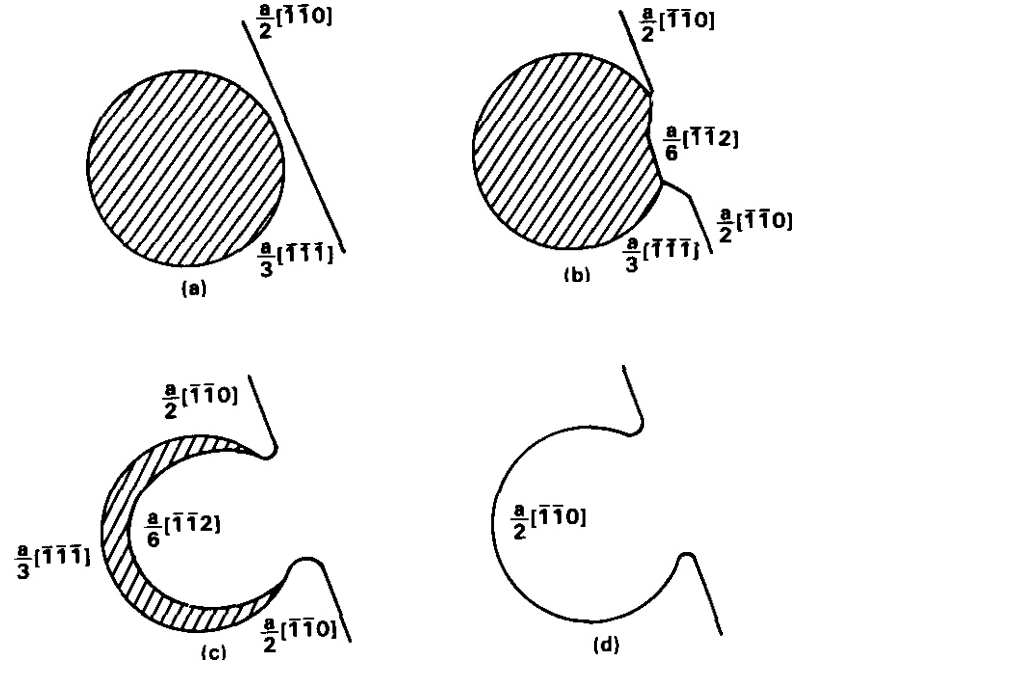

FIGURE 3. Frank Loop Unfaulting Mechanism Results from the Interaction of a Perfect Dislocation with the Frank Loop.

FIGURE 4. Micrograph Showing Border of Unfaulted Region in Specimen AV75, Showing Faulted Loops Being Unfaulted by Perfect Dislocations as Illustrated in Figure 3. Voids are also Visible in this Micrograph.

the applied stresses. In effect, the loops sow the seeds of their own destruction. Even though loops on some planes are growing through their size distribution at accelerated rates, they are also being unfaulted at accelerated rates. Since the total network density is relatively independent of all variables, including stress,[18] a micrograph can only capture the size distribution of loops and not their transit speed through the distribution, and the loop record of the stress state is lost at high fluence.

5.2.2 High Fluence Specimens

The two higher fluence specimens (AX41 and FT08) possess higher dislocation densities than AV75, and appear to confirm that the continued irradiation of a stressed network-dominated microstructure will maintain and enhance the network anisotropy. It is proposed that this enhancement would occur by anisotropic growth and climb of favored network dislocation vectors.

Wolfer[19] has shown, using the methods of isotropic linear-elasticity theory, that the sink bias for interstitials for a straight edge dislocation can be written as

$$Z = 1 + \frac{b^2}{16a^2 \ell n(d/a)} \left\{ (0.197 \frac{vG}{kT})^2 - 0.01654 \frac{\alpha^K}{kT} - 0.1089 \frac{\alpha^G}{kT} - 0.005514 \frac{\alpha^G \sigma_{kk}}{(kT)^2} - (0.0224 \frac{\alpha^G}{b^2} b_i b_j + 0.00448 \alpha^G n_i n_j) \frac{v s_{ij}}{(kT)^2} \right\} . \quad (3)$$

Here G is the shear modulus, k is the Boltzmann constant, T the absolute temperature, b the Burgers vector, σ_{kk} the trace of the stress tensor, s_{ij} the deviatoric stress tensor, $a \tilde{=} 7b$ chosen to be an effective core radius, and $d = 1/\sqrt{\pi\rho}$ the average distance between dislocations with density ρ. Other parameters are the relaxation volume, v, and the elastic polarizabilities α^k and α^G of the point defects. For interstitials $\alpha^k \tilde{=} 100$ eV, $\alpha^G \tilde{=} -150$ eV and $v \tilde{=} 1.4\Omega$ (Ω = atomic volume).

Note that the trace, σ_{kk}, is invariant with respect to the orientation of the stress state. Hence, the first four terms in brackets { } on the right hand side constitute an orientation-independent bias contribution. The last term give the orientation dependence through the orientation-dependent deviatoric stress, s_{ij}. A parameter Ψ, where Ψ can be defined to describe the influence of the SIPA competitive climb mechanism is

$$\Psi = \frac{1}{6} s_{ij} \left(5 \frac{b_i b_j}{b^2} + n_i n_j\right) \quad . \tag{4}$$

Here, n is the dislocation line direction. Note that the factors in (4) are chosen to properly weight the deviatoric normal term, $s_{ij} b_i b_j$, and the deviatoric line tension term, $s_{ij} n_i n_j$, according to the ratios given in equation (3).

Both high fluence specimens (and also AV75) were analyzed using equation (4). Local specimen stress states are readily calculable for these specimens since their orientations with respect to the applied stress were precisely determined. For the specimens AV75 and AX41, the orientations are identical, with the normal to the specimen coinciding with the dominant texture component for the drawn tubing from which the specimens were derived. The normal of specimen BT08 was found to be coincident with a minor texture component, as shown in Table 5.

TABLE 5

ORIENTATION OF TEXTURE COMPONENTS FOR STRESSED SPECIMENS

TUBE COORDINATE	AV75, AX41	BT08
x (radial direction)	[112]	[112]
y (hoop direction)	[110]	[5 $\bar{1}\bar{1}$ 81
z (axial direction)	[111]	[531]

Six variants of the a/2 <100>{100} edge dislocation mode are possible in FCC materials. Figures 5, 6 and 7 show the variation of dislocation density for each of the six variants in specimens AV75, AX41 and BT08 with their corresponding SIPA parameter, Ψ (see also Table 6).

A trend for increasing dislocation density with increasing Ψ is noted in all three specimens. At lower fluences (AV75, $\phi t \sim 2 \times 10^{22}$ n/cm^2 E>0.1 MeV) the trend is very clear, but may reflect the combined influence of stress on all three evolutionary stages. In the specimens at higher fluence a larger scatter is observed. Specimen BT08 shows one variant (<$\bar{1}$10>[001]) at substantial deviation from the general trend. In all specimens, however, the general trend of increasing density with increasing Ψ is reasonably well established.

Notably, specimens AV75 and AX41, which are coincident with the dominant texture component, show the best agreement over the entire range of stresses. It is to be expected, in view of the texture-induced internal stress fields, that the specimen with the dominant texture component as normal will experience the least effect from internal stresses. Specimen BT08, on the other hand, is oriented in coincidence with a minor texture component and is subject to larger internal stresses.

5.3 Conclusions

When stress is applied to a metal during high temperature irradiation, both the Frank loops and their resulting dislocation products develop an anisotropy in the Burgers vector distribution. The anisotropy appears to develop in all three important stages of microstructural development: first in the planar distribution of loops, then in their unfaulting and finally in the post-unfaulting growth of the network components. The first and last of these three stages appear to be dominated by the Stress-Induced Preferential Absorption (SIPA) mechanism of irradiation creep for the system studied.

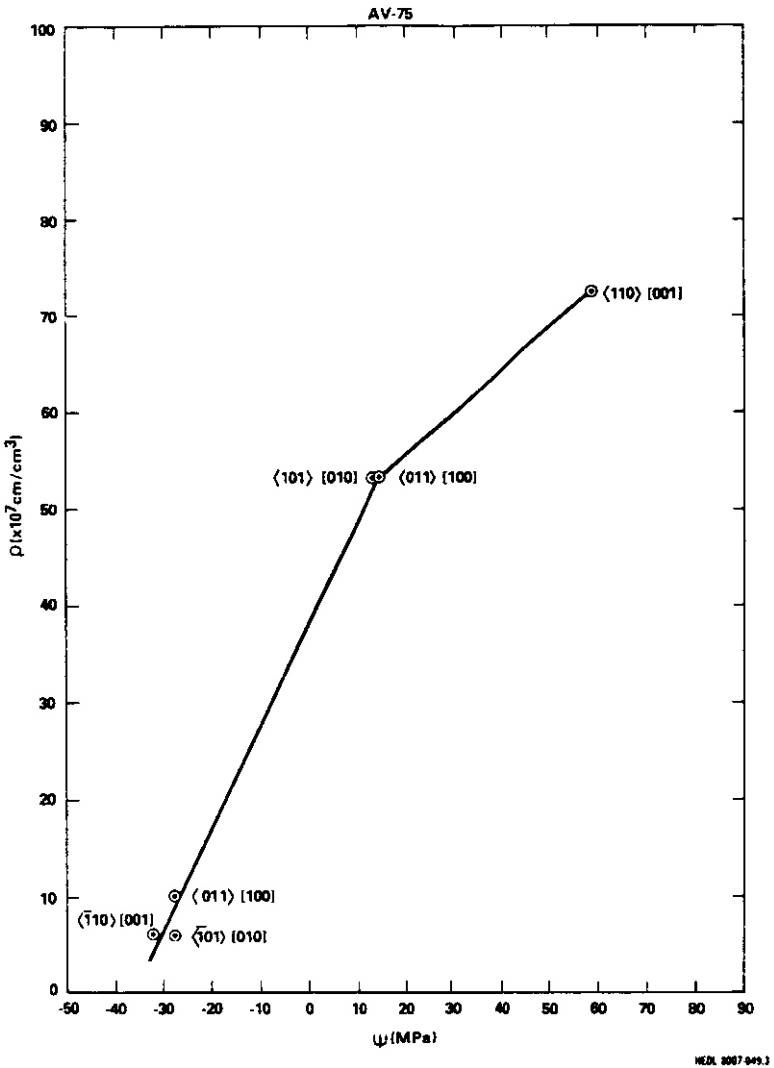

FIGURE 5. Variation of Dislocation Density with SIPA Stress Parameter, Ψ, for Specimen AV75.

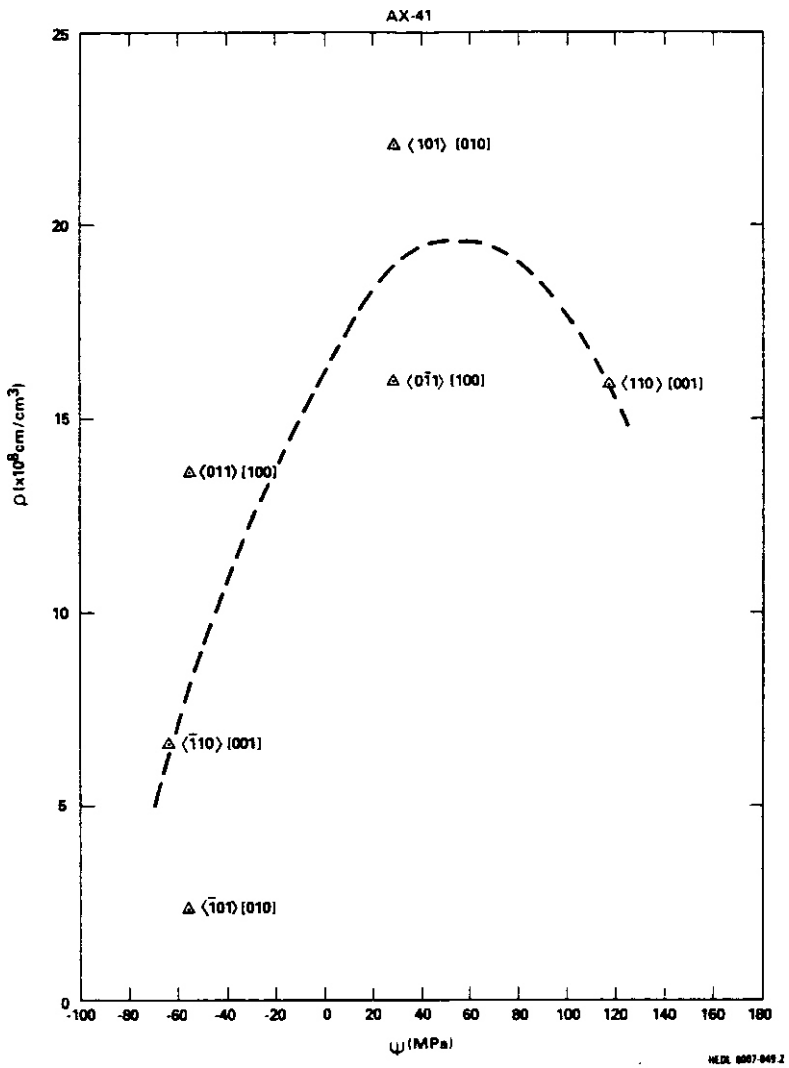

FIGURE 6. Variation of Dislocation Density with SIPA Parameter, Ψ, for Specimen AX41.

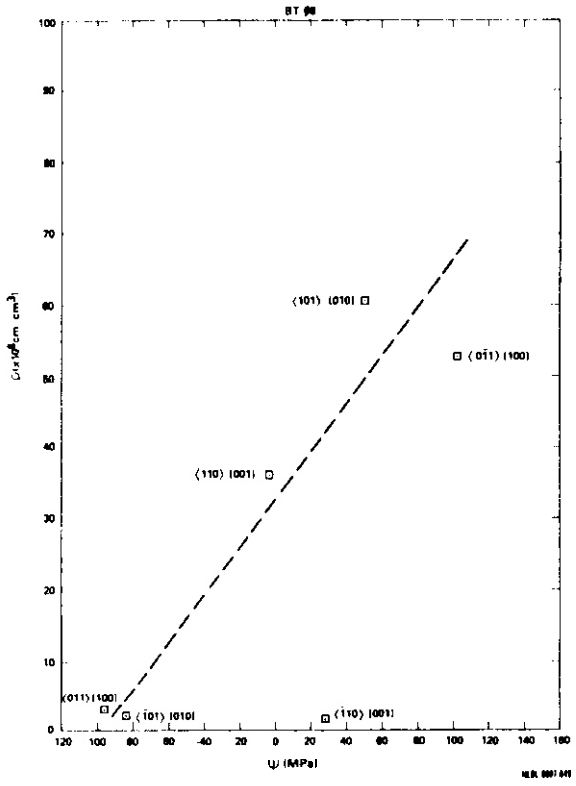

FIGURE 7. Variation of Dislocation Density with SIPA Parameter, ψ, for Specimen BT08.

DISLOCATION VARIANT	Ψ (MPa)		
	AV75	AX41	BT08
$<11\bar{0}>[001]/\sqrt{2}$	-32.0	-64.0	29.0
$<110>[001]/\sqrt{2}$	58.6	117.2	-1.6
$<\bar{1}01>[010]/\sqrt{2}$	-27.9	-55.8	-84.3
$<101>[010]/\sqrt{2}$	14.4	28.8	51.7
$<011>[100]/\sqrt{2}$	-27.7	-55.4	-96.9
$<0\bar{1}1>[100]/\sqrt{2}$	14.4	28.8	102.1

It appears that one consequence of the anisotropy of network dislocations may be the loss at high fluence of the previously observable microstructural record of the stress state expressed in the distribution of Frank loops on the various close-packed planes.

6.0 References

1. Okamoto, P. R., and Harkness, S. D., Journal of Nuclear Materials, Vol. 48, 1973, p. 49.

2. Brager, H. R.; Garner, F. A.; and Guthrie, G. L., Journal of Nuclear Materials, Vol. 66, 1977, p. 301.

3. Garner, F. A.; Wolfer, W. G., and Brager, H. R., in Effects of Radiation on Structural Materials, ASTM STP 683, J. A. Sprague and D. Kramer, Eds., American Society for Testing and Materials, 1979, pp. 160-183.

4. Gelles, D. S.; Garner, F. A., and Braqer, H. R., "Frank Loop Formation in Irradiated Metals in Response to Applied and Internal Stresses." Effects of Radiation on Materials: Tenth Conference, ASTM STP 725, David Kramer; H. R. Brager and J. S. Perrin, Eds., American Society for Testing and Materials, 1981, pp. 735-753.

5. Tabata, T.; Nakajima, Y.; Kida, T., and Fujita, H., Proceedings 5th International Conference on High Voltage Electron Microscopy, Kyota, Japan, 1977, p. 519.

6. Caillard, D.; Martin, J. L., and Jouffrey, B., Acta Met. 28, 1980, pp. 1059-1067.

7. Martin, J. L., "High Voltage Microscopy and Models of Deformation", in Dislocation Models of Physical Systems, Eds. M. F. Ashby, R. Bullough, C. S. Hartley and J. P. Hirth, 1981, pp. 193-196.

8. Atkins. T.. and McElroy, R. J.. "Irradiation Creep of Dilute Nickel Alloys;" Effects of Radiation on Materials: Eleventh Conference, ASTM STP 782, H. R. Brager and J. S. Perrin, Eds., American Society of Testing and Materials, 1982, pp. 841-855.

9. Zuppiroli, L.; Pouchou, J. L.; Francois, A.; Leteurtre, J., and Quere, Y., Phil. Mag., 1977 35, No. 4, pp. 853-870.

10. Gelles, D. S., "A Frank Loop Unfaultinq Mechanism in fcc Metals During Neutron Irradiation," in Ref. 7, pp. 158-162.

11. Garner, F. A., and Wolfer, W. G., Transactions, American Nuclear Society, 1978, p. 144.

12. Nabarro, F. R. N., Theory of Crystal Dislocations, Oxford University Press, London (1967), p. 361.

13. Hirth, J. P., and Lothe, J., Theory of Dislocations, McGraw-Hill, New York (1968), p. 305.

14. Swart, V. P., and Kritzinger, S., Eishth International Congress on Electron Microscopy, Canberra, Vol. 1 (1974), p. 456.

15. Saada, G., and Washburn, J., J. Phys. Soc. of Japan, 18, Sup. #1 (1963), p. 43.

16. Strudel, J. L., and Washburn, J., Phil. Mag., 9, 491 (1964).

17. Wolfer, W. G., "Correlation of Radiation Creep Theory with Experimental Evidence," University of Wisconsin Report UWFDM-312; also Journal of Nuclear Materials, 90 (1980), pp. 175-192.

18. Garner, F. A., and Wolfer, W. G., "A Model for the Evolution of Network Density in Irradiated Metals", in Ref. 8, pp. 1073-1087.

7.0 Future Work

This effort will continue, concentrating on the analysis of recently published data.

8.0 Publications

None.

ACCELERATION OF IRRADIATION CREEP WITH FLUENCE: ABSENCE OF A DEFINITIVE MICROSTRUCTURAL RECORD

F. A. Garner (Hanford Engineering Development Laboratory) and W. G. Wolfer (University of Wisconsin)

1.0 Objective

The object of this effort is to develop models which describe the evolution and behavior of radiation-induced microstructure and to apply these models to the prediction of material response in environments that lie outside the current range of available data.

2.0 Summary

The irradiation creep rate of AISI 316 is known to accelerate during the period when the alloy matrix undergoes a microchemical evolution. No concurrent change is observed in the densities and distributions of the components of microstructure responsible for creep deformation however. A model has been developed to explain how the network dislocation density and the Frank loop density can be relatively insensitive to changes in matrix chemistry while the creep rate can be changed substantially.

3.0 Program

Title: Irradiation Effects Analysis (AKJ)
Principal Investigator: D. G. Doran
Affiliation: Hanford Engineering Development Laboratory

4.0 Relevant DAFS Program Plan Task/Subtask

II.C.14 Models of Flow and Fracture Under Irradiation
II.C.18 Relating Low and High Exposure Microstructures

5.0 Accomplishments and Status

5.1 Introduction

In a recent report it was shown that both the Frank loop and network dislocation densities of irradiated metals approach saturation levels at relatively low fluence.[1] The transient stage of this evolution is over rather quickly, however, compared to the onset of swelling, the concurrent microchemical evolution and an associated acceleration of the irradiation creep rate,[2-3] as shown in Figures 1 and 2.

One would anticipate that the creep rate would be proportional to the number of dislocation components and the speed at which they move through the alloy matrix. The first creep transient shown in the right hand side of Figure 1 indeed appears to be related to an irradiation-induced transient involving a reduction of network dislocation density in cold-worked material. It has been shown however that both the network dislocation density and Frank loop density do not change during the fluence interval in which the acceleration of creep rate occurs.[1]

If one accepts the previously proposed suggestion[2] that the acceleration of both swelling and irradiation creep in austenitic steels arises from the microchemical evolution of the alloy matrix, one might reasonably expect that some evidence of this evolution would be expressed in the densities of the creep components of microstructure.

The concept of microstructural records imprinted on the alloy matrix by irradiation creep is a relatively new idea, but one that has shown a great deal of success in several areas.[4-7] The lack of a dislocation record of the progress of the microchemical evolution casts some doubt on the validity and utility of such records however. How can one reconcile the saturation of dislocation and loop microstructure with a continued increase in creep rate?

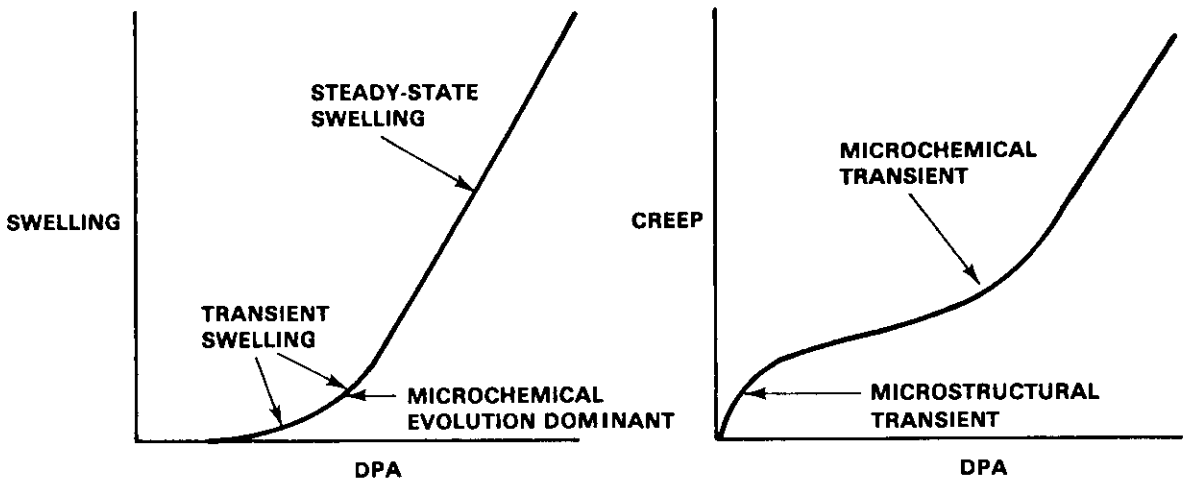

FIGURE 1. Schematic Representation of Transient and Quasi-Steady-State Regimes Observed in the Swelling and Irradiation Creep of Cold-Worked AISI 316.

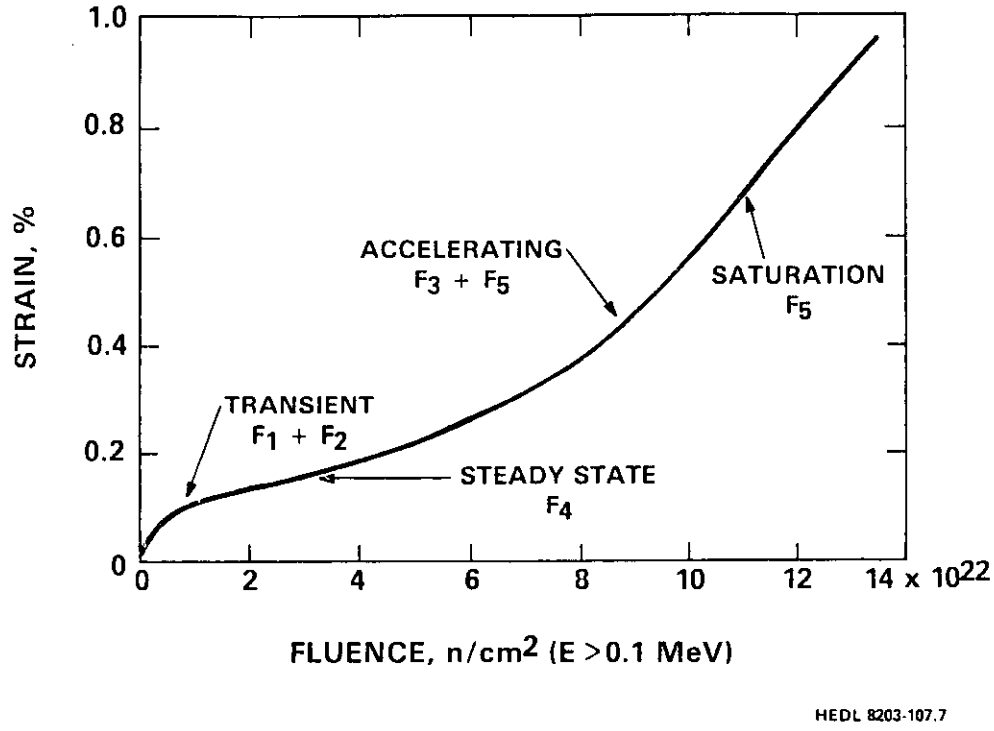

FIGURE 2. Fluence Dependence of the In-Reactor Creep Correlation Developed by Puigh and Coworkers.[3] The F-terms indicate the components of the creep correlation that give rise to the various transient or steady-state terms.

The answer lies primarily in the nature of the difference between the microstructural records left by swelling and irradiation creep. Whereas the void microstructure represents a time-integrated record of the swelling behavior, the distribution and density of dislocation components are a record only of the instantaneous and recent dislocation history. There is no total record of prior component growth or movement; nor is there any record of the rate at which these components were redistributing mass when the irradiation was interrupted. This latter point has some rather subtle but important implications which will be explored in more depth in later sections.

5.2 Factors Which Determine the Loop Size Distribution

The microstructural record for Frank loops is contained in its loop size distribution and its total density. It should also be noted that at typical fast reactor displacement rates Frank loops are not found in appreciable densities in micrographs taken at temperatures approaching 550°C and above.[8-9]

Wolfer and coworkers[10] have provided the theoretical description that can explain the invariance of the loop size distribution and yet allow a change of the creep rate. This treatment employs a continuum description which condenses the rate equations for interstitial loop populations into Fokker-Planck equations. These equations can be interpreted as diffusion equations with drift terms.

The normalized steady-state size distribution of loops is given by

$$\frac{G(x)g(x)}{G(x_o)\,g_o} = \frac{\int_x^{x_1} dx' \exp\left\{-\int_x^{x'} dx'' \, H/G\right\}}{\int_{x_o}^{x_1} dx' \exp\left\{-\int_{x_o}^{x'} dx'' \, H/G\right\}} \qquad [1]$$

where x is the number of atoms in the cluster, $g(x)$ is the number of clusters at size X and H and G are the "drift" and "diffusion" functions defined by the following relations. The number of loop embryos is g_o and in this treatment the embryo is considered to be the di-interstitial.

$$H(x) = A^{\ell}\left[\left(z_i^{\ell}\bar{z}_v - z_v^{\ell}\bar{z}_i\right) F - z_v^{\ell}D_v\left(\bar{C}_v^{s} - C_v^{\ell}\right)\right] \qquad [2]$$

$$G(x) = \frac{1}{2} A^{\ell}\left[\left(z_i^{\ell}\bar{z}_v + z_v^{\ell}\bar{z}_i\right) F + z_v^{\ell}D_v\left(\bar{C}_v^{s} + C_v^{\ell}\right)\right] \qquad [3]$$

Here, A^{ℓ} is a geometric factor appropriate for loops, Z is a bias factor for interstitials (i) or vacancies (V) for either the loop (ℓ) or the average bias $\bar{z}$ for the entire microstructural network; F is a condensation of various factors defined in Reference 10 (page 850) and D_v is the vacancy diffusivity. The average concentration of vacancies $\bar{C}_v^{s}$ at all sinks (s) is balanced against the concentration at loops *(a)*.

For temperatures below 600°C the thermal vacancy emission terms can be neglected and for typical breeder reactor displacement rates

$$\frac{H(x)}{G(x)} \simeq 2\,\frac{z_i^{\ell}(x)/z_v^{\ell}(x) - \bar{z}_i/\bar{z}_v}{z_i^{\ell}(x)/z_v^{\ell}(x) + \bar{z}_i/\bar{z}_v} \qquad [4]$$

Except for the fact that the average bias factors $\bar{z}_i$ and $\bar{z}_v$ depend on the microstructure [and its associated segregation[11]] produced by the irradiation, the ratio H/G is independent of the environmental conditions or defect diffusivities. Therefore the normalized size distribution defined in Equation 1 *is* also independent of variables such as D_v and depends only on bias factors.

Note that Equation 1 says nothing about the flux or current of loops through the size distribution; that is defined by Equation 3 and is strongly dependent on D_v.

The vacancy mobility is expressed by D_v and is one of the major determinants of the rate at which loops flow through the size distribution. The size distribution is determined only by the dependence on loop size of the bias factors[10] and the size dependence of the loop intersection probability. The latter is largely fixed by the temperature-insensitive saturation density of network dislocations and the temperature-sensitive loop line length, as shown in References 9 and 12.

As has been shown many times before the defect fluxes D_vC_v and D_IC_I are dependent on D_v but are essentially independent of D_I as long as $D_I >> D_v$. Therefore the effect on loop transit current of changes in the vacancy mobility was investigated. In another report it was shown that large changes can occur in D_v due to relatively small changes in the vacancy migration energy E_v^m, as various fast diffusing solute species are removed from or added to the alloy matrix.[13]

5.3 Calculation of Loop Fluxes and Loop Size Distributions

Employing a comprehensive loop evolution computer code described earlier,[10] the steady state current of loops through the time-independent or "stationary" distribution was calculated for various values of E_v^m. Since g_o is not known as a function of temperature the values are given as rates normalized to the current ϕE_v^m calculated for E_v^m = 1.4 eV. It was also assumed that g_o is independent of E_v^m. Thermal vacancy emission has not been neglected as was assumed in development of Equation 1. Table 1 contains a compilation of computed loop currents.

The normalized loop size distributions are shown in Figures 3 and 4. Note that while the loop size distributions are relatively insensitive to E_v^m, the loop fluxes are not at all insensitive. Note also that the greatest effect is at high temperatures where thermal vacancy emission is an important negative contribution to the rate of loop growth.

TABLE 1

RATIO OF LOOP CURRENTS (E_v^m)

Temperature °C	$\Phi(1.2)/\Phi(1.4)$	$\Phi(1.6)/\Phi(1.4)$
300	7.5	0.3
400	5.38	0.18
500	33.6	0.16
600	1.7×10^{23}	0.4×10^{-11}

5.4 Discussion

There are a number of important insights derived from this analysis:

(a) The microstructural record is not as definitive as one might expect. If the vacancy migration energy changes during irradiation due to a microchemical evolution then the microstructural record expressed by the loop size distribution and total number density will not contain a record of this change unless the overall bias factors of the microstructure are changed substantially. This latter condition is not likely to be met. As will be shown later, the bias of the network dislocations is unlikely to be changed and the void bias contribution to the total is relatively small during the transient regime of the microchemical evolution.

(b) The rate of loop growth through the size distribution (and therefore the loop contribution to irradiation creep) is very sensitive to factors which affect vacancy migration.

(c) The microstructural record expressed in the loop population is selective in the variables to which it responds. Since an anisotropic stress field affects the bias factors, a record is left, while the application of a completely isotropic stress field would not change the relative bias factors,[6] and no record would be left, just as in the case of changes in E_v^m.

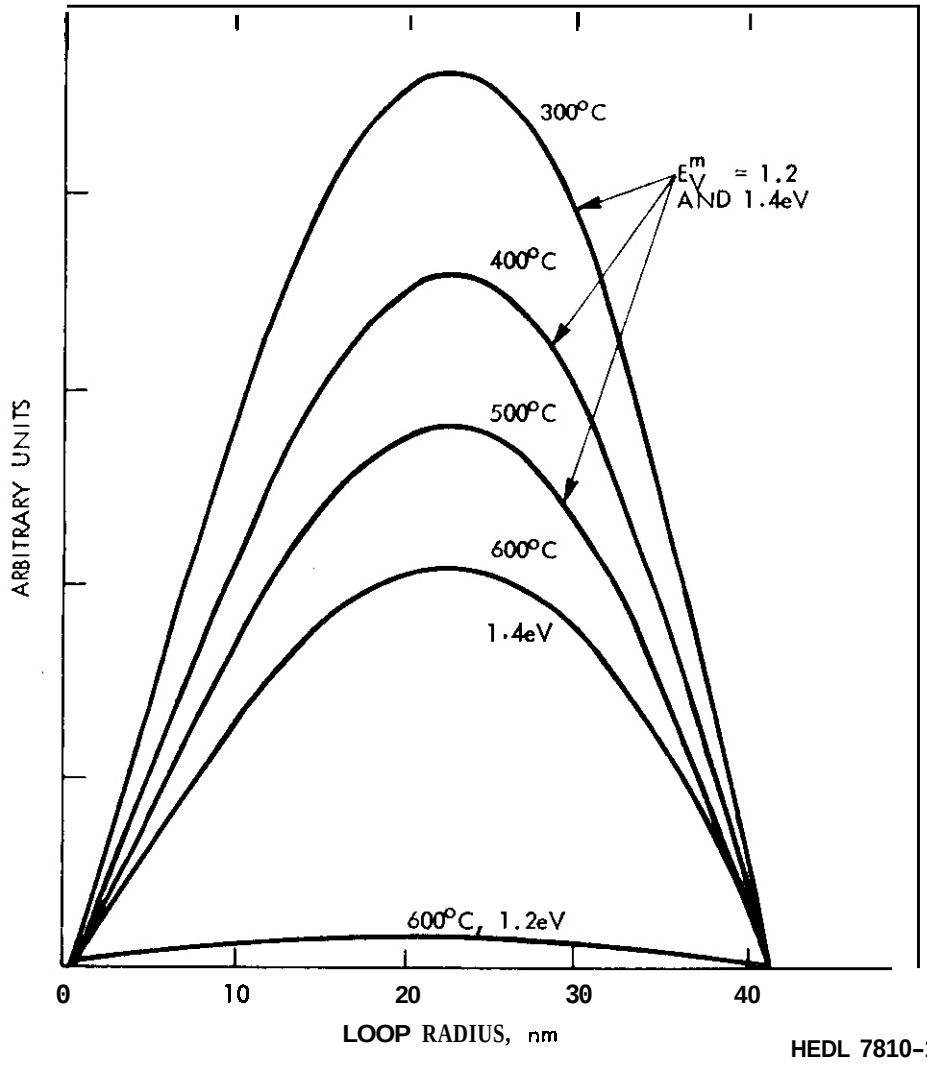

Figure 3. Normalized Loop-Size Distributions Calculated for E_V^m = 1.2 and 1.4 eV. Except at 600°C all curves are identical. All loops are assumed to unfault at R = 40 nm. Note that loop size distribution almost disappears at 600°C for E_V^m = 1.2 eV.

(d) At high temperatures slight changes in E_v^m due to matrix compositional variations not only change the loop transit current drastically but can lead to the establishment of a loop size distribution where none previously existed, or destroy one which existed earlier. The loop densities at these temperatures are generally too low to observe such changes however.

(e) If irradiation creep scales only with loop current then the acceleration of creep with fluence cannot be explained with removal of fast-diffusing species. Note in Table 1 that as the fast diffusing solute is removed, E_v^m increases and the loop flux drops. Therefore other factors must dominate the creep rate.

(f) In Reference 1 it was shown that the saturation level of network dislocation density was defined as

$$\rho_d^* = \frac{Z_i^\ell D_i C_i - Z_v^\ell D_v C_v + Z_v^\ell D_v C_{vo}^\ell}{Z_i^d D_i C_i - Z_v^d D_v C_v + Z_v^d D_v C_{vo}^d + v_{th}} \qquad [5]$$

where v_{th} is the thermal climb velocity and the subscripts d and ℓ refer to network dislocations and loops respectively. If the temperature is low enough that v_{th} can be neglected then ρ_d^* is relatively constant with temperature and displacement rate. It is also rather insensitive to changes in the point defect diffusivities since the defect fluxes D_iC_i and D_vC_v are essentially constant regardless of changes in D_i and D_v. In addition there can be no effective segregation (comparable to that at voids[11]) to network dislocations that are quite mobile during irradiation. Therefore, one would not expect either the bias or density of network dislocations to change during the microchemical evolution.

5.5 Conclusions

A model has been developed to describe the evolution of loop microstructures in irradiated metals. It predicts that except at temperatures above that where Frank loops are normally found, both the Frank loop distribution and

density as well as the network dislocation density should be relatively insensitive to changes in matrix chemistry and point defect diffusivity arising from radiation-induced microchemical evolution. The creep rate during this evolution can change substantially however.

6.0 References

1. F. A. Garner and W. G. Wolfer, "A Model for the Evolution of Network Dislocation Density in Irradiated Metals," DOE/ER-0046/10, p. 106. Also in abbreviated form in ASTM STP 782, pp. 1073-1087.

2. F. A. Garner, "The Microchemical Evolution of Irradiated Stainless Steels," in Phase Stability During Irradiation, Edited by J. R. Holland, L. K. Mansur and D. I. Potter, The Metallurgical Society of AIME, 1980, p. 165.

3. R. J. Puigh, E. R. Gilbert and B. A. Chin, "An In-Reactor Creep Correlation for 20% Cold Worked AISI 316 Stainless Steel," Effects of Radiation on Materials: Eleventh Conference, ASTM STP 782, H. R. Brager and J. S. Perrin, Eds., American Society for Testing and Materials, 1982, p. 108 - 121.

4. W. G. Wolfer and F. A. Garner, "Swelling-Induced Stresses in Ion-Bombarded Surfaces: Effect of Crystalline Orientation,'' J. Nucl. Mater., 85 and 86 (1979) 583-589.

5. F. A. Garner and W. G. Wolfer, "Microstructural Evidence Supporting the Existence of the SIPA Creep Mechanism," in Transactions of the American Nuclear Society Annual Meeting, 1978, p. 144.

6. F. A. Garner, W. G. Wolfer and H. R. Brager, "A Reassessment of the Role of Stress in Development of Radiation-Induced Microstructure," in Effects of Radiation on Structural Materials, ASTP STP 683, J. A. Sprague and D. Kramer, Eds., American Society for Testing and Materials, 1979, pp. 160-183.

7. D. S. Gelles, F. A. Garner and H. R. Brager, "Frank Loop Formation in Irradiated Metals in Response to Applied and Internal Stresses," in Effects of Radiation on Materials: Tenth Conference, ASTP STP 725, D. Kramer, H. R. Brager and J. S. Perrin, Eds., American Society for Testing and Materials, 1981, pp. 735-753.

8. H. R. Brager and J. L. Straalsund, J. Nucl. Mater., 66 (1973) 134-158.

9. H. R. Brager, F. A. Garner, E. R. Gilbert, J. E. Flinn and W. G. Wolfer, "Stress-Affected Microstructural Development and the Creep-Swelling Interrelationship," Radiation Effects in Breeder Reactor Structural Materials, M. L. Bleiberg and J. W. Bennett, Eds., June 1977, p. 727.

10. W. G. Wolfer, L. K. Mansur and J. A. Sprague, "Theory of Swelling and Irradiation Creep," in Reference 9, p. 841.

11. W. G. Wolfer, F. A. Garner and L. E. Thomas, "On Radiation-Induced Segregation and the Compositional Dependence of Swelling in Fe-Ni-Cr Alloys," in Reference 3, pp. 1023-1041.

12. H. R. Brager, F. A. Garner and G. L. Guthrie, J. Nucl. Mater., 66 (1977) 301.

13. F. A. Garner and W. G. Wolfer, "The Effect of Solute Additions on Void Nucleation," J. Nucl. Mater., 102 (1981) 143-150.

7.0 Future Work

This effort will continue concentrating on the growth rate and size distribution of loops at high temperature.

CHAPTER 4

CORRELATION METHODOLOGY

MICROSTRUCTURAL AND MICROCHEMICAL COMPARISONS OF AISI 316 IRRADIATED IN HFIR AND EBR-II

H. R. Brager and F. A. Garner (Westinghouse Hanford Co.)

1.0 Objective

The objective of this effort is to provide microstructural data that will provide guidance for the development of swelling correlations for fusion applications.

2.0 Summary

Two alternative models have been proposed in recent papers by several groups of authors to predict the influence of large helium levels on the swelling of AISI 316. To test the validity of each model, a series of microstructural and microchemical examinations were conducted on specimens after irradiation in EBR-II and HFIR. These reactors differ greatly in neutron spectra, helium/dpa ratios and solid transmutant generation rates. The results of these studies show that helium's influence on swelling is manifested in the cavity density but not in the dislocation density or the microchemical evolution of the alloy matrix. The results also suggest that the influence of helium is not strong on either the total swelling or the steady-state swelling rate.

At least in the range 500-720°C the steady-state swelling rate of AISI 316 appears to be relatively insensitive to both helium level and temperature. The attainment of steady-state swelling appears to be governed primarily by the rate of microchemical evolution of the alloy matrix and only secondarily by the He/dpa ratio. It is expected that this conclusion will not be changed in the intermediate helium/dpa environment anticipated in fusion reactors.

3.0 Program

Title: Irradiation Effects Analysis (AKJ)
Principal Investigator: D. G. Doran
Affiliation: Westinghouse Hanford Co.

4.0 Relevant DAFS Program Plan Task/Subtask

II.C.1 Effects of Material Parameters on Microstructure
II.C.2 Effect of Helium on Microstructure
II.C.4 Effect of Solid Transmutants on Microstructure

5.0 Accomplishments and Status

5.1 Introduction

The influence of helium on macroscopic properties and dimensional changes of metals is of great interest to the designers of future fusion devices. The overwhelming majority of relevant experimental data for this subject has been derived from irradiations conducted in fast reactors such as EBR-II,* where the helium to displacement per atom ratio (helium/dpa) is much smaller than that anticipated in fusion environments. There is also a smaller amount of relevant data derived from the mixed-spectrum reactor designated HFIR.* While the displacement rates of these two reactors are comparable, the helium/dpa ratio of nickel-bearing alloys in HFIR can be much greater than even that of projected fusion devices.[1]

It has, therefore, been proposed that comparison of data from the two fission reactors would allow definition of the influence of helium, and that some sort of interpolation would yield a prediction for the intermediate

*EBR-II and HFIR are acronyms for the Experimental Breeder Reactor II at Aryonne National Laboratory in Idaho Falls, ID and the High Flux Isotope Reactor at Oak Ridge National Laboratory, respectively.

helium/dpa levels typical of various fusion environments. This optimistic expectation has subsequently been tempered by the realization that many factors other than helium may enter into the comparison.[2]

The complexity of the problem involved is best illustrated by recent fission reactor studies directed toward assessment of the effect of helium on microstructural development in 20% cold-worked AISI 316 stainless steel. Two quite different interpretations of the available data have arisen; both are described in this paper. Since no other relevant neutron data will be available for several years, it was decided to test certain features and predictions of both models through further examination of the original specimens. The additional data tend to support one of these interpretations. It also will be shown that recent dual-ion simulation studies provide additional support for this interpretation.

5.2 The Data and Its Several Interpretations

While all heats of AISI 316 have been found to eventually swell at essentially the same rate, the duration of the transient or incubation regime of swelling has been found to be sensitive to a host of material and environmental variables.[8,9,15,24] This sensitivity requires that HFIR and EBR-II studies of the influence of helium on swelling can only proceed on specimens made from the same heat of steel and given identical thermo-mechanical treatments. Only one heat of steel meets this criterion; it is designated DO-heat and is a commercial quality heat of steel obtained from Oak Ridge National Laboratory. Unfortunately, there are only twelve data points of 20% cold-worked specimens available from the two reactors, covering a temperature range of 400-800°C and an exposure range of 10-75 dpa.

The analysis of alloy response in the two fission reactors is complicated by temperature uncertainties and differences in transmutation products other than helium. Tne temperature assignments for HFIR irradiations have been revised upward by 50-125°C to reflect improved estimates *of* the large gamma-heating rates inherent in highly thermalized reactor

spectra.[4-6,10] In addition, there are temperature uncertainties associated with EBR-II irradiation.

It is important to note that helium is not the only transmutation product to be enhanced in HFIR. A significant amount of vanadium (~0.4%) is formed in AISI 316 at exposures less than 20 dpa during HFIR irradiation and the manganese level is depleted in a relatively continuous manner.[11] The swelling of this steel has been shown to be influenced by both of these elements[11,12] but the data are insufficient to determine whether these elements affect the transient regime of swelling only or whether the steady-state regime is also affected. In addition, the transmutation reaction $^{59}Ni(n,\alpha)^{56}Fe$ producing the majority of the helium in AISI 316 irradiated in HFIR leads to a 13% increase in the number of displacements which were not previously considered in comparisons of EBR-II and HFIR data.[13] In nickel-rich precipitates the percentage increase is much larger, ranging as large as 75% in γ' precipitates.[41]

Attempts to subdivide this small data field covering a wide range of variables into smaller subsets does not lend confidence to conclusions concerning the action of one of these variables. However, there is a recent insight derived from extensive fast reactor irradiations of many other heats of AISI 316 which allows the data field to be analyzed for helium's influence without subdividing it into smaller temperature increments. The steady-state swelling rate of 300 series stainless steels is remarkably insensitive to irradiation temperature over a wide range as shown in Figures 1 and 2 and discussed later in this paper. The limited temperature dependence of swelling is exhibited in the transient regime and is often quite small.[14,15] This insight supports an analysis using the DO-heat swelling data in aggregate.[3] It also reduces the impact of temperature uncertainties on the analysis. Figure 3 shows that the limited DO-heat swelling data do exhibit this behavior, namely a relative insensitivity to both temperature and helium content. The inclusion of the 680°C (nominal) datum needs to be justified. This specimen was irradiated somewhere above 700°C and has been

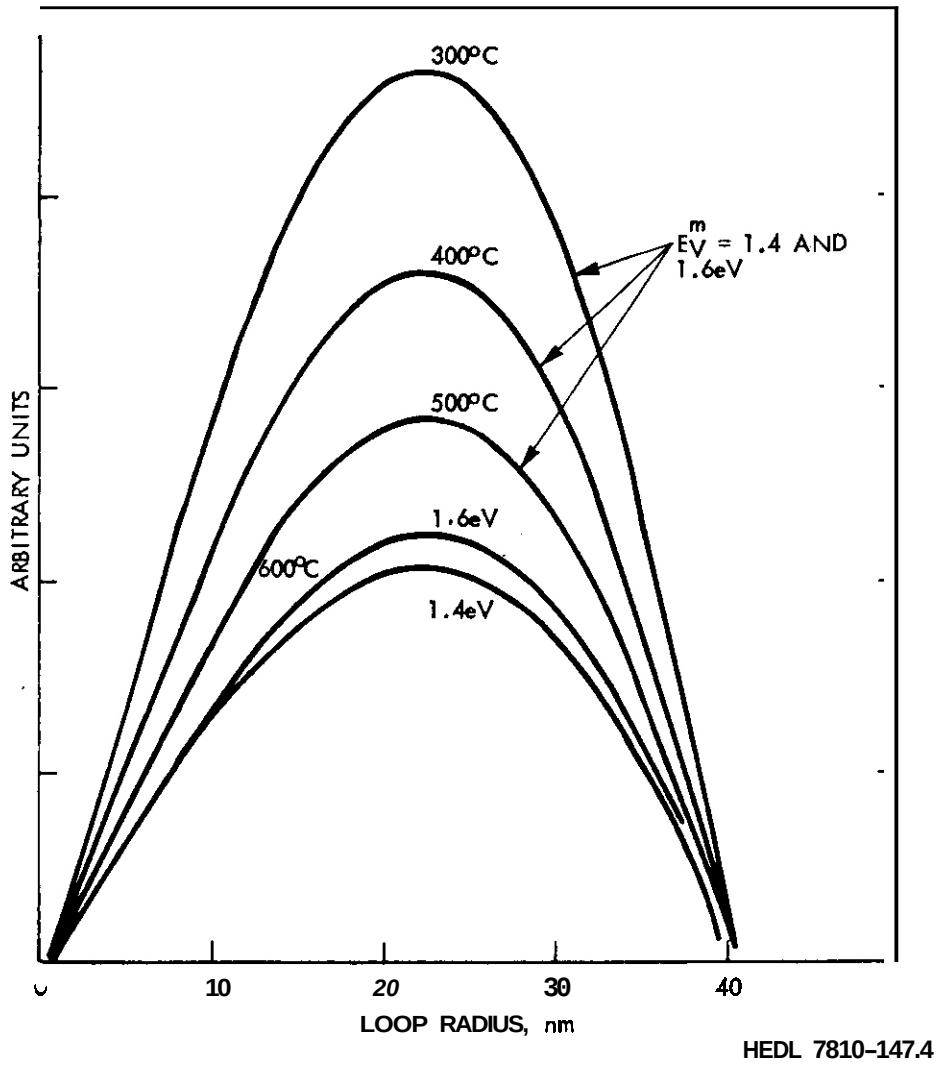

Figure 4. Normalized Loop-Size Distributions Calculated for E_V^m = 1.4 and 1.6 eV. Except for 600°C all curves are independent of the value E_V^m.

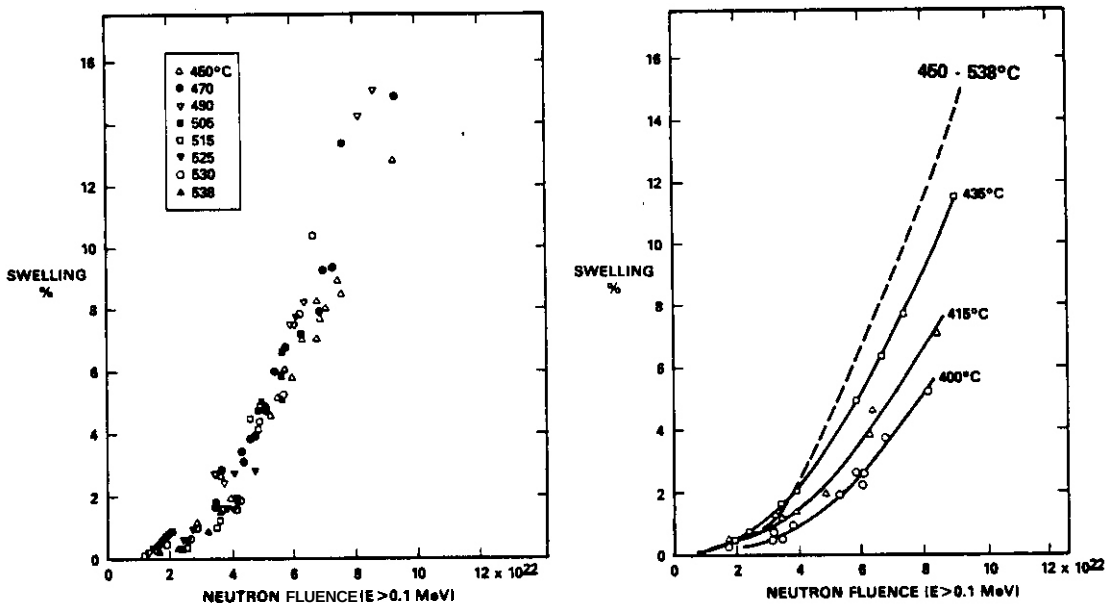

FIGURE 1. Swelling Behavior of Annealed 304L Fuel Capsules Reported by Garner and Porter Showing Relative Independence of Swelling on Temperature in the Range 450-538°C.[14] When corrected to dpa, the curves below 450° become even more parallel to those above 450°C.

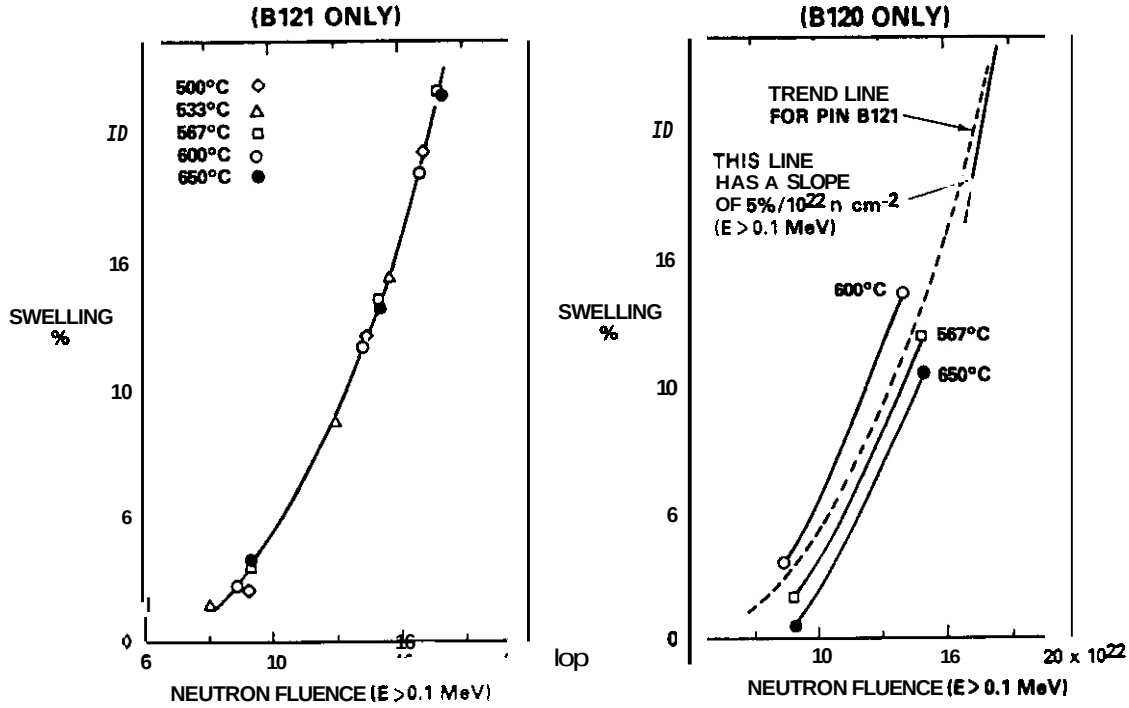

FIGURE 2. Isothermal Swelling Data Published by Yang and Garner[15] Showing Relative Temperature Insensitivity of Swelling in AISI 316 Heat Designated 87210 (N-lot).

considered to be in a helium-driven rather than a bias-driven void swelling regime. Evidence against this assumption will be presented in a later section.

If the 680°C datum is ignored, however, there are no other HFIR data on cold-worked material to support or refute the contention that the high swelling rate associated with fast reactor irradiation will eventually be realized in HFIR. There are, however, additional HFIR data relevant to this question.[7] Breeder reactor studies[16] have shown that the steady-state swelling rate of AISI 316 is independent of cold work level, and that increasing the cold work level results in only extending the transient regime of swelling as shown in Figure 4. As shown in this report and elsewhere,[3,4,7] the microstructural densities of dislocations and voids developed in HFIR are essentially identical for both the annealed and cold-worked steels. It would therefore be expected that HFIR irradiation of DO-heat in the solution annealed condition would reveal the eventual swelling rate expected for cold-worked DO-heat. Comparison in Figure 5 of the swelling of annealed and cold-worked DO-heat irradiated in HFIR indeed supports the eventual higher swelling rate postulated for cold-worked material in HFIR.

An alternative interpretation has been proposed.[17] It asserts that the higher cavity densitites induced by HFIR irradiation will lead to earlier swelling and to steady-state swelling rates that are much lower at 500-600°C than that obtained in fast reactors.[17] This assumption is based on rate theory considerations and does not incorporate microchemical evolution. In effect, it is assumed in this approach that no additional curvature occurs in the swelling curve beyond the last HFIR datum as demonstrated in Figure 6. This approach does not consider the fact that the reported cavity densities[7] of the annealed steel are comparable to those of the cold-worked steel at all temperatures investigated (Figure 7), and would predict that the HFIR-induced swelling rate of the annealed steel would be depressed in the same way as is proposed to happen in the cold-worked steel.

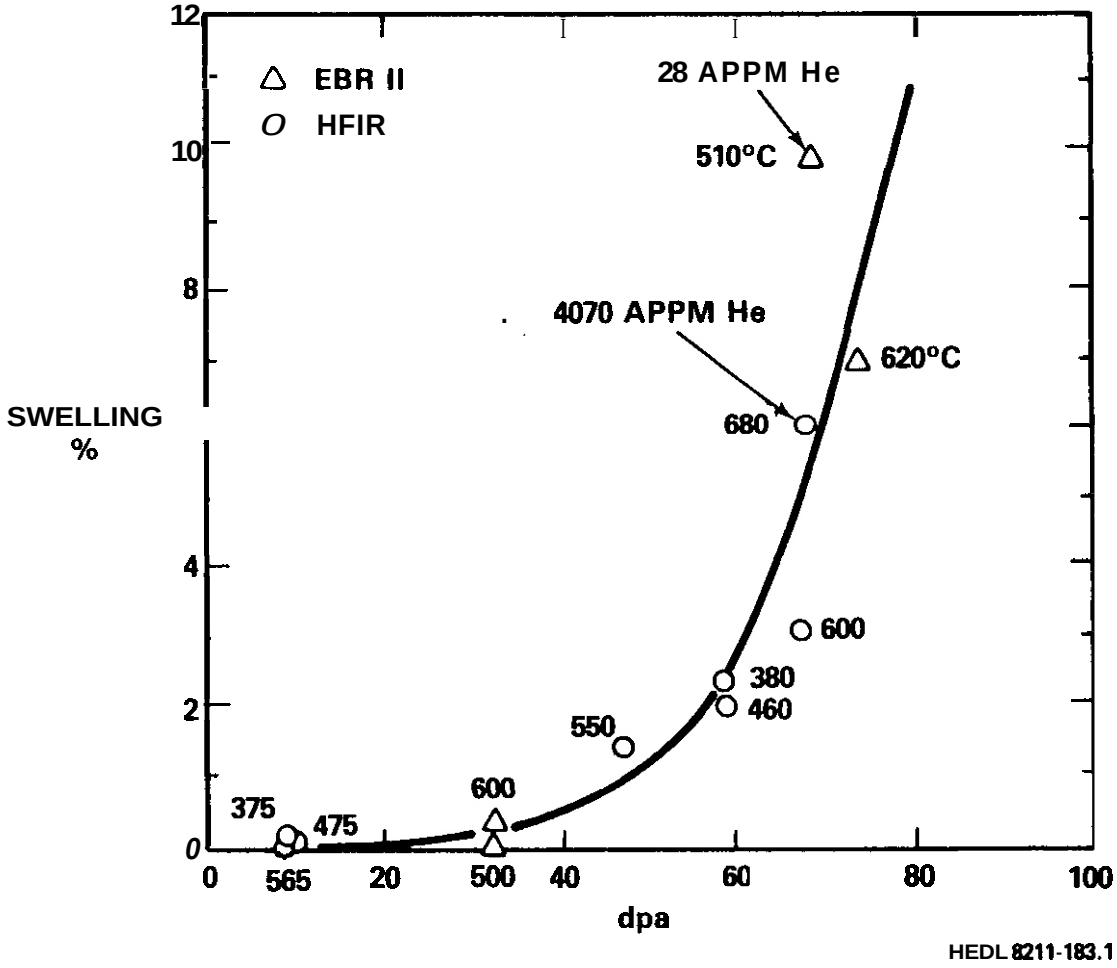

FIGURE 3. Comparison of Cavity Volumes Observed in 20% cw DO-Heat Irradiated in E8R-II and HFIR. (Only nominal temperatures used.) The composite HFIR/E8R-II trend curve drawn is typical of swelling curves for AISI 316 in E8R-II. Corrections have been included in this figure for the displacements produced in HFIR by the ^{56}Fe recoil that accompanies the production of helium from the ^{59}Ni (n,α) reaction.

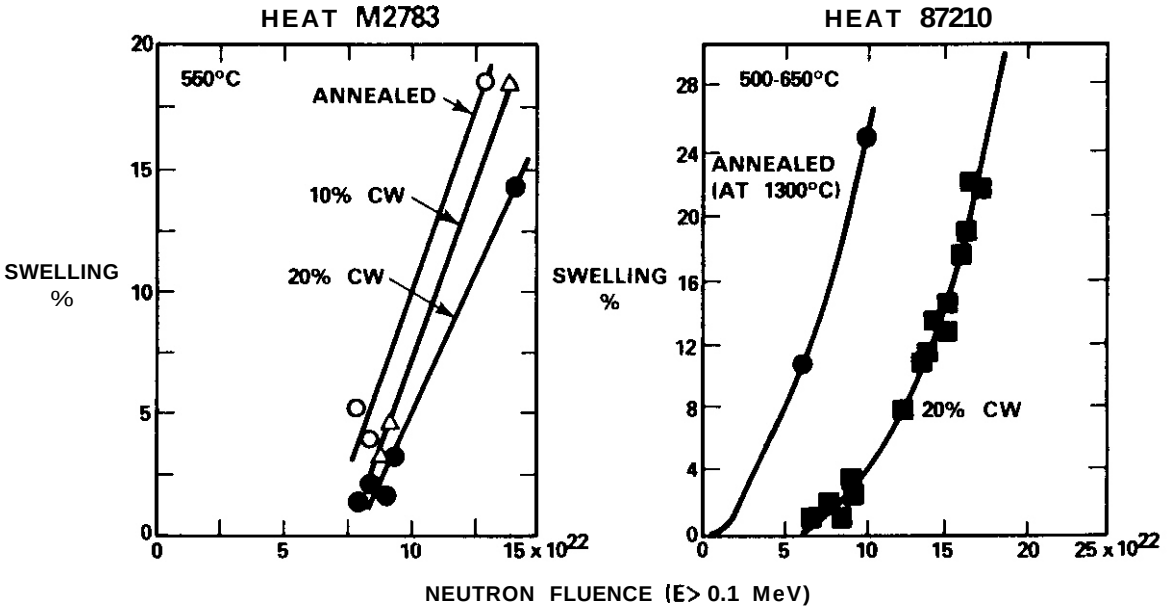

FIGURE 4. Examples of the Influence of Cold Work on Extending the Duration of the Transient Regime of Swelling. The amount of extension depends on the heat, its annealing and cold working conditions and the irradiation temperature.

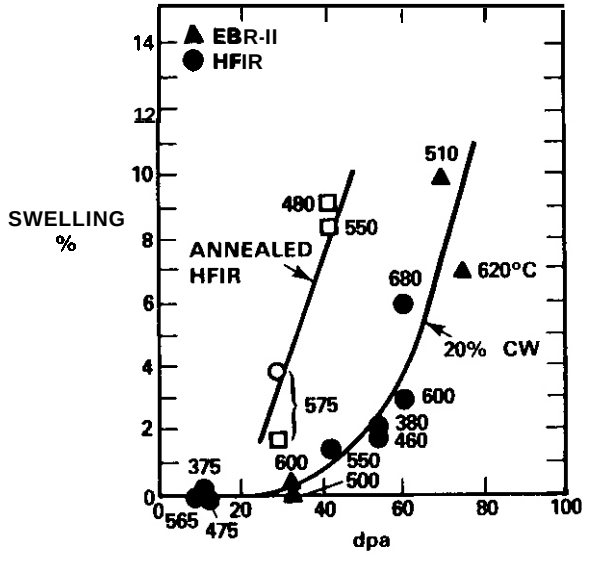

FIGURE 5. Comparison of Swelling in Annealed and Cold-Worked DO-Heat in HFIR with That of Cold-Worked DO-Heat in EBR-II. All temperatures used are the nominal irradiation temperatures quoted for the original experiments. The solid symbols refer to cold-worked specimens, circles for HFIR and triangles for EBR-II. The open symbols designate annealed specimens irradiated in HFIR, where the swelling is determined by microscopy (squares) or bulk density change (circle).(3,7)

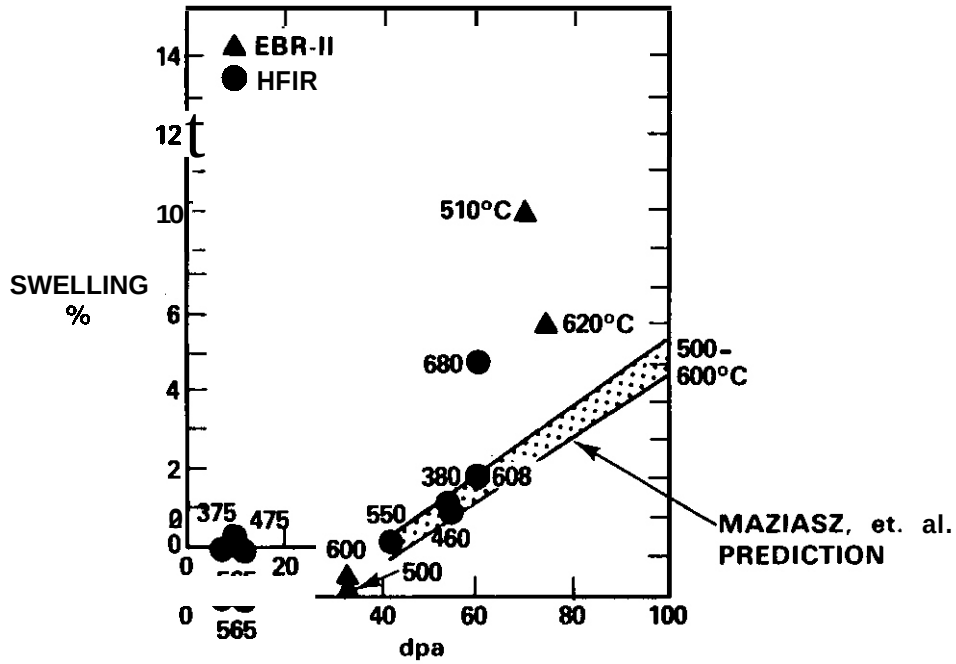

FIGURE 6. Comparison of Composite Swelling Curve for 20% Cold-Worked DO-Heat with Predictions Based on HFIR Cold-Worked Data Only and Rate Theory Principles.(17)

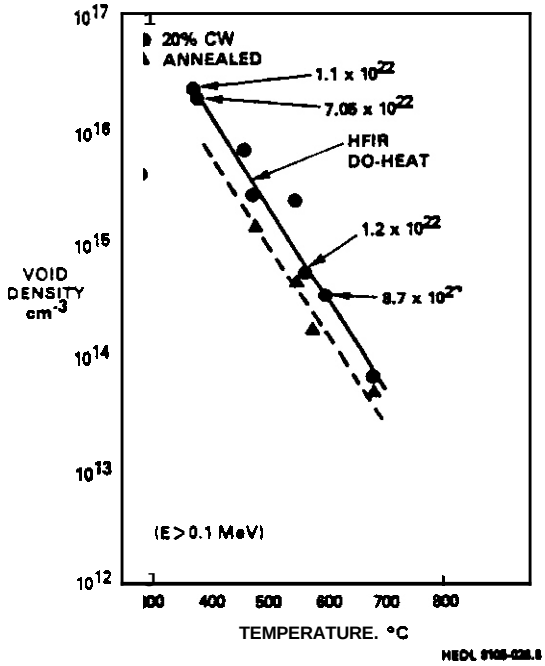

FIGURE 7. Comparison of Cavity Densities Reported by P. J. Maziasz for DO-Heat Irradiated in HFIR.(7)

5.3 Experimental Resolution of the Different Helium Interpretations

Resolution of the divergent interpretations requires that maximum use be made of available specimens. Our approach has been to identify the underlying assumptions of each analysis and then to subject these assumptions to experimental verification.

The principal difference between the two interpretations lies in the perception of the relative importance to swelling of the radiation-induced microchemical evolution and the helium-dependent microstructural evolution. The authors approach is based on extensive fast reactor irradiation studies of AISI 316 which show that the microchemical evolution is an inevitable phenomenon with its eventual endpoint independent of most environmental and thermal-mechanical variables.[18-26] Central to this approach is the radiation-induced solute segregation of elements such as nickel and silicon. The removal of these elements is thought to be the rate-controlling process governing the instantaneous swelling rate, with the microstructural evolution playing a necessary but not rate-determining role in stainless steels containing large amounts of solutes such as carbon and silicon. The inevitability of this evolution has also been recently demonstrated in niobium-modified and titanium-modified stainless steels.[27-29] The proposed roles of silicon and nickel have been examined theoretically in other papers.[30,31]

Proponents of the alternate approach reason that "high swelling and radiation-induced solute segregation are not inevitable" and "indeed are separable phenomena" with "helium affecting both."[6]

The "inevitability" of the microchemical evolution and its possible correlation with high swelling rates and helium-affected void densities was addressed in this study first. The second question addressed was whether the details of the cavity and dislocation microstructure found in HFIR irradiations are consistent with the observed or predicted swelling rates. Third, should the 680°C HFIR datum (the only HFIR datum to suggest breeder-like swelling rates) be included in the analysis? Fourth, if cavity growth

above 700° does not require large amounts of helium, is the correlation between swelling and microchemical evolution still preserved at these temperatures? Finally, are the details of the phase development during irradiation in the two reactors similar and can any differences be confidently ascribed only to the influence of helium?

5.4 Experimental Results

5.4.1 Examination of Solution-Annealed AISI 316 Irradiated in HFIR

Since the acceleration of swelling has been correlated with the degree of microchemical evolution,[21,24,32] particularly the removal of nickel and silicon from the alloy matrix, a reasonable test of the inevitability of this process would be to examine whether or not a consistant correlation between swelling and nickel removal is observed in both HFIR and E8R-II irradiations. Data from only two HFIR and four E8R-II specimens are available for such a comparison.[3,4]

In two previous papers[3,4] it was shown that the microstructural and microchemical evolution of one cold-worked DO-heat specimen irradiated in HFIR at 550°C (nominal) to 42 dpa* was completely typical, not only of other heats of steel in E8R-II, but also of the same heat when irradiated in E8R-II to a comparable exposure. Unfortunately, however, the swelling level of this specimen, 1.4 - 1.9%,[4] is not sufficient to adequately address either the microchemical inevitability or high swelling rate questions.

Note in Figure 5 that there is an annealed specimen irradiated in HFIR at a nominal temperature of 480°C which exhibits swelling greater than 8%. This specimen was also exposed to 42 dpa* and had accumulated 2950 appm of helium. It was examined using both the JEOL JEM-100CX and VACUUM GENERATORS

*When the displacements produced by the ^{56}Fe recoil are included, 42 dpa becomes 47 dpa. Since this contribution is not uniformly distributed the dose will be listed hereafter as 42-47 dpa.

HB501 microscopes, employing conventional electron microscopy and energy-dispersive X-ray analysis. Precipitates were analyzed both in thin foil and on carbon extraction replicas prepared using 10% HCl in methanol. The higher radioactivity of HFIR-irradiated specimens complicates X-ray analysis and requires more stringent preparation and examination techniques than employed for specimens irradiated in EBR-II. These techniques have been described earlier.[4]

The dislocation density of this specimen was found to average 6 x 10^{10} cm^{-2}, similar to that reported in HFIR[4] and in EBR-II irradiated specimens.[18] The cavities were fairly uniformly distributed but were clearly composed of two quite different size groups. Figure 8 shows that there are relatively large cavities at a density of ~1 x 10^{15} cm^{-3} with a mean diameter on the order of 50 nm. This implies a swelling level of about 6%. Maziasz and coworkers had earlier examined another specimen cut from the same test component and measured 8.8 + 1.2% swelling from 1.4 x 10^{15} cm^{-3} cavities with a mean diameter of 39.6 nm.[7]

As shown in both figures 8 and 9, however, there is a second cavity component that was not reported in the earlier study by Maziasz or shown in figure 7. It is composed of a very high number density (~1.7 x 10^{17} cm^{-3}) of exceptionally small cavities (~2.0 nm). These very small cavities are most likely helium bubbles while the larger cavities observed in both studies are probably voids.

There are also the usual M_6C, Laves and G-phase precipitates[26,33] observed in this steel at this temperature (assumed to be ~550°C) with significant enrichment in nickel, molybdenum and silicon. As shown in figure 10, this enrichment is at the expense of the matrix. The data in Table 1 demonstrate that the matrix nickel level has fallen to an average value of ~8%. From a previously published empirical relationship using starting silicon and nickel levels, a saturation value of ~8% is predicted for this heat.[25] The various precipitates extracted by carbon replication were found to have an average composition (in weight %) of 26% fe,

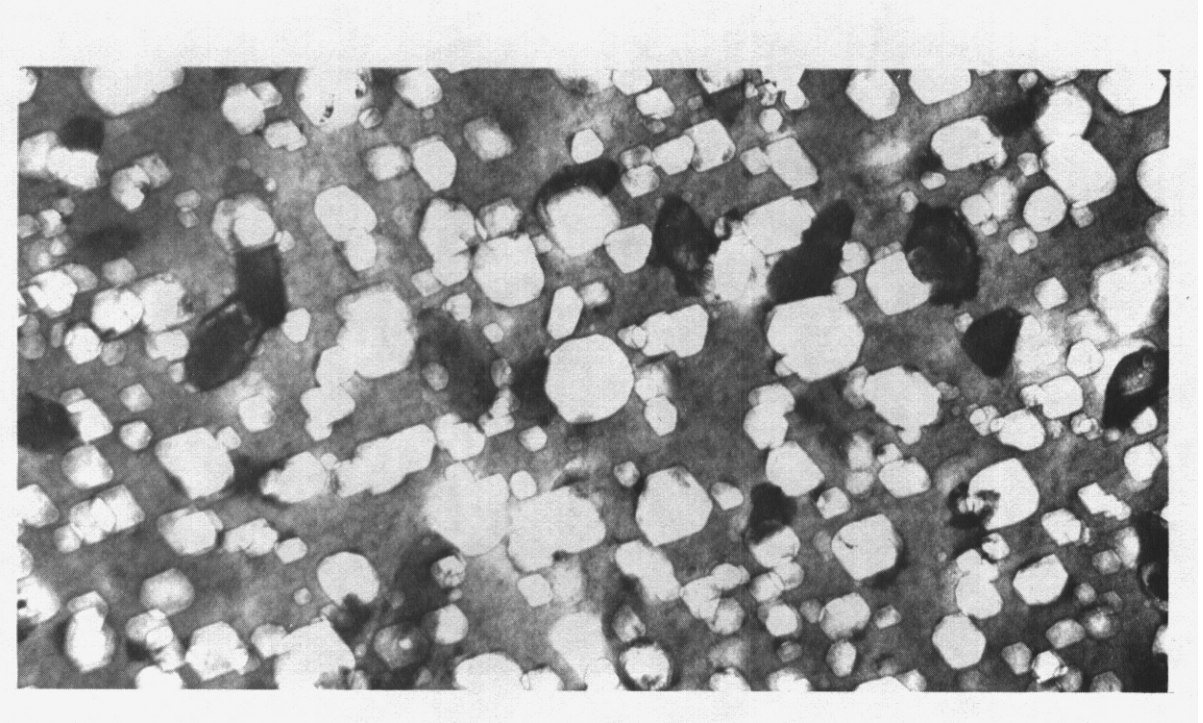

FIGURE 8. Micrograph of Annealed DO-Heat Specimen Irradiated at a Nominal Temperature of 480°C to 42-47 dpa in HFIR. Note two distinct classes of cavities with diameters of ~2.0 nm and 50 nm.

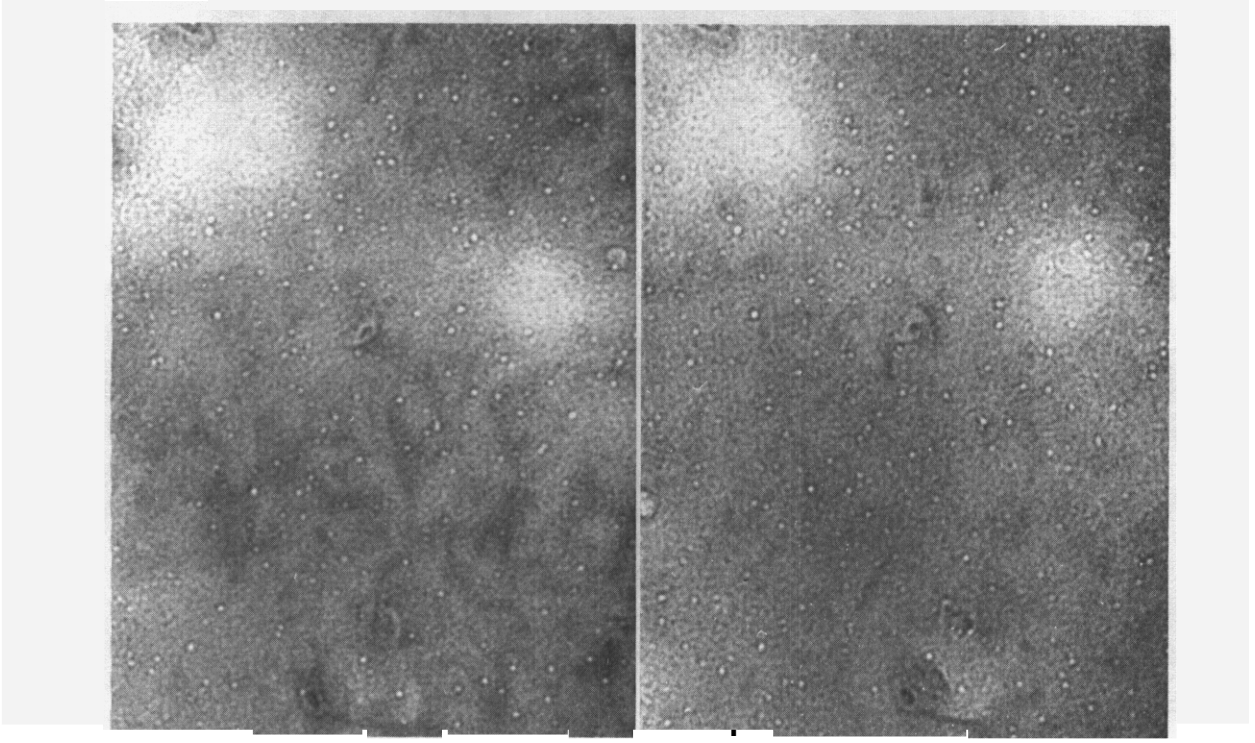

FIGURE 9. Stereo Pair Showing Smaller Cavities Seen in Figure 8.

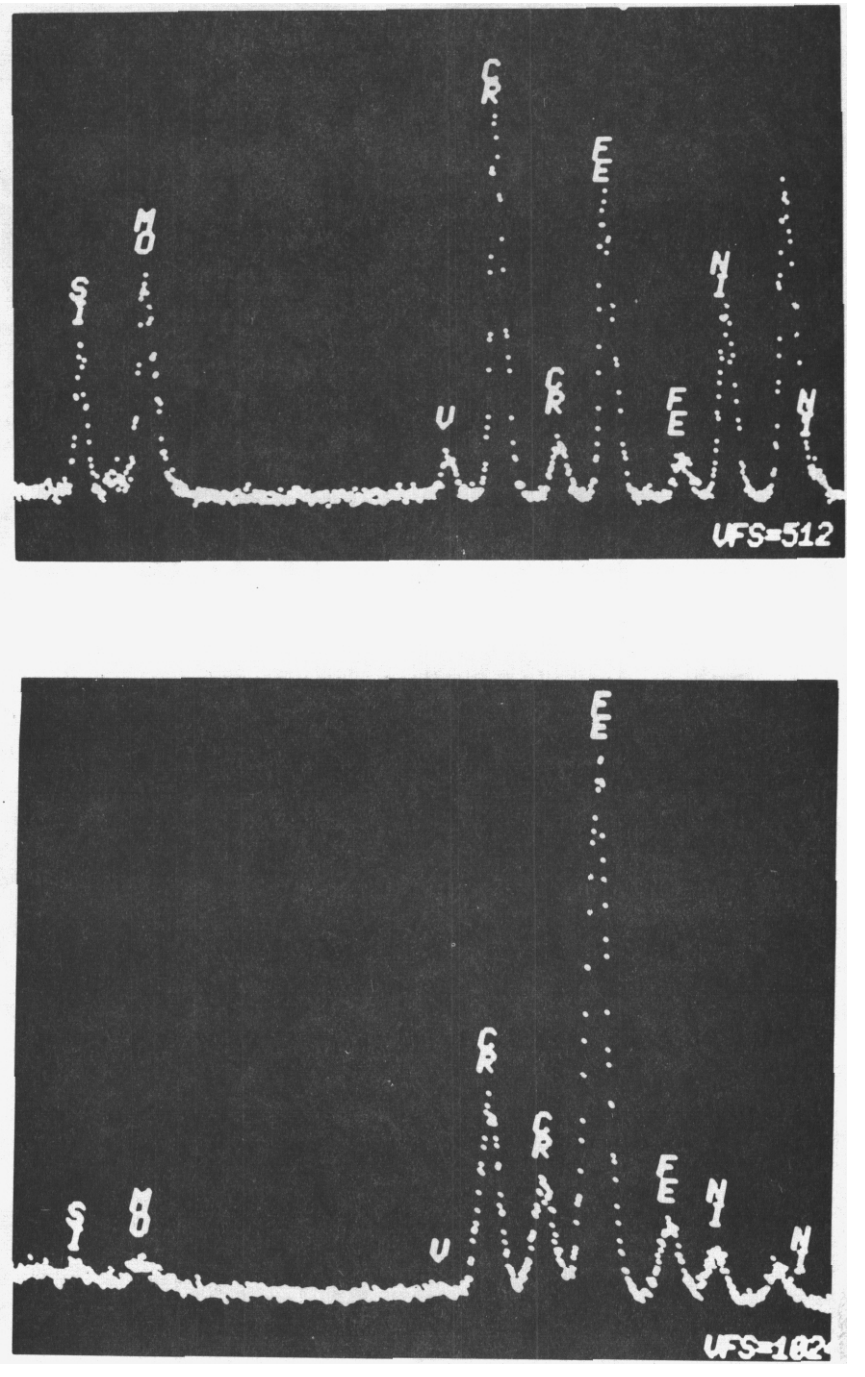

FIGURE 10. Comparison of In-Foil X-ray Analysis Spectra of a Typical Precipitate and One Matrix Area of a Solution-Annealed Specimen Irradiated at 480°C (Nominal) in HFIR to 42-47 dpa.

TABLE 1

SPOT-MEASUREMENTS OF ELEMENTAL COMPOSITION IN MATRIX REGIONS OF HFIR-IRRADIATED SPECIMEN OF ANNEALED DO-HEAT AISI 316 (after irradiation to 42- 47 dpa at a nominal temperature of 480°C and an estimated temperature of >550°C)

	wt%			
	Fe	Ni	Cr	Mn
1	71.2	9.1	17.1	2.4
2	72.3	6.7	19.7	0.5
3	70.9	7.1	19.4	2.4
4	72.3	6.3	18.8	2.4
5	72.7	6.9	20.2	0.1
6	71.5	8.3	19.3	0.8
7	69.6	7.2	19.5	3.6
8	68.0	10.7	18.5	2.6
9	71.7	7.8	18.8	1.6
		7.8% average nickel content		

*Matrix levels of Si, Mo and V were at unresolvable levels.

24% Cr, 22% Mo, 16% Ni, 8% Si, and 2.5% V. Note that the ~0.4% vanadium produced by transmutation during irradiation in HFIR has concentrated in the precipitates as was observed in the cold-worked specimen examined in an earlier report.(4)

The γ' phase was not found, which may or may not be significant since this specimen was irradiated near the upper temperature limit of its range of existence, based on results from EBR-II irradiations of AISI 316 with 0.5 wt% silicon.(19)

5.4.2 Examination of Cold-Worked AISI 316 Irradiated in E8R-II at High Temperature

It appears that the original temperature assignments for HFIR irradiations of DO-heat may be as much as 125°C too low.[10] When comparisons are made between E8R-II and HFIR data it is important that specimens be compared at nearly identical irradiation temperatures. Data on swelling in E8R-II to temperatures in excess of 700°C are desired. While no DO-heat data in this range are available, such data have just recently been published for an FFTF* heat of steel.[34] They allow an assessment of the assumptions of "inevitability" and the temperature-independence of swelling.

Although the swelling and microstructurally-oriented experiments of the U.S. Breeder Program did not probe the temperature regime above 650°C, pressurized tubes used to study irradiation creep were irradiated at temperatures as high as 720°C. (Above this temperature the thermal creep rate is too high to permit the service of AISI 316 in a breeder reactor.) Two nominally unstressed specimens irradiated at temperatures above 700°C have been examined by electron microscopy and energy dispersive X-ray analysis. Both specimens were irradiated for several E8R-II irradiation cycles in one subassembly and their irradiation was completed in another. The first irradiation was a controlled-flow temperature-monitored experiment while the latter was an uninstrumented isothermal heat-pipe experiment.

The examination of these specimens is reported in detail in Reference 34. Only a summary of the results pertinent to this paper will be covered in the following sections.

5.4.3 Cavities Produced at High Temperatures in E8R-II

The first specimen was extracted from a tube designated K65 fabricated from a tubing lot of 20% CW steel designated CN-13. This heat is known to

*FFTF is an acronym for Fast Flux Test Facility, a fast neutron test reactor in Richland, Washington.

swell relatively early compared to the N-lot and 00-heats, but is otherwise expected to exhibit comparable post-transient swelling behavior.[9] The K65 specimen was irradiated to 7.5 x 10^{22} n/cm^2 (~38 dpa) at a nominal temperature of 700°C. The actual temperature varied from 667 to 710°C with about half of the total fluence accumulated at 710°C. Diameter and density change measurements showed that a volumetric increase of 2.5% had occurred. It is known that some fraction of this volume change is due to volume changes arising from formation of intermetallic phases.[35] As shown in Figure 11, void swelling is several percent in this specimen. This figure also shows that the swelling at ~700°C is comparable to that observed in another experiment on this and three closely related heats of AISI 316 irradiated at 650°C.

The second specimen was derived from another CN-13 tube designated KE6. This specimen reached 1.2 x 10^{22} n/cm^2 (E > 0.1 MeV) at 718°C, continued to 2.3 x n/cm^2 at 700°C and finally reached 6.2 x 10^{22} n/cm^2 (~31 dpa) at 710°C. The density change of this specimen as 2.8%. Some fraction of the volume change in this specimen is due to the formation of large intermetallic precipitates,[35] one of which is shown in Figure 12.

5.4.4 X-Ray Analysis of Specimen K65 (667-710°C)

Void formation was found to be relatively homogeneous within any one grain but to be rather heterogeneous from grain-to-grain. Grain boundaries frequently separated heavily voided grains from totally unvoided grains. The possible relationship of such behavior to the details of the local microchemical environment was investigated using three different types of measurements.

First, entire grains were scanned with the electron beam. Each grain chosen for examination had a relatively uniform void array and was adjacent to other grains with widely differing swelling levels. These areas inevitably contained some precipitates but the level of precipitation was rather low compared to that which evolves at lower temperatures. As shown in Table 2

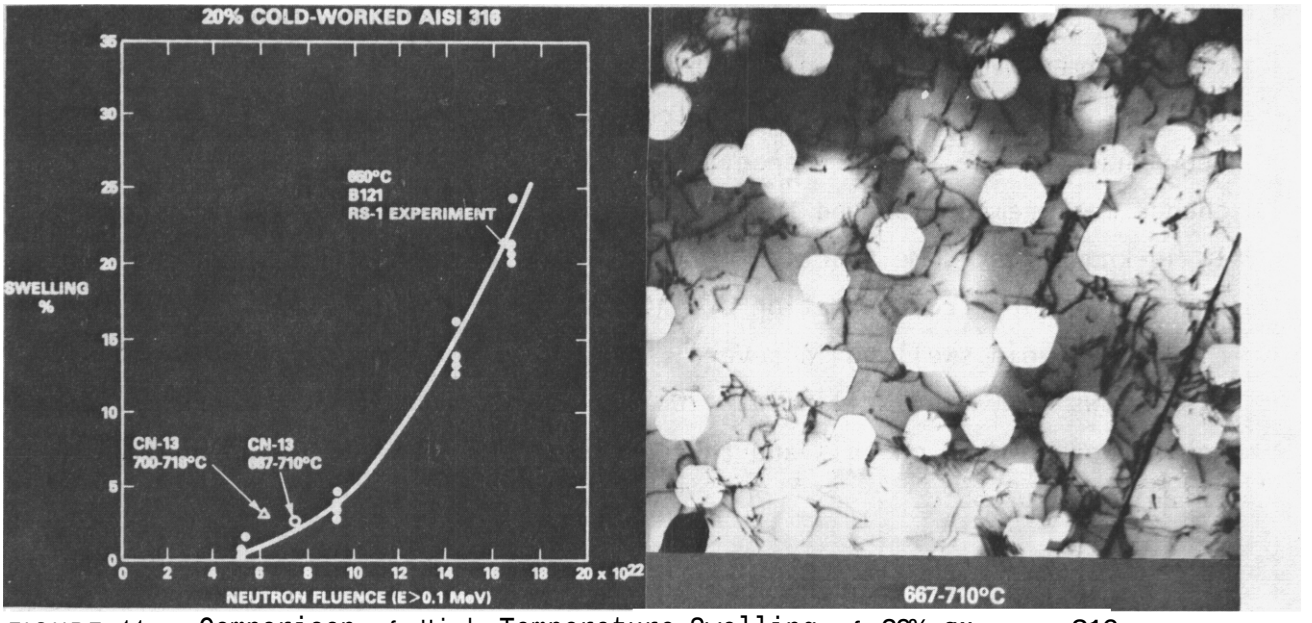

FIGURE 11. Comparison of High Temperature Swelling of 20% cw AISI 316 Stainless Steel Specimens from CN-13 Creep Tubes and Three Closely Related Heats Irradiated at 650°C.[9,15]

the nickel level in those areas which contained voids was lower than in the non-voided regions. In this comparison the voided regions also had higher molybdenum levels.

The second type of measurement used a smaller electron probe, about 10 nm in diameter, to randomly sample the matrix concentrations in the area previously scanned by the broader beam. These measurements determined the average matrix composition away from both void and precipitate boundaries. As shown in Table 3 and Figure 13, the mean matrix nickel level of voided regions was found to be 9.8 wt.%, while that of an adjacent unvoided region as 13.4%. The bulk average composition of this steel is 13.7% nickel. There were no other significant differences in elemental composition found between the two regions selected for analysis. (A comparison of the spectra obtained by the two measurement techniques is shown in Figure 14.)

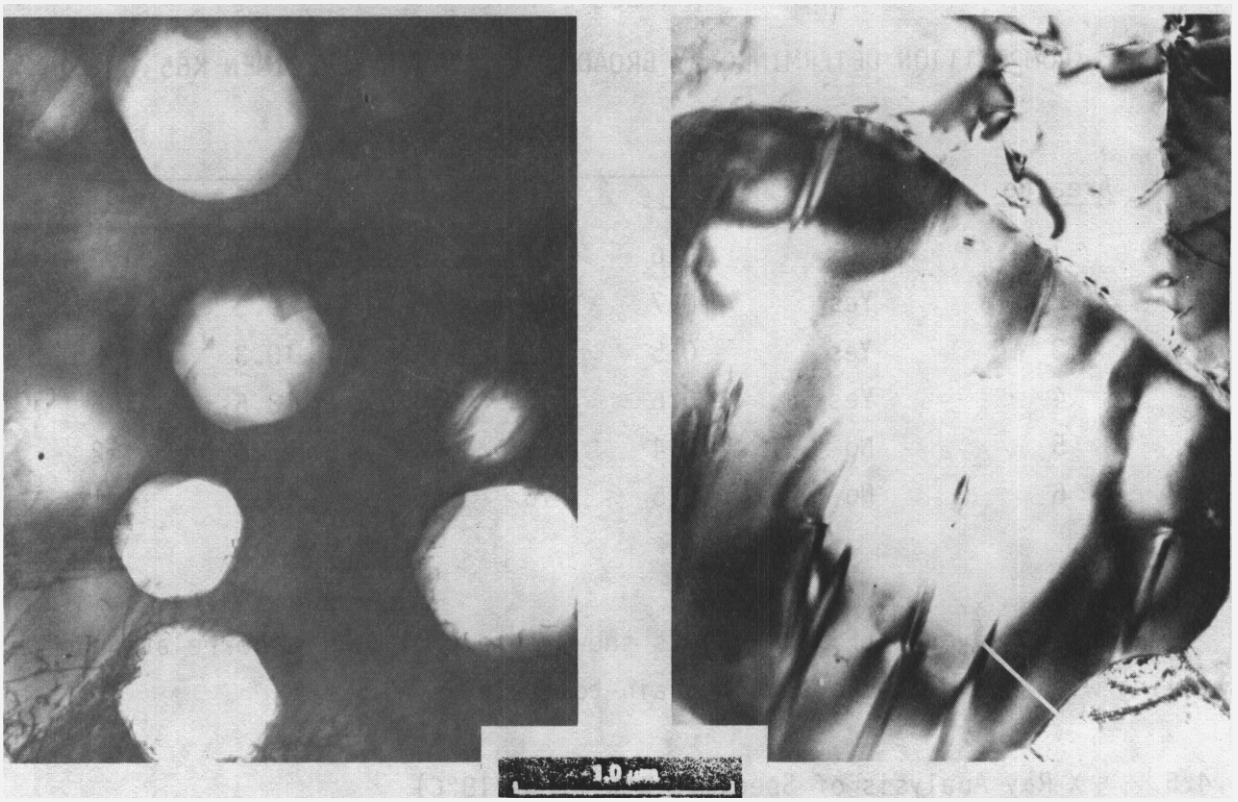

FIGURE 12. High Temperature Swelling of CN-13 Creep Tube KE6 at 700-718°C and 6.2 x 10^{22} n/cm^2 (E > 0.1 MeV). The swelling is very non-uniform and the voids are very large and at low densities ($\sim 10^{13}$ cm^{-3}). Some areas contain large intermetallic precipitates.

A third type of X-ray measurement employed in these studies was the line-of-sight average composition obtained along a traverse through the alloy. When a composition gradient exists, a traverse of measurements along that gradient can yield information on the direction of flow of various elements. These measurements have been used extensively in the study of DO-heat and other specimens.[3,4,22,31,34] As shown in the more detailed report on these specimens, nickel was found to be segregating to both void surfaces and precipitates.[34] The presence of gradients extending far from precipitate surfaces was evidence that the microchemical evolution was still in progress when the specimen was removed from E8R-II.

TABLE 2

COMPOSITION DETERMINED BY BROAD BEAM SCAN IN SPECIMEN K65

Area No.	Voids?	wt% Si	Cr	Fe	Ni	Mo
1	Yes	0.6	17	66	12.8	1.8
2	Yes	0.7	23	61	9.5	3.4
3	Yes	0.5	22	63	10.3	3.0
4	Yes	0.6	16	67	13.6	1.6
5	No	0.4	16	66	15.6	1.2
6	No	0.5	16	66	15.3	1.1

One such traverse (Figure 15) is shown to emphasize the correlation of swelling with nickel content on a grain-to-grain level.

5.4.5 X-Ray Analysis of Specimen KE6 (700-718°C)

The voids in this specimen are in general much larger than those observed in K65 and are even more nonuniformly distributed. Once again the swelling was observed to be relatively uniform within any given grain, however. The substantial heterogeneity of swelling did not allow an estimate of the relative contributions of voids and phase-related density changes to the measured density change of 2.3%.

Table 4 shows that in unvoided grains the analyses of the matrix composition at discrete locations (spot-matrix) and of large portions of a grain (scanned-matrix) agree, showing a relatively high nickel content of 15-16%. In an adjacent voided grain the nickel content was lower at 13%. The silicon level was also lower.

EDX measurements of the nickel content using line-of-sight average compositions showed enrichments at void surfaces approaching 21%. The actual enrichment is larger than 21%.[22]

TABLE 3

MATRIX SPOT ANALYSIS OF COMPOSITION IN SPECIMEN K65

Area Number	Voids?	weight % Si	Cr	Fe	Ni	Mo
#2	Yes	0.7	19	69	9.3	0.6
	Yes	0.7	18	68	10.0	1.2
	Yes	0.7	19	68	10.0	1.2
	Yes	0.7	19	69	8.6	1.4
	Yes	0.7	19	68	9.8	1.3
	Yes	0.6	19	68	9.2	1.7
	Yes	0.7	19	69	9.3	1.3
	Yes	0.7	19	67	11.1	1.1
	Yes	0.6	19	68	9.9	1.0
	Yes	0.6	20	67	9.9	1.4
	Yes	0.6	19	69	9.5	0.9
					average 9.7% compared to 9.5% by broad beam analysis	
#3	Yes	0.4	19	70	9.3	0.8
	Yes	0.5	20	68	9.8	1.1
	Yes	0.4	19	67	11.7	1.0
	Yes	0.3	19	68	10.7	1.0
	Yes	0.4	19	69	10.0	1.2
					average 10.3% compared to 10.3% by broad beam analysis	
#4	Yes	0.3	19	68	9.5	1.8
	Yes	0.4	19	68	10.3	1.9
	Yes	0.3	20	69	8.5	2.0
					average 9.4% compared to 13.6% by broad beam analysis	
#5	No	0.7	18	69	9.5	1.1
	No	0.6	15	66	15.9	1.1
	No	0.5	17	69	11.2	1.2
	No	0.4	17	66	14.3	1.5
	No	0.7	18	68	10.2	1.6
	No	0.4	15	66	16.1	1.1
	No	0.3	16	67	14.5	1.2
	No	0.4	16	66	15.5	1.2
	No	0.3	17	67	12.7	1.4
	No	0.2	18	68	11.9	1.2
	No	0.3	17	67	14.0	1.2
	No	0.5	16	67	14.6	0.8
	Averages	0.4	17	67	13.4	1.2

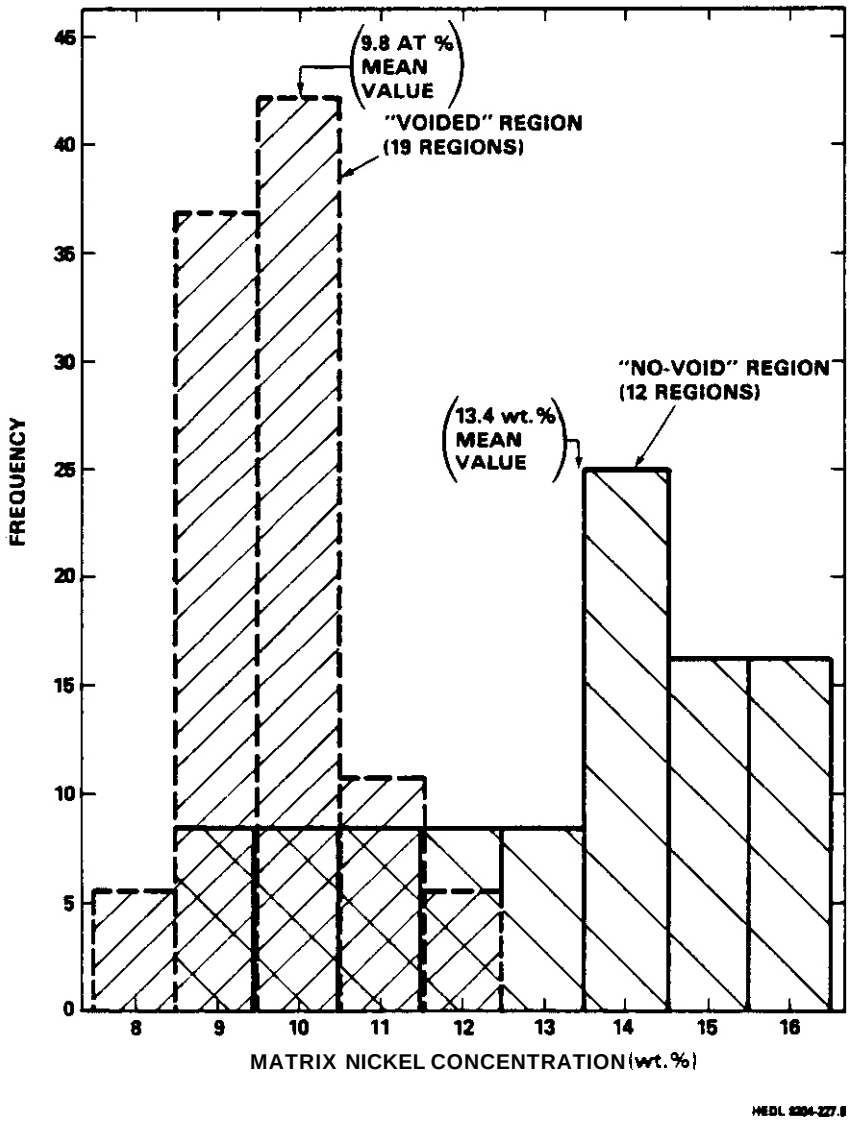

FIGURE 13. Local Matrix Composition of Nickel in Two Adjacent Grains of Specimen K65 of 20% Cold-Worked AISI 316 Irradiated at 667-710°C and 7.5 x 10^{22} n/cm^2 (E > 0.1 MeV). Note that voided regions have lower average nickel content than non-voided regions.

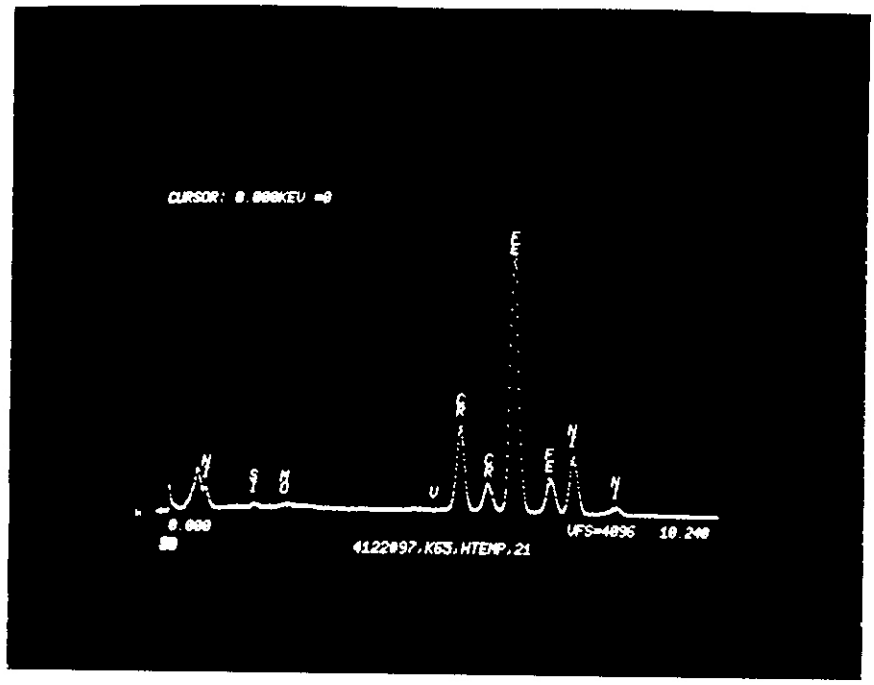

(a)

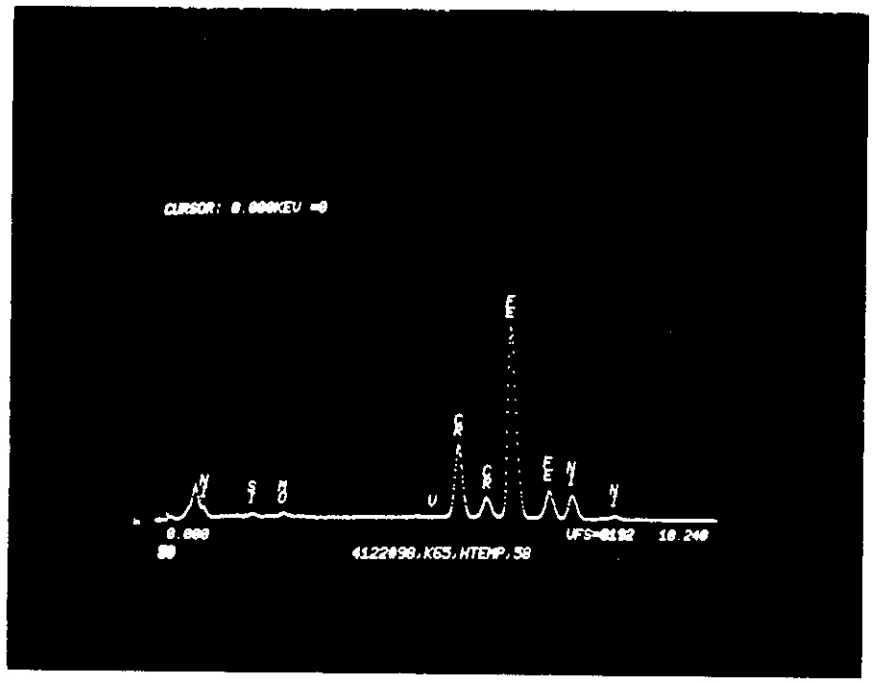

(b)

FIGURE 14. Typical EDX Spectra of Specimen K65. Spectrum (a) is a between-void spot-analysis and (b) is a broad matrix scan of a no-void region. There is a 9.2% nickel in the former and 15.6% nickel in the latter. Note the absence of a vanadium peak, in contrast to that found in AISI 316 irradiated in HFIR.

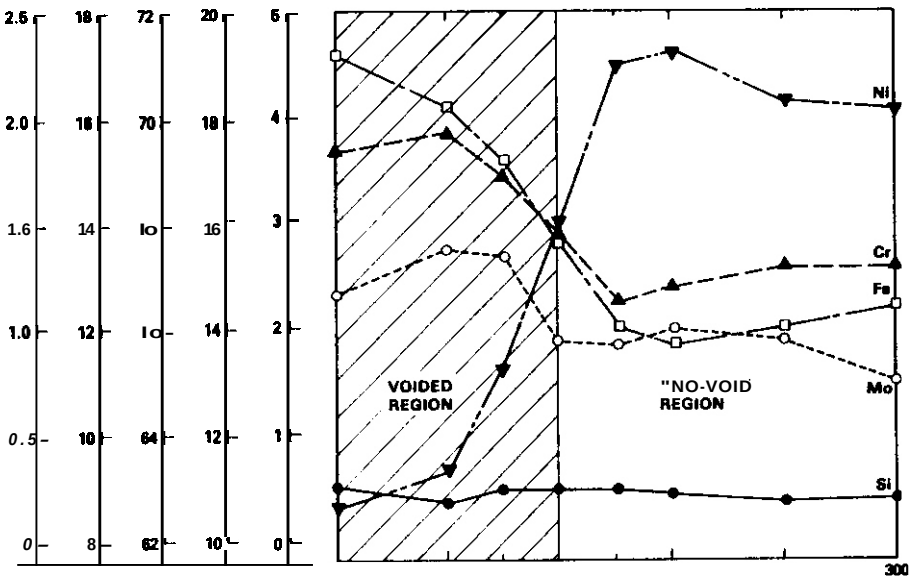

FIGURE 15.

imen

5.4.6 Summary of EBR-II High Temperature Data

It has previously been shown that the average nickel content of the alloy matrix can be used as an index of the degree of completion of the microchemical evolution.,[21,32] In this study, the validity of this index was tested and again has been confirmed. When swelling is just starting to accelerate to measurable levels, those regions which fall below 12-13% nickel first exhibit swelling. The existence of threshold nickel levels for void growth has been observed in earlier studies on several alloys.[21,27] The possibility exists, however, that the variation in nickel contents (12-16%) about the bulk average of 13.7% on a grain-to-grain level represents more the original natural heterogeneity of the steel than just a consequence of the radiation-induced nickel segregation process.

TABLE 4

EOX ANALYSIS OF SPECIMEN KE6

Voids	weight % Si	Cr	Fe	Ni	Mo
			MATRIX SCAN ANALYSIS		
No	0.4	17	66	14	2.0
No	0.3	16	63	18	1.7
No	0.6	17	65	15	0.8
No	0.5	18	68	12	0.8
No	0.7	15	62	19	1.0
No	0.8	16	62	19	0.7
No	0.8	16	63	18	0.6
No	0.8	17	65	16	0.8
No	0.7	16	66	15	0.7
No	0.7	16	66	15	0.8
Averages	0.6	16	65	16	1.0
			MATRIX SPOT ANALYSIS		
No	0.7	17	66	14	1.2
No	0.5	17	65	15	0.9
No	0.7	17	64	14	2.0
No	0.7	16	64	16	1.3
No	0.6	16	65	16	1.0
No	0.3	17	66	14	0.8
Averages	0.6	17	65	15	1.2
			MATRIX SCAN ANALYSIS		
Yes	0.3	18	67	13	1.0
Yes	0.3	18	67	12	1.3
Yes	0.4	17	66	13	1.1
Yes	0.3	18	67	13	1.4
Yes	0.2	18	67	13	0.9
Yes	0.3	18	66	13	1.4
Yes	0.3	19	67	12	1.0
Yes	0.2	19	67	12	1.0
Averages	0.3	18	67	13	1.1

The reduction of the matrix nickel to levels approaching 9% by the time substantial swelling has occurred is typical of that observed in other studies[21,22,24] when the silicon level is ~0.5 wt.%. This value appears to be relatively independent of temperature. For higher silicon levels, the nickel content of the matrix falls even lower and can be predicted from the original silicon and nickel levels.[25]

A more significant result of this portion of the study lies in the observation that not only does swelling occur in AISI 316 at temperatures above 700°C, but that the swelling does not decline with temperaure in the range 600-720°C as previously anticipated. It is usually thought that swelling would not occur at 650-720°C in EBR-II due to its low helium/dpa ratio and defect supersaturations. It therefore appears that the total swelling does not depend very strongly on the helium level at any temperature investigated to date, even though the void density is sensitive to the helium content.

5.5 Discussion

The experimental results described above (and those of Reference 4) clearly indicate that the presence of large amounts of helium or the elevation of irradiation temperature do not substantially alter either the inevitability or the predictability of the microchemical evolution. Figure 16 contains a compilation of the microchemical measurements from this and previous papers[3,4] and shows that the development of higher swelling levels correlates with the removal of nickel (and silicon) from the alloy matrix. The results also suggest that the appearance of voids can be correlated to the attainment of a critical nickel level in the matrix, although this is probably not a prerequisite for the many small helium bubbles observed in the solution-annealed specimen. While the cavity density (voids and/or bubbles) is clearly sensitive to the helium level, the dislocation density does not appear to be sensitive to the temperature, helium content, cold work level, or changes in manganese and vanadium concentrations.

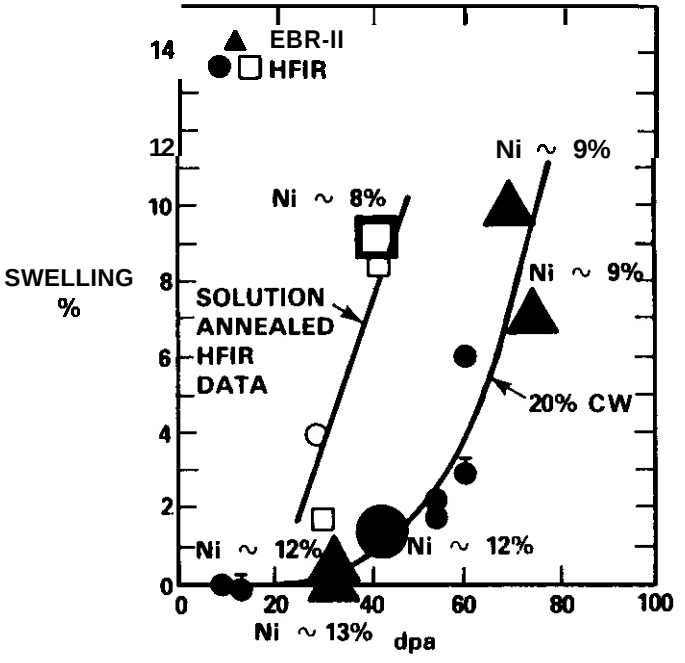

FIGURE 16. Correlation of Increased Swelling with Removal of Nickel from the Alloy Matrix. The average nickel contents of the matrix are shown beside selected swelling measurements. The saturation level of nickel in the DO-heat is predicted to be 8%.

An important question, however, is whether the steady-state swelling rate is strongly sensitive to the cavity density. There are two clues from these studies which address this question. First, recall that the total cavity density in the annealed specimen exceeds $10^{17} cm^{-3}$. Using the concepts advanced in Reference 6, one would predict that the cold-worked specimen would swell at a higher rate than the annealed specimen because the latter is clearly more cavity-dominated than the former. (In order to assure the validity of this statement, the cold-worked HFIR specimen examined in Reference 4 was reexamined in this study. A similar high density of small cavities was not found.)

Second, the results of the previous section can be combined with published EBR-II data on the swelling of AISI 316 to produce Figure 17. This shows once again that swelling rate of a specific heat of AISI 316 can be considered to be independent of temperature over the range 500-700°C. It also appears that below 500°C the swelling rate is approaching the same

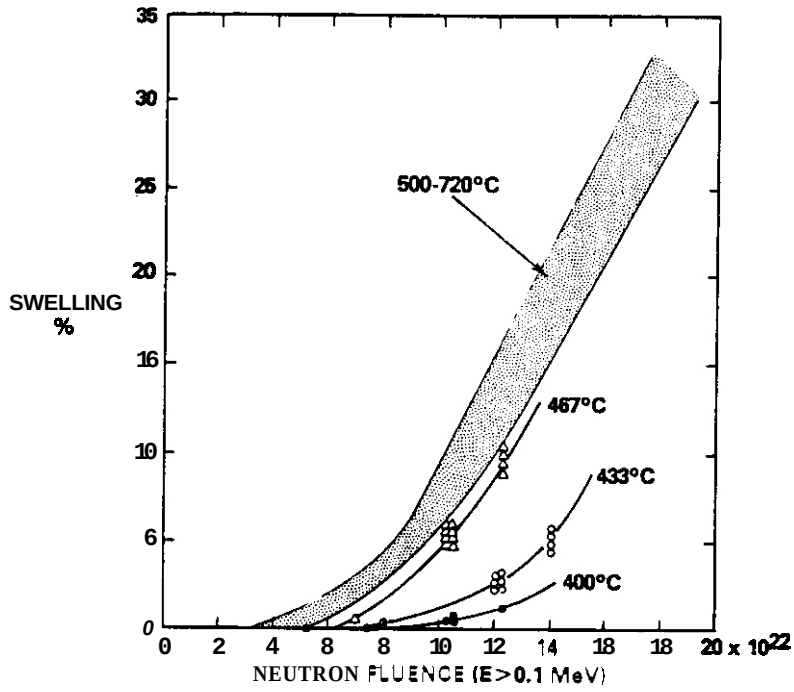

FIGURE 17. Relative Temperature Independence of Steady-State Swelling Rate for FFTF First Core Heats of Steel.[9,15]

value as found above 500°C, but with a longer transient.[15,32] The void density over this large temperature range varies almost three orders of magnitude while the steady-state swelling rate exhibits almost no change. It is doubtful, therefore, that the void density per se is an important determinant of the swelling rate in neutron irradiations. The same conclusion can be drawn from irradiations of AISI 304 stainless steel as shown in Figure 1.

Another way to assess the relative importance of helium and matrix nickel content would be to use simple Fe-Ni-Cr ternary alloys which do not have the complicating influence of solutes such as silicon, carbon or molybdenum. Rather than study the onset of swelling during nickel removal from the matrix, one can remove nickel from the alloy prior to irradiation. Figure 18 (reproduced from Reference 36) shows ion bombardment studies that demonstrate that a reduction of nickel content from 25 to 20% has a greater

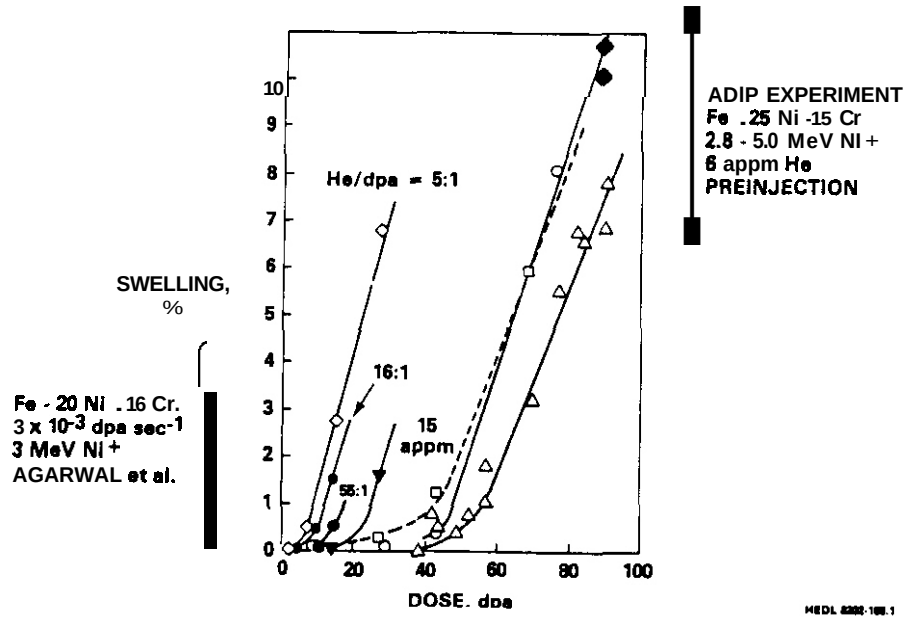

FIGURE 18. Comparison of Nickel Ion Irradiation Results Showing Relative Influence of Nickel Level and Helium/dpa Ratio for Fe-Ni-Cr Alloys.[36-38]

effect on the duration of the transient regime than does substantial variation in the helium/dpa ratio.* It is important to note that the effect of both helium and nickel content lies in the transient regime of swelling and not in the steady-state regime.

A similar result has been observed in recently published dual-ion irradiation studies[39,40] on AISI 316, as shown in Figure 19. This figure also demonstrates the relative insensitivity of steady-state swelling rate to irradiation temperature.

It appears to be a quite valid procedure to treat the twelve 00-heat swelling data points in aggregate and to ignore differences in temperature and details of cavity, microstructure and phase development. The alternative of breaking these limited data into subsets based on hard-to-define

*As shown in Reference 36, the "effective" helium/dpa ratios for the studies shown in Figures 18 and 19 are larger than reported by at least a factor of five.

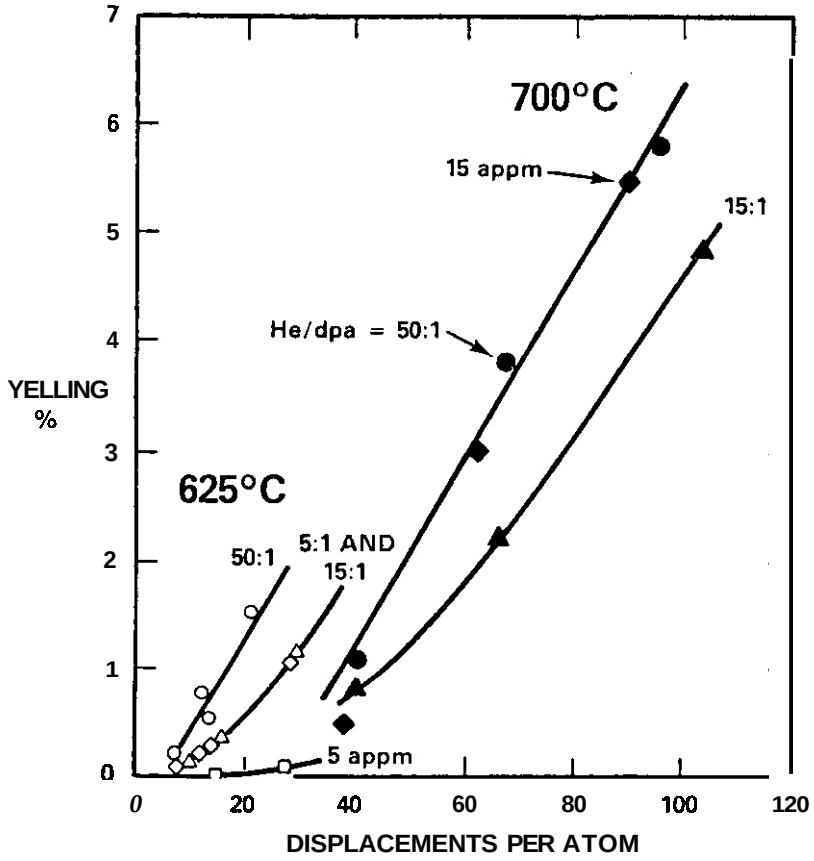

FIGURE 19. Comparison of Dual Ion Irradiation Results on Annealed and Aged AISI 316 at 625 and 700°C Showing That The Effect of Helium/dpa Ratio and Temperature Resides Only in the Transient Regime of Swelling.[39,40]

temperature increments poses a danger of reaching erroneous conclusions due to data scatter (in swelling measurements, temperature and dose as well as dose rate differences), while ignoring the consistent general trends exhibited by DO-heat and all 316 heats irradiated in both HFIR and EBR-II. This is particularly true when all of the cold-worked data from HFIR (with the exception of the 680°C datum) are well within the transient regime for both swelling and microchemical evolution. Furthermore, subdivisions of the data field place large burdens on the accuracy of both the temperature and displacement assignments.

While the microchemical evolution of the matrix (especially nickel content) of a specific heat has been shown to be reproducible, the path by

which the evolution proceeds is quite variable within a grain, from grain-to-grain and from experiment to experiment, in response to the large number of variables affecting phase development.[26] To draw conclusions concerning the effect of helium on phase development ignores not only the differences in operational history between **EBR-II** and **HFIR** but also the very pronounced differences in displacement generation and transmutation for these two reactors. Those precipitates with increased nickel level will be subjected to proportionately larger internal displacement rates relative to that of the surrounding nickel-poor matrix.[41] Since the range of the recoiling iron atoms is comparable to the size of most precipitate phases formed at low temperature, the precipitates will also become net sources of vacancies and will be surrounded by enhanced concentrations of interstitial atoms.[41] The helium atoms produced by this reaction will come to rest far from the precipitate, however. It is therefore quite possible that these indirect consequences of helium production will alter the stability of some phases, particularly the ordered low-temperature nickel-enriched γ' phase.

If one adds to this consideration the depletion of manganese (an essential constituent of G-phase formation for AISI 316) in **HFIR** and the generation of vanadium (a strong carbide-forming element found in this study to concentrate in M_6C precipitates) then one should not be surprised to find differences in phase evolution between specimens irradiated in **HFIR** and **EBR-II.** The consequences of these differences on the matrix evolution are not expected to be great, however, and no convincing evidence links phase evolution and helium level in this study.

It appears, therefore, that the correlation between microchemical evolution and swelling is not perturbed by the differences in helium content, solid transmutant concentrations and operational history characteristics of EBR-II and **HFIR** irradiations. Providing that swelling can be correlated with be dpa for 14-MeV neutron irradiations, it is not anticipated that this conclusion will be significantly altered in the intermediate helium/dpa range typical of projected fusion environments.

5.6 Conclusions

The microstructural evolution of AISI 316, namely the number of cavities formed and the minor details of phase evolution, is perturbed by the differences existing in the irradiation environments of EBR-II and HFIR. It is important to note that the minor phase differences are attributed to the combined effect of differences in helium level, spatial differences in damage production, the depletion of manganese and the generation of vanadium. However, the dislocation density, the total amount of swelling, the steady-state swelling rate and the microchemical evolution of the matrix are not perturbed substantially.

It also appears that the microchemical evolution of the alloy matrix is largely unchanged and is the dominant determinant of the swelling rate during neutron irradiation of this alloy. The influence of helium on total swelling in the He/dpa range spanned by EBR-II and HFIR is not as large as originally anticipated.' Ion bombardment studies in the relevant He/dpa range confirm these conclusions.

6.0 References

1. J. Weitman, N. Davernog and S. Farvolden, Trans. Am. Nucl. Soc. 13, p. 557, 1970.
2. F. A. Garner, H. R. Brager and F. M. Mann, "Factors Relevant to the Development of Fission-Fusion Correlations," this conference.
3. H. R. Brager and F. A. Garner, J. Nucl. Mater. 103 & 104, p. 993, 1982.
4. H. R. Brager and F. A. Garner, J. Nucl. Mater. 108 & 109, p. 347, 1982.
5. P. J. Maziasz and M. L. Grossbeck, J. Nucl. Mater. 103 & 104, p. 987, 1982.
6. P. J. Maziasz, J. Nucl. Mater. 108 & 109, p. 359, 1982.
7. P. J. Maziasz, F. W. Wiffen and E. E. Bloom, Proc. Conf. Radiation Effects and Tritium Technology for Fusion Reactors, CONt-750989, Vol. I, p.259.

8. F. A. Garner, J. J. Laidler and G. L. Guthrie, "Development and Evaluation of a Stress-Free Swelling Correlation for 20% CW Type 316 Stainless Steel," Irradiation Effects on the Microstructure and Properties of Metals, ASTM STP 611, American Society for Testing and Materials, pp. 208-226, 1976.

9. J. F. Bates and M. K. Korenko, Nucl. Technol. 48, p. 303, 1980.

10. G. R. Odette, P. J. Maziasz and J. A. Spitznagel, J. Nucl. Mater. 103 & 104, p. 283, 1982.

11. J. F. Bates, F. A. Garner and F. M. Mann, J. Nucl. Mater. 103 & 104, p. 999, and F. A. Garner, F. M. Mann and H. R. Brager, "Measurement and Calculation of Solid Transmutants Formed in AISI 316," Damage Analysis and Fundamental Studies Quarterly Progress Report, DOE/ER-0046/7, P. 198, November 1981.

12. J. F. Bates and W. G. Johnston, "Effects of Alloy Composition on Void Swelling," Radiation Effects in Breeder Reactor Structural Materials, M. L. Bleiberg and J. W. Bennett, Eds, The Metallurgical Society of AIME, p. 625, 1977.

13. L. R. Greenwood and R. K. Smither, "Neutron Dosimetry Measurements for the HFIR-CTR3 Irradiation," Damage Analysis and Fundamental Studies Quarterly Progress Report, DOE/ER- 6/9, P. 32, May 1982.

14. F. A. Garner and D. L. Porter, "Factors Influencing the Swelling of 300 Series Stainless Steels," Ibid., p. 170.

15. W. J. S. Yang and F. A. Garner, "Relationship Between Phase Development and Swelling of AISI 316 During Temperature Changes," Effects of Radiation on Materials: Eleventh Conference, ASTM STP 782, H. R. Brager and J. S. Perrin, Eds., American Society for Testing and Materials, pp. 186-206, 1982.

16. W. K. Appleby, E. E. Bloom, J. E. Flinn, and F. A. Garner, "Swelling in Neutron-Irradiated 300 Series Stainless Steels," Radiation Effects in Breeder Reactor Structural Materials, p. 509, 1977.

17. P. J. Maziasz and M. L. Grossbeck, "Equations to Describe the Swelling of 20% Cold-Worked Type 316 Stainless Steel Irradiated in HFIR," Alloy Development for Irradiation Performance Semiannual Progress Report, DOE/ER-0045/7, p. 98, March 1982.

18. H. R. Brager, F. A. Garner, E. R. Gilbert, J. E. Flinn and W. G. Wolfer, "Stress-Affected Microstructural Development and the Creep-Swelling Interrelationship," Radiation Effects in Breeder Reactor Structural Materials, p. 727, 1977.

19. H. R. Brager and F. A. Garner, J. Nucl. Mater. 73, p. 9, 1978.

20. H. R. Brager and F. A. Garner, "Dependence of Void Formation on Phase Stability in Neutron Irradiated Type 316 Stainless Steel," Effects of Radiation on Structural Materials, ASTM STP 683, J. A. Sprague and D. Kramer Eds., pp. 207-232, 1979.

21. H. R. Brager and F. A. Garner, "Microchemical Evolution of Neutron-Irradiated Stainless Steels," Effects of Radiation on Materials, ASTM STP 725, D. Kramer, H. R. Brager and J. S. Perrin Eds., pp. 470-483, 1981.

22. H. R. Brager and F. A. Garner, "Analysis of Radiation-Induced Microchemical Evolution in 300 Series Stainless Steels," Proceedings of Symposium on Advanced Techniques for the Characterization of Metals, The Metallurgical Society of AIME, F. W. Wiffen and J. A. Spitznagel Eds. p. 97, 1982.

23. H. R. Brager and F. A Garner, "Stability of the Radiation-Induced Gamma Prime Phase in 316 Stainless Steel," to be published in J. Nucl. Mater.

24. F. A. Garner, "The Microchemical Evolution of Irradiated Stainless Steels," Proceedings of Symposium on Phase Stability During Irradiation, J. R. Holland, L. K. Mansur and D. I. Potter Eds., The Metallurgical Society of AIME, p. 165, 1981.

25. H. R. Brager and F. A. Garner, "Radiation-Induced Evolution of the Austenitic Matrix in Silicon-Modified AISI 316 Alloys," Ibid., p. 219.

26. W. J. S. Yang, H. R. Brager and F. A. Garner, "Radiation-Induced Phase Development in AISI 316," Ibid., p. 257.

27. L. E. Thomas, "Analytical Electron Microscopy of Neutron-Irradiated Reactor Alloys," Proc. of 1982 EMSA Meeting, Washington, DC, Claitors, (in press).

28. G. Brun, J. LeNaour and M. Vouillon, J. Nucl. Mater. 101, p. 109, 1981.

29. T. M. Williams. "Precipitation in Irradiated and Unirradiated Austenitic Steels," Effects of Radiation on Materials: 11th Conf., ASTM STP 782, p. 166, 1982.

30. F. A. Garner and W. G. Wolfer, J. Nucl. Mater. 102, p. 143, 1981.

31. W. G. Wolfer. F. A. Garner and L. E. Thomas. "On Radiation-Induced Segregation and the Compositional Dependence of Swelling in Fe-Ni-Cr Alloys," Effects of Radiation on Materials: 11th Conf., ASTM STP 782, p. 1023, 1982.

32. F. A. Garner and D. L. Porter, "History Dependence and Consequences of the Microchemical Evolution of AISI 316," Ibid., p. 295.

33. E. H. Lee, P. J. Maziasz and A. F. Rowcliffe, "The Structure and Composition of Phases Occuring in Austenitic Stainless Steels in Thermal and Irradiation Environments," Proceedings of Symposium on Phase Stability During Irradiation, p. 191.

34. H. R. Brager, W. J. S. Yang and F. A. Garner, "Microstructural/Microchemical Evolution of AISI 316 at Temperatures in the Range 650-750°C," Damage Analysis and Fundamental Studies Quarterly Progress Report, DOE/ER-0046/10, p. 233, August 1982.

35. F. A. Garner, Extraoolation of Stress-Affected Swelling Models into Compressive and cyciic Stress States," Damage Analysis-and Fundamental Studies Quarterly Progress Report, DOE/ER-0046/5, p. 198, May 1981.

36. F. A. Garner, "Correlation of Charged Particle and Neutron-Induced Radiation Damage: The ADIP Experiment Revisited," this conference.

37. S. C. Agarwal, G. Ayrault, 0. I. Potter, A. Taylor and F. V. Nolfi Jr., J. Nucl. Mater. 85 & 86, 1979, p. 653, DOE/ER-0046/10, p. 145.

38. F. A. Garner et al., "Summary Report on the Alloy Development Intercorrelation Program Experiment," Proceedings of the Workshop of Neutron and Charged-Particle Damage, CONF-760673, Oak Ridge National Laboratory, June 8-10, 1976.

39. G. Ayrault, H. A. Hoff, F. V. Nolfi Jr., and A. P. L. Turner, J. Nucl. Mater. 103 & 104, 1035, 1981.

40. Supplied by B. Loomis, G. Ayrault and Z. Wang in advance of publication.

41. F. A. Garner and F. M. Mann, "The Impact of the $^{59}Ni(n,\alpha)^{56}Fe$ Reaction on Damage Calculations for HFIR," Damage Analysis and Fundamental Studies Quarterly Progress Report, DOE/ER-0046/9, p. 41, May 1982.

7.0 Future Accomplishments

No further work on the AISI 316 00-heat is anticipated.

8.0 Publications

Portions of this effort were previously published in references 3 and 4. The full results of this study will be published in J. Nuclear Materials as the Proceedings of the TMS-AIME Symposium on Radiation Damage Analysis for fusion reactors, held in St. Louis, MO on October 24-28, 1982.

Acknowledgments

The authors wish to thank P. J. Maziasz of Oak Ridge National Laboratory for participating in an exchange of specimens. This work was supported by the U.S. Department of Energy.

INFLUENCE OF HELIUM INJECTION SCHEDULE AND PRIOR THERMOMECHANICAL TREATMENT ON THE MICROSTRUCTURE OF ION-IRRADIATED TYPE 316 STAINLESS STEEL

A. Kohyama, G. Ayrault and B. A. Loomis (Argonne National Laboratory)

1.0 Objective

The objective of this work is to determine the evolution of the microstructure in first wall materials during irradiation with special emphasis on the effects of helium production, displacement damage rates and temperature.

2.0 Summary

The influence of different helium injection schedules on the development of the microstructure in 316 SS irradiated at 625°C with 3.0-MeV $^{58}Ni^{+}$ ions to 25 dpa is described. Hot- or cold-preinjection of helium in 316 SS followed by single-ion irradiation produced lower swelling than dual-ion irradiation in the case of solution annnealed or solution annealed and aged specimens. Hot-preinjection of helium in 20% cold-worked specimens followed by single-ion irradiation produced greater swelling than dual-ion irradiation. In solution annealed or solution annealed and aged specimens, the dislocation density increased rapidly up to about 5 dpa and then gradually increased to a saturation density at 25 dpa. This transition of dislocation density to saturation corresponded to the rapid decrease of the Frank loop density by unfaulting. The dislocation density in cold-worked specimens decreased very rapidly with increasing damage up *to* 5 dpa and then increased slowly to the saturation density at 25 dpa where the fraction of Frank loops attained a low, steady-state value. Dual-ion irradiation of solution annealed or solution annealed and aged specimens produced a strongly bimodal distribution of cavity sizes at 25 dpa. Single-ion irradiation followed by dual-ion irradiation of these materials to the same dose and helium level produced a cavity size distribution with a substantial component of intermediate size cavities. Dual-ion irradiation of 20% cold-worked material produced only very small cavities, whereas helium injection followed by dual-ion irradiation produced some intermediate size cavities. There was little difference in the swelling

of the 20% cold-worked material for the two different schedules of irradiation.

3.0 Program

Title: Effects of Irradiation on Fusion Reactor Materials
Principal Investigator: B. A. Loomis
Affiliation: Argonne National Laboratory

4.0 Relevant DAFS Program Plan Task/Subtask

Subtask II.C.2.1 Mobility, Distribution and Bubble Nucleation

5.0 Accomplishments and Status

5.1 Introduction

Mixed-spectrum reactor irradiation is commonly used for the study of helium effects on radiation damage in nickel-bearing alloys. Helium is generated via the two-step reaction

$$^{58}Ni(n,\gamma)^{59}Ni, \text{ and}$$

$$^{59}Ni(n,\alpha)^{56}Fe \ .$$

At sufficiently high neutron fluence, the ^{59}Ni concentration in austenitic SS alloys can reach levels where the helium generation rate attains or exceeds the high level expected in magnetic fusion reactors (~15 appm He/dpa). However, during the early phase of microstructure development in these materials irradiated in mixed spectrum reactors, there is essentially no helium present in the material. In contrast, the neutrons produced in a magnetic fusion reactor (MFR) will rapidly generate helium even at the lowest fluence. In this study, we have irradiated 316 SS specimens with dual-ions (Ni^+ and He^+) using helium injection schedules that are intended to either (1)

approximate the MFR condition of steady helium generation or (2) mimic the mixed-spectrum reactor condition of no helium production at low neutron fluence and rapid helium production at high neutron fluence. Helium preinjection (usually 10 to 30 appm) is often used to compensate for the lack of helium production in the early phase of microstructure development in reactor irradiations. In addition to the dual-ion irradiations, we have hot- or cold-preinjected 316 SS specimens with helium, and then irradiated the specimens with single-ions to test the validity of helium preinjection as a simulation for the production of transmutant helium.

Specimens with three different thermomechanical histories, i.e., either cold-worked, solution annealed, or solution annealed and aged, were utilized in this study. The microstructures of these specimens following irradiation have been previously reported in Ref. [1].

5.2 Materials and Procedures

The material for this study was 316 SS from the MFE No. 15893 heat. Specimens of this material with three different thermomechanical treatments, i.e., solution annealed (0.5 h at 1050°C), solution annealed and aged (1 h at 1050°C, 10 h at 800°C), and 20% cold-worked were irradiated at 625°C, which is near the peak swelling temperature. The specimens were irradiated with 3.0-MeV $^{58}Ni^{+}$ ions which caused a damage production rate of 3 x 10^{-3} dpa·s^{-1}. The helium injections (simultaneous and preinjection) were performed with degraded 0.83-MeV $^{3}He^{+}$ ions.

Specimens of the 316 SS were irradiated with six dose/helium histories. For simplicity, each of these histories is assigned a discriptive code, e.g., 5S for (1) below, which is listed with each dose/helium history. The histories were:

(1) single-ion irradiation to 5 dpa (5S),
(2) dual-ion irradiation to 5 dpa with 15 appm He/dpa (50)
(3) single-ion irradiation to 5 dpa followed by 20 dpa of dual-ion

irradiation with *18.8* appm He/dpa to give the same final helium concentration as (4) (25SD),

(4) dual-ion irradiation to 25 dpa with 15 appm He/dpa (25D),

(5) 15 appm (cold) helium preinjection (at room temperature) followed by 25 dpa of single-ion irradiation (25CP), and

(6) 15 appm (hot) helium preinjection (at 650°C) followed by 25 dpa of single-ion irradiation (25HP).

Histories (3) and (4) (25SD and 25D) are intended to mimic the mixed-spectrum reactor and MFR irradiation, respectively. Histories (1) and (2) (5S and 5D) provide information on the microstructures that the 25 dpa samples (25SD and 25D) had at low dose.

The microstructures of the irradiated specimens were obtained from observation in the JEM 100CX electron microscope. The photomicrographs for microstructure analyses were recorded in the (200) two beam diffraction condition for dislocation contrast or were recorded in underfocused absorption contrast to image the cavities. The carbon spot method was used to determine the foil thickness of the observed microstructures, and the cavity-size distributions were obtained from observations of photomicrographs with a Zeiss particle size analyzer.

5.3 Experimental Results

5.3.1 Simultaneous Helium Injection and Production of Irradiation Damage

The dependence of the dislocation density on irradiation damage in solution annealed (SA), solution annealed and aged (SAA), and 20% cold-worked (CW) specimens is shown in Figure 1. The dislocation structures in solution annealed (SA) or solution annealed and aged (SAA) specimens that were irradiated to 5 dpa, i.e., 5S and 5D, were predominatly of the Frank loop type with a slight difference in the number density of loops between 5S and 5D. The average diameter of Frank loops in SA materials was larger than in SAA materials. At damage levels between 5 dpa and 15 dpa, unfaulting of the Frank loops occurred with glide and climb of dislocations to form a tangled

dislocation network. This unfaulting of Frank loops led to a saturation of the dislocation density at about 10 dpa in SA and SAA materials. In 20% cold-worked (CW) specimens, substantial recovery of the as-prepared dislocation density occurred initially (< 5 dpa) and then the irradiation-produced

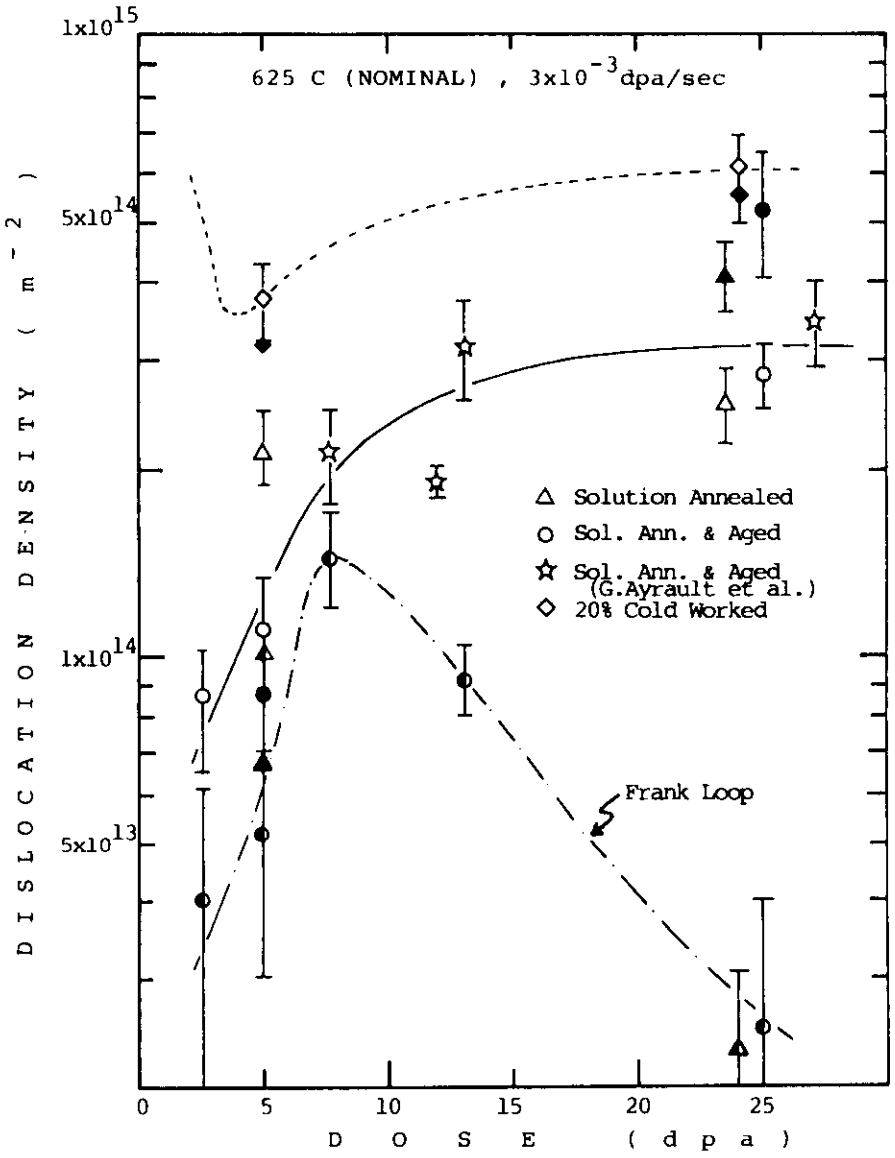

FIGURE 1. Dislocation Density in Dual-Ion Irradiated (total density: blank mark, Frank loop density: half-filled mark) and Single or Single Plus Dual-Ion Irradiated (total density: filled mark) Type 316 SS.

dislocation density increased to the saturation value. Needle-like precipitates that were formed during irradiation were observed in all of the specimens. In SA and SAA materials irradiated to 5 dpa, the needle-like precipitates exhibited a preferential orientation. The precipitates in 5D specimens were more highly aligned than those in 5S specimens. However, the number density of precipitates in 5S material was higher than in the 5D material. In the case of SA and SAA materials irradiated to 25 dpa. the number density of precipitates was not significantly different for the 25SD and 25D irradiation schedules. The grain-boundary and needle-like precipitates in SAA materials were larger than in SA materials. The needle-like precipitates were poorly aligned in the SAA material in comparison with the SA material. In CW material, numerous needle-like precipitates could be observed that were smaller than in SA and SAA materials. The precipitates in CW materials did not appear to be well aligned and the number density of precipitates was very low.

The cavity microstructures in solution annealed (SA) specimens irradiated to 5 dpa (5S and 5D) were quite different from one another. Cavities were not visible in single-ion irradiated specimens (5S), whereas dual-ion irradiation produced significant cavity nucleation and growth (5D). Even though the 25SD and 25D specimens (SA) at 25 dpa had similar dislocation microstructures, their cavity microstructures were different. The cavity size distribution in the 25D specimen was clearly bimodal in nature (Figure 2) with a high number density of small cavities ($\lesssim$ 7 nm) and a lower number density of large cavities (up to ~40 nm). The 25SD specimen contained a high number density of small cavities and the maximum cavity size was similar to that in the 25D sample. However, the size distribution in the 25SD specimen was not as strongly bimodal as in the 25D sample; there were many cavities in the 7 to 30 nm size range.

Cavity development in the solution annealed and aged (SAA) material closely paralleled their development in SA specimens. Cavities were not visible in the 5S specimen whereas at 5 dpa cavity growth was well underway in the 5D specimen. As shown in Figure 3, the 25D and 25SD irradiation produced a

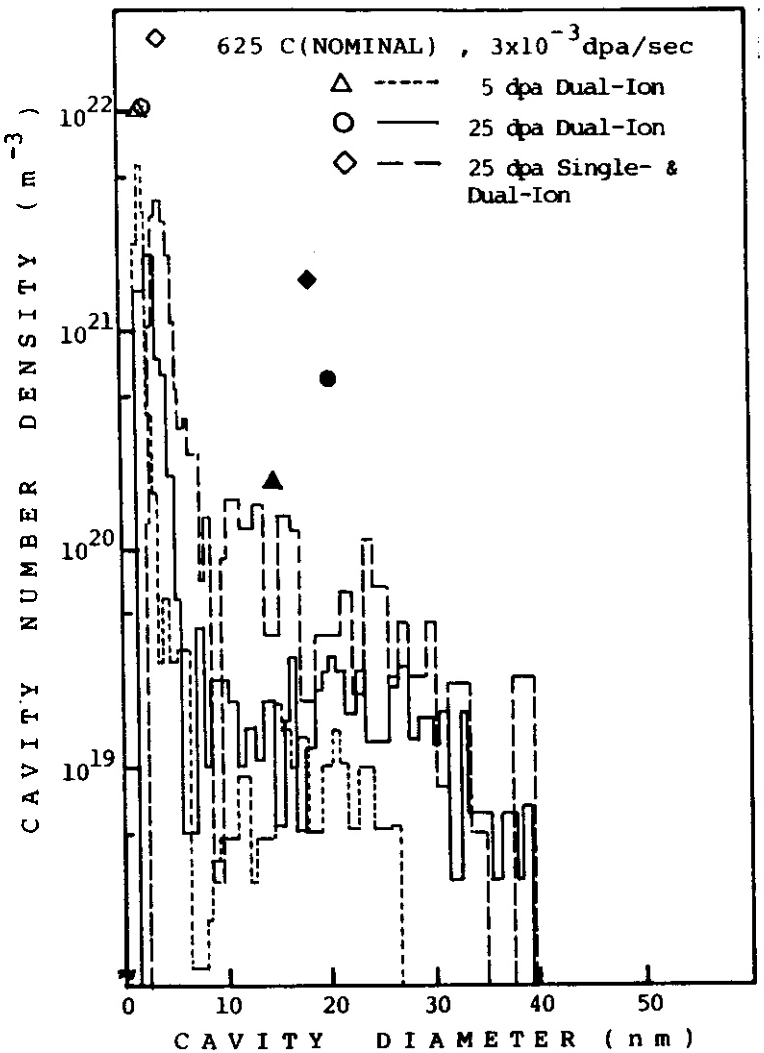

FIGURE 2 Cavity-Size Distribution in Solution-Annealed Type 316 SS.(Average cavity diameter: Small cavity--open symbol, large cavity--filled symbol.

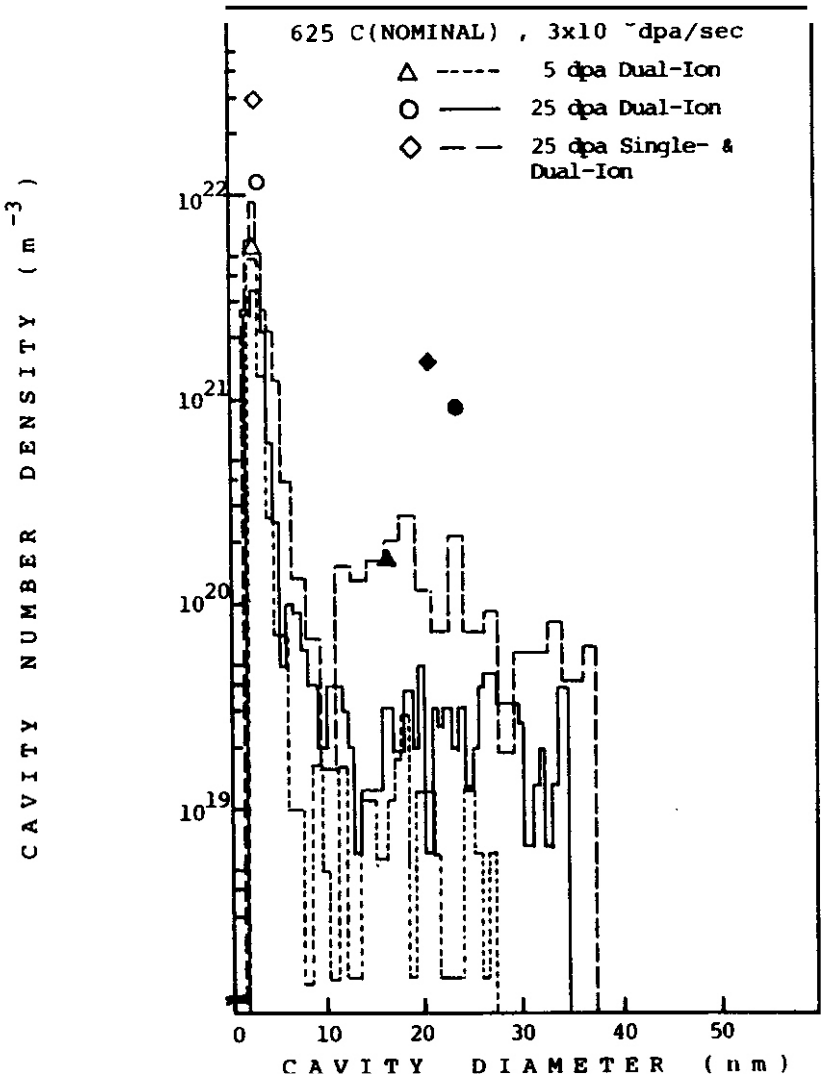

FIGURE 3 Cavity-Size Distribution in Solution-Annealed and Aged Type 316 SS (Average cavity diameter: small cavity--open symbol, large cavity--filled symbol.

strongly bimodal cavity size distribution but cavities of intermediate size (10-30 nm) were more profuse in the case of the 25SD irradiation.

The cavity size distributions in 20% cold-worked (CW) specimens are shown in Figure 4. The microstructures of the single- or dual-ion irradiated specimens at 5 dpa appeared nearly identical except for a few barely resolvable cavities in the 5D specimen. At 25 dpa, the 25D specimen contained no cavities larger than 8 nm. Small cavities ($\leq$ 3 nm) were profusely distributed and most, if not all, were associated with dislocations. The 25SD history produced, in addition to the high number of density of small cavities, a very low number density of cavities as large as 15 nm. Although the cavity volume fraction is low in both cases, it is higher for the 25SD specimen. The lack of helium at low dose seemed to enhance the swelling.

The dependence of the average cavity diameter in the SA, SAA, and CW specimens on irradiation damage is shown in Figure 5. The dependence for large and small cavit'ies on damage level is similar for the three differenct thermo-mechanical treatments prior to the irradiation. The average size of the small cavities ($-$3 nm) is independent of the dose. The average cavity diameter for large cavities increases with increasing total dose. The average large cavity size in the 25SD specimens are smaller than in the 25D specimens. The dependence of the cavity number density on irradiation dose is shown in Figure 6. The dependence of the number density on irradiation dose for large and small cavities is similar for SA, SAA, and CW materials. The large cavities have a rather strong dependence on dose without a saturation tendency, and the small cavities have a weak dependence on dose. The number density of small cavities in 25SD CW, SA, and SAA materials is slightly higher than for the dual-ion irradiated materials.

The average cavity volume fraction ($\Delta V/V$) that was computed from the average cavity diameters and cavity number densities in the SA, SAA and CW specimens is shown in Figure 7. The cavity $\Delta V/V$ data for SAA specimens that were obtained in this study are in good agreement with the previous data obtained by G. Ayrault, et al. [2]. The $\Delta V/V$ in SA specimens is lower than in SAA

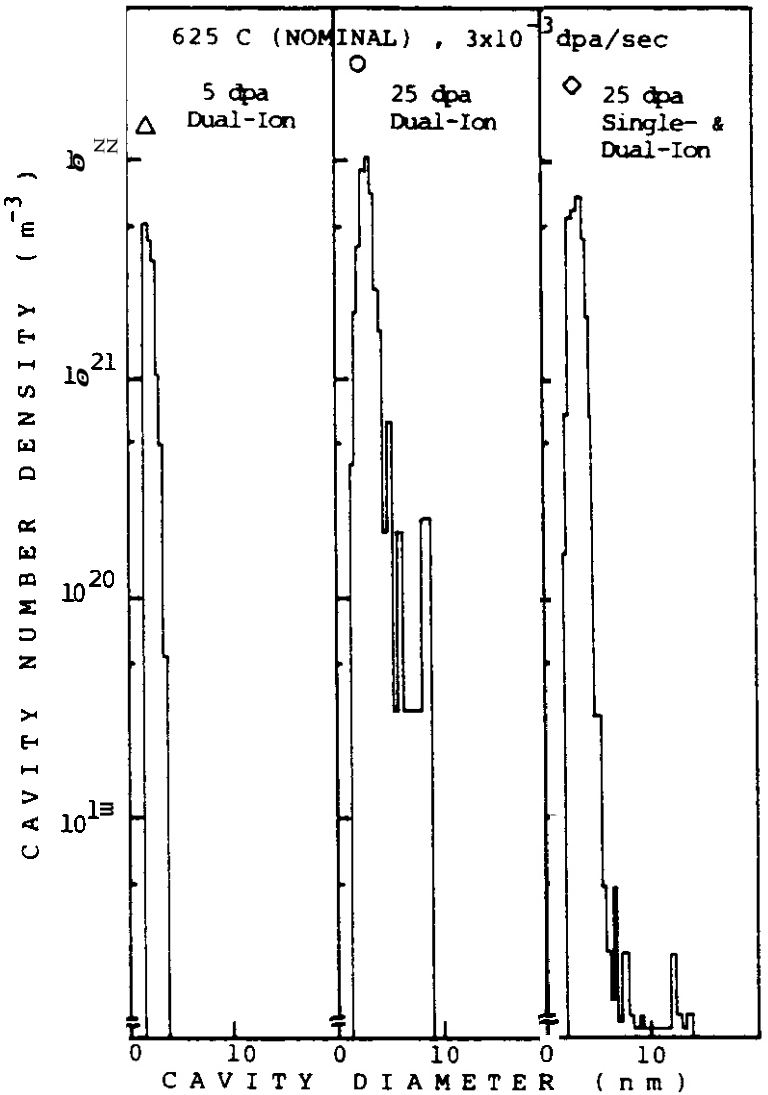

FIGURE 4 Cavity-Size Distribution in 20% Cold Worked Type 316 SS (open symbol-- average cavity diameter).

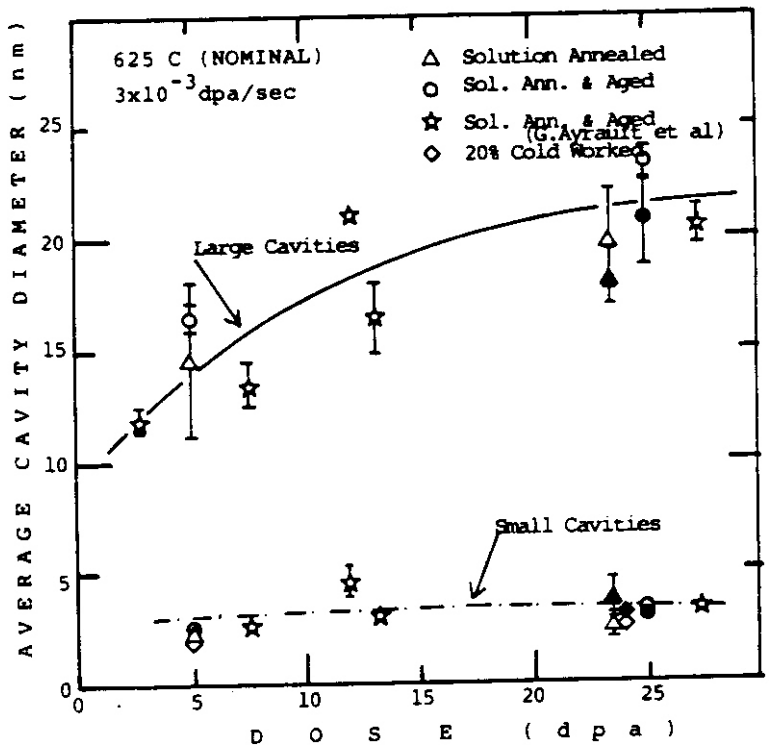

FIGURE 5. Dependence of Average Cavity Diameter on Irradiation Dose in Dual-Ion Irradiated (blank mark) and Single- Plus Dual-Ion Irradiated (filled mark) Type 316 SS.

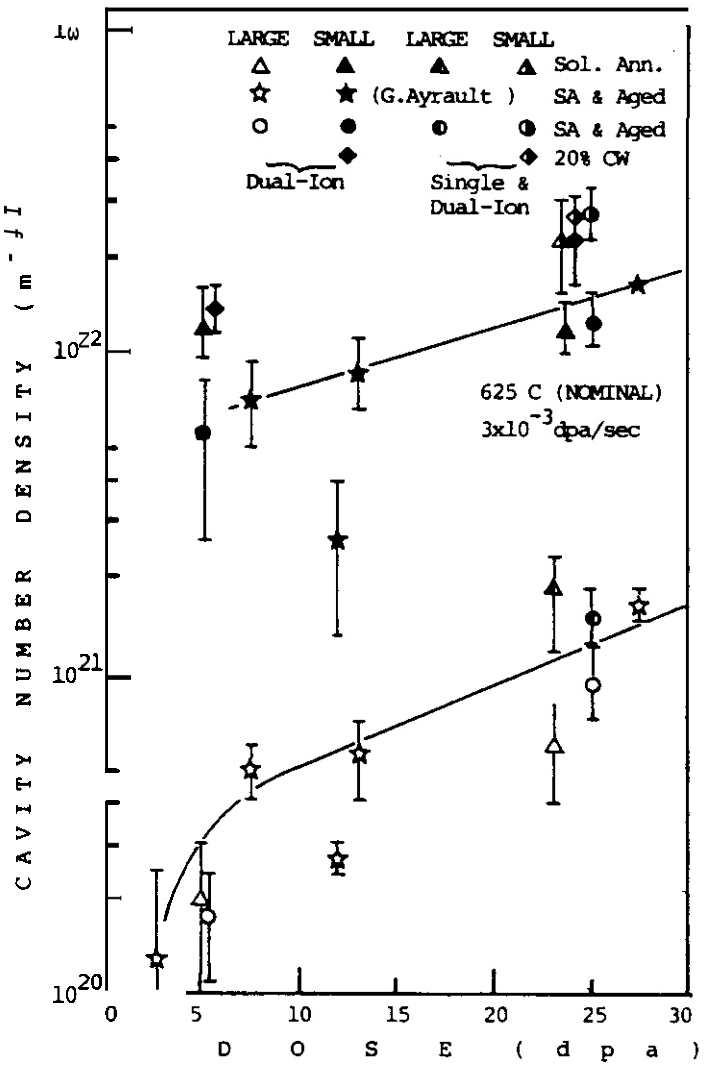

FIGURE 6. Dependence on Irradiation Dose of Cavity Number Density in Solution-Annealed Solution-Annealed and Aged, and 20% CW Type 316 SS.

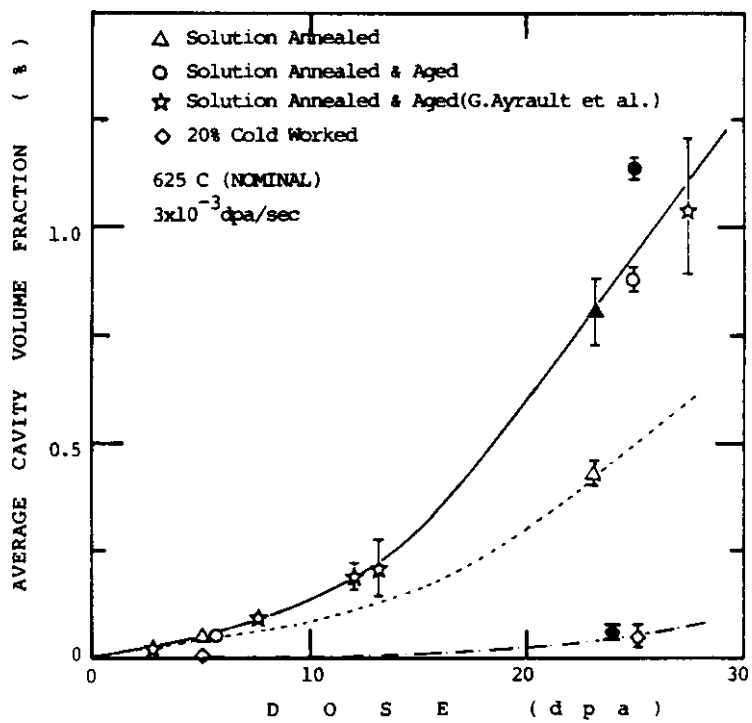

FIGURE 7. Dependence of the Average Cavity Volume Fraction in SA, SAA, and CW Type 316 SS on Dual-Ion (blank mark) or Single-Plus Dual-Ion (filled mark) Irradiation.

specimens because of a lower average cavity diameter of large cavities and a lower number density of large cavities. The average $\Delta V/V$ in the 25SD specimens is higher than the $\Delta V/V$ in the 25D specimens, especially for SA and SAA specimens. The higher number density of large cavities in the 25SD specimens in comparison with the 25D specimens for SA and SAA materials caused the higher $\Delta V/V$ in the 25SD specimens. These differences appear to have a close relation to the dislocation and precipitate density in these materials.

5.3.2 Helium Preinjection and Subsequent Irradiation Damage

The size distribution of cavities in SA, SAA and CW specimens that contained hot- or cold-preinjected helium and were single-ion irradiated to 25 dpa are presented in Figures 8, 9 and 10, respectively. For comparison with the dual-ion irradiation results, we have included the 25D results in each figure. The different helium injection procedure for the 25CP, 25HP and 25D specimens produced significantly different microstructures in specimens with different prior thermomechanical treatment. The cavity microstructures in either SA or SAA material were similar for a given helium injection schedule, but the microstructures of CW material were entirely different. There were very small cavities (1-2 nm diameter) which were very close to the visibility limit by TEM in 25CP or 25HP specimens of SA and SAA material. The number density of the large diameter cavities in the 25CP or 25HP material was significantly less than in the same materials following dual-ion irradiation. By careful observations of the small cavities, the size distributions of cavities were revealed to be bimodal in He preinjected samples of SA, SAA, and CW material. The average cavity diameters of large cavities in the HP, CP and D specimens were highest in 25HP samples and lowest in 25CP samples for SA and SAA material as shown in Figures 8-11. Dual-ion irradiation produced no large cavities in CW specimens (Figure 10), but 25HP and 25CP produced large cavities with a bimodal cavity size distribution (Figure 11). In the case of the average cavity size of small cavities, the helium preinjections caused the average cavity size to be very close to the visibility limit except for the 25HP sample of CW material. The dependence of the cavity number density on irradiation dose is shown in Figure 12. For both large and small cavities,

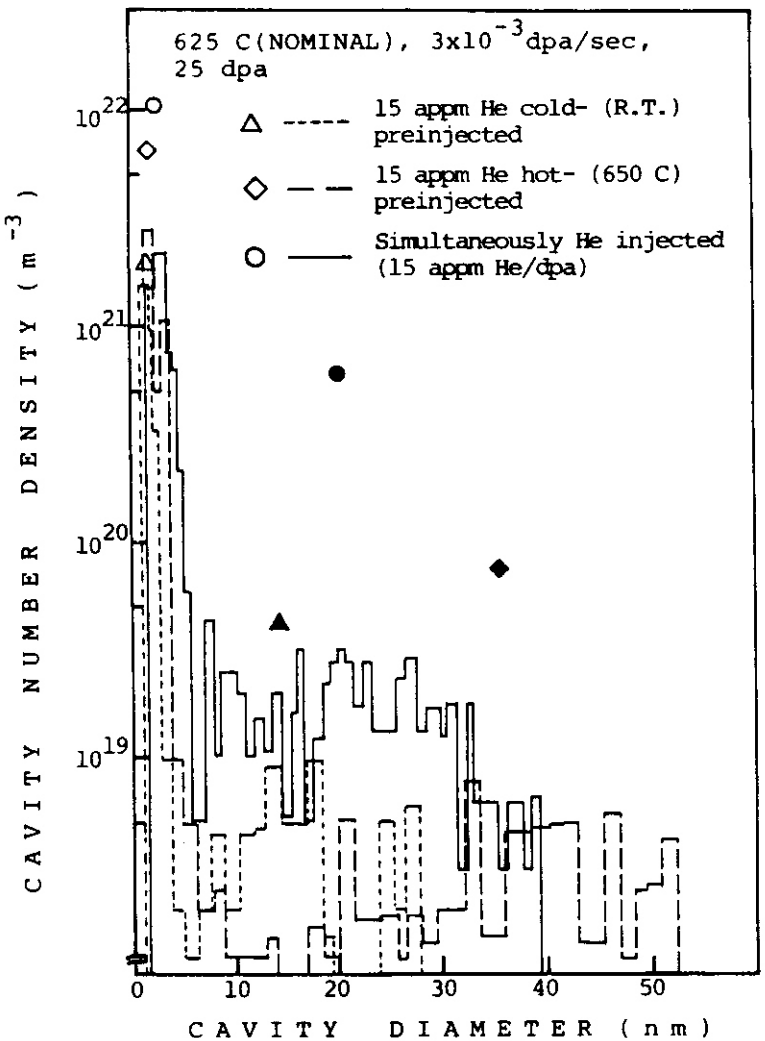

FIGURE 8 Size Distribution of Cavities in Solution-Annealed Type 316 SS. (Average cavity diameter: small cavities--open symbol, large cavities--filled symbol.)

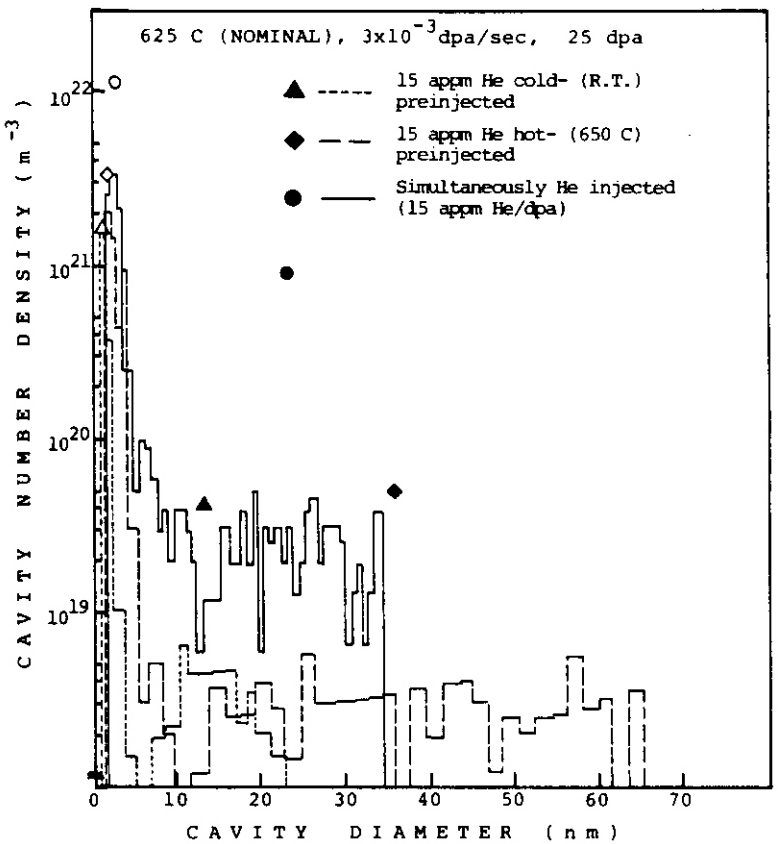

FIGURE 9. Size Distribution of Cavities in Solution-Annealed and Aged Type 316 SS. (Average cavity diameter: small cavities--open symbol, large cavities--filled symbol.)

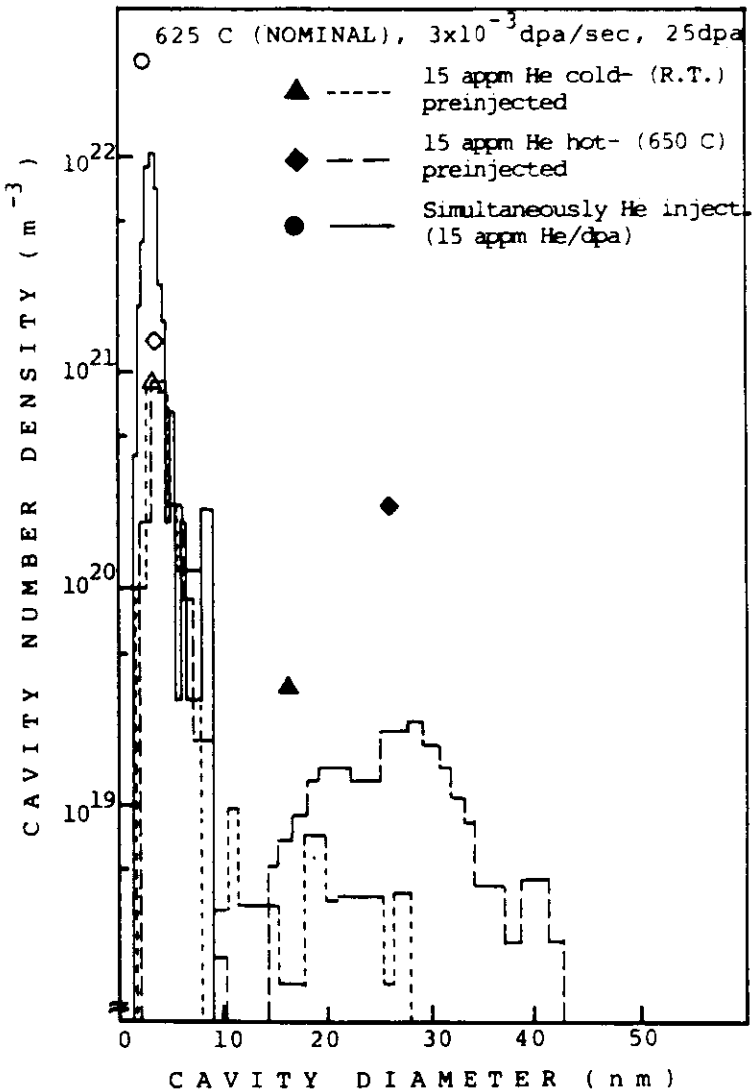

FIGURE 10. Size Distribution of Cavities in 20% CW Type 316 SS. (Average cavity diameter: small cavities--open symbol, large cavities--filled symbol.)

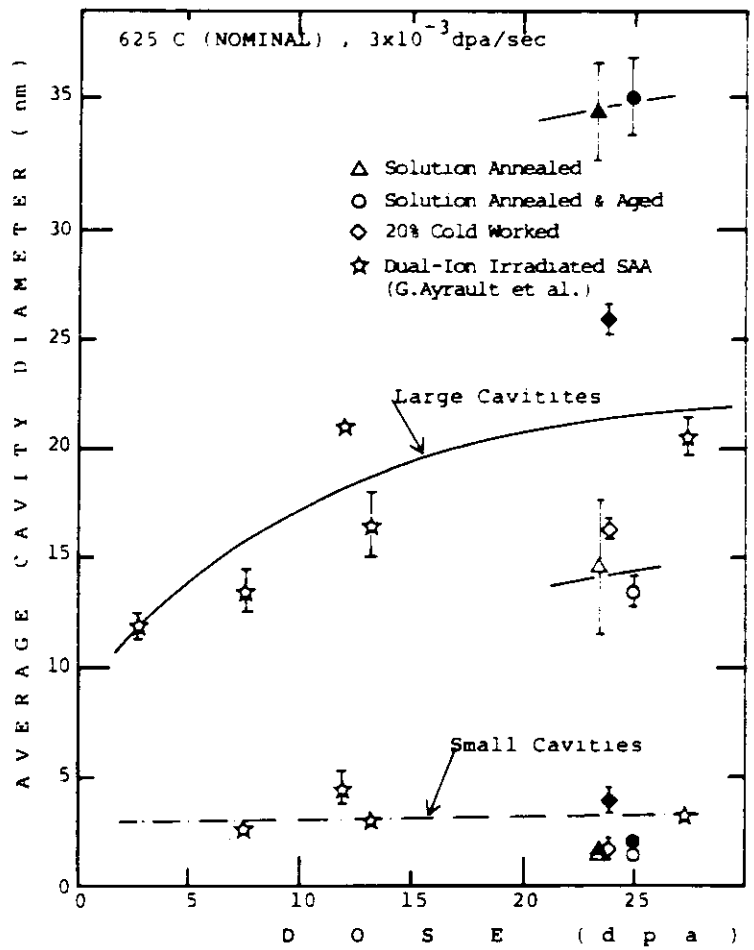

FIGURE 11. Dependence of Average Cavity Diameter on Irradiation Dose in Cold (Blank Mark) and Hot (Filled Mark) He Preinjected and Ion-Irradiated Type 316 SS.

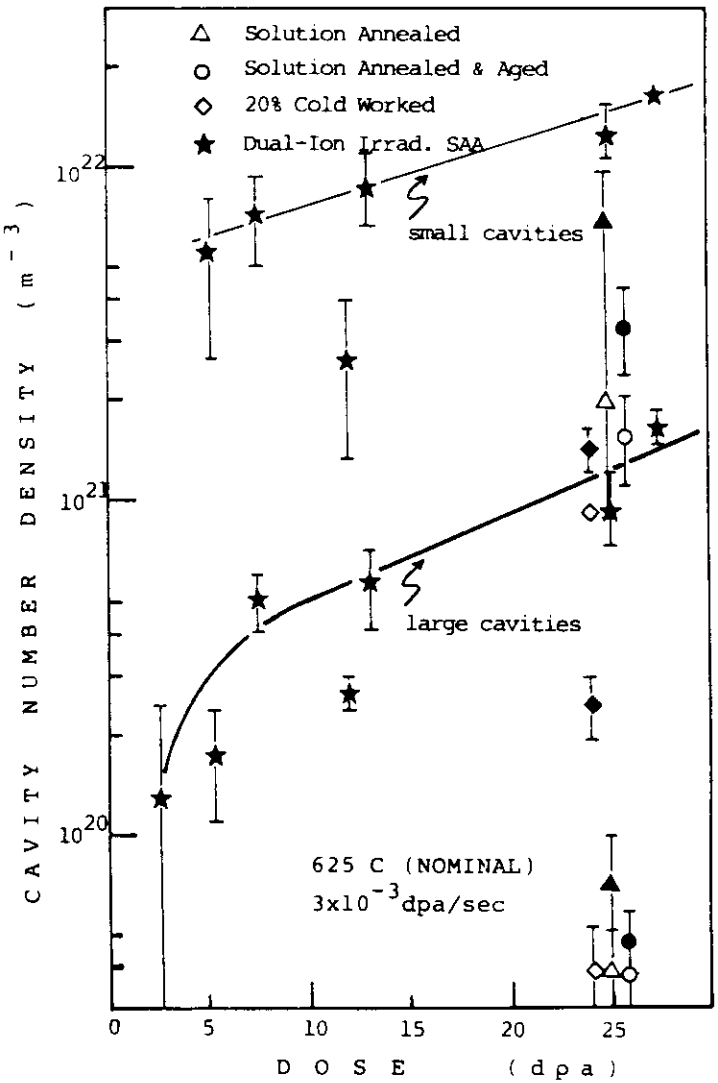

FIGURE 12. Dependence of Cavity Number Density on Irradiation Dose for Cold (Blank Mark) and Hot (Filled Mark) He Preinjected and Ion-Irradiated Type 316 SS.

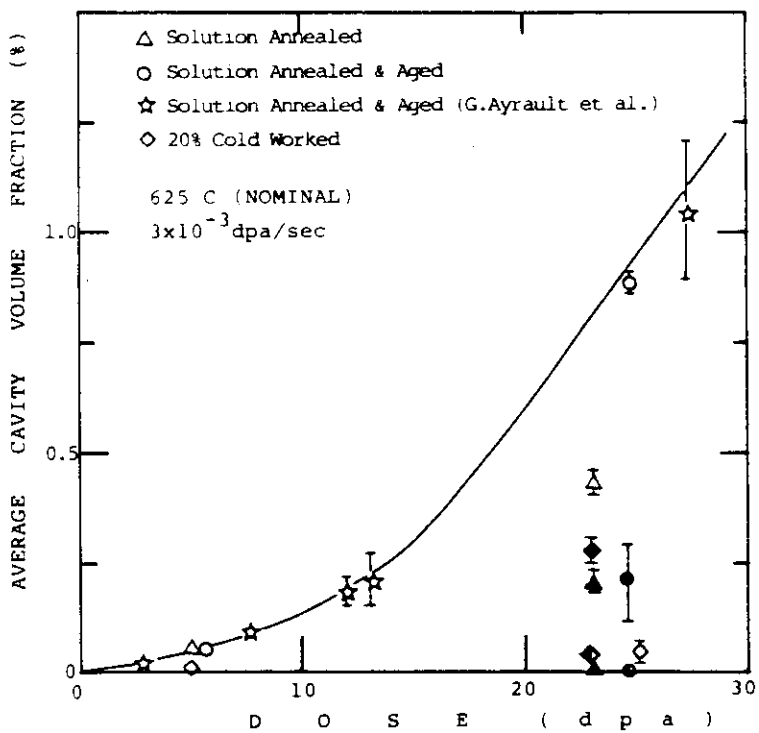

FIGURE 13. Dependence of Average Cavity Volume Fraction on Irradiation Dose for Hot (Filled Mark) and Cold (Half-Filled Mark) He Preinjection Followed by Ion Irradiation and for Dual-Ion Irradiation (Blank Mark) of Type 316 SS.

helium preinjection caused the cavity number density to be significantly lower than in dual-ion irradiated specimens. The cavity number density in 25HP specimens was higher than in 25CP specimens for both large cavities and small cavities in materials with the three prior thermomechanical treatments.

The dependence of the average cavity $\Delta V/V$ on irradiation dose for hot- and cold-helium preinjection followed by single-ion irradiation and for dual-ion irradiation is shown in Figure 13. Hot- and possibly cold-preinjection of helium enhanced the $\Delta V/V$ in cold-worked specimens relative to the $\Delta V/V$ obtained on dual-ion irradiation whereas the V/V in SA and SAA material was diminished. It can also be noted that V/V in hot- and cold-oreinjected, cold-worked specimens appears to be as high, or possibly even higher, than the V/V in preinjected SA or SAA samples. This unexpected result will require further investigation.

5.5 Discussion

The experimental results show that the helium effects on the microstructures of ion-irradiated Type 316 SS are strongly dependent on the thermomechanical treatment for the Type 316 SS prior to irradiation and on the schedule for helium implantation. These effects are shown by comparing the swelling for hot- and cold-preinjected helium, single-ion irradiated specimens and by comparing these results with the results obtained for dual-ion irradiated specimens. In the case of SA and SAA specimens, the swelling for the hot-preinjected helium specimens was larger than the swelling for the cold-preinjected helium specimens. The swelling for these hot- and cold-preinjected helium specimens (SA and SAA) was significantly less than the swelling for the dual-ion irradiated specimens. On the other hand, the hot-preinjection of helium in CW specimens caused swelling that was greater than the swelling for dual-ion irradiated, CW specimens. The swelling for the cold-preinjected helium, CW specimen was approximately the same or slightly less than the swelling for the dual-ion irradiated, CW material.

The microstructures for Type 316 SS resulting from single plus dual-ion irradiation (25SD) or from dual-ion irradiation (25D) were also strongly dependent on thermomechanical treatment and helium-injection schedule. In the case of SA and SAA materials, the swelling that was determined for the single plus dual-ion irradiated specimens (25SD) was significantly greater than the swelling for the dual-ion irradiated specimens. In the case of the CW material, the swelling was approximately the same for both schedules of irradiation. These results, i.e., results for 25SD and 250, may have a direct relationship to results that may be obtained from mixed-spectrum reactor and MFR irradiations of Type 316 SS.

6.0 References

1. A. Kohyama and G. Ayrault, OAFS Quarterly Report, No. 16, Oct.-Dec. 1981.

2. G. Ayrault, H. A. Hoff, F. V. Nolfi, Jr. and A. P. L. Turner, J. Nucl. Mater. 103 and 104, p. 1035, 1981.

7.0 Future Work

No future work on these materials is planned.

8.0 Publications

1. Z. Wang, G. Ayrault and H. Wiedersich, "Segregation in Irradiated Titanium Alloys", J. Nucl. Mater. 108 and 109, p. 331, 1982.

CORRELATION OF CHARGED PARTICLE AND NEUTRON-INDUCED RADIATION DAMAGE: THE ADIP EXPERIMENT REVISITED

F. A. Garner (Westinghouse Hanford Co.)

1.0 Objective

The purpose of this study is to explore the applicability of dual-ion bombardment studies to the development of fission-fusion correlations.

2.0 Summary

The successful conclusion of an intercorrelation program developed in the U.S. Breeder program has provided significant insight on the factors governing the swelling that develops in ion-bombardment studies and its relationship to the swelling that occurs during neutron irradiation. It appears that the injected interstitial or a related phenomenon exerts a pronounced influence on ion-induced swelling. This conclusion has ramifications with respect to the conduct and interpretation of ion irradiation experiments employed to study the effect of helium or composition on swelling.

3.0 Program

Title: Irradiation Effects Analysis (AKJ)
Principal Investigator: D. G. Doran
Affiliation: Westinghouse-Hanford Co.

4.0 Relevant OAFS Program Plan Task/Subtask

Subtask II.C.2 Effect of Helium on Microstructure

5.0 Accomplishments and Status

5.1 Introduction

The development of property correlations to predict material response in fusion devices is frequently complicated by one of two problems. First, there is often a total absence of data relevant to the material, property and environment of interest. Second, relevant data may be available but insufficient to yield an unambiguous correlation. A good example of the latter problem is the divergent predictions of the effect of large helium levels on swelling of stainless steels.[1-5]

One approach used to overcome these two problems is to employ ion bombardment experiments to provide insight on the role of helium or other fusion-relevant variables. The confident use of this approach requires that one assess the impact on the correlation of the shortcomings and trade-offs inherent in such accelerated simulation studies.[6-7] One particular area of concern involves the definition of equivalent exposures and irradiation conditions. Does the exposure parameter designated as displacements per atom (dpa) adequately account for differences in primary recoil spectra? If so, what temperature and how many displacements per atom (dpa) for a given charged particle represent an adequate simulation for a certain level of neutron exposure at some lower temperature and displacement rate? This question becomes particularly important when defining the helium/dpa ratios and total damage levels required in ion bombardment experiments to assess the effect of helium on swelling.

This paper reaches back to one of the major experimental studies conducted to address these concerns, compares the published results with more recent data, and draws conclusions concerning the relative equivalencies of the neutron and charged particle environments. The impact of these conclusions on the interpretation of the influence of helium on swelling is then discussed. The implications of these conclusions on the influence of compositional variations are also discussed, particularly with respect to the relative importance of helium and composition.

5.2 The ADIP Intercorrelation Experiment*

In 1976 the results were published of the first phase of an ambitious national intercorrelation experiment designed to answer questions relevant to the simulation of fast reactor neutron damage using charged particles.[8] Designated the Alloy Development Intercorrelation Program (ADIP) experiment, it involved the comparative irradiation by six American laboratories of a simple well-characterized alloy (Fe-15Cr-25Ni). Irradiation was conducted using fast neutrons in the EBR-II reactor, 1.0 MeV-electrons, 0.75-MeV protons and nickel ions at three incident energies, 2.8, 3.5, and 5.0 MeV. While this report will concentrate primarily on comparisons between the neutron and nickel ion results, the major experimental details for all ADIP irradiations are listed in Table 1. Six appm of helium had been uniformly implanted in all charged particle specimens at room temperature prior to irradiation. No helium was preinjected into the EBR-II specimens.

The Phase I ADIP report[8] established "dose equivalencies" by requiring steady-state swelling rates for all bombarding species to be identical. At that time, however, the neutron data had not exceeded 14 dpa or 1% swelling, and the definition of dose equivalency for neutrons was deferred until higher fluence data became available. Nickel ions at all three incident energies were found to create swelling in the steady-state regime at essentially the same rate per dpa, although the duration of the transient regime of swelling was somewhat variable for the three ion energies. Electrons at 1.0 MeV were found to be approximately six times more effective per calculated displacement than nickel ions in creating swelling and 0.75-MeV protons appeared to be roughly twenty times more effective than 1.0-MeV electrons.

*The ADIP experiment predates the formation of the Alloy Development for Irradiation Performance task group of the U. S. Fusion Materials Program. The two "ADIP" activities are not related to each other.

TABLE 1

MAJOR EXPERIMENTAL DETAILS+ OF ADIP PHASE I EXPERIMENT

Laboratory	Particle	Displacement Rate (dpa/sec)	Data Extraction Technique
Atomics International	0.75 MeV p^+	2×10^{-4} (nominal)	1.5 - 3.5 μm TEM, sectioning
General Electric+	5.0 MeV Ni^+	2×10^{-2}*	TEM, section at peak dose
Westinghouse Hanford	1.0 MeV e-	2.1×10^{-3} (E_d = 40 barn)	Uniform displacement profile, HVEM stereomicroscopy
	EBR-II neutrons	1.0×10^{-6}	TEM
Naval Research Laboratory	2.8 MeV Ni^+	2.0×10^{-2}*	TEM, section at peak dose
Westinghouse Advanced Reactor Division	3.5 Mev Ni^+	5×10^{-3}*	HVEM full-range stereomicroscopy

*Measured at peak displacement rate.
†Six appm He uniformly implanted in all specimens.
+Two GE laboratories were involved, the Metallurgy and Ceramics Laboratory in Schenectady, NY, and the Breeder Reactor Department in Sunnyvale, CA.

There were two other important objectives of the ADIP experiment. One was to assess the validity of using the dose equivalencies derived from this experiment to predict swelling behavior in neutron environments. The other was to determine the impact on these predictions of using different data extraction procedures. This latter consideration will be shown in this paper to be quite important to our current objectives of simulating the effect of helium on swelling in the fusion environment and determining the effect of compositional variations on swelling in any reactor.

5.3 Review of ADIP Nickel Ion Data

The ion studies were conducted at 600, 650, 700 and 750°C, a range determined from earlier studies on related alloys by Johnston and coworkers at General Electric Corporation (GE) to cover the peak swelling regime at the accelerated displacement rates employed in this study.[9] It is important to note that in the original ADIP study only two of the three major data extraction techniques were employed. Both were microscopy techniques. One examined the swelling near the peak damage region of a number of specimens at different total ion exposures and the other used only one specimen at one ion exposure, extracting the dose dependence using full-range stereomicroscopy.[10] The third technique is the measurement of the integrated swelling along the ion path by the step-height technique.[11] This technique was employed in earlier studies of various structural steels as well as a range of Fe-Ni-Cr ternary alloys.[9] Step-height measurements were not employed in the ADIP experiment, but were utilized in some post-ADIP studies described in this report.

The full-range stereomicroscopy technique was employed by researchers at Westinghouse Advanced Reactors Division (WARD) on specimens irradiated with nickel ions at the intermediate energy of 3.5 MeV. Figures 1 and 2 present a condensation of these results, reported in more detail in Reference 12. Note that the incubation period is quite sensitive to irradiation temperature in the 600-750°C range but that the steady-state swelling rate is not. It is also important to note that the incubation exposures

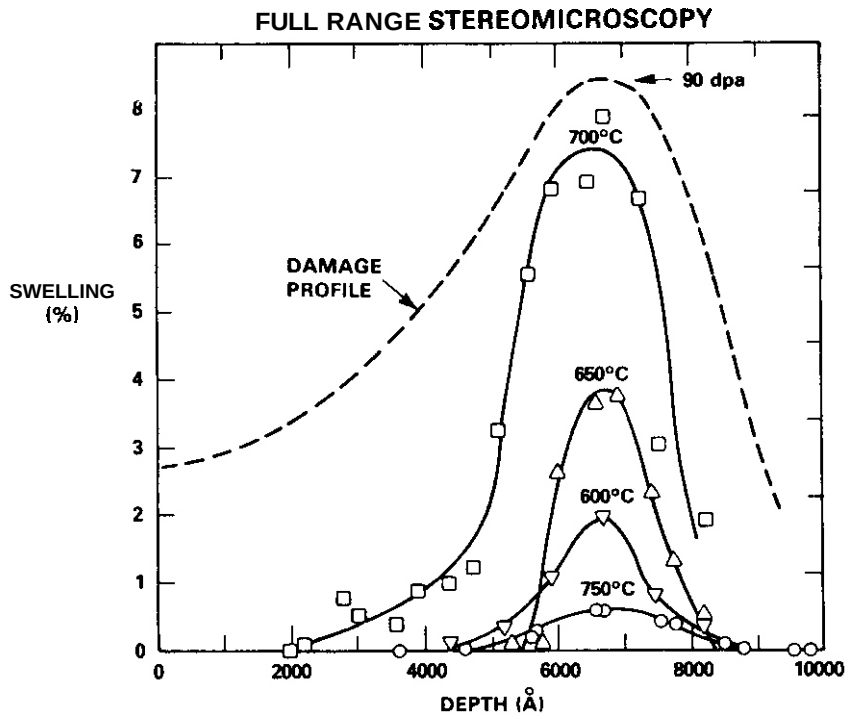

FIGURE 1 Comparison of Damage Profile Curve and Swelling Determined at 90 dpa by Diamond and Coworkers for the ADIP Alloy.(12)

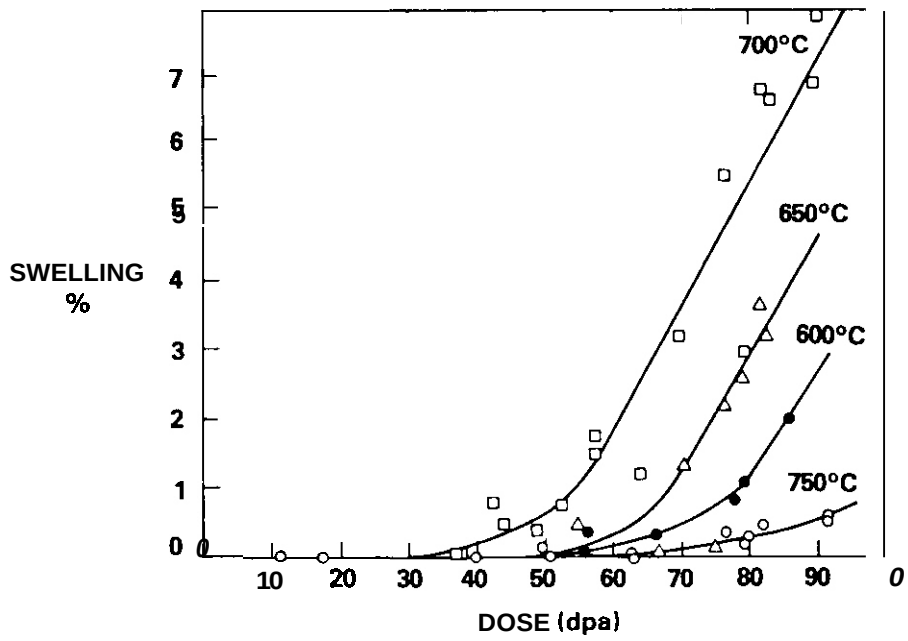

FIGURE 2. Swelling vs Dose Profiles for the ADIP Alloy, Derived From Figure 1.(12)

are all greater than 40 dpa. The significance of this observation arises from the fact that the two other ion irradiation studies consistently had shorter (and usually equal) incubation periods, as shown in Figure 3. There was, therefore, swelling along a greater portion of the ion range in the 2.8- and 5.0-MeV specimens, but the near-surface material was removed during specimen preparation. Thus the full-range technique, which had the potential for assessing swelling along the entire ion path, was not applied to a specimen where swelling existed near the incident surface of the specimen. As will be shown later, this was an unfortunate circumstance.

The consistently longer incubation period for the 3.5-MeV WARD experiment as compared to that of the 2.8-MeV and 5.0-MeV experiments was ascribed in the ADIP Phase I report to differences in pre-irradiation preparation of specimen surfaces. The softness of these alloys and the ease of introducing near-surface dislocations had been investigated in the program and was thought to affect the duration of the transient regime of swelling. It now appears that another explanation is more appropriate. Note in Figure 3 and Table 1 that the WARD irradiation proceeded at a calculated peak displacement rate that was one-quarter of that employed at the other two ion energies. The longer irradiation period probably reflects the additional difficulty of nucleating dislocation loops and voids at high temperature in competition with the influence of the surface on point defect populations.

This possibility appears to be confirmed in a post-ADIP exercise in which the WARD researchers analyzed the highest swelling (8%) Naval Research Laboratory (NRL) specimen at 700°C by full-range analysis using a thicker portion of the foil. As demonstrated in Figures 3 and 4, the analysis shows that the higher exposure portions of the full range data lie on the extrapolated NRL-GE curve while the lower exposure and displacement rate data lie toward the WARD curve. This strongly suggests that the incubation period at any depth is sensitive to displacement rate in a relatively reproducible manner.

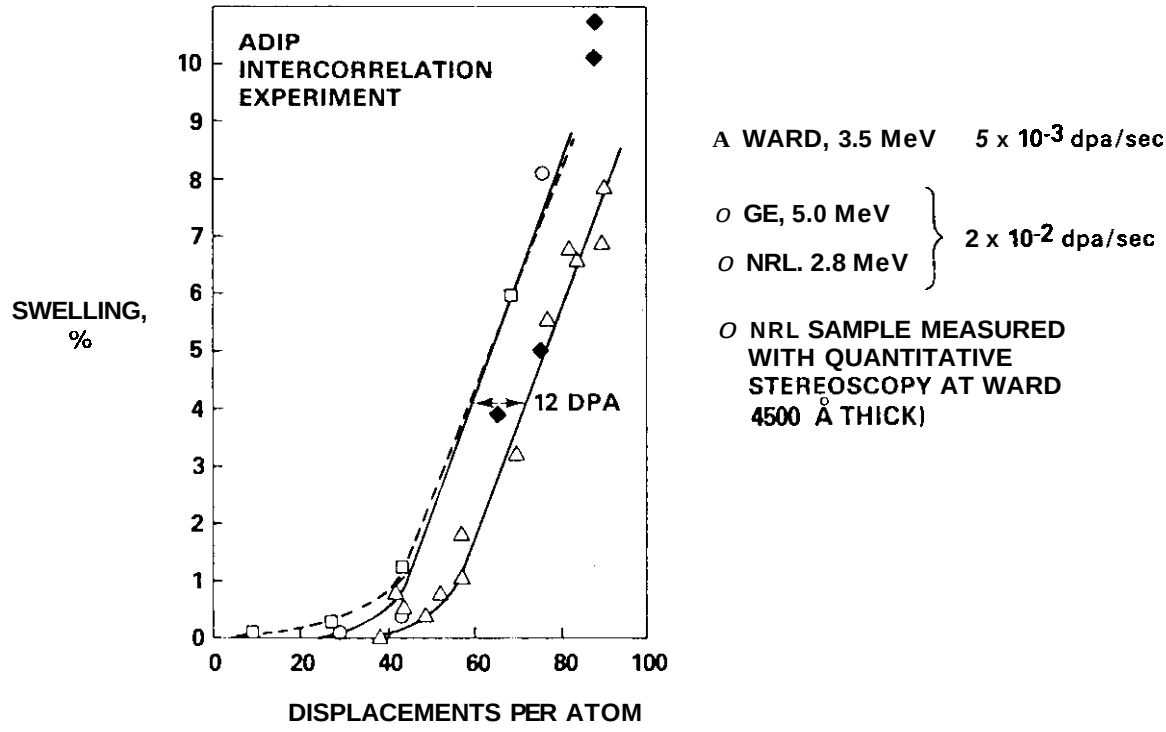

FIGURE 3. Comparison of Ni^+ Ion-Induced Swelling of the ADIP Alloy at 700°C as Measured by Three Laboratories, Each Using a Different Incident Energy.[8] The lower displacement rate employed by WARD researchers caused an increase in the incubation period of roughly 12 dpa.

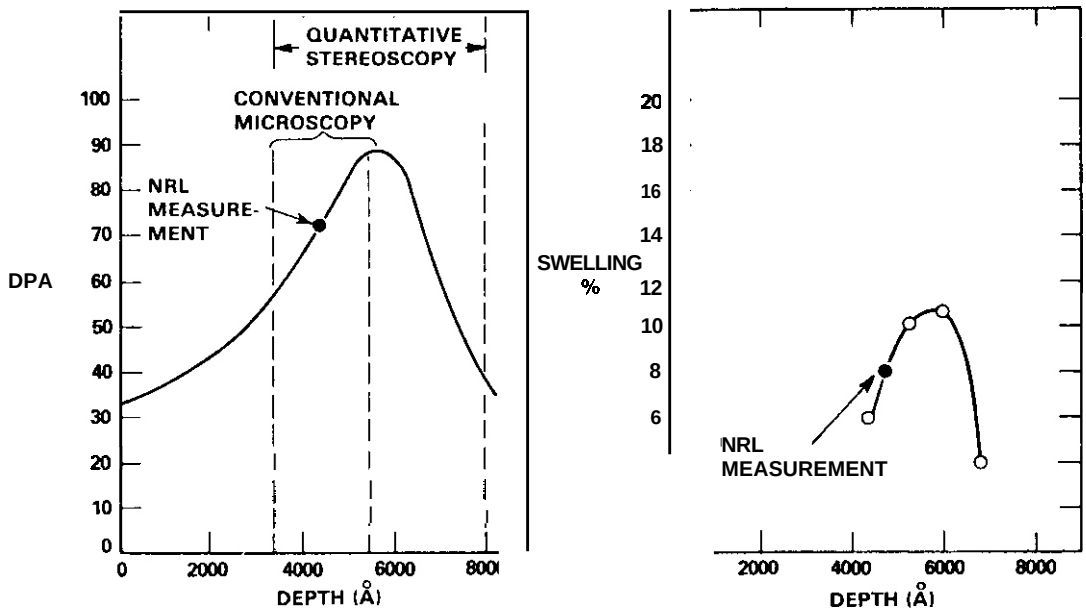

FIGURE 4. Comparison of Data Extraction Techniques and Swelling Results Obtained by NRL and WARD on a Single ADIP Specimen at 700°C.[8] The WARD researchers used full range stereomicroscopy while the NRL researchers used microscopy in the region on the front of the displacement peak.

The uniformity of the post-incubation swelling rate at 0.2%/dpa in all three ion irradiations was quite satisfying to the researchers involved, particularly since the three techniques covered a range of ion energies, penetration depths, displacement rates, specimen preparation methods and data extraction procedures. There was, however, one unsettling and unresolved set of data whose significance was not fully realized in the ADIP and post-ADIP studies. Note in Figure 5 that the ADIP data, when extrapolated to 115 dpa, would lead to a prediction of 12-15% swelling in the range 650-700°C. Data published earlier on an extensive study of Fe-Ni-Cr ternary alloys at the intermediate temperature of 675°C would predict a swelling level at 115 dpa of about 45% for the ADIP alloy. While the three ADIP studies are internally consistent, they differ from the prediction of the earlier studies by roughly a factor of three. In fact, it is impossible to reach approximately 45% swelling at 0.2%/dpa by 115 dpa even in the absence of an incubation period. This lack of agreement conflicts with the degree of consistency and reproducibility shown by the simple ternary alloys, and by comparative irradiations of 316 stainless steel at Oak Ridge National Laboratory and two different GE installations.[9] This latter comparison will be shown later in Figure 9c.

In order to assess the origins of this apparent discrepancy the original Phase I alloy, designated €20, and a related alloy, E19 (FE-15Cr-20Ni), were prepared by Johnston and coworkers in the same manner as employed for the earlier GE studies and irradiated to 115 dpa at 675°C. As is also shown in Figure 5, both the ADIP and E19 alloys developed swelling consistent with the earlier GE studies rather than with the ADIP studies.

In the original ADIP Phase I report it was proposed that the divergent behavior of the ADIP alloy may have been due to the different specimen preparation techniques employed in each study. (In unpublished post-ADIP studies Johnston showed that the behavior did not arise from differences in helium or oxygen content that might have occurred during specimen preparation.) It will be shown that this interpretation was wrong and that the discrepancy arose because the two studies did not use the same measurement technique for

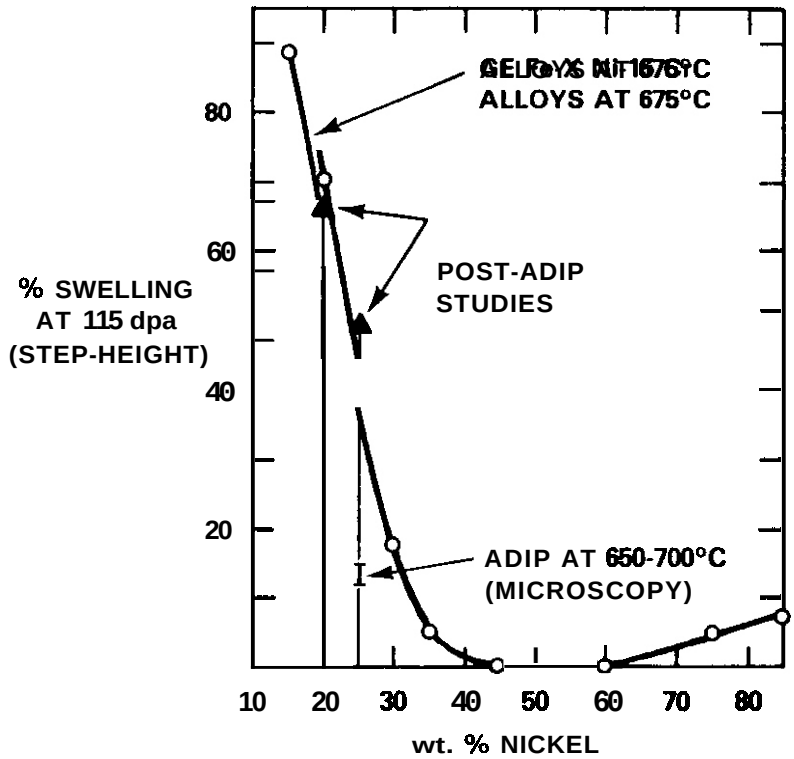

FIGURE 5. Comparison of Swelling Measured by Various Techniques in the ADIP Alloy, GE Ternary Alloy Series and the Alloys E19 and E20. The latter is the ADIP alloy prior to specimen preparation. All measurements except that labelled ADIP are by step-height measurement.

swelling. It also will be shown that step-height and peak microscopy measurements are not equivalent measurements for alloys with relatively short incubation periods.

5.4 Summary of Neutron Data for the ADIP Alloy

The ADIP alloy was irradiated in EBR-II in sodium-filled subcapsules in the form of small disks suitable for both microscopy and immersion density measurements. Neutron exposures have been accumulated to levels as large as 12 x 10^{22} n/cm^2 (E > 0.1 MeV) for temperatures of 400, 427, 454, 482, 510, 538, 593 and 650°C. The swelling values measured by immersion density are presented in Figure 6 and show that, for the five irradiation temperatures spanning the range 400-510°C, the swelling rate, as well as the total swelling, is quite independent of temperature. At 538°C the incubation or transient regime of swelling is longer but the steady-state swelling rate is eventually identical at 5%/ 10^{22} n/cm^2 (E > 0.1 MeV).

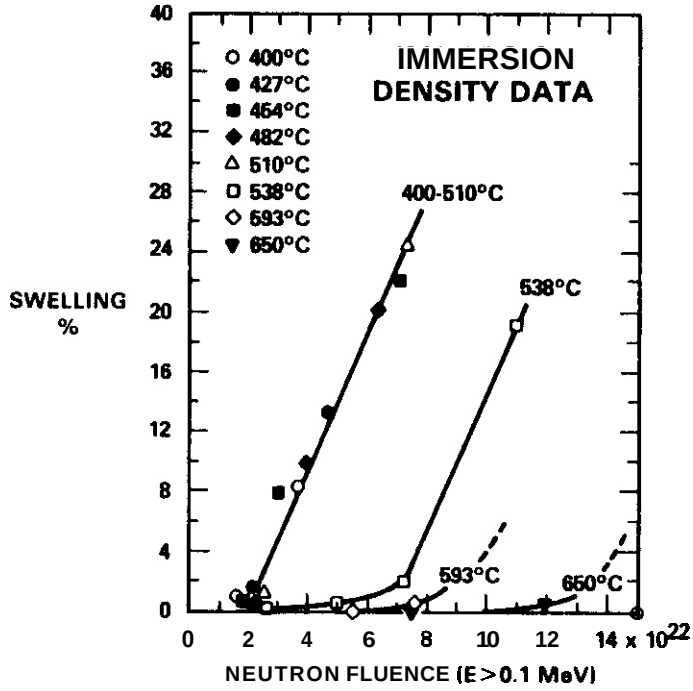

FIGURE 6. Swelling of ADIP Alloy in EBR-If in the Range 400-650°C, as Measured by Immersion Density.

The transient regime *of* swelling continues to increase in duration with temperature above 538°C. Insufficient fluence has been accumulated at 593 and 650°C to make any estimate of the eventual steady-state swelling rate. Comparisons with the behavior of neutron-irradiated ternary alloys having a lower nickel content imply, however, that the steady-state swelling rate at these higher temperatures will eventually be the same as that observed at lower temperatures.

For the neutron spectra of the EBR-II experiment, the swelling rate of $5\%/10^{22}$ n/cm^2 (E > 0.1 MeV) is equivalent to 1.0%/dpa. Thus the peak swelling rate per calculated dpa is five times larger than that of the ADIP nickel ion irradiation experiments.

As shown in several recent reports[13,14] a relatively temperature-independent value of 1%/dpa is typical for neutron irradiation of a wide variety of austenitic solution-strengthened alloys with nickel contents below 35%. It is also interesting to note that Farrell and Packan determined that, on the basis of total swelling rather than swelling rate, 4.0-MeV

nickel ions are only one-third as effective as EBR-II neutrons in creating swelling in a simple Fe-17Cr-16.7Ni-2.5Mo-0.005C alloy.[15]

We are, therefore, presented with clear experimental evidence from the ADIP and Farrell-Packan studies that nickel ion irradiation is less effective in creating swelling than is neutron irradiation. This difference in effectiveness is too large to be rationalized in terms of either the uncertainties in nuclear and electronic cross sections or differences in cascade sizes and displacement distribution within the cascade. As will be shown shortly, however, the conclusion of reduced effectiveness of nickel ions is subtly misleading. It is proposed here that nickel ions are as effective in creating swelling per calculated dpa as are neutrons, providing some large perturbation of which we are unaware does not intervene. That perturbation has been identified and appears to be something related to the injected interstitial effect.

5.5 Review of Other Ion Bombardment Data

The failure of the ion-irradiated ADIP alloy to produce the same swelling results when measured with step-heights or with microscopy at the peak damage region is directly related to the factor of five difference found in dose equivalency between neutrons and ions. In each case, the cause of the discrepancy is that the swelling rate measured near the peak displacement position for nickel ions is depressed by a factor of roughly five compared to the swelling rate in front of the region where the nickel ions come to rest.

Johnston and coworkers derived an empirical correlation factor of 60Å step height per percent swelling at the displacement peak.[11] Garner and coworkers showed how such a correlation might arise assuming swelling was proportional to the displacement level and the incubation period was relatively small.[16] Unfortunately, Johnston's correlation was established using stainless steels with relatively long incubation periods. The lower displacement level accumulated near the front surface of the specimens, therefore, should have caused little or no swelling in these regions. In

later work, however, Johnston noted that in many specimens substantial and unexpected amounts of swelling were obtained in the region 0.1 to 0.5 μm from the surface.[17-19] This was designated "excess subsurface swelling" and was often " more than five times as great as would be seen for the same dpa in the peak damage region for 5 MeV Ni^{+} ions."[18] The origin of this phenomenon was first attributed [17] to the "internal temperature shift" proposed by Garner and Guthrie.[20] It was later attributed at least partially to the influence of composition change along the ion range produced by radiation-induced segregation.[18] Figure 7 shows two typical examples of the "excess subsurface swelling" found by Johnston and coworkers.

If the empirically derived *60* Å/% swelling conversion factor was developed from specimens having little swelling near the front surface and suppressed swelling at the peak, one might expect that this conversion factor would not be applicable for cases where swelling was occurring thoroughout the ion range. This latter condition is most easily met by pure metals such as nickel or ternary Fe-Ni-Cr alloys without significant solute content.

The inapplicability of 60 Å/% as a universal factor can be demonstrated in several ways. If we assume that the irradiated metal is attempting to swell at a neutron-representative rate of 1%/dpa at the front surface and 0.2%/dpa at the peak displacement region, then one would expect an intermediate swelling rate when measured by step-heights. How close the intermediate value falls toward either the 0.2%/dpa or the 1%/dpa values depends on the magnitude of the dpa level at the peak relative to the incubation fluence. Figure 8 shows an excellent example of the fact that microscopy measurements at the peak and step-height measurements can agree and still yield a swelling rate of 0.7%/dpa for a case where substantial subsurface swelling is occurring.[21] Figure 9 contains three data sets showing intermediate swelling rates ranging from 0.45 to 0.7% when the swelling is determined by step-height measurements.[22,23] Note that the Fe-15Cr-20Ni Alloy shown in Figure 9b is the ADIP alloy which was found to swell only 0.2%/dpa at the peak.

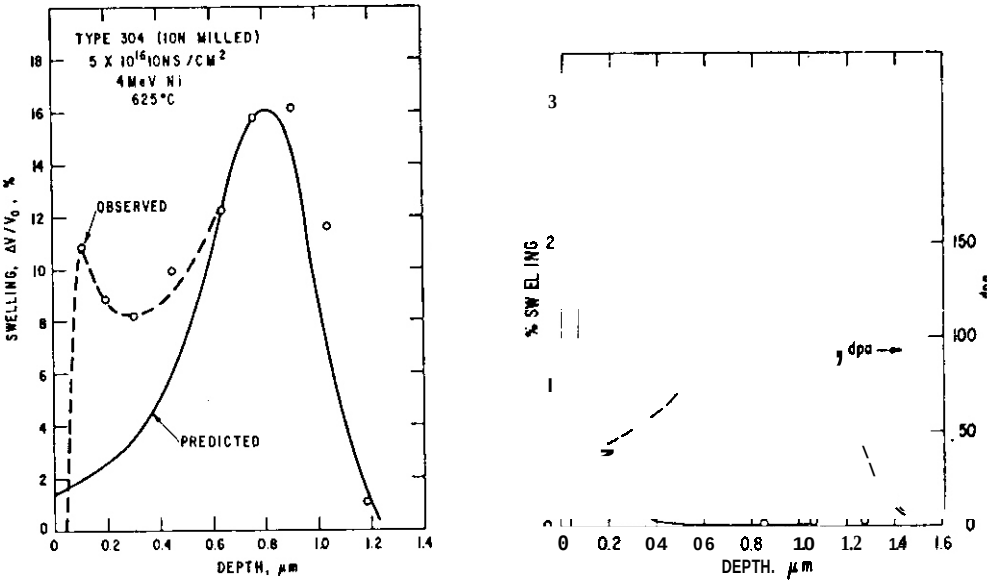

FIGURE 7. Examples of "Excess Subsurface Swelling" Drawn From Work of Johnston and Coworkers. (17,18)

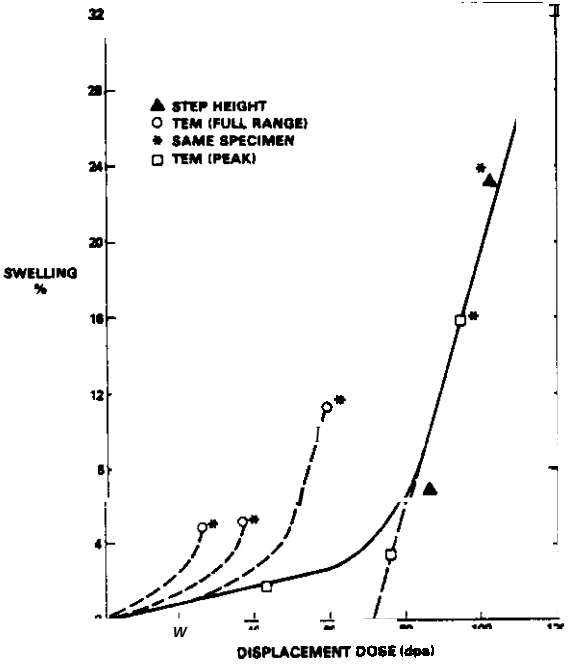

FIGURE 8. Comparison of Step-Height, Full-Range and Peak Microscopy Determinations of the Swelling vs dpa Behavior of Annealed AISI 316 Irradiated with 4-MeV Ni^+ Ions at 625°C. (Courtesy of T. Lauritzen)

Figure 9 also demonstrates another very important point. The foregoing discussion leads to the conclusion that, as the incubation period increases, the applicability of the 60 Å/% factor increases and the integrated average swelling falls toward 0.2%/dpa. The slowly decreasing slope observed for increasing nickel or silicon is therefore only an artifact of the competing phenomena of sub-surface swelling and peak suppression effects. Soon-to-be published neutron data show that nickel and silicon levels affect only the duration of the transient and not the steady-state swelling rate.

Another way to demonstrate the nonuniversality of the 60 Å/% factor is to directly measure step-heights and peak swelling for a variety of alloys. Note in Figure 10 that 60 Å/% was not observed for the ADIP alloy, pure nickel and Fe-37Cr-44Ni indicating very large subsurface swellings. The value of 60 Å/% appears to be valid only for alloys in which there are both long incubation periods and large peak swellings. Another example of this type of data is shown in the next section.

5.6 Clues to the Nature of the Suppression Phenomenon

There are four additional sets of ion data which provide both a confirmation of the suppression effect and provide clues concerning its origin. The first involves the bombardment with 4-MeV nickel ions of solution-annealed AISI 316 which had been previously irradiated to 40 dpa in EBR-II at several temperatures, developing 2-4% voidage. For each neutron irradiation temperature three ion irradiation temperatures were chosen to study the effects of displacement rate and temperature shift. Note in Figure 11a that the step-height conversion factor is always greater than 60 Å/%. This is exactly what one would expect when the incubation period is already essentially over. Note also in Figure 11a that the conversion factor increases strongly with decreasing temperature for the previously neutron irradiated specimens.

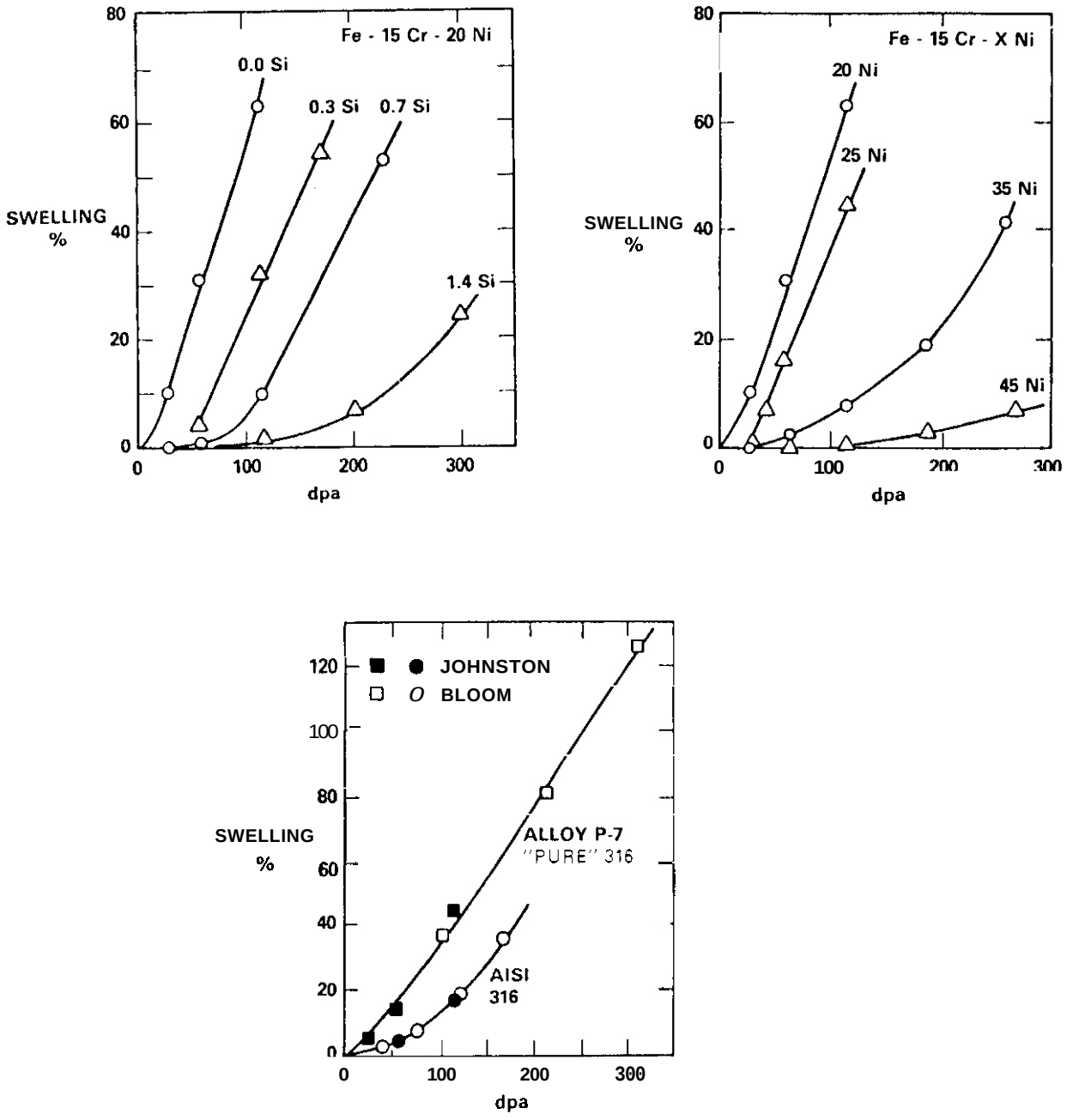

FIGURE 9. Determinations of Swelling as a Function of Composition and Displacement Dose in Ni^+ Irradiated Fe-Ni-Cr Alloys by Step-Height Measurements.[9,22,23] The solid squares in the bottom figure represent previously unpublished data supplied by W. G. Johnston. Squares represent 5 MeV Ni^+ ion data at 625°C while circles represent 4-MeV Ni^+ data at 635°C.

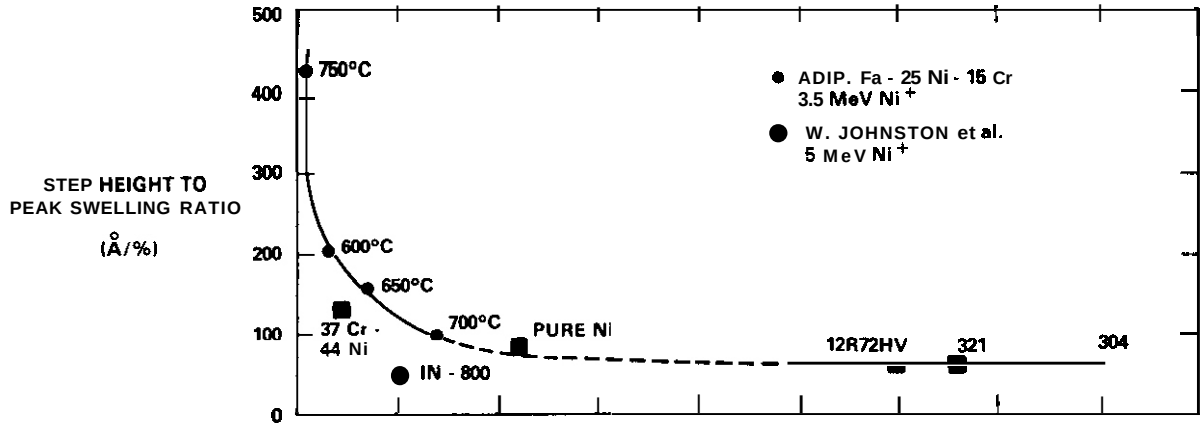

FIGURE 10. Ratio of Step-Height to Swelling at the Peak Determined for a Variety of Alloys.(24)

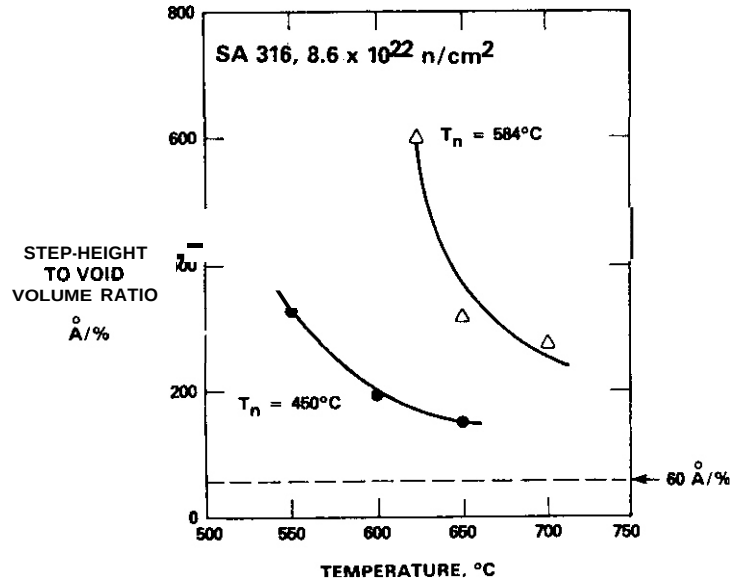

FIGURE 11a. The Influence of Injected Interstitials on Ion-Induced Swelling and Step-Height Measurements in Neutron-Preirradiated Solution-Annealed AISI 316, as Published by Lee and Coworkers.(25) T_n is the neutron irradiation temperature.

Figure 12 shows the additional ion-induced swelling along a portion of the ion path for two separate neutron/ion irradiations reported by Lee and coworkers.[25] The suppression of swelling at the peak displacement portion of each specimen is very pronounced. The attainment at this position of only 2% swelling for 60 ion-induced dpa implies a very low average swelling rate of about 0.03%/dpa. This suggests that the swelling rate may be vanishing, leading to an eventual saturation of swelling at this position. Rowcliffe, Lee and Sklad indeed reported that saturation occurred in these studies for a variety of ion irradiation temperatures.[26]

The clues drawn from this experiment are that the suppression phenomenon affects the swelling rate beyond the transient regime, exerts its maximum influence where the injected ions come to rest, and is very sensitive to temperature. Based on this evidence, Lee and coworkers felt that the suppression was caused by the injected interstitials.[25]

The second set of data represents an extension of the first set. Portions of the results have been published in References 26 and 27 and a few additional unpublished data have been supplied by T. A. Lauritzen and A. F. Rowcliffe. Note in Figure llb that step-height measurements on the same heat of steel shown in Figure lla (but without prior neutron irradiation) show no substantial amount of enhanced subsurface swelling and no dependence on ion irradiation temperature. This is consistent with the behavior expected when the incubation period of swelling is a large fraction of the accumulated ion exposure.

Note also in Figure llb that the relative amount of subsurface enhancement increases with ion exposure as would be expected for previously neutron-irradiated material where the incubation period is effectively over before the ion irradiation proceeds. It should also be noted that the enhancement does not decrease continually with increasing temperature as suggested by the more limited data in Figure lla.

If the suppression of swelling by injected interstitials can be 80% or more, why not 100%, or even dissolution of preexisting voids? The latter

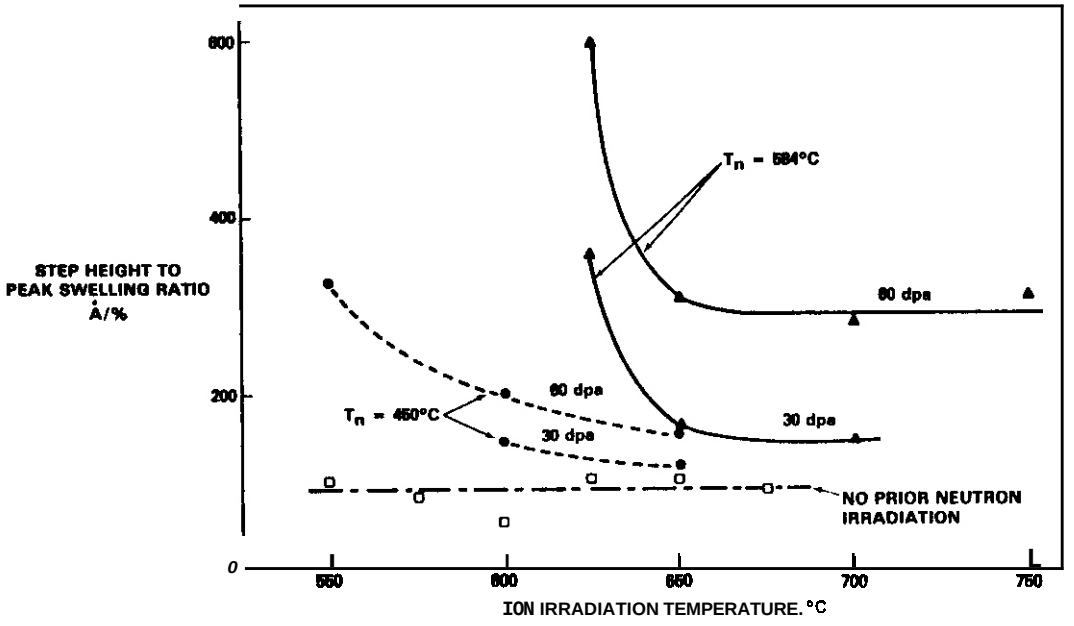

FIGURE IIb. Additional Data From Experiments Described in References 25-27, Supplied in Advance of Publication by T. Lauritzen of General Electeric Corp. and A. F. Rowcliffe of Oak Ridge National Laboratory.

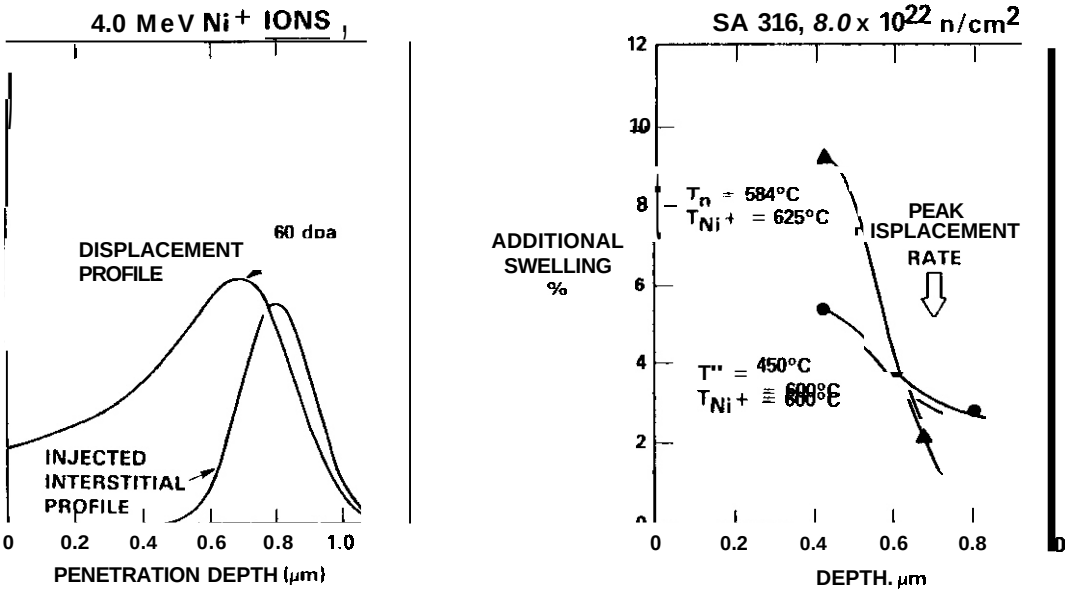

FIGURE 12. (a) Schematic Representation of Displacement and Injected Interstitial Profiles for 4.0-MeV Ni^+ Ions; (b) Depth-Dependent Swelling Increment Added by Ion Irradiation of Two Specimens Already Containing Uniformly Distributed Neutron-Produced Voids. (25)

If the suppression of swelling by injected interstitials can be 80% or more, why not 100%, or even dissolution of preexisting voids? The latter possibility has been demonstrated in this series of experiments for a 735°C ion irradiation of a specimen previously irradiated with neutrons at 450°C.(26) Additional swelling forward of the peak dose region was indicated by a step-height measurement of 240 Å, but the swelling at the peak actually decreased by 0.82%, a change of roughly one-half of the original neutron-produced voidage.

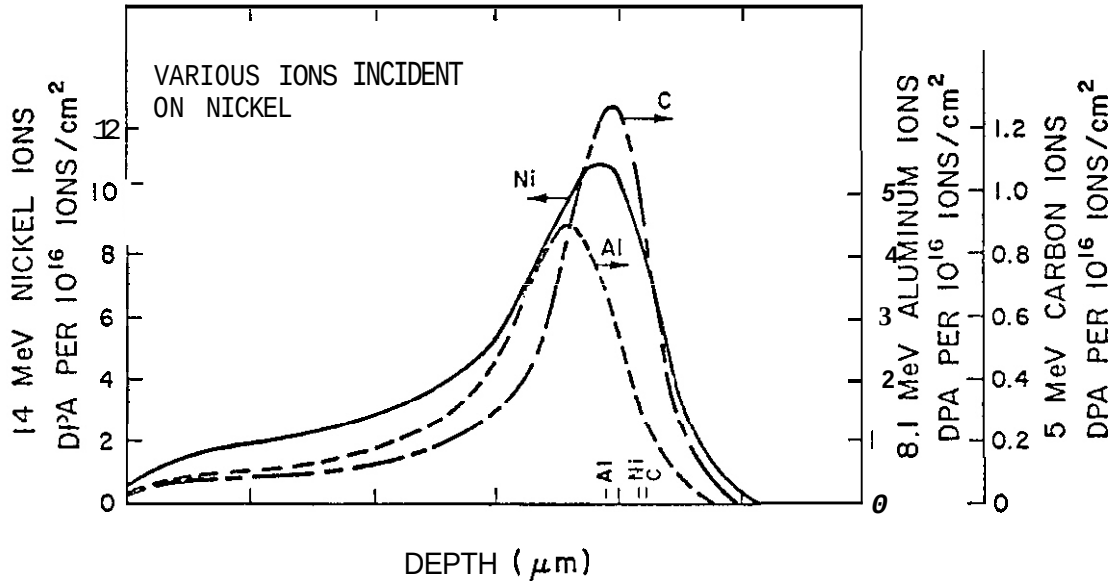

FIGURE 13. Displacement Damage vs Depth for 14-MeV Nickel, 8.1-MeV Aluminum, and 5-MeV Carbon Ions Incident on Nickel, as Published by Whitley.(26) Note the different scales for the different ions. Also shown near the base of the curves are the mean ion ranges.

Whitley discounted the injected interstitial as a major influence on shaping the swelling vs depth profiles, preferring to concentrate on the effect of displacement rate on the "internal temperature shift".[20] He found that the swelling rate increased strongly as he approached the specimen surface where lower displacement rates predominate.

For each of the three major ions employed in these studies, the swelling rate ranged from about 0.2%/dpa at the peak to values approaching 1.0%/dpa near the surface, as shown in Figure 14. Whitley also showed that the duration of the incubation period decreased as he approached the specimen surface. Once again saturation appeared to be involved, as all points on the ion path eventually saturated at about 3% swelling.

Another surprising feature of Figure 14 is that the swelling rate curves for each ion are separated, even though the swelling obtained at a given dpa for a given depth is essentially independent of the ion employed. If one is thinking in terms of the injected interstitial, however, it should be recognized that it takes about two and one-half aluminum ions and roughly eleven

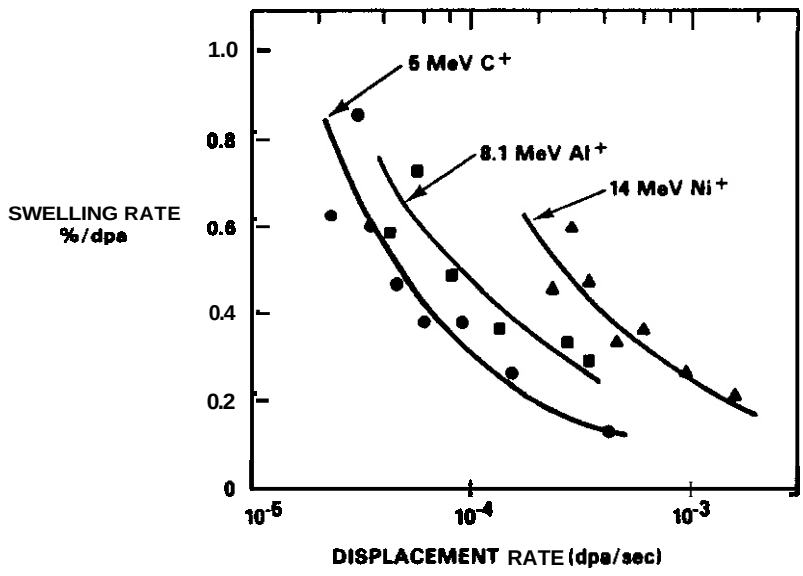

FIGURE 14. Correlation by Whitley of Swelling Rate with Displacement Rate Along the Ion Path for Three Separate Ions Injected into Pure Nickel at 525°C.[28]

carbon ions to produce the same peak dpa level as one nickel ion. Therefore, the injected interstitial effect is correspondingly more effective per dpa for the lighter ions and one would expect the injected interstitial rate per dpa to be the best correlation parameter. Figure 15 represents a rough comparison on this basis, multiplying the x-axis coordinate of the aluminum curve by 2.4 and that of the carbon curve by eleven. In the regime where the injected interstitials come to rest, the swelling rate vs injected interstitial rate is essentially independent of ion identity. (Remember that it does not have to be the original carbon or aluminum atom which falls into the void.)

Whitley[28] also provided a graphic demonstration of the increased suppression power of the injected interstitial at lower temperature. In Figure 16 the swelling in the injected interstitial region has been completely suppressed, while swelling exists on both sides of that region. The step-height/peak swelling ratio here would be infinite.

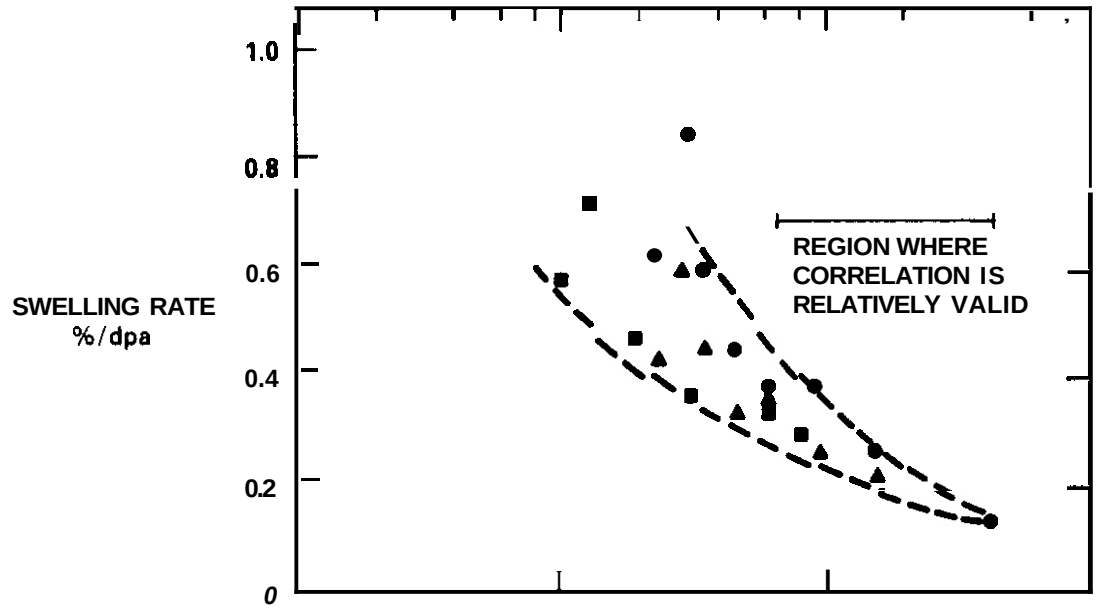

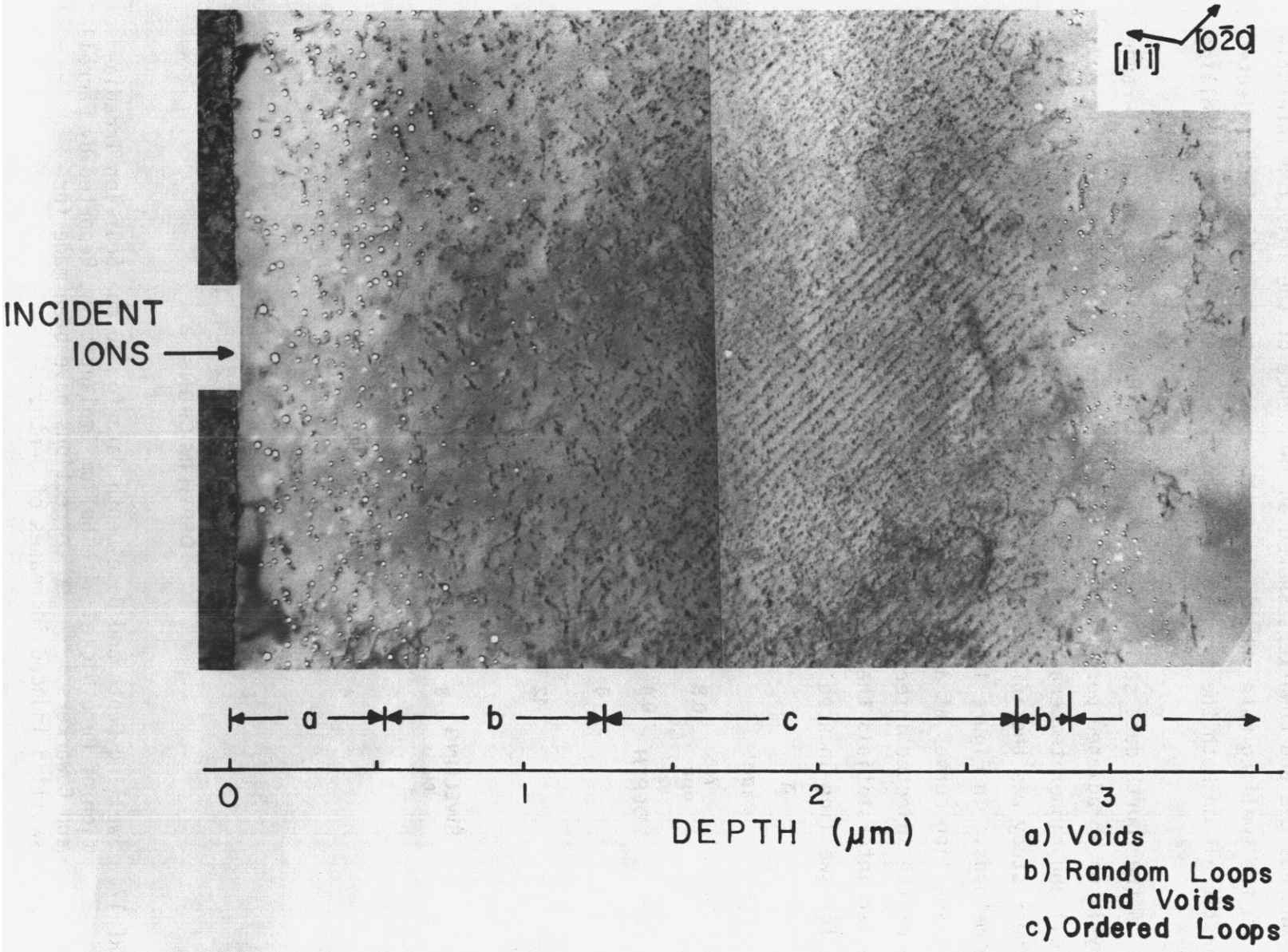

FIGURE 16. Swelling Observed by Whitley[28] Along the Range of 14-MeV Copper Ions in Nickel at 400°C and 5×10^{16} Ions/cm^2.

Whereas Lee and coworkers showed an influence of the injected interstitial on the swelling rate, Whitley's work demonstrates an effect of injected interstitials on both the transient and the steady-state regimes of swelling.

In the fourth data set Farrell, Packan and Houston performed full-range analysis on irradiated pure nickel.[30] They used lower energy ions (4-MeV nickel) and higher temperature (600°C rather than 525°C). The primary focus of their study was the influence of both helium/dpa ratios and helium injection methods. In Figure 17 one can see that there is a depression in two of their swelling curves at about 0.8 μm, corresponding roughly to the location of the injected interstitial. Outside the region of injected helium and injected interstitials the swelling levels are identical once corrections are made for swelling-induced changes in depth.

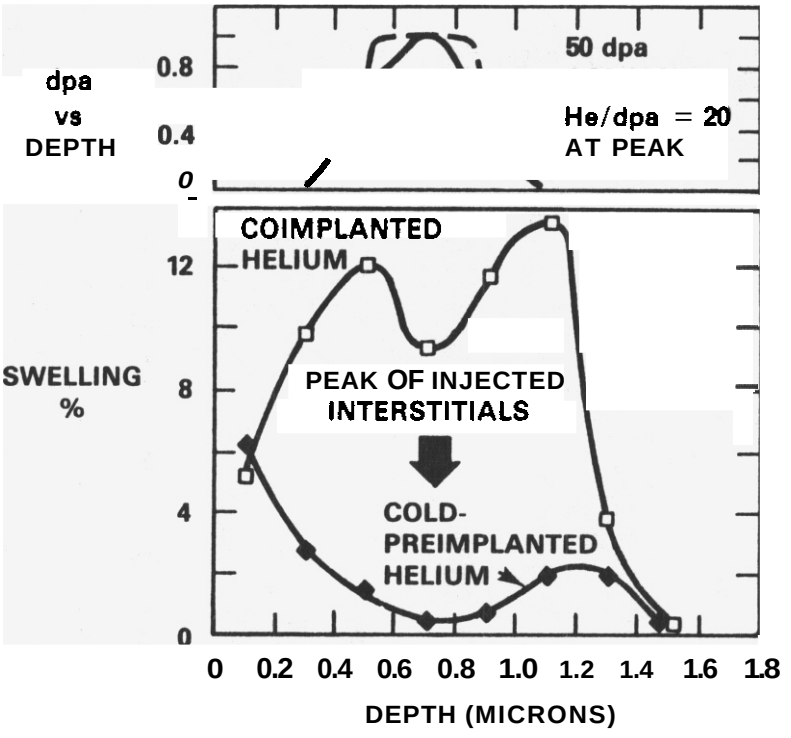

FIGURE 17. Swelling-Depth and Dose-Depth Data for 50 dpa Self-Ion Irradiation of Pure Nickel with Helium Implantation, Reported by Farrell and Coworkers.[30] No corrections have been made for swelling-induced increases of depth.

The swelling rates forward of the peak are larger than those of the peak region and there is evidence from the helium-implanted curves of a tendency toward saturation along the ion path. A similar trend was observed by Whitley. The level of saturation appears to be quite sensitive, however, to the magnitude of the helium-induced cavity density. A similar suppression of the swelling rate at high cavity density was earlier observed by Packan and Farrell in a Fe-17Cr-16.7Ni-2.5Mo alloy with 1400 appm preinjected helium.[31]

5.7 Insights Gained and Their Application to Fusion-Relevant Problems

There are currently two major areas where ion data are being used to provide guidance for the development of fusion-relevant design correlations using data derived in fission environments.[32] The first of these is the relative influence of helium and radiation-induced microchemical evolution on swelling and the second is the prediction of swelling behavior for alloys such as PCA (Prime Candidate Alloy), where changes have been made in the alloy composition in an attempt to improve the swelling resistance.

Studies directed toward the first question must recognize that the suppression of swelling at the peak corresponds to a reduction in the effectiveness of the calculated dpa. If microscopy at the peak displacement position is the data extraction technique employed, then the helium levels must also be scaled down by a factor of five. Otherwise the simulation of the effect of helium on swelling will be conducted in a He/dpa regime outside the range of interest. In addition, if full-range implantation of helium is employed as shown in Figure 17, when the variation with depth in helium/dpa ratio is steeper than originally envisioned by a factor of five.

Figure 18 shows an ion simulation of the effect of helium on the swelling of AISI 316 at 625 and 700°C.[33] The swelling is measured at the peak displacement region and averages about 0.1%/dpa. The helium affects primarily the duration of the transient regime, however, and not the steady-state swelling rate. No corrections have yet been made to increase the

effective helium/dpa ratios shown in Figure 18. Note also the relative independence of swelling rate on temperature in the range 625-700°C.

Another facet of the helium question is whether helium's role is second order compared to that of the microchemical evolution and precipitation that occurs during irradiation.[7] This evolution was identified earlier as the principal determinant of the duration of the transient regime of swelling in solute-bearing stainless steels.[34] Major physical roles for both silicon[35] and nickel[36] have been proposed, with their influence manifesting itself primarily in the duration of the incubation regime, as confirmed by the ion irradiation studies shown in Figure 9.

The relative roles of helium and nickel can be studied using ion bombardment. Complications related to the segregation and precipitation aspects can be avoided by varying the nickel content of the alloy prior to irradiation. Figure 19 shows a comparison of the results of the ADIP study and the results of Agarwal and coworkers.[37] Note that a 5% difference in nickel level has a much more pronounced effect on the duration of the transient regime than does a large variation in helium/dpa ratio. Note also that the helium/dpa ratios employed in this figure have not yet been corrected upward for the reduced effectiveness of the nickel ions. Most importantly, however, the influence of helium/dpa ratio does not lie in the steady-state regime but only in the transient regime. Continuation of the Fe-20Ni-15Cr irradiations to higher fluences confirms that the influence of helium on swelling lies primarily in the transient regime,[38] as shown in Figure 20.

The second area of interest to fundamental fusion-relevant studies lies in providing guidance for alloy development. The ion data shown in Figures 9 and 19 tell us that the primary effect of changes in nickel and silicon content is to change the duration of the transient regime of swelling. When the limitations of step-height measurements pointed out in this study are considered, it appears that even the slight dependence of the steady-state swelling rate on these elements is an artifact of the data extraction procedure.

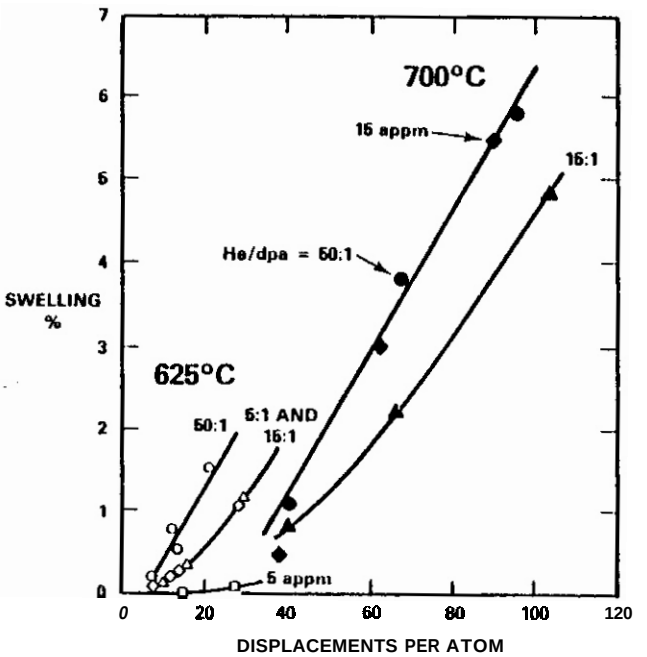

FIGURE 18. Effect of Helium on Swelling of Annealed and Aged AISI 316, as Observed During 3.0-MeV Ni^+ Ion Irradiation at 625 and 700°C.(33)

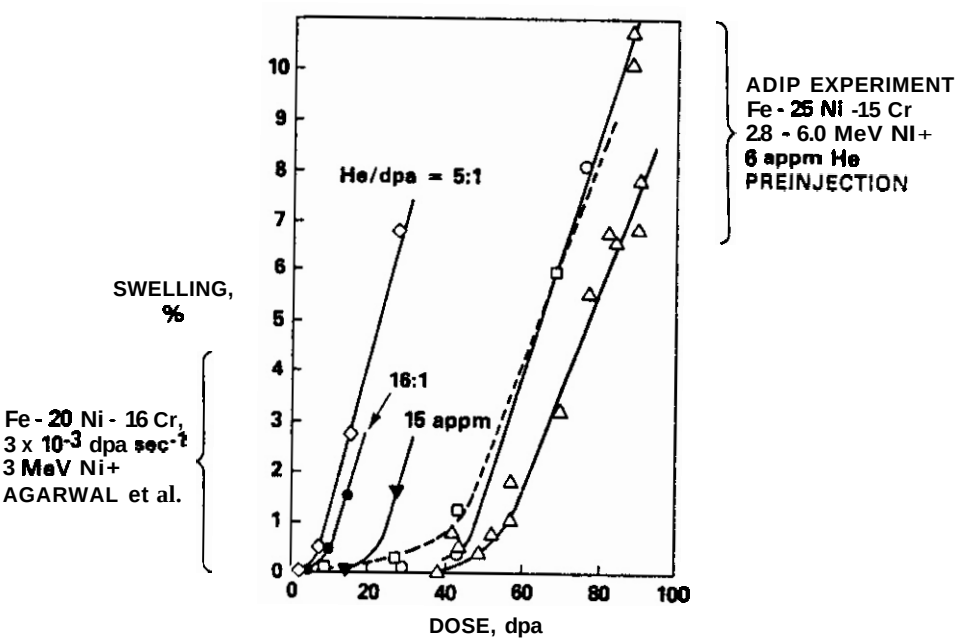

FIGURE 19. Relative Influence of Helium and Nickel Content on Swelling of Ternary Alloys at 700°C Using Nickel Ions.(7,37)

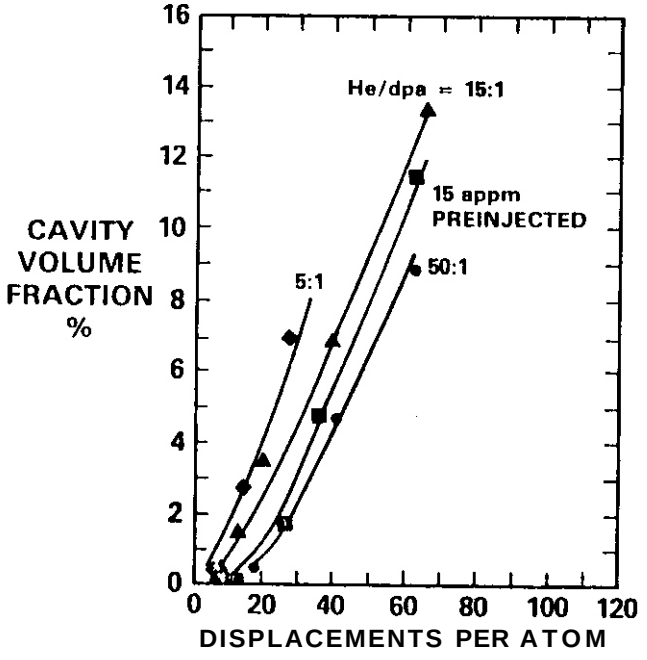

FIGURE 20. Effect of Helium on Swelling of Fe-20Ni-15Cr as Observed During Bombardment With 3-MeV Nickel Ions at 700°C.[38]

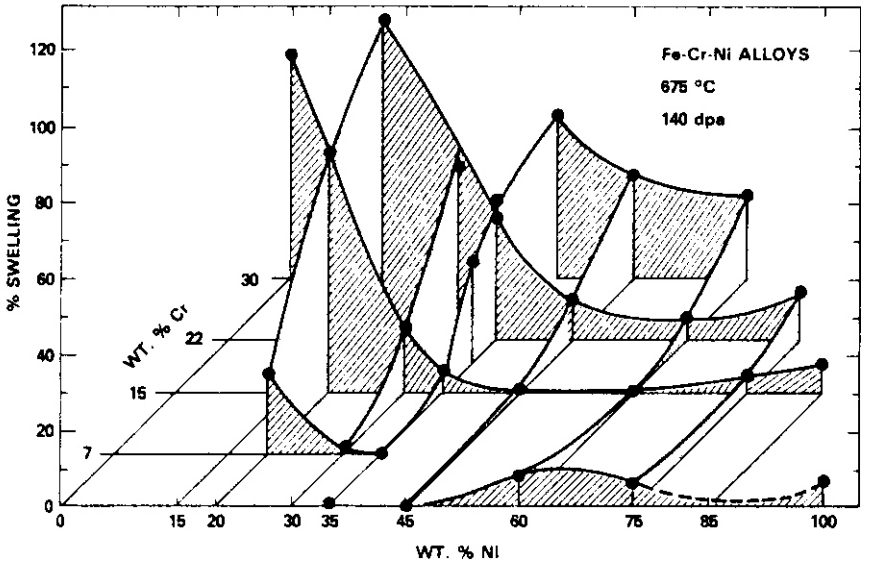

FIGURE 21. Composition Dependence of Swelling in the Fe-Ni-Cr System as Published by Johnston and Coworkers Using 5-MeV Nickel Ions and Step-Height Measurements.[22,23] While the trends shown are correct, the magnitudes of swelling cannot be accepted without correction. The curves are also somewhat distorted compared to those produced by neutrons.

These insights are important when assessing composition-related data fields such as that shown in Figure 21. These trends are not changed by the insights gained in this paper but the magnitudes of swelling must be corrected before making predictions of swelling in a neutron environment. The required correction factors vary, however, and are largest where the swelling is the lowest. Thus the trends shown in Figure 21 are distorted, magnifying the depth of the swelling minimum found at 35-45% nickel and low chromium levels.

Various conclusions of this study have not weakened the case for using ion bombardments to study the effect of helium or composition on swelling. On the contrary, once the apparent discrepancies in various ion and neutron studies are resolved, the ion data can be more confidently applied to fusion-relevant questions. Areas where such studies will be valuable are the separation of the effects of nickel-generated helium and nickel itself in the thermal irradiation of nickel-doped ferritic alloys,[39] the influence of titanium on swelling and its interactions with helium,[40] and the influence of solid transmutants on swelling.[41]

5.8 Implications of these results on Theoretical Development

There are a number of conclusions drawn from this study which impact the development of swelling theory. For instance, there is a steadily increasing body of data which demonstrates that the steady-state swelling rate of many austenitic alloys is relatively insensitive to temperature in neutron irradiations.[13,14,45, 47, and this study] If there is no peak swelling temperature, but only a swelling plateau, then there cannot be a definitive temperature shift based on temperature-sensitive swelling rates. Most ion data clearly show a swelling rate that peaks with temperature, however. Based on the knowledge gained in this and other studies, what is the origin of this peak?

Note in Figures 10 and 11 that the influence of the injected interstitial increases strongly as the temperature decreases. The net result of

such action would be to steepen the apparent swelling rate at low temperatures regardless of the measurement technique employed. It has long been known that at higher temperatures the proximity of the surface tends to reduce the point defect concentrations and therefore the swelling, artificially reducing the swelling rate.[6,42] A theoretical study by Bullough and Hayns[43] has demonstrated that surface effects will overwhelm ion irradiation studies conducted at 4.2 MeV at temperatures well below those attained in irradiations with 46.5-MeV ions that penetrate to greater depths. This has been demonstrated experimentally by Blamires and Worth[44] as shown in Figures 22 and 23. The 46.5-MeV data shown in this figure also are probably strongly influenced by surface effects at the higher temperatures. Brager and coworkers have recently shown that this steel swells without hint of declining swelling rate to at least 720°C in the EBR-II fast reactor.[45] Makin has shown that, after low temperature "seeding" of voids to overcome the surface influence in electron irradiations, this steel swells untill 900°C at displacement rates typical of ion bombardment studies.[46]

It therefore appears that the steeply peaked temperature dependence produced in ion irradiations is largely an artifact of the combined effect of both the surface and the injected interstitials. If this is true, what is the origin of the temperature shift?

Figure 3 suggests that the cause of the temperature shift arises from the dependence on displacement rate of the transient regime of swelling. The conventional arguments advanced to explain the boundaries of the temperature dependence of swelling are recombination-dominated point defect concentrations at low temperature and the emission of thermal vacancies at high temperature. The effect of displacement rate on these mechanisms could easily produce the temperature shift by controlling the rate of void nucleation and thus the duration of the transient regime. In addition, some of the phases which precede swelling in microchemically dominated alloys are directly sensitive to displacement rate or to time in reactor.[34,47] Seran and Dupouy have recently demonstrated in neutron irradiations of annealed AISI 316 stainless steel that the displacement rate influences only the duration of the transient regime of swelling.[48]

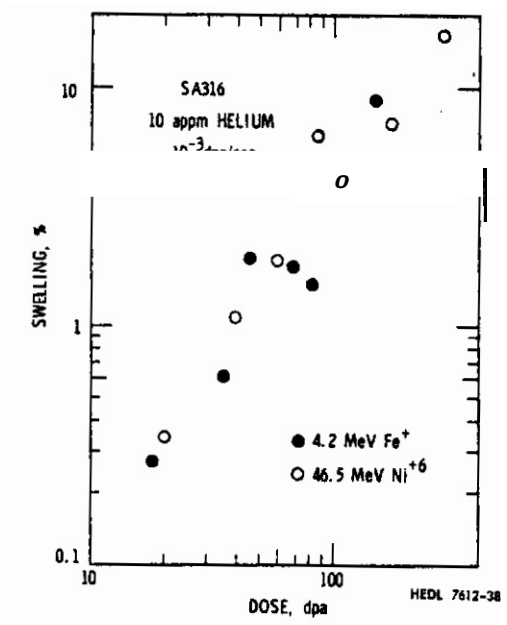

FIGURE 22. Demonstration by Blamires and Worth That at 525°C the Swelling[44] Behavior for Shallow and Deep Penetrating Ions is Identical. The injected interstitial effect would be comparable for both ions since both sets of data were extracted in their respective peak damage regions.

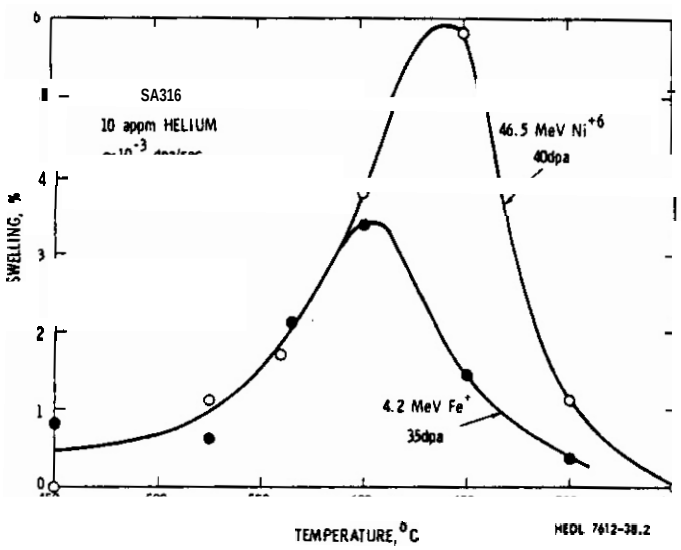

FIGURE 23. The Effect of Surface Influence on Ion-Induced Swelling.[44] At higher temperatures the data of Blamires and Worth show that the effect of the surface depresses the swelling at 4.2 MeV, and yields a low estimate of the "peak" swelling temperature. It is proposed here that the surface influence is suppressing the swelling even for 46.5-MeV ions above 650°C.

It is rather satisfying to find that the neutron-produced displacements that lead to swelling at reactor-relevant temperatures are essentially equivalent to those produced by self-ions. There has never been much enthusiasm from researchers participating in the American intercorrelation efforts for rationalizing even a factor of two difference in displacement effectiveness based on differences in mean PKA energy or defect distribution within the cascades. Recent equivalence studies based on electrical resistivity changes of pure metals bombarded at low temperatures do not support differences between heavy ion and neutron-produced displacements.[49] In swelling studies using self-ions in the range 2-5 MeV this equivalence was masked by the injected interstitial suppression effect on swelling at end-of-range. A similar masking occurred in studies using higher energy ions where data was extracted from the peak damage region.

In effect, this insight shifts the burden of theory from one previously designated "problem" to another. The "excess subsurface swelling" was not in fact a problem and was actually a reflection of the relatively unperturbed swelling behavior. Since subsurface swelling was observed in pure nickel[28-30] as well as multi-component alloys, there is no need to ascribe it to radiation-induced compositional segregation. We now know from both neutron data and ion studies that compositional variations along the ion path would not affect the selling rate, only the duration of the transient.

The burden of theory thus shifts to rationalizing the suppression at end of range. The evidence presented in this report and that of Lee and coworkers[25] tends to indict the injected interstitial or some quantity proportional to it. Brailsford and Mansur[50] originally explored the sensitivity of ion irradiations to injected interstitials and concluded that the suppression increases at lower temperatures where recombination is the dominant fate of point defects. The suppression, however, was predicted in that study to range from a few percent to several tens of percent for the particular conditions employed. In a later paper Mansur and Yoo predicted potentially much larger or even total suppression for alloys with high vacancy migration energy, low bias or low sink strength.[51] In materials with the opposite properties, the suppression was predicted to be negligible.

The results of this study show a suppression of about 80% not only for the ADIP alloy at the mid-range of the temperature regime of swelling but also for a variety of 300 series stainless steels. These alloys do not appear to match Mansur and Yoo's description of suppression-prone metals. With measured swelling rates of 1%/dpa the bias must be quite large and the sink strengths are not particularly low. In addition the migration energy for vacancies has been significantly revised recently based on measurements by Khanna and Sonnenberg[52] and Smedskjaer and coworkers.[53] Whereas the widely accepted migration energy was previously 1.4 eV, it is now clear that the value is actually lower at 1.1 ± 0.1 eV. According to Mansur and Yoo this is a relatively low migration energy and the injected interstitial effect would be rather small. This suggests that the theory may have to be recalibrated and/or expanded to account for the experimental observations. It should also be noted that the current theory addresses only the swelling rate, assuming in advance a strong effect of temperature on swelling rate. The results of Whitley[28,29] show that there is probably an effect of the injected interstitial on void nucleation.

Another intriguing possibility has been raised by this study concerning the role of injected interstitials. If a reduction of 80% or greater in the swelling rate is routine, might it not be possible to cause the swelling rate to vanish entirely at some level of voidage, leading to saturation of swelling? A tendency toward saturation indeed recurs in all of the ion bombardment studies shown in one of the preceding sections, the data of Lee and coworkers[25], Rowcliffe and coworkers[26]) and that of Whitley[28] being the *most* convincing. Whitley's data also show that saturation occurs far from the region of injected interstitials, however, so that the saturation phenomenon may be independent of or slightly perturbed by the presence of injected interstitials. The most convincing demonstrations of saturation occur in irradiations where large levels of helium produce higher than normal void densities, as shown in Figure 17, and in References 31 and 54.

It would be expected that the injected interstitial effect would be enhanced by any variable which increased the chance that the extra interstitial found a void prior to finding some other sink. Helum-induced increases in cavity density would raise the probability of such an event.

There are, however, two other ways in which the extra interstitial would find an increased probability of reaching a void. The first would occur as the voids grow larger without substantial coalescence-induced decreases in void density. The second is by the increased void density that evolves at lower temperature. Perhaps the temperature dependence of the injected interstitial effect is not so much a product of the degree of recombination, but is partly due to the increased void density at lower temperature.

Another question remains for further study. If the injected interstitial effect is sensitive to the density of cavities, what are we studying when we perform dual ion irradiations? **Is** it the effect of helium on swelling or the effect of helium on the injected interstitial effect? If it is the latter we would expect a lesser influence in neutron irradiations. As shown in Reference 1, the effect of helium on swelling in fission reactors does not appear to be discernible in the range 500-750°C, even though void densities are sensitive to helium level.

The preceding discussion has so far ignored the synergistic effects of diffusional spreading of point defects down the displacement gradient, surface losses, the internal temperature shift and extension of the ion range and straggling resulting from accumulated voidage. The potential interactions of these variables has been covered in many papers, for example References 20, 28 and 51. The proper calibration of the injected interstitial effect in theory development requires that all relevant factors be included in the calibration. The results of this study tend to diminish the potential importance of the internal temperature shift, however.

5.9 Conclusions

It appears that the displacements produced by self-ions are as effective in creating swelling as are neutrons in fast reactors. Whenever swelling is measured in a volume where the injected ion comes to rest, however, there is a substantial local reduction in the swelling rate. Depending on the data extraction technique employed, the reduction can range from 30 to 80% in the mid-range of the temperature regime of swelling. At lower temperatures the suppression is even larger. The dependence of swelling on injected interstitials at low temperature and surface influence at high temperature gives rise to a sharply-peaked distribution of ion-induced swelling with temperature that is not found in neutron irradiations. The temperature shift that occurs with varying displacement rate appears to be related to the sensitivity of the transient or incubation regime to the rate of displacement generation.

The influence of such perturbations on ion-induced swelling requires that some care be taken in interpretation of ion bombardment data directed toward the prediction of swelling in fission or fusion reactor environments. While the trends with respect to a given variable are often preserved in both ion and neutron irradiations, the relative shape with respect to that variable in ion irradiations may be somewhat distorted. It also appears that helium/dpa ratios employed in ion bombardment simulations of the fusion environment are larger than intended by a factor of five in the mid-range of the swelling temperature regime and even larger at lower temperatures.

The data presented in this report confirm that, in the absence of the injected interstitial effect, the primary influence of many environmental and material variables is on the duration of the incubation period. It was also shown that helium is a second order variable when compared with changes in composition of elements such as nickel or silicon.

6.0 References

1. H. R. Brager and F. A. Garner, "Microstructural and Microchemical Comparison of AISI 316 Irradiated in HFIR and HE8R-II," this conference.

2. H. R. Brager and F. A. Garner, J. Nucl. Mater. 103 and 104 p. 993. 1982.

3. H. R. Brager and F. A Garner, J. Nucl. Mater. 108 and 109 p. 347, 1982.

4. P. J. Maziasz, J. Nucl.Mater., p. 359, 1982.

5. P. J. Maziasz and M. L. Grossbeck, "Equations to Describe the Swelling of 20% Cold Worked Type 316 Stainless Steel Irradiated in HFIR," Alloy Development for Irradiation Performance Semiannual Progress Report, DOE/ER-0045/7, p. 98, March 1982.

6. F. A. Garner and J. J. Laidler, "Review of Neutron and Charged Particle Intercorrelation Programs," Proc. of the Workshop of Neutron and Charged Particle Damage, CONF-760673, Oak Ridge National Laboratory, Oak Ridge, TN, p. 177, June 8-10, 1976.

7. F. A. Garner, R. W. Powell. S. Diamond. T. Lauritzen. A. F. Rowcliffe. J. A. Sprague and D. Keefer, "Simulation of High Fluence Swelling Behavior on Technological Materials," Radiation Effects in Breeder Reactor Structural Materials, M. L. Bleiberg and J. W. Bennett Eds., The Metallurgical Society of AIME, p. 543, 1977.

8. F. A. Garner et al., "Summary Report on the Alloy Development Intercorrelation Program Experiment," CONF-760673, p. 147, 1976.

9. W. G. Johnston, T. Lauritzen, J. H. Rosolowski and A. M. Turkalo, "The Effect of Metallurgical Variables on Void Swelling," Radiation Damage in Metals, ASM, Cleveland, OH, p. 227, 1976.

10. L. E. Thomas and S. Lentz, in Proceedings of the 32nd Annual Electron Microscope Society Meeting, Claitors, St. Louis, MO, 1974, p. 362.

11. W. G. Johnston, J. H. Rosolowski, A. M. Turkalo and T. Lauritzen, J. Nucl. Mater. 46, p. 273, 1973.

12. S. Diamond, M. L. Bleiberg, I. M. Baron, R. Bajaj and R. W. Chickering, "HVEM Quantitative Stereoscopy Through the Full Damage Range of an Ion-Bombarded Fe-Cr-Ni Alloy," Radiation Effects and Tritium Technology for Fusion Reactors, Gatlinburg, TN, October 1-3, 1975, CONF-750989, p. 1-207.

13. W. J. S. Yang and F. A. Garner, "Relationship Between Phase Development and Swelling of AISI 316 During Temperature Changes," Effects of Radiation on Materials: Eleventh Conference, ASTM STP 782, H. R. Brager and J. S. Perrin Eds., American Society for Testing and Materials, pp. 186-206, 1982.

14. F. A. Garner and D. L. Porter, "Factors Influencing the Swelling of 300 Series Stainless Steels," Damage Analysis and Fundamental Studies Quarterly Progress R

15. K. Farrell and N. H. Packan, "Comparison of Neutron and Heavy Ion Damage in a Single Phase Austenite,'' ASTM STP 782, p. 953, 1982.

16. F. A. Garner, G. L. Wire and E. R. Gilbert, "Stress Effects in Ion Bombardment Experiments," CONF-750989, p. 1-474, 1975.

17. W. G. Johnston, J. H. Rosolowski and A. M. Turkalo, J. Nucl. Mater. 62 pp. 167-180, 1976.

18. W. G. Johnston. W. G. Morris and A. M. Turkalo. "Excess Subsurface Swelling Produced by Ni Ion Bombardment," Radiation Effects in Breeder Reactor Structural Materials, p. 421, 1977.

19. W. G. Johnston, N. H. Packan and F. A. Smidt, Jr., Summary of Workshop Discussion, CONF-760673, p. 313, 1976.

20. F. A. Garner and G. L. Guthrie, "The Influence of Displacement Gradients on the Interpretation of Charged Particle Simulation Experiments," CONF-750989, p. 1-491, 1975.

21. Unpublished work, courtesy of T. Lauritzen.

22. J. F. Bates and W. G. Johnston, "Effects of Alloy Composition on Void Swelling," Radiation Effects in Breeder Reactor Structural Materials, p. 625, 1977.

23. W. G. Johnston, T. Lauritzen, J. H. Rosolowski and A. M. Turkalo, "The Effect of Metallurgical Variables on Void Swelling, " General Electric Report 76CRD010, Jan. 1976; also J. M. Leitnaker, E. E. Bloom and J. O. Steigler, J. Nucl. Mater. 49 pp. 57-66, 1973.

24. Unpublished data, courtesy of R. Chickering and M. L. Bleiberg, Westinghouse Advanced Reactor Division, Waltz Mill, PA, and W. G. Johnston of General Electric, Schnectady, NY.

25. E. H. Lee, L. K. Mansur and M. H. Yoo, J. Nucl. Mater. 85 and 86, p. 577-581, 1979.

26. A. F. Rowcliffe, E. H. Lee and P. S. Sklad, "The Effect of Phase Instabilities on the Correlation of Nickel Ion and Neutron Irradiation Swelling in Solution Annealed 316 Stainless Steel," Proceedings Symposium on Irradiation Behavior of Metallic Materials in Fast Reactor Core Components, Corsica, June 1979.

27. T. A. Lauritzen, W. K. Appleby and W. L. Bell, "A comparison of Neutron Irradiation and Nickel Ion Bombardment in the Production of Swelling in AISI 316 Stainless Steel," ibid.

28. J. B. Whitley, "Depth Dependent Damage in Heavy-Ion Irradiated Nickel", Thesis for Doctor of Philosophy - Nuclear Engineering, University of Wisconsin-Madison, 1978.

29. J. B. Whitley, G. L. Kulcinsky, P. Wilkes and J. Billen, J. Nucl. Mater. 85 and 86, pp. 701-706, 1979.

30. K. Farrell, N. H. Packan and J. T. Houston, Radiation Effects, 62, pp. 39-52, 1982.

31. N. H. Packan and K. Farrell, J. Nucl. Mater. 85 and 86, pp. 677-681, 1979.

32. F. A. Garner, H. R. Brager, F. M. Mann, H. L. Heinisch and R. L. Simons, "Factors Relevent to the Development of Fission-Fusion Correlations," this conference.

33. C. Ayrault, H. A. Hoff, F. V. Nolfi, Jr., and A. P. L. Turner, J. Nucl. Mater. 103 and 104 (1981) 1035, 625°C data only; 700°C data supplied in advance of publication by B. Loomis, G. Ayrault and Z. Wang.

34. F. A. Garner, "The Microchemical Evolution of Irradiated Stainless Steel," in Phase Stability During Irradiation," J. R. Holland, L. K. Mansur and D. I. Potter. Eds.. The Metallurgical Society of AIME, pp. 165-189, 1980.

35. F. A. Garner and W. G. Wolfer, J. Nucl. Mater. 102, pp. 143-150, 1981.

36. W. G. Wolfer, F. A. Garner and L. E. Thomas, "On Radiation-Induced Segregation and the Compositional Dependence of Swelling in Fe-Ni-Cr Alloys, ASTM STM 782, pp. 1023-1041, 1982.

37. S. C. Agarwal, G. Ayrault, D. I. Potter, A. Taylor and F. V. Nolfi Jr., J. Nucl. Mater. 85 and 86, pp. 653-657, 1979.

38. Data provided in advance of publication by B. Loomis of Argonne National Laboratory. Also in Damage Analysis and Fundamental Studies Quarterly Progress Report, DOE/ER-0046/10, p. 145, August 1982.

39. G. Ayrault, "Single and Dual Ion Irradiations of Ferritic Alloys and Type 316 Stainless Steel ," Damage Analysis and Fundamental Studies Quarterly Progress Report, DOE/ER-0046/7, p. 167, November 1981.

40. P. J. Maziasz, Scripta Met. 14, pp. 1251-1256, 1982.

41. J. F. Bates, F. A. Garner and F. M. Mann, J. Nucl. Mater. 103 and 104 pp. 999-1004, 1981.

42. F. A. Garner and L. E. Thomas, "Production of Voids in Stainless Steels by High Voltage Electrons," Effects of Radiation on Substructure and Mechanical Properties of Metals and Alloys, ASTM STP 529, American Society for Testing and Materials, pp. 305-325, 1973.

43. R. Bullough and M. R. Hayns, J. Nucl. Mater. 68, pp. 286-293, 1977.

44. N. G. Blamires and J. H. Worth, "Comparison of 42 MeV Fe^{+} and 46.5 MeV Ni^{+} Irradiation for the Study of Void Swelling, Harwell Report, AERE-R-7479, 1975.

45. H. R. Brager, W. J. S. Yang and F. A. Garner, "Microstructural/Microchemical Evolution of AISI 316 at Temoeratures in the Range 650-750°C," Damage Analysis and Fundamental Studies Quarterly Progress Report, DOE/ER-0046/10, p. 233, August 1982.

46. M. J. Makin, G. P. Walters and A. J. E. Foreman, J. Nucl. Mater. 95 p. 155, 1980.

47. F. A. Garner and O. L. Porter, "History Dependence and Consequences of the Microchemical Evolution of AISI 316," ASTM STP 782, pp. 295-309, 1982.

48. J. L. Seran and J. M. Dupouy, "The Swelling of Solution-Annealed 316 Cladding in Rapsodie and Phenix," Ibid., pp. 5-16.

49. P. Jung and nine coauthors, "Defect Production Rates by Electrons, Ions and Neutrons in Cubic Metals," Ibid., pp. 963-982.

50. A. D. Brailsford and L. K. Mansur, J. Nucl. Mater. 71 p. 110, 1977.

51. L. K. Mansur and M. H. Yoo, J. Nucl. Mater. 85 and 86, pp. 523-532, 1979.

52. S. K. Khanna and K. Sonnenberg, Radiation Effects, 59, pp. 91-92, 1981.

53. L. C. Smedskjaer, M. J. Fluss, D. G. Legnini, M. K. Chason, and R. W. Siegel, J. Phys. F.: Metal Physics 11, pp. 2221-2230, 1981.

54. N. H. Packan and K. Farrell, "Ion Damage in 316 Stainless Steel Over a Broad Dose Range," ASTM STP 782, pp. 885-894, 1982.

7.0 Future Work

This work is nearing completion and will focus on the saturation phenomenon and its relevance to the study of the effect of helium on swelling.

8.0 Publications

This paper will be published in J. Nucl. Mater. as part of the proceedings of the TMS-AIME Symposium on Radiation Damage Analysis for Fusion Reactors, St. Louis MO, October 24-28, 1982.

Acknowledgments

It has been over eight years since the inception of the ADIP experiments ahd very few of the original ADIP participants are still working in the area described in this paper. The other participants were R. W. Powell of Westinghouse Hanford; D. W. Keefer, A. G. Pard, K. R. Garr and M. M. Nakata of Atomics International Corporation; T. Lauritzen, W. L. Bell, W. G. Johnston and W. K. Appleby of General Electric Corporation; S. Diamond, M. Baron, R. Chickering, R. Bajaj and M. L. Bleiberg of Westinghouse Advanced Reactors Division; J. A Sprague, F. A. Smidt and J. E. Westmoreland of Naval Research Laboratory. The successful conclusion of this experiment is the direct result of their combined efforts.

Since the publication by the above researchers of the Phase I ADIP results in 1976, other individuals have made important contributions which enabled the author of this paper to unravel some of the "mysteries" of simulation experiments. These are M. M. Korenko, J. F. Bates and D. T. Peterson of Westinghouse Hanford; N. F. Packan, K. Farrell, A. F. Rowcliffe, E. A. Lee, and P. S. Sklad of Oak Ridge National Laboratory; J. B. Whitley and W. G. Wolfer of the University of Wisconsin. All participants in the ADIP and subsequent studies were supported by various branches of the United States Energy Research and Development Administration or its successor the Department of Energy.

VOID SWELLING OF PROTON-IRRADIATED STAINLESS STEEL AT LARGE DISPLACEMENT LEVELS

A. Kumar (University of Missouri-Rolla) and F. A. Garner (Westinghouse Hanford Company)

1.0 Objective

The purpose of this study is to determine whether saturation of void swelling in AISI 316 stainless steel can be made to occur at any level relevant to engineering design and to decide whether saturation is sensitive to irradiation variables such as helium/dpa ratio or simulation artifacts such as injected interstitials.

2.0 Summary

There is some evidence which suggests that void swelling may not increase continuously with increasing irradiation but may saturate at a level dependent on irradiation conditions, helium/dpa level or artifacts of the simulation such as the presence of injected interstitials. An experiment was therefore performed to determine the saturation level of swelling of annealed AISI 316 at 625°C in the absence of helium and injected interstitials. Using 140-KeV protons and step height measurements it was found that saturation did not occur until 260% swelling was achieved at ~500 dpa. Prior to saturation the swelling curve exhibited the anticipated bilinear form with a steady state swelling rate of 0.8 %/dpa based on a 25-eV threshold energy.

3.0 Program

Title: Irradiation Effects Analysis (AKJ)
Principal Investigator: D. G. Doran
Affiliation: Westinghouse-Hanford Company

4.0 Relevant DAFS Program Plan Task/Subtask

Subtask II.C.1 Effects of Material Parameters on Microstructure

Subtask II.C.2 Effects of Helium on Microstructure

5.0 Accomplishments and Status

5.1 Introduction

The void-induced swelling caused by neutron irradiation of AISI 316 stainless steel has been found to reach very large levels without any indication of eventual saturation. As shown in Figures 1 and 2 the neutron-induced swelling of several heats of this alloy has reached values of 25-30 volume percent.[1] While 30% swelling is too large to be incorporated into a sound design for a fast breeder or fusion reactor, there is reason to speculate whether saturation will eventually occur and at what level. The attainment of saturation would allow its examination for clues as to how it might be induced at lower swelling levels.

In order to reach exposures well above those attained in-reactor, one must turn to charged particle simulation. Not all charged particle techniques are suitable for this purpose, however. Since it is known in advance that saturation (if indeed it exists) lies above 30%, one cannot use electron irradiation of thin foils where swelling data can only be extracted by microscopy examination. It is very difficult to measure accurately by microscopy swelling levels in excess of 15-20%. In addition, an artificially imposed saturation can arise from the proximity of foil surfaces in such experiments.[2,3,4]

It has also been shown that irradiation with low energy self-ions can lead to surface-affected suppression of swelling at high temperatures.[5] In addition, there is strong evidence that suggests that at higher incident energies the injected interstitial atom resulting from the impinging ion

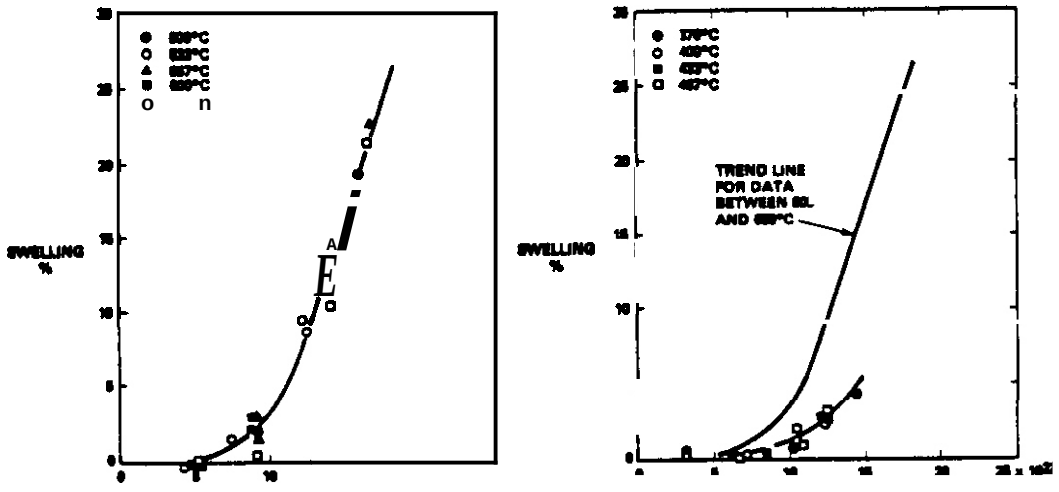

FIGURE 1. old-Worked (1)

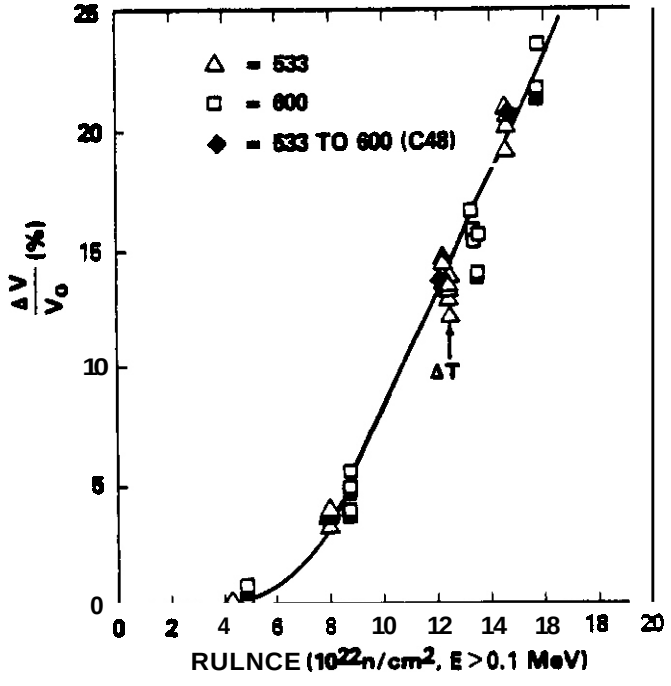

FIGURE 2. Isothermal and Non-Isothermal Behavior of CN-13 Heat of 20% Cold-Worked AISI 316 in EBR-II, as Reported by Yang and Garner.(1)

reduces the rate of swelling[6,7] and might possibly lead to an artificial saturation atypical of that which would occur during neutron irradiation. Indeed, self-ion irradiations of AISI 316 by several groups of researchers have exhibited saturation at levels ranging from 12 to 20%.[8,9,10] Other irradiation studies by Johnston and coworkers[11] and Lauritzen and co-workers[12] on the same alloys did not yield saturation, however, although swelling levels roughly twice as large were attained.

Saturation of swelling at low levels during self-ion irradiation has been observed in simple metals such as nickel,[13,14] but this phenomenon has not yet been reported for neutron-irradiated nickel.

It was therefore decided that the pursuit of saturation in AISI 316 best proceed using protons rather than self-ions. There is no injected interstitial influence since the protons immediately diffuse out of the irradiated volume, as demonstrated by Keefer and Pard.[15] It is also anticipated that microscopy examination will be of very limited use at large levels of swelling and that the total integrated swelling along the proton's path will have to be measured by step-height techniques developed by Johnston and Coworkers.[16] This type of swelling data requires some unfolding in order to extract the dependence of swelling on accumulated exposure, however.

5.2 Experimental Details

The specimens were prepared as disks of one inch diameter and 3/8" thickness from AISI 316 stock supplied by Carpenter Technology. After annealing one hour under argon at 1010°C and then water-quenching, the specimen surfaces were vibratory-polished using a water slurry of 500 Å alumina powder.

During irradiation the specimens were maintained at 1×10^{-8} Torr and their temperatures monitored by thermocouples which were spot-welded to the specimens' front surfaces. The full details of the irradiation facility and

procedure have been published previously.[17] Five specimens were irradiated at 625 ± 10°C over a 1/8" diameter central area with a uniform beam of 140-keV protons at 8×10^{14} ions/cm^2 sec. As shown in Figure 3 these ions create a damage peak below the specimen surface. Total ion fluences achieved were 2.25×10^{19}, 4.5×10^{19}, 8.1×10^{19}, 1.45×10^{20} and 2.0×10^{20} cm^{-2}. No helium was injected into these specimens before or during the irradiation.

An unirradiated area in the shape of a cross was formed on each specimen by two ten-mil tungsten wires mounted at right angles on the collimator, thereby interrupting a portion of the beam. The integrated swelling was then measured across the masked area at eight different places, using a Clevite Surfanalyzer System 150 profilometer. The stylus employed a 5-μm diamond tip exerting 50 mg of force on the specimen surface.

5.3 Results

Figure 4 shows the surface of a typical irradiated area. The low contrast portions within and outside the irradiated circular area retain the original fine polish, while the areas exposed to the proton beam have become quite rough due to sputtering and differential swelling, as shown in Figure 5. A typical profilometer trace across the central irradiated and unirradiated areas is shown in Figure 6. The relative roughness of the two surfaces is also evident in the trace.

The step-height measurements attained in this study are shown in Figure 7. Each value is an average of eight separate measurements at different locations; the range of these measurements is also shown in the height of the error bars. A small correction has also been made for sputtering of the surfaces. Assuming a sputtering yield of 5×10^{-4} atoms/proton,[18] the largest correction was less than 80A.

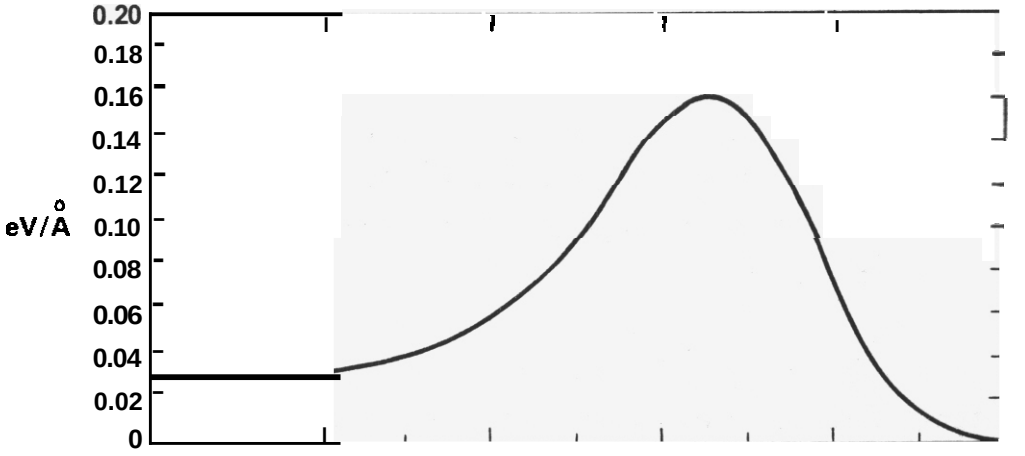

FIGURE 3. Nuclear Energy Deposition in fcc Iron by 140-keV Protons, Courtesy of O. S. Oen of Oak Ridge National Laboratory.

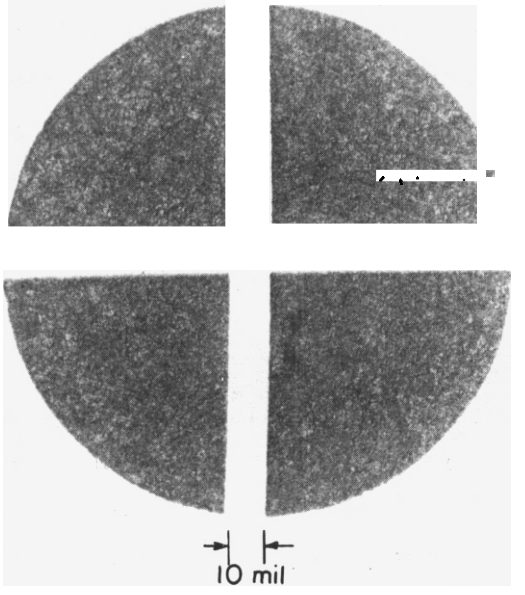

FIGURE 4. Scanning Electron Micrograph of Surface of AISI 316 After Irradiation with 140-keV Protons at 625°C.

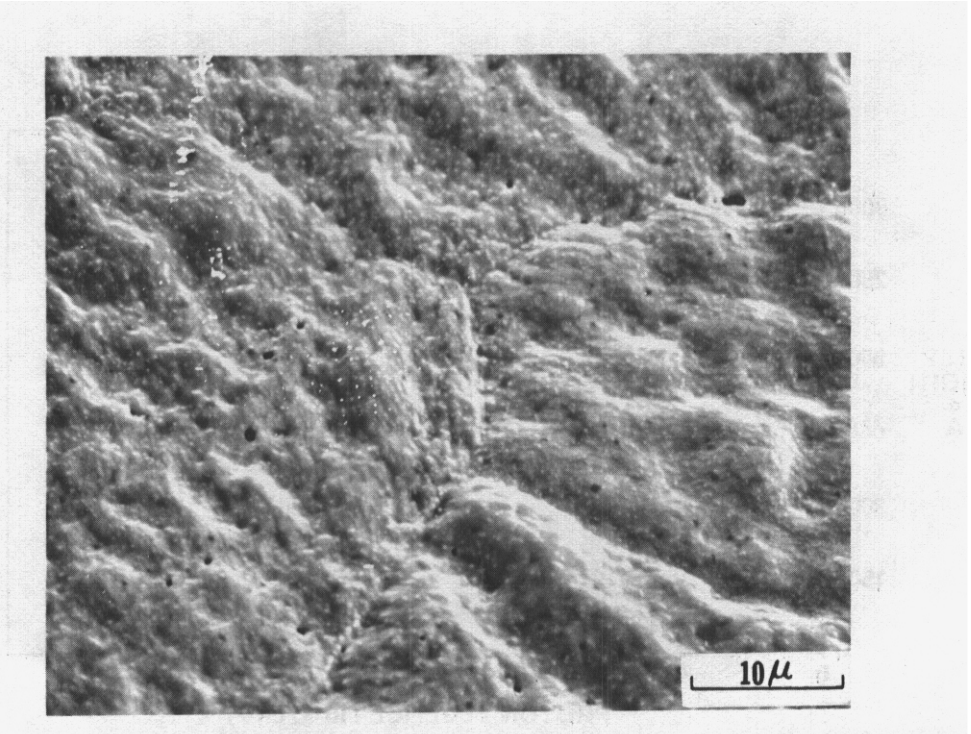

FIGURE 5. Scanning Electron Micrograph at High Magnification of Irradiated Surface Showing Roughness That Develops Due to Proton-Induced Sputtering and Differential Swelling.

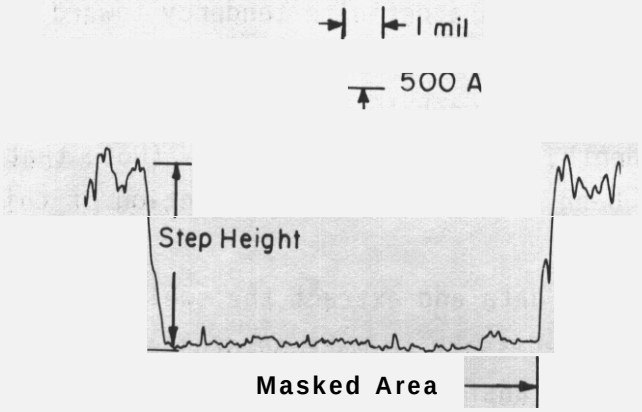

FIGURE 6. Typical Profilometer Trace Across the Masked Area, Showing Swelling of Irradiated Area and Also the Relative Roughness of the Two Surfaces.

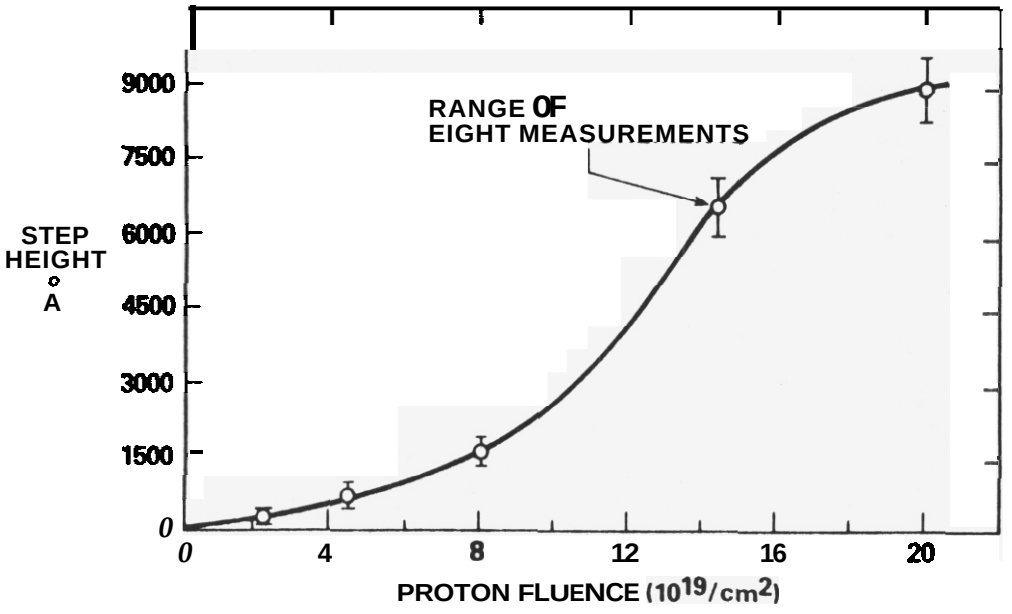

FIGURE 7. Step-Heights (Average of Eight Measurements) Induced in Annealed AISI 316 by Bombardment with 140-keV Protons at 625°C.

Note that Figure 7 exhibits a definite tendency toward saturation of swelling at high exposure, but at a very large swelling level. The saturation behavior is camouflaged somewhat, however, by the nonlinear creation of displacements with depth, as shown in Figure 3. (Note that a displacement threshold of 25 eV has been assumed in the construction of this curve.)

In order to unfold the data and extract the swelling behavior vs. displacement level, it is necessary to make several assumptions. First, the required swelling vs. dose transform must be assumed to be solely dependent on the total number of displacements and not dependent on any other depth-dependent variables such as displacement rate. For accelerated bombardments this assumption appears to be reasonably valid. At a not-too-different temperature (575°C) Makin and coworkers have irradiated annealed AISI 316 at three displacement rates spanning a factor of roughly four and observed a

complete independence of the void volume on this variable.[19] The damage deposition curve shown in Figure 3 involves a comparable range of damage rates (a factor of roughly five) from the front surface to the peak damage position. At the much lower displacement rates typical of breeder reactors, the duration of the transient regime (but not the steady-state regime) of swelling is known to be sensitive to displacement rate in some temperature ranges, however.[20]

Second, it must be assumed that any influence of the surface in perturbing the swelling behavior has a negligible influence on the total step-height. As shown by earlier studies,[3,21] there are zones denuded of swelling near specimen surfaces. Frequently, however there is often a counterbalancing increase in swelling just beyond the denuded boundary.[22]

The procedure involved in determining the swelling transform $S(dpa)$ where $dpa = f(x)$ from five step-height measurements H_i requires that the sum of the absolute differences between the transform predictions and the individual step-height measurements be minimized. Therefore

$$\sum_{i=1}^{5} \left(H_i - \int S(x)dx\right)^2 = \text{SUM} \qquad (1)$$

should be a minimum. The uniqueness of the transform is only assured for large values of i, but a reasonably close approximation can be obtained for the current purpose.

The integral in Equation 1 can be approximated by

$$\sum_{i=1}^{10} S(\overline{dpa_i})\, \Delta x_i$$

where the dpa vs. depth curve is approximated by ten increments of thickness $\Delta x = 0.1\ \mu m$ having an average dose of dpa_i.

A suitable transform was obtained employing a trial and error approach. As shown in Figure *8*, it conforms to the incubation-plus-linear behavior normally observed in this steel but confirms that saturation is indeed occurring, but a a very high level of 260%. At swelling levels of this magnitude microscopy techniques are useless for determining the microstructural origins of the saturation process. A swelling rate of 0.8 %/dpa was observed in the steady-state regime, assuming a threshold displacement energy of 25 eV. While this steay-state swelling rate is subject to some uncertainties based on the limited number of irradiations performed, the conclusion concerning the large magnitude at which saturation occurs is not affected very much.

5.4 Discussion

It should be noted that *9000* Å of step-height and 260% swelling imply a step height conversion factor of 35 Å per percent swelling at the position of peak displacement rate. This number is quite different from the value of

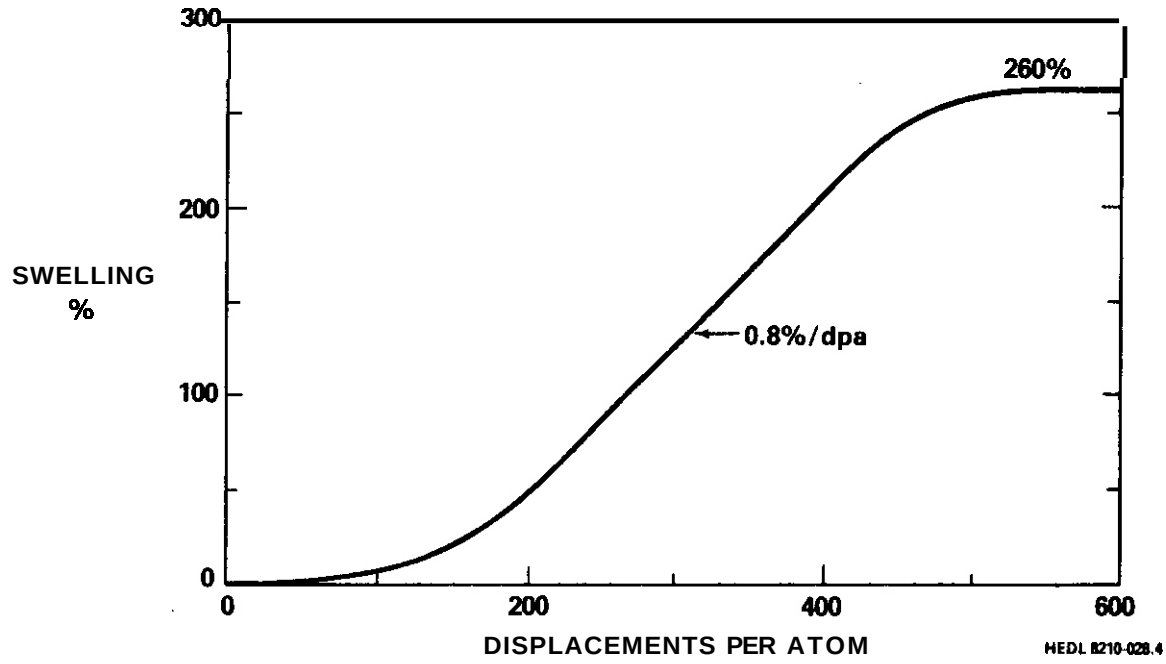

FIGURE *8*. Transform Derived from This Study for Swelling vs Displacement Dose of AISI 316 Irradiated with 140-keV Protons at 625°C.

60 Å/% employed by Johnston and coworkers.[4,12,16,21] However, it has been shown that the 60 Å/% figure is specific only to 5-MeV Ni^+ ions and represents the asymptotic limit at large swelling of the integrated swelling. The difference in damage energy profiles with depth leads to different conversion factors for each ion and ion energy.[23]

As shown by Garner, Wire and Gilbert[23] the step height conversion factor at high swelling approaches $h_D = R_{max}\ \bar{D}/D_{max}$ where

$$\bar{D} = R_{max}^{-1} \int_0^{R_{max}} D(x)d(x)$$

The maximum range R_{max} of the ion takes into account the maximum amount of straggling and $\bar{D}$ is the average damage deposition rate along the damage deposition curve $D(x)$ with a peak at D_{max}.

For 140-keV ions, $\bar{D}/D_{max} = 0.33$, R_{max} is 10,000 Å and the step height conversion factor is 33 Å/%. This agrees very well with the value of 35 Å/% derived from this study.

The results of this study and that of the neutron studies shown in Figures 1 and 2 reinforce the suspicion that the saturation of swelling observed in self-ion bombardment experiments may be an artifact associated with some extraneous influence such as either the injected interstitial or the surface proximity effect. Until this possibility is examined, one cannot make a confident assessment of the role of helium on saturation behavior. A review of all saturation-relevant data is now in progress to aid in making this assessment.

5.5 Conclusions

An experiment was performed to determine the saturation level of annealed AISI 316 in the absence of helium and injected interstitials. Using

140-keV protons and step-height measurements it was found that saturation did not occur at 625°C until 260 % swelling was achieved at ~500 dpa. Prior to saturation, the swelling curve exhibited the anticipated bilinear behavior with a steady-state swelling rate of 0.8 %/dpa based on a 25 eV-threshold energy.

6.0 References

1. W. S. J. Yang and F. A. Garner, "Relationship Between Phase Development and Swelling of AISI 316 During Temperature Changes," Effects of Radiation on Materials: Eleventh Conference, ASTM STP 782, H. R. Brager and J. S. Perrin, Eds., American Society for Testing and Materials, pp. 186-206, 1982.

2. J. J. Laidler and 8. Mastel, "Dynamic Irradiation Damage Studies with the HVEM," Quarterly Progress Report: Irradiation Effects on Reactor Structural Materials, HEDL-TME 72-64, p. HEDL-50, February-April 1972.

3. F. A. Garner and L. E. Thomas, "Production of Voids in Stainless Steel by High-Voltage Electrons," Effects of Radiation on Substructure and Mechanical Properties of Metals and Alloys, ASTM STP 529, American Society for Testing and Materials, pp. 303-325, 1973.

4. J. J. Laidler, F. A. Garner and L. E. Thomas, "Simulation Experiments with High Voltage Electron Microscope," in Radiation Damage in Metals, N. L. Peterson and S. D. Harkness, Eds., American Society for Metals, pp. 194-226, 1976.

5. F. A. Garner and J. J. Laidler, "Review of Neutron and Charged Particle Intercorrelation Programs," in Workshop on Correlation of Neutron and Charged Particle Damage, Oak Ridge National Laboratory, June 8-10, 1976, CONF-760673, pp. 177-240.

6. E. A. Lee, L. K. Mansur and M. H. Yoo, J. Nuclear Materials, 85 and 86 (1979), pp. 577-581, also L. K. Mansur and M. H. Yoo, J. Nuclear Mater., 85 and 86, pp. 523-532, 1979.

7. F. A. Garner. "Correlation of Charged Particle and Neutron-Induced Radiation Damage: The ADIP Experiment Revisited," Proceedings of TMS-AIME Symposium on Radiation Damage Analysis for Fusion Reactors, St. Louis, MO, October 24-28, 1982.

8. N. H. Packan and K. Farrell, "Ion Damage in 316 Stainless Steel Over a Broad Dose Range," Effects of Radiation on Materials: Eleventh Conference, ASTM STP 782, Eds., American Society for Testing and Materials, pp. 885-894, 1982.

9. J. J. Laidler in Discussion by Attendees, Proceedings of International Conference on Radiation-Induced Voids in Metals, J. W. Corbett and L. C. Ianniello, Eds., 1972, USAEC Symposium Series #26, CONF-610601, p. 447.

10. D. J. Mazey, J. A. Hudson and R. S. Nelson, J. Nuclear Mater., 41, pp. 257-273, 1971.

11. W. G. Johnston, J. H. Rosolowski, A. M. Turkalo and T. Lauritzen, J. Nucl. Mater. 48, p. 330, 1973.

12. T. A. Lauritzen, W. K. Appleby and W. L. Bell, "A comparison of Neutron Irradiation and Nickel Ion Bombardment in the Production of Swelling in AISI 316 Stainless Steel," Proceedings of Irradiation Behavior of Metallic Materials for Fast Reactor Core Components, Ajaccio, Corsica, June 4-8, 1979, pp. 161-167.

13. G. L. Kulcinski, J. L. Brimhall and H. E. Kissinger, "Production of Voids in Pure Metals by High-Energy Heavy-Ion Bombardment, CONF-610601, pp. 449-476, 1972.

14. J. B. Whitley, "Depth Dependent Damage in Heavy-Ion Irradiated Nickel", (Ph.D. Dissertation), University of Wisconsin-Madison, 1978.

15. D. W. Keefer and A. G. Pard, J. Nuclear Mater., 47, p. 97, 1973.

16. W. G. Johnston, J. H. Rosolowski, A. M. Turkalo and T. Lauritzen, J. Nucl. Mater. 46 p. 273, 1973.

17. A. K. Srivastava, "Proton-Induced Swelling in Type 316 Stainless Steel," Ph.D. Dissertation, University of California at Berkeley, Lawrence Berkeley Laboratory Report LBL-4595, February 1977.

18. F. Fairbrother, Jr., et al., Vacuum, 4, p. 112, 1954.

19. M. J. Makin, G. P. Walters and A. J. E. Foreman, J. Nucl. Mater. 95, pp. 155-170, 1980.

20. J. L. Seran and J. M. Dupouy, "The Swelling of Solution-Annealed 316 Cladding in Rapsodie and Phenix," Effects of Radiation on Materials: Eleventh Conference, ASTM STP 782, H. R. Brager and J. S. Perrin, Eds., American Society for Testing and Materials, pp. 5-16, 1982.

21. W. G. Johnston, W. G. Morris and A. M. Turkalo, "Excess Sub-Surface Swelling Produced by Ni^+ Ion Bombardment," Radiation Effects in Breeder Reactor Structural Materials, M. L. Bleiberg and J. W. Bennett, Eds., The Metallurgical Society of AIME, pp. 421-430, 1977.

22. F. A. Garner, J. J. Laidler and G. L. Guthrie, "Development and Evaluation of a Stress-Free Swelling Correlation for 20 Percent Cold-Worked Type 316 Stainless Steel," Irradiation Effects on the Microstructure and Properties of Metals, ASTM STP 611, American Society for Testing and Materials, pp. 208-226, 1976.

23. F. A. Garner, G. L. Wire and E. R. Gilbert, "Stress Effects in Ion Bombardment Experiments," Radiation Effects and Tritium Technology for Fusion Reactors, CONF-750989, Gatlinburg, TN, October 1-3, 1975, p. I-474.

7.0 Future Work

This effort will continue, concentrating primarily on analysis of other data on saturation in an attempt to determine the origin of saturation and its relevance to fission-fusion correlations involving the effects of helium on swelling.

8.0 Publications

None.

DEPENDENCE OF SWELLING OF Fe-Ni-Cr ALLOYS ON CHROMIUM AND NICKEL CONTENT

H. R. Brager and F. A. Garner (Westinghouse Hanford Company)

1.0 Objective

The purpose of this study is to identify the microstructural and microchemical origins of the compositional dependence of radiation-induced swelling, creep and changes in mechanical properties.

2.0 Summary

The first results from the AD-1 neutron irradiation experiment on swelling of Fe-Ni-Cr alloys agree with previous results from the AA-VII neutron irradiation experiment as well as earlier ion bombardment experiments. The swelling of these alloys was found to be sensitive to the nickel and chromium content. Segregation of nickel to various microstructural sinks is invoked to explain both the compositional dependence of swelling and a concurrent densification that occurs. The data also indicate that the dislocation evolution may be sensitive to composition.

3.0 Program

Title: Irradiation Effects Analysis (AKJ)
Principal Investigator: D. G. Doran
Affiliation: Westinghouse Hanford Company

4.0 Relevant DAFS Program Plan Task/SubTask

Subtask II.C.1. Effect of Material Parameters on Microstructure.

5.0 Accomplishments and Status

5.1 Introduction

Several ongoing OAFS experiments have as one of their objectives the determination of the influence of composition on radiation-induced microstructure and swelling of Fe-Ni-Cr alloys. There are also some limited experiments to measure radiation-induced changes in mechanical properties of these alloys. The first OAFS results from the AD-1 and AA-VII experiments are now becoming available. Both experiments were irradiated in EBR-II with the AD-1 specimens in the form of tensile flats and the AA-VII specimens in the form of microscopy disks.

5.2 Results

Immersion density measurements were performed on the AD-1 flat tensile specimens irradiated at 395, 450 and 550°C to fluences of 2.1 to 2.5 x 10^{22} n/cm^2 (E>0.1 MeV). (1) The results are shown in Table 1. Figures 1 through 3 show comparisons of the AD-1 data with density change data for the identical[t] alloys irradiated in the AA-VII experiment. All density measurements are considered reproducible within ± 0.16% swelling. Where it is possible to make comparisons the data appear to be in excellent agreement. At ~15% chromium swelling decreases with increasing nickel content, while at ~35% nickel swelling increases with increasing chromium level.

Microscopy has now been initiated on the ternary alloy series irradiated in AA-VII. Two specimens have been examined to date. The first specimen was E25 (Fe-35.1Ni-21.7Cr) irradiated to 7.2 x 10^{22} n/cm^2 (E>0.1MeV) at 538°C and E37 (Fe-35.5 Ni-7.5Cr) irradiated to 7.6 x 10^{22} n/cm^2 at 593°C. While the fluences are comparable, the specimens span a composition range where a substantial chromium dependence exists(2) and also a temperature range where a substantial effect of temperature on the incubation period has been observed.(3)

[t] Identical starting stock but somewhat different annealing conditions (945°C/15 min/AC in AD-1 and 1038°C/1 hr/AC in AA-VII)

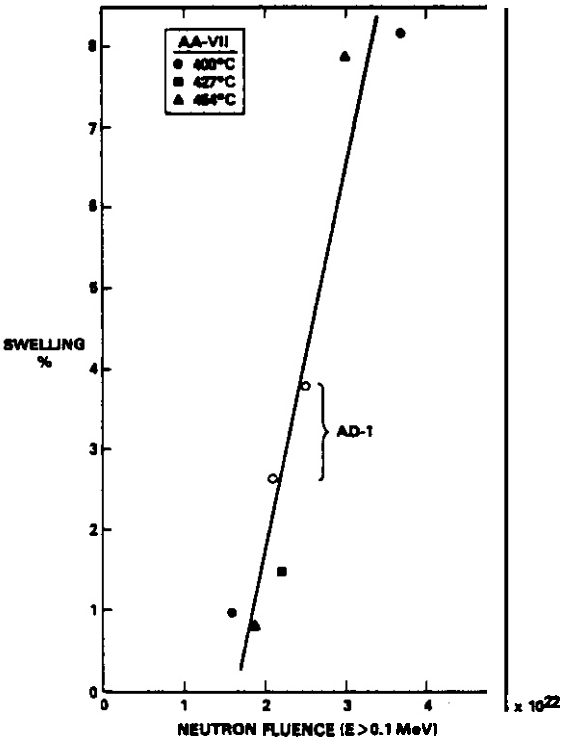

FIGURE 1. Comparison of the AD-1 Data for E20 at 395 and 450°C with the AA-VII Data for this Alloy at 400, 427 and 454°C, Showing the Excellent Agreement Between the Two Experiments.

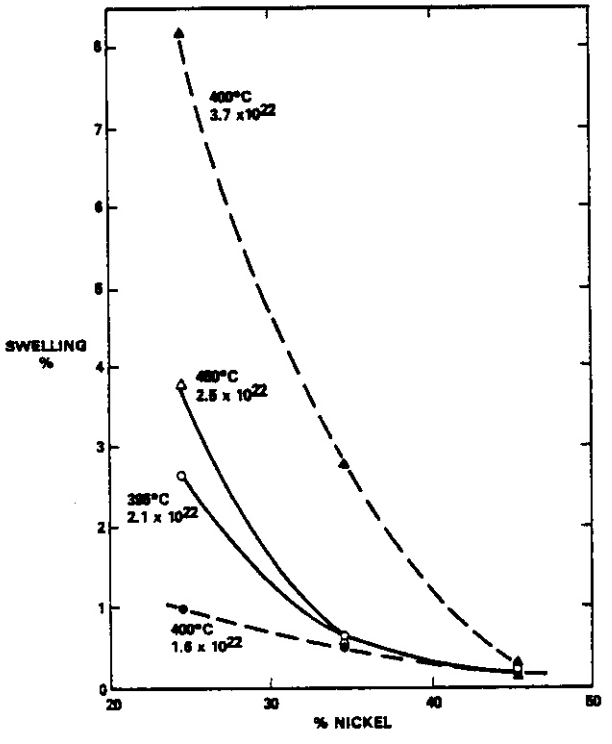

FIGURE 2. Comparison of AD-1 (solid lines) and AA-VII (dotted lines) Data Showing Dependence of Swelling on Nickel Content at ~15% Chromium.

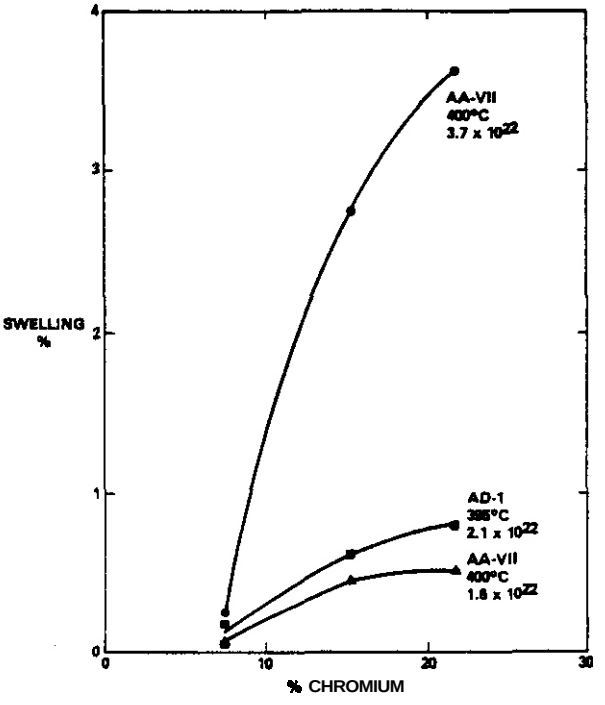

FIGURE 3. Comparison of AD-1 and AA-VII Data Showing Influence of Chromium Level on Swelling at 1.35% Nickel.

TABLE 1

IMMERSION DENSITY RESULTS FOR THE AD-1 EXPERIMENT

Alloy	Composition WGT.%	Swelling % 2.1* 395°C	2.5 450°C	2.5 550°C
E20	Fe-24.4Ni-14.9Cr	2.65	3.76	0.02
E22	Fe-34.5Ni-15.1 Cr	0.63	0.54	-0.02
E23	Fe-45.3Ni-15.0Cr	0.22	0.17	-0.04
E37**	Fe-35.5Ni-7.5Cr	0.18	- .005	0.13
		0.04	. .060	-0.14
E25	Fe-35.1Ni-21.7Cr	0.81	0.58	-0.10

* Neutron fluence in units of 10^{22} n/cm^2 (E > 0.1 MeV)
**Two specimens were measured

Figure 4 shows that the large density of voids found in E25 at 538°C is consistent with the 7.7% swelling measured by immersion density and that the dislocation density is moderately high. In E37 at 593°C, however, there were very few voids of substantial size and these were always associated with rod-like precipitates (See Figure 5). This alloy did not exhibit swelling when determined by immersion density however but actually densified 0.86%.

There are two other important microstructural features in Figure 5. First, the dislocation density is rather low compared to that observed in the E25 specimen. Second, there is also a high density of very small cavities ($\leq$5 nm). These are imaged in Figure 5 in both underfocused and overfocused conditions. The microchemical evaluation of these alloys is now in progress but some conclusions can be drawn at this time.

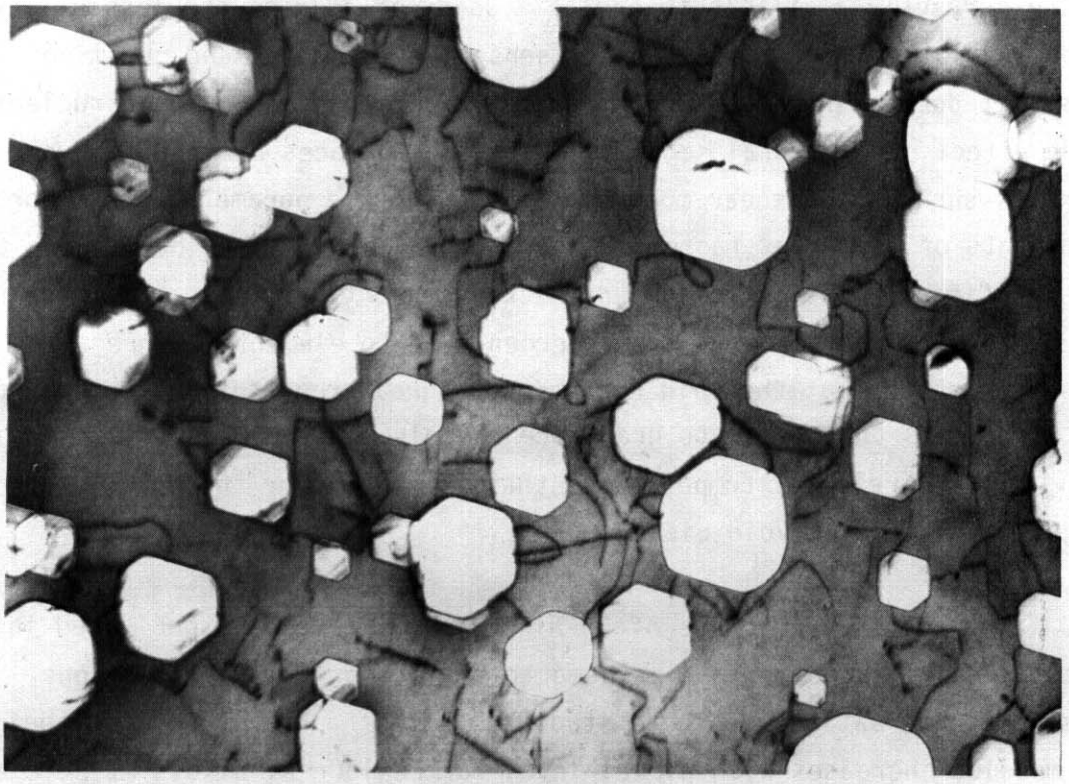

FIGURE 4. Void and Dislocation Structure Observed in Alloy E25 at 538°C and 7.2×10^{22} n/cm^2 (E > 0.1MeV). Magnification 200,000X.

5.3 Discussion

The density data presented in Figures 1-3 suggest that both the chromium and nickel levels are important determinants of the swelling behavior in simple ternary alloys. This conclusion is consistent with the trends observed in nickel ion irradiations of ternary alloys.[2]

The microscopy data of Figures 4 and 5 suggest that, with few precipitate-assisted exceptions, the small cavities formed in the E37 alloy at 593°C either nucleated later or are not growing as rapidly at 7.6 x 10^{22} n/cm2 as are those in the E25 alloy. It also appears that the dislocation evolution is hindered in E37 due to the combined effect of higher temperature and higher chromium level.

The currently available theory[4,5] does not address the possibility that the evolution of dislocations is sensitive to nickel and chromium levels. It does address the effect of matrix composition on void nucleation and the effect of elemental segregation at the surfaces of void embryos. Properties such as the shear modulus and the lattice parameter are important determinants of void bias factors and growth rates, and have been shown to vary significantly with chromium and nickel content. If the shear modulus at the void surface increases a few percent due to elemental segregation, it has been shown that the void resists to a greater extent the acceptance of interstitials and begins to grow more rapidly. Of course it is the shear modulus at void-relevant temperatures that is needed for the calculation of segregation effects on void bias.

Data on the shear modulus of Fe-Ni-Cr alloys have been published in this temperature range and can be used to test theoretical predictions against the observations of these studies. Bates[6] has shown that the shear modulus increases with nickel level for Fe-15Cr-Ni alloys at 24°C and also in the range 450-650°C as shown in Figure 6. He also showed, however, the the shear modulus of Fe-7.5Cr-Ni alloys in the range 20-35% nickel loses its sensitivity to nickel content as the temperature rises, as shown in Figure 7.

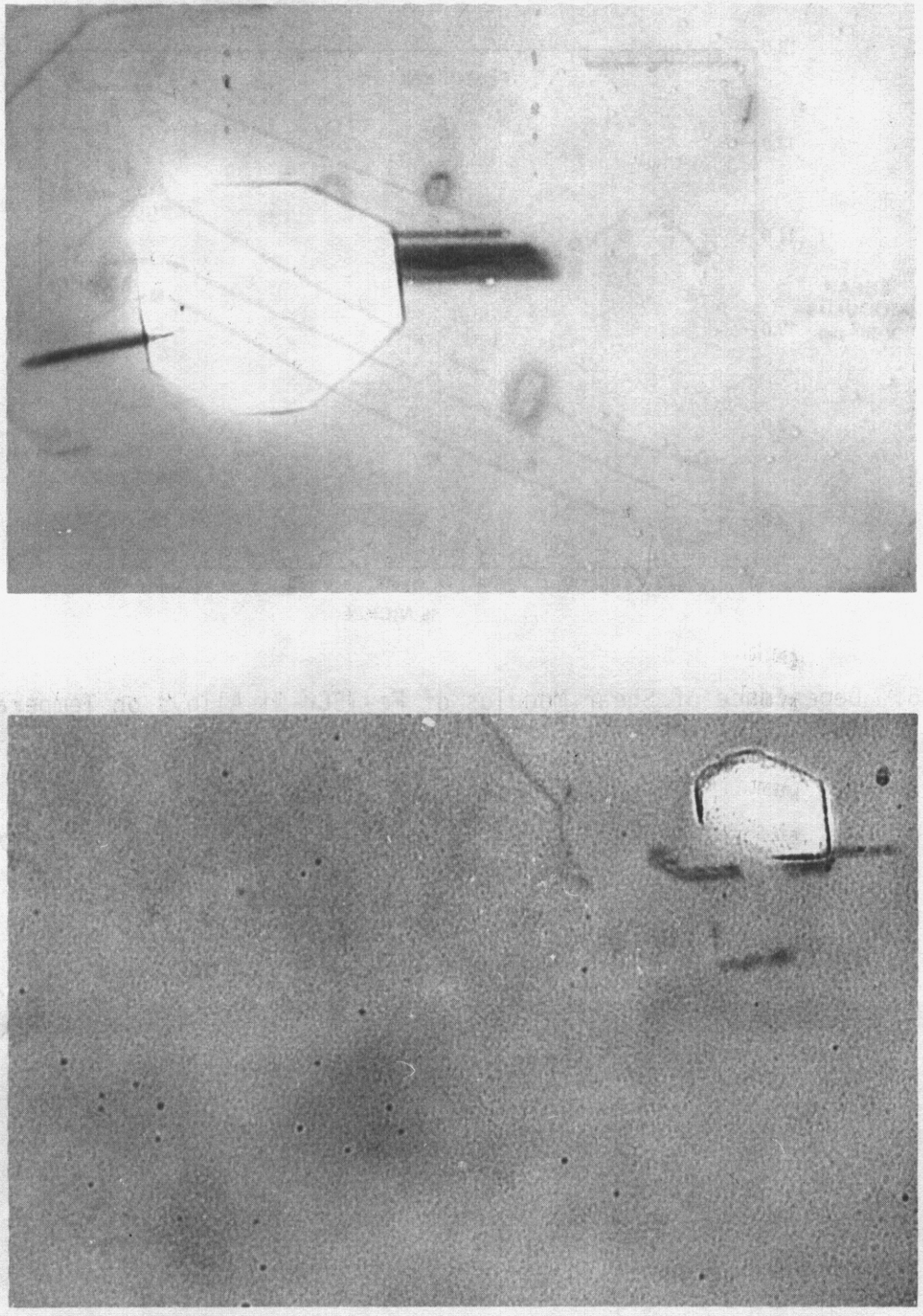

FIGURE 5. Cavity and Dislocation Structure Observed in Alloy E37 After Irradiation to 7.6 x 10^{22} n/cm^2 (E > 0.1 MeV) at 593°C. Small cavities are shown in both overfocused and underfocused conditions. Magnification 200,000x.

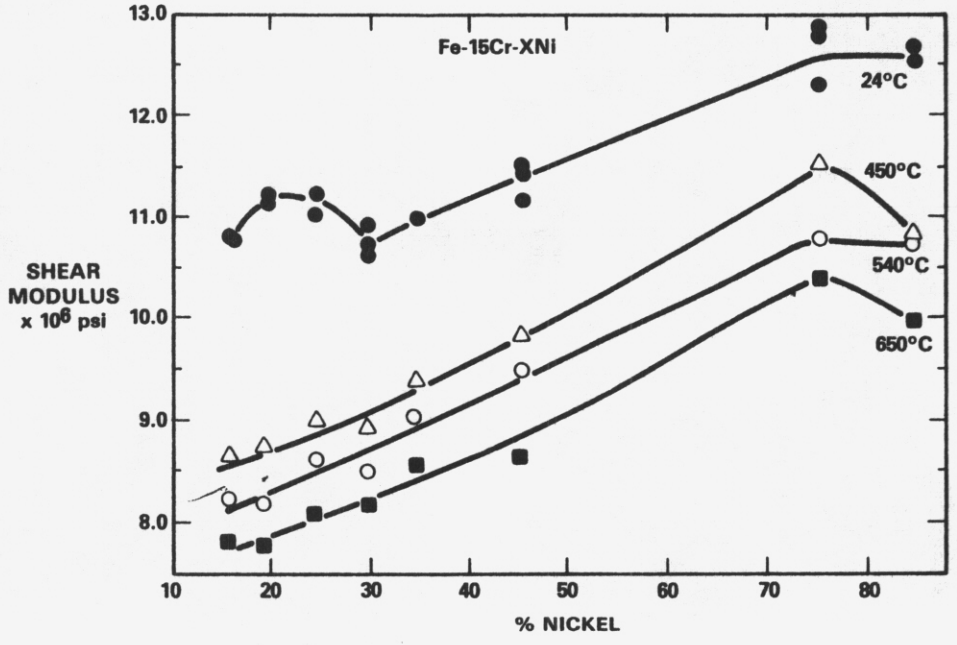

FIGURE 6. Dependence of Shear Modulus of Fe-15Cr-Ni Alloys on Temperature and Nickel Content.(6)

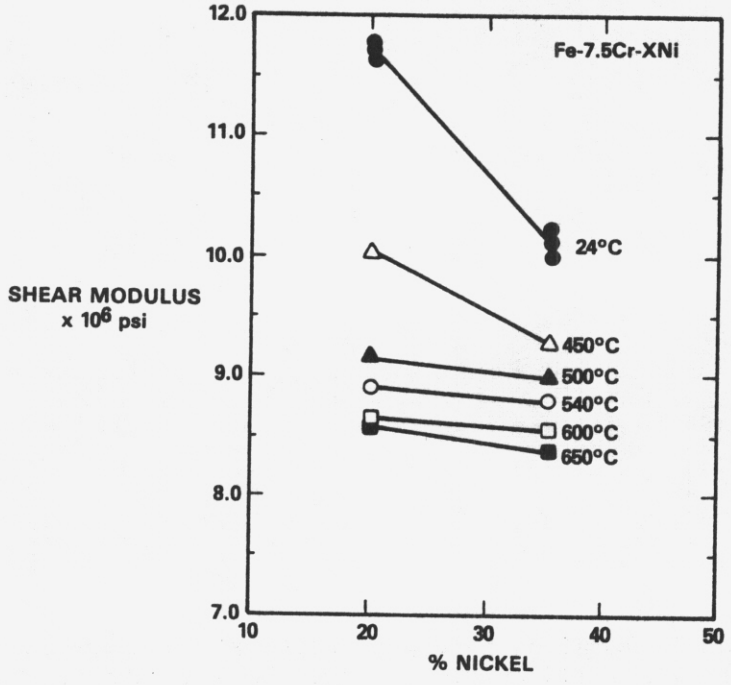

FIGURE 7. Dependence of Shear Modulus of Fe-7.5Cr-Ni Alloys on Temperature and Nickel Content.(6)

In other words there may be no benefit to void growth resulting from segregation of nickel to void surfaces when the chromium level is ~ 7.5%. However, there could be a benefit to void growth when the chromium level is 15% or greater. Thus the relative resistance to void growth in Fe-7.5Cr-35Ni alloy may be a direct consequence of the compositional and temperature dependence of the shear modulus.

It is interesting to note that the minimum in swelling observed by Johnston and coworkers occurs not just at 35-40% nickel but at very low chromium levels,[2] as demonstrated in Figure 8. The segregation of nickel to void surfaces is accompanied by a reduction in chromium level in these alloys.[5]

There are two other observations of interest in these studies. First, the swelling is insensitive to the difference in annealing conditions in the two experiments (954°C/15 min/AC in AD-1 and 1038°C/1 hr/AC in AA-VII). This insensitivity is in contrast to that observed in AISI 316 and reflects the lack of solute atoms such as carbon, silicon and molybdenum, as well as the sensitivity to annealing conditions of the precipitates that form in the presence of these elements. Second, the E37 specimen was observed to densify in AA-VII even though some swelling was present. A similar behavior can be seen for a number of alloys in Table I. What is the origin of this densification in the absence of second phase formation or prior cold-working? A possible explanation[5] lies in the fact that there is a minimum in density in the Fe-Cr-Ni alloy system which at room temperature occurs at 60Fe-40Ni.[5] Figure 9 shows the non-ideal behavior of density with iron and nickel content at zero chromium. Since the E37 alloy lies very close to the minimum in density it is quite possible that the nickel segregation that is known to occur[5] will cause portions of the alloy to have nickel contents both greater and less than the value at the minimum. A consequence of such segregation would be an increase in density. A search for sufficient partitioning of nickel to cause the observed densification is now in progress.

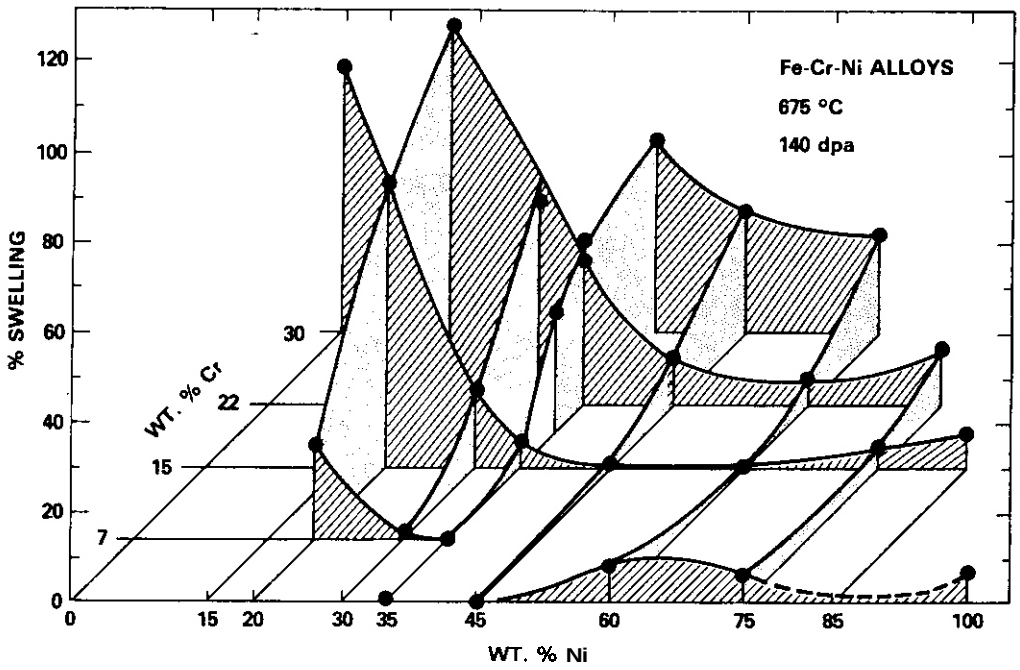

FIGURE 8. Composition Dependence of Swelling in the Fe-Ni-Cr System as Determined by Johnston and Coworkers Using 5-MeV Nickel Ions and Step-Height Measurements.(2)

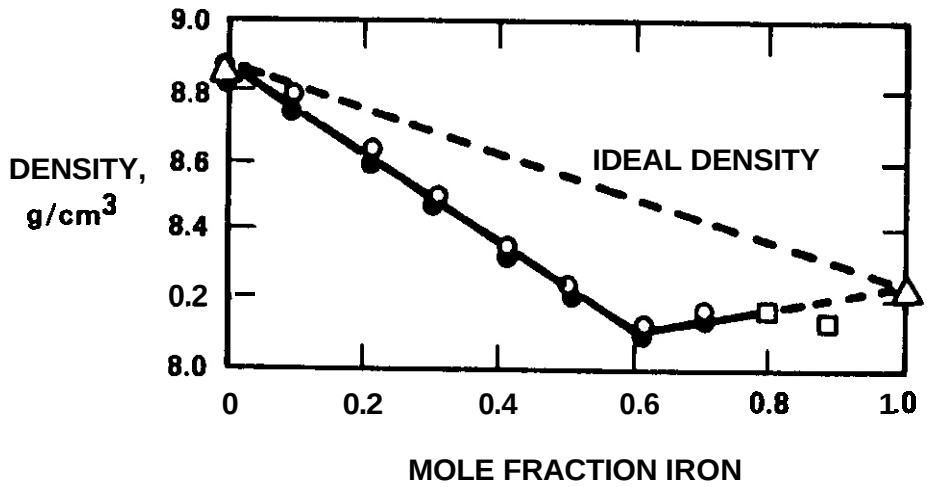

FIGURE 9. The Density of Fe-Ni Binary Alloys at 23°C, as Published by Tomlinson and Andrews.(7)

5.4 Conclusion

The results of two neutron irradiation experiments agree with the conclusions of previous ion irradiations and demonstrate the sensitivity of void growth to nickel and chromium levels in Fe-Ni-Cr alloys. Segregation of nickel to various sinks is invoked to explain both the compositional dependence of swelling and a concurrent densification that occurs. The data also indicate that the dislocation evolution may be sensitive to composition.

6.0 References

1. E8R-II Fusion Test (Capsules 8-284, 8-285 and 8-286), Meeting Record of 6th ADIP Task Group Meeting, August 9-10, 1978, St. Louis, MO, 0-2

2. W. G. Johnston, T. Lauritzen, J. H. Rosolowski and A. M. Turkalo, "The Effect of Metallurgical Variables on Void Swelling," Radiation Damage in Metals, ASM, Cleveland, OH, p. 227, 1976.

3. F. A. Garner, "Correlation of Charged Particle and Neutron-Induced Radiation Damage: The ADIP Experiment Revisited," this report.

4. W. G. Wolfer, "Drift Forces on Vacancies and Interstitials in Alloys with Radiation-Induced Segregation," University of Wisconsin Report UWFOM-483, September 1982; accepted for publication in J. Nucl. Mater.

5. W. G. Wolfer, F. A. Garner and L. E. Thomas, "On Radiation-Induced Segregation and the Compositional Dependence of Swelling in Fe-Ni-Cr Alloys," Effects of Radiation on Materials: Eleventh Conference, ASTM STP 782, H. R. Braaer and J. S. Perrin, Eds., American Society for Testing and Materials, pp. 1023-1041, 1982.

6. J. F. Bates, J. Nucl. Mater. 87 pp. 409-415, 1979.

7. W. J. Tomlinson and A. J. Andrews, Metal Science, 12 (5), pp. 263-264.

7.0 Future Work

This effort will continue, concentrating on further examinations of AA-VII specimens and on tensile tests of the AD-1 specimens. Additional shear modulus measurements are also being performed.

8.0 Publications

None.

DISTRIBUTION

UC-20 (108)

UC-20c (76)

DOE-HQ/Office of Breeder Technology Projects
NE-53
Washington, DC 20545

PB Hemmig, Asst Director, Reactor Physics Tech

DOE-HQ/Office of Fusion Energy (2)
Washington, DC 20545

JF Clark, ER-70
JF Decker, ER-54, G-256

DOE-RL/Office of Asst Manager for Projects & Facilities Management (2)
FMIT Project Office

GM Chenevert, Project Manager

DOE-RL/Office of Asst Manager for Advanced Reactor Programs
Breeder Technology Division

KR Absher, Chief, Technology Development Branch

Argonne National Laboratory (5)
9700 South Cass Avenue
Argonne, IL 60439

LR Greenwood
A. Taylor
RE Nygren
BA Loomis
H. Wiedersich

Battelle Memorial Institute (3)
Pacific Northwest Laboratory
P.O. Box 999
Richland, WA 99352

JL Brimhall
OA Oingee
TD Chikalla

Brookhaven National Laboratory
Associated Universities
Upton, Long Island, NY 11973

Chairman, Nuclear Energy Dept

Columbia University
Plasma Physics Laboratory
New York, NY 10027

RA Gross

General Atomic Company (2)
P.O. Box 81608
San Diego, CA 92138

GR Hopkins
JR Gilleland

INESCO
11011 Torreyana Rd
San Diego, CA 92121

RD Stevenson

Lawrence Livermore Laboratory (3)
P.O. Box 808
Livermore, CA 94550

WL Barmore
MW Guinan, L-396
CM Logan

Los Alamos National Laboratory (4)
P.O. Box 1663
Los Alamos, NM 87544

DJ Dudziak
CR Emigh
J. Fowler, E-546
G. Hurley, E-546

Massachusetts Institute of Technology (5)
77 Massachusetts Avenue
Cambridge, MA 02139

L. Lidsky
NJ Grant, 8-305
JB Vander Sande, 13-5025
I-W Chen, 13-5118
OB Montgomery, NW21

DISTRIBUTION (Cont'd)

Massachusetts Institute of Technology
Nuclear Reactor Laboratory
138 Albany St
Cambridge, MA 02139

OK Harling, NW12-204

McDonnell-Douglas Astronautics Co.
P.O. Box 516
St. Louis, MO 63'166

O. Kummer

Mound Laboratory
P.O. Box 32
Miamisburg, OH 45342

Manager, Tech Appl & Dev

National Bureau of Standards
Gaithersburg, MD 20760

JA Grundl

Naval Research Laboratory (3)
Washington, OC 20375

I. Manning, Code 6672
JA Sprague, Code 6395
LE Steele, Code 6390

North Carolina State University
Department of Nuclear Engineering
Raleigh, NC 26707

JR Beeler, Jr.

Oak Ridge National Laboratory (12)
P.O. Box X
Oak Ridge, TN 37830

K. Farrell
ML Grossbeck
PJ Maziasz
LK Mansur
NH Packan
M. Roberts
Oirector
FG Perey
J. Sheffield
JO Stiegler
C. Weishin
FW Wiffen
Bldg 9204-1
Bldg 9201-2

Princeton University (2)
Plasma Physics Laboratory
Forrestal Campus
P.O. Box 451
Princeton, NJ 08544

K. Wakefield
H. Furth

Rockwell International
8900 DeSoto Ave
Canoga Park, CA 91304

O. Kramer

Sandia Laboratories (2)
P.O. Box 5800
Alhuquerque, NM 87185

FL Vook, Org 5100

Sandia Laboratories
Livermore, CA 94550

WD Wilson

Science Applications, Inc.
1200 Prospect
LaJolla, CA 92037

Or. H. Gurol

University of California (2)
Los Angeles, CA 90024

RW Conn
NM Ghoniem

University of Michigan
Nuclear Engineering
Ann Arbor, MI 48109

T. Kammash

University of Missouri
Mechanical & Aerospace Engineering
1006 Engineering Bldg
Columbia, MO 65211

M. Jolles

DISTRIBUTION (Cont'd)

University of Missouri
Dept of Nuclear Engineering
Rolla, MO 65401

A. Kumar

University of Virginia
Dept of Materials Science
Charlottesville, VA 22901

WA Jesser

University of Wisconsin
1500 W. Johnson Drive
Madison, WI 53706

WG Wolfer

Westinghouse
Advanced Reactors Division
P.O. Box 158
Madison, PA 15663

A. Boltax

Westinghouse
Research and Development Center (2)
1310 Beulah Road
Pittsburgh, PA 15235

S. Wood
JA Spitznagel

Commission for the European Communities
200, rue de la Loi
8-1049 Brussels, Belgium

J. Darvas

Energieonderzoek Centrum Nederland
Westerdionweg 3
NL-1755 ZG Petten, The Netherlands

B. Van Der Schaaf

EURATOM
Joint Research Center Ispra
Materials Science Division
I-21020 Ispra, Varese, Italy

P. Schiller

Hahn-Meitner Institute fur Kernforschung
Glienickerstrasse 100
D-1000 Berlin,
Federal Republic of Germany

H. Wollenberger

Hokkaido University (2)
Faculty of Engineering
Kita hu, Sapporo, Japan, 060

M. Kiritani, Precision Eng
T. Takeyama

Japan Atomic Energy Research Institute (2)
Physical Metallurgy Laboratory
Tokai Research Establishment
Tokai-mura, Naka-gun, Ibaraki-ken, Japan

S. Iwata, Physics
K. Shiraishi, Nuclear Fuel Research

Kernforschungsanlage Julich GmbH
Postfach 1913
D-517 Julich,
Federal Republic of Germany

H. Ullmaier

Kernforschungsanlage Karlsruhe
Institut fur Reaktorbauelemente
Postfach 3640
D-7500 Karlsruhe 1,
Federal Republic of Germany

K. Ehrlich

DISTRIBUTION (Cont'd)

Kyushu University
Research Institute for Applied Mechanics
6-10-1 Hakozaki, Higashi-ku,
Fukuoka, Japan 812

K. Kitajima

National Research Council
Montreal Road
Ottawa, Canada

EV Kornelson

National Research Institute for Metals
Nuclear Materials Division
1-2-1 Sengen, Sakura-mura,
Niihari-gun, Ibaraki 305, Japan

N. Kishimoto

Netherlands Energy Research Foundation
Materials Department
P.O. Box 1
NL-1755 ZG Petten, The Netherlands

W. Van Witzenburg

Osaka University
Dept of Nuclear Engineering
2-1, Yamada-oka, Suita,
Osaka, Japan 565

K. Sumita

Science University of Tokyo
Engineering Dept
Kagurazaka, Shinjuku-ku,
Tokyo, Japan 162

RR Hasiguti

Studiecentrum voor Kernenergie
Centre d'Etude de l'Energie Nucleaire
Boeretang 200
B-2400 Mol, Belgium

J. Nihoul

Swiss Federal Institute
for Reactor Research
CH-5303 Wuerenlingen, Switzerland

WV Green

Tokyo Institute of Technology
12-1, 2-Chome, O-Okayama
Meguro-ku, Tokyo, Japan

K. Kawamura

United Kingdom Atomic Energy Authority
Atomic Energy Research Establishment
Metallurgy Division
Building 388
Oxfordshire, OX11 ORA, UK

DR Harries

University of Tokyo (3)
7-3-1 Hongo
Bunkyo-ku, Tokyo, Japan 113

Naohira Igata, Met & Mater Science
Shiori Ishino, Nuclear Eng
Taijiro Uchida

DISTRIBUTION (Cont'd)

HEDL (35)

SD Adkin	W/A-58	EK Dpperman	W/A-58
TK Bierlein	W/A-1	NF Panayotou	W/A-65
HR Brager	W/A-64	EF Parker	W/E-17
LL Carter	W/B-47	RW Powell	W/A-64
DG Doran (5)	W/A-57	RJ Puigh	W/A-58
EA Evans	W/C-23	FH Ruddy	W/C-39
FA Garner	W/A-57	FA Schmittroth	W/A-4
DS Gelles	W/A-64	WF Sheely	W/C-62
R. Gold	W/C-39	RL Simons	W/A-57
HL Heinisch	W/A-57	JL Straalsund	W/A-61
DL Johnson	W/A-4	HH Yoshikawa	W/C-44
GD Johnson	W/A-65	Central Files (3)	W/C-110
NE Kenny	W/C-115	Publ Services	W/C-115
FM Mann	W/A-4	Doc Clearance	W/C-123
WN McElroy	W/C-39		